THE MANGROVE TANGLE

SHORT-TERM BIO-PHYSICAL INTERACTIONS IN COASTAL MANGROVES

Erik M. Horstman

THE MANGROVE TANGLE

SHORT-TERM BIO-PHYSICAL INTERACTIONS
IN COASTAL MANGROVES

Cover photo: Mangroves fringing the coast of Ko Libong, Thailand (by Erik Horstman)

THE MANGROVE TANGLE

SHORT-TERM BIO-PHYSICAL INTERACTIONS
IN COASTAL MANGROVES

PROEFSCHRIFT

ter verkrijging van
de graad van doctor aan de Universiteit Twente,
op gezag van de rector magnificus,
prof. dr. H. Brinksma,
volgens besluit van het College voor Promoties
in het openbaar te verdedigen
op vrijdag 25 april 2014 om 16.45 uur

door

Erik Martijn Horstman
geboren op 6 december 1983
te Enschede

Dit proefschrift is goedgekeurd door:

prof. dr. S.J.M.H. Hulscher   promotor
dr. ir. C.M. Dohmen-Janssen   co-promotor

Although nature commences with reason and ends in experience
it is necessary for us to do the opposite,
that is to commence with experience
and from this to proceed to investigate the reason.

- Leonardo Da Vinci (1452-1519)

CONTENTS

PREFACE

It is one of these great contradictions, you finish your thesis by writing the preface. The only part that is read by everybody – don't worry, I do the same – and, even better, it is not subject to reviews and revisions. Finally! Off we go…

I should start this preface with Marjolein, my daily supervisor. It's almost twelve years ago now that I had my first class in university, and it was by you. You guided me through the entire scientific rollercoaster by supervising my BSc, MSc and PhD theses! And it has really been a pleasure. You were the one who always believed I could manage whatever problem we faced, more than I ever did myself, and you coped with all my moods and insecurities. I enjoyed your mentorship, the countless meetings, the regular chats and your visit (together with Tjeerd) when I was overseas. I couldn't have accomplished all this without your relentless support, for which I'm truly thankful.

Suzanne, you're my second 'mother in science'. After my master's thesis, you didn't let me go. While I never really considered a scientific career, I thankfully accepted your offer to write a PhD proposal. The proposal didn't make it, but I'm very glad I got this great opportunity to move to the mangroves instead. Throughout my PhD, your critical yet supportive attitude has been of great value to whatever I did. Even these days, you keep on encouraging me to embrace new opportunities for future research, and I sincerely appreciate that.

Well, talking about my 'mothers in science', I should finish the triplet with Kathelijne. You were in charge of my MSc graduation committee and ever since, we've been collaborating on multiple occasions. Organising NCK (theme)days (together with Lisette and Wouter) and doing consultancy research for Deltares and Rijnland, it were the less regular activities we undertook together, but they were nice distractions. And we always succeeded! Thank you for all the 'jobs' you created for me.

Although my supervisors were important, this thesis would never have come into existence without the help of Martijn and Niels-Jasper. Together, we battled mud, mosquitos, monkeys and some snakes. Not to forget about all the problems we faced in arranging our fieldwork and

our living in a country totally different than what we were used to. Fieldwork was incredibly tough and we made insane hours. But it was definitely worth it: we got an awesome set of data. Thank you guys, for not giving up right the first time when I dropped you in the mud loaded with backpacks and for not letting me down on my way-too-optimistic fieldwork planning. And… work hard, party harder! The road trips from Singapore to Trang and back, with Martijn and Demis, were unforgettable experiences. Somehow we managed to get ourselves and a van full of weird looking research equipment through customs at disputed borders. We also enjoyed local life in Trang and made some great trips. Thanks too to Ali and Jos for visiting us, cheering us up and for taking us on an island tour. The best times were when the research buddies (aka party squad) from Singapore came over. Alison, Thorsten, Eva and Siti, it was great fun hosting your stays and having you around. Alison, our visit to your family was truly unforgettable!

Our stay and work in Thailand would have been impossible and much less comfortable without the help of many local people. I would like to thank Chanyut for introducing us to the Trang mangroves and for hosting some of our laboratory work on the beautiful campus of the Rajamangala University of Technology Srivijaya in Trang. Siron was our great boatman, he knew exactly how and when to get to our field sites and somehow he always managed to get my very basic Thai phrases, even on the phone. Katai and her family helped us out with arranging our housing and transport. They even got me to sign a contract I couldn't read a single letter of! We could always count on them when we didn't know how or where to purchase simple things as steel or bamboo rods or where to go for the best food in town. 'Kop kun krap' to all of you!

All these adventures started when I moved to Singapore early 2010. Together with Thorsten, I was warmly welcomed in the APE lab at the National University of Singapore. Ted, Dan and Demis greatly contributed to the preparation of the field campaign. The many field trips with Thorsten, exploring the mangroves around the Malay peninsula, were great experiences. Except from chasing me with a tremendous amount of forms and regulations, the SDWA staff also facilitated my research, in Singapore as well as in Thailand. Thanks Claire, Ivy, Sae'dah, Juli and Sally for being on top of all the paper work. Next to the inspiring working environment, living in Singapore wouldn't have been so much fun without all the people I met within and outside the university. Siti (and friends), Rachel (and Foxy), Jen and the APE lab crew, you're just a few of them, but I'm mostly grateful for meeting you.

Being part of the SDWA research program, we also had regular mangrove meetings with the Dutch counterparts. Thorsten, Tjeerd and Claire were always there to share the latest research output. Sometimes Peter and Bas joined in as well. I'm indebted to all of you for the helpful and inspiring feedback. Tjeerd, I would like to thank you as well for all your support and your positive attitude throughout this project. I'm also indebted to Pedro and Jurjen, for devoting their final master's projects to the processing and analysis of the wave data. Your efforts have definitely helped to better understand some of the field data.

Without a doubt, my PhD wouldn't have been the same without the endless support by my colleagues form the WEM department. They organized a great goodbye party when I left, always stayed in touch while I was away and they were still there when I returned! It was awesome to meet up with Jolanthe, Wiebe, Bas and Wouter in Shanghai, but I felt a bit lost when you went back to Twente and I had to wait for my plane back to Singapore. Thinking of conferences… there were many more nice travels involved in my PhD. But the best one was definitely with Olav and Suleyman to Beijing, extended with some holidays in Yangshuo and Xiamen. Back home, I had a bunch of great 'roomies' that helped me survive the long office hours. Henriëtte, Tanya, Olav, Jolanthe, Arjan and Anne, I enjoyed all the teas, coffees, cookies and stories we shared. Ronald and Suleyman, I think you count as a 'roomies' as well! There are many more colleagues I would like to thank for making my stay at the WEM department as enjoyable as it was. Joep, Joanne, Lianne, Wouter, Bas, Jord, Pieter, Juan Pablo, Wenlong, René, Jan, Denie, Nicolas, Sameer, Kurt, Fenneke, Lisette, thanks for sharing lunch walks, running during lunch, cycling after working hours, joining in the BATA team, occasional dinners, having beers together, or whatever (crazy) things we did. And, of course, thanks to Brigitte, Anke and Joke for making everything work and for cheering up our days at the office.

Getting there… I would also like to thank my friends for the distraction they offered whenever I thought I actually needed to work. Jaap, Mats and Marcel, thanks for dropping by in Singapore. Han and Michiel, thanks for getting me on a road bike and for the great trips we made. Sander and Jessica, thanks for challenging my running performance. The occasional unplanned dinners with Wing, Wiebe, Jolanthe and Freek, Michiel and Hendrika and Joanne and Bernd were a great pastime too. I really should start planning some dinners at my place now in return. You're invited!

Olav and Jolanthe, my 'paranimfen', your names popped up several times before. Never a dull moment in 'Ollie and Jollie's coffee corner'! We shared so many experiences over the past couple of years that I couldn't imagine defending this thesis without you at my side.

De basis voor al dit werk lag natuurlijk bij mijn familie. Zij hebben mij altijd onvoorwaardelijk gesteund, waar ik ook ging en wat ik ook deed. Mamma, je hebt het lang niet altijd makkelijk, maar je bent er altijd voor me. Samen met pappa heb jij me de kans gegeven om door te leren en ervoor gezorgd dat het me aan niets ontbrak. Iris, je bent de beste zus die ik me kan wensen. Ik kan altijd bij je terecht met m'n eindeloze geklaag, maar we doen samen ook de leukste dingen en samen met Kahraman sta je altijd voor me klaar. Oma, je bent een taaie, ik wist dat je er nog bij zou zijn. Hopelijk heb ik nu weer wat meer tijd om jullie te helpen en om samen meer leuke dingen te doen.

Pappa, ik denk dat ik ons 'vrolijk orthodoxe' geloof een beetje kwijt ben geraakt door de drukte de afgelopen jaren. Jij vond dat het wel wat minder kon met al dat geleer en eigenlijk denk ik dat je wel gelijk had. Maar je had het vast geweldig gevonden om mij de wereld rond te zien reizen en om dit boekje te zien. En m'n 'geloof', daar ga ik aan werken.

SUMMARY

Mangroves are coastal wetland ecosystems in the upper intertidal area, consisting of salt-tolerant vegetation dwelling on fine substrates. These ecosystems occur in the tropics and sub-tropics and thrive in sheltered, low-energy environments such as estuaries and lagoons. This thesis focusses on mangroves' regulating services providing coastal safety. These services are the result of characteristic bio-physical interactions between the mangrove vegetation, hydrodynamics and sediment dynamics in the intertidal. The spectrum of bio-physical interactions in mangroves comprises temporal scales ranging from seconds to centuries and spatial scales ranging from microscopic mud particles to the continental shelf (Chapter 1). Enhancing our understanding of the mechanisms determining the contribution of mangroves to coastal safety, in terms of sediment trapping and wave attenuation, requires sound knowledge of the short-term bio-physical interactions. This thesis investigates (i) the effects of the biogeophysical mangrove settings on tidal-scale flow routing, (ii) the sensitivity of the tidal-scale hydro-dynamics and sediment deposition patterns to instantaneous changes of the biogeophysical mangrove settings and (iii) the relation of wave attenuation in coastal mangroves with vegetation densities and sediment deposition rates.

COMBINING FIELD OBSERVATIONS AND NUMERICAL SIMULATIONS
The short-term bio-physical interactions in coastal mangroves were studied by a combined observational-numerical approach. Field data were obtained at three field sites in relatively undisturbed mangroves fringing the Thai Andaman coast. These sites featured differences in their hydrodynamic exposure and morphology. Consequently, contrasting vegetation compositions and densities were observed both between and within sites. At one site, the mangrove forest was elevated above mean sea level, had steep cliffs and was dissected by tidal creeks (Figure IA). At the other two sites, the intertidal area consisted of gently sloping mudflats overgrown with mangrove vegetation starting at elevations slightly below mean sea level (Figure IIA). Vegetation at the latter sites was clearly zonated, in accordance with tidal inundation regimes, while the mixed vegetation composition at the former site is typical for less exposed mangroves.

In addition to direct observations from the field, a numerical model of one of the study sites was constructed in Delft3D (Chapter 3). This model allowed for the variation of physical parameters beyond the conditions observed in the field. Mangrove vegetation was represented by rigid vertical cylinders in this model, causing additional drag and turbulence. Based on a detailed calibration and validation of both a three-dimensional model (3D) and a depth-averaged two-dimensional model (2DH; neglecting vegetation induced turbulence), we concluded that both models accurately represented field observations. The 2DH model had 80-90% shorter calculation times than the 3D model, enabling us to perform a comprehensive sensitivity analysis. Representative depth-averaged vegetation characteristics were obtained at an elevation of about one-third to one-half of the maximum tidal inundation depth of the mangroves.

LINKING TIDAL-SCALE FLOW ROUTING AND BIOGEOPHYSICAL MANGROVE SETTINGS

Flow routing in mangroves has great implications for the transport and distribution of sediments and nutrients and hence for mangroves' development and survival. Chapter 2 addresses the tidal-scale hydrodynamics in the different field sites and the correlation with the specific topography, vegetation and hydrodynamic exposure of these sites. At the elevated mangrove site dissected by tidal creeks, two distinct flow regimes were observed: *creek flow* prevailed when water levels remained below a dense vegetation layer at the mangrove fringe bordering the estuary (Figure IB), while *sheet flow* prevailed when this threshold was exceeded and direct inflow over the forest fringe was facilitated (Figure IC). At the gently sloping sites without creeks, tidal flows were typically sheet flows. In contrary to the sheet flows in the elevated mangrove site, sheet flow directions at the low-lying sites were susceptible to forcing by river discharges. With decreasing water depths and/or increasing vegetation densities, the persistence of this forcing reduced and sheet flows obeyed the vegetation induced cross-shore water level gradients.

Flow velocities in the creeks were up to an order of magnitude greater ($O(10^{-1})$m/s) than those within the vegetation ($O(10^{-2})$m/s), where velocities decreased along with increasing vegetation densities. Distinct vertical variations of the bed and the vegetation were found to cause irregular velocity patterns along the vertical, within the vegetation as well as in the creeks. Global tidal flux calculations demonstrated the significant contribution of the creek flow to the total tidal prism in higher elevated mangroves. These findings provide observational evidence for the flow routing phenomena in coastal mangroves.

EFFECTS OF CHANGING BIOGEOPHYSICAL SETTINGS TO TIDAL MANGROVE DYNAMICS

Chapter 3 elaborates on the establishment of characteristic tidal-scale flow routing and sedimentation patterns due to bio-physical interactions in a creek-dissected mangrove system. The relative contribution of vegetation and topography to both the tidal flow routing and to sediment deposition patterns was investigated. Field observations in the elevated mangrove site showed that the sheltered interior of the forest was an effective sediment sink during the higher tides (Figure IB,C). Numerical simulations indicated that both the tidal-scale flow routing and

the sediment deposition rates and patterns were greatly induced by the characteristic topography of this field site. Model simulations also confirmed that the studied mangrove site was in a stable condition, wherein vegetation densities hardly affected the deposition rates. On the other hand, simulated deposition rates changed in concordance with the removal of topographic features or changes of the relative elevation of the site.

This chapter also presents an exploration of the sensitivity of the tidal-scale bio-physical interactions to instantaneous changes of the vegetation, relative elevation, sediment supply and landward mangrove extent. The initial system response – or its adaptive capacity – to these instantaneous changes was simulated with the depth-averaged numerical model. Sediment trapping within the mangroves reduced substantially when sediment inputs diminished and with a loss of inland mangrove area, as caused by for example river damming or the construction of aquaculture ponds. Deeper inundations, as may result from sea level rise, were found to disturb the present stable state of the mangrove system: sheet flows through the forest increased (Figure ID), and spatially averaged deposition rates dropped markedly when deeper inundations coincided with decreasing vegetation densities (Figure IE). These results indicate the sensitivity of mangroves' ecosystem engineering ability, in terms of sedimentation, to environmental change.

QUANTIFYING WAVE ATTENUATION AND SEDIMENT TRAPPING IN MANGROVES

Chapter 4 presents a mechanistic study into the changes of wave parameters along cross-shore transects through mangroves and the correlation of the observed wave attenuation with vegetation characteristics and sediment dynamics. These processes were studied along two cross-shore transects at the gently sloping sites, where vegetation composition and structure were mapped thoroughly. Wave attenuation rates were found to be greater within denser vegetation (Figure IIB) and for higher incident waves (Figure IIC). Generalized wave attenuation rates, comprising a range of incident wave heights and water depths, increased from 0.002 m^{-1} in the sparsely vegetated forest fringes to 0.012 m^{-1} in the dense *Rhizophora* vegetation at the landward extent of the transects. Further analysis of the observed attenuation rates showed that decreasing water depths, and consequently increasing volumetric vegetation densities, induced wave attenuation to increase substantially in the densest *Rhizophora* vegetation, while such an effect was absent in the sparser *Avicennia*/*Sonneratia* vegetation (Figure IID,E).

Amelioration of wave energy by the mangroves facilitated greater deposition rates along both transects (Figure IIB,C). Reduced hydrodynamic activity towards the denser vegetated back of the mangrove forest allowed for the deposition of finer sediments, as confirmed by the gradual fining of the bed material. Together with the simulation results of Chapter 3, these findings corroborate the positive correlation between vegetation density and sediment trapping within exposed mangroves at elevations around mean sea level (Figure IIE). These results provide insights in the coastal defence function of mangroves by quantifying their contribution to wave attenuation and sediment trapping.
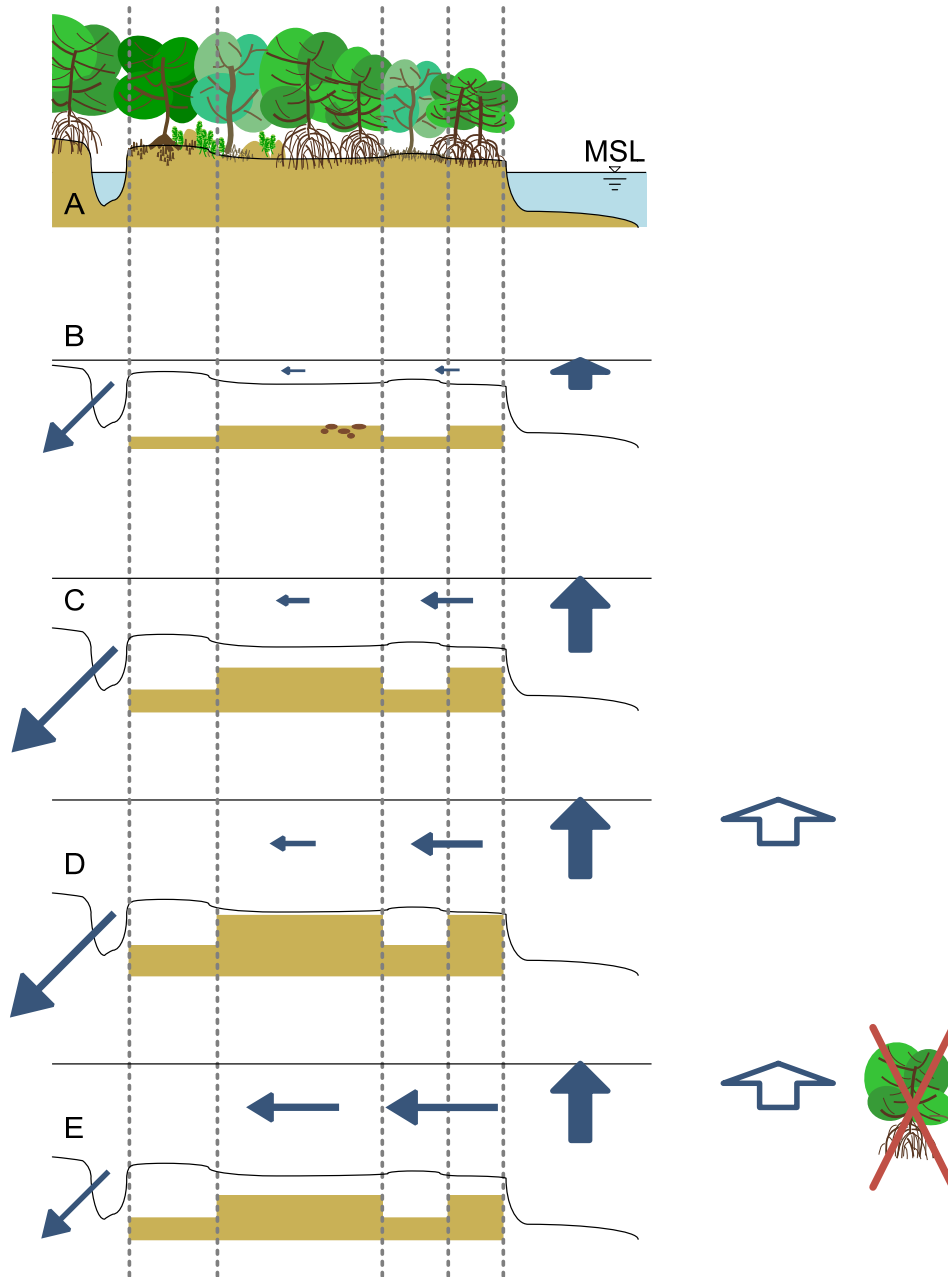
Figure I – Observed and simulated trends in tidal-scale flow routing and sediment deposition in (A) an elevated mangrove stand dissected by tidal creeks. (B) Tidal flow routing and deposition rates under normal conditions. The lower plots indicate the effects of (C) spring tides, (D) an instantaneous increase of the sea level and (E) an instantaneous increase of the sea level coinciding with the removal of mangrove vegetation. Blue arrows represent flow velocity magnitudes and sand coloured boxes indicate deposition patterns. Indicated zones represent (left to right): creek banks, the mangrove interior, a levee and the forest fringe.

Figuur I – Geobserveerde en gesimuleerde trends in de getijstroming en sedimentdepositie in (A) een hooggelegen mangrovegebied doorsneden door getijkreken. (B) Patronen in de getijstroming en sedimentdepositie onder normale omstandigheden. De figuren eronder laten het effect zien van (C) springtij, (D) een plotselinge verhoging van de zeespiegel en (E) een plotselinge stijging van de zeespiegel in combinatie met het verdwijnen van de mangroven. De blauwe pijlen geven een indicatie van de relatieve stroomsnelheden en de zandkleurige blokken representeren het depositiepatroon. De onderscheiden zones zijn (van links naar rechts): kreekbanken, het hart van het bos, een lage bank in het bos en de rand van het bos.
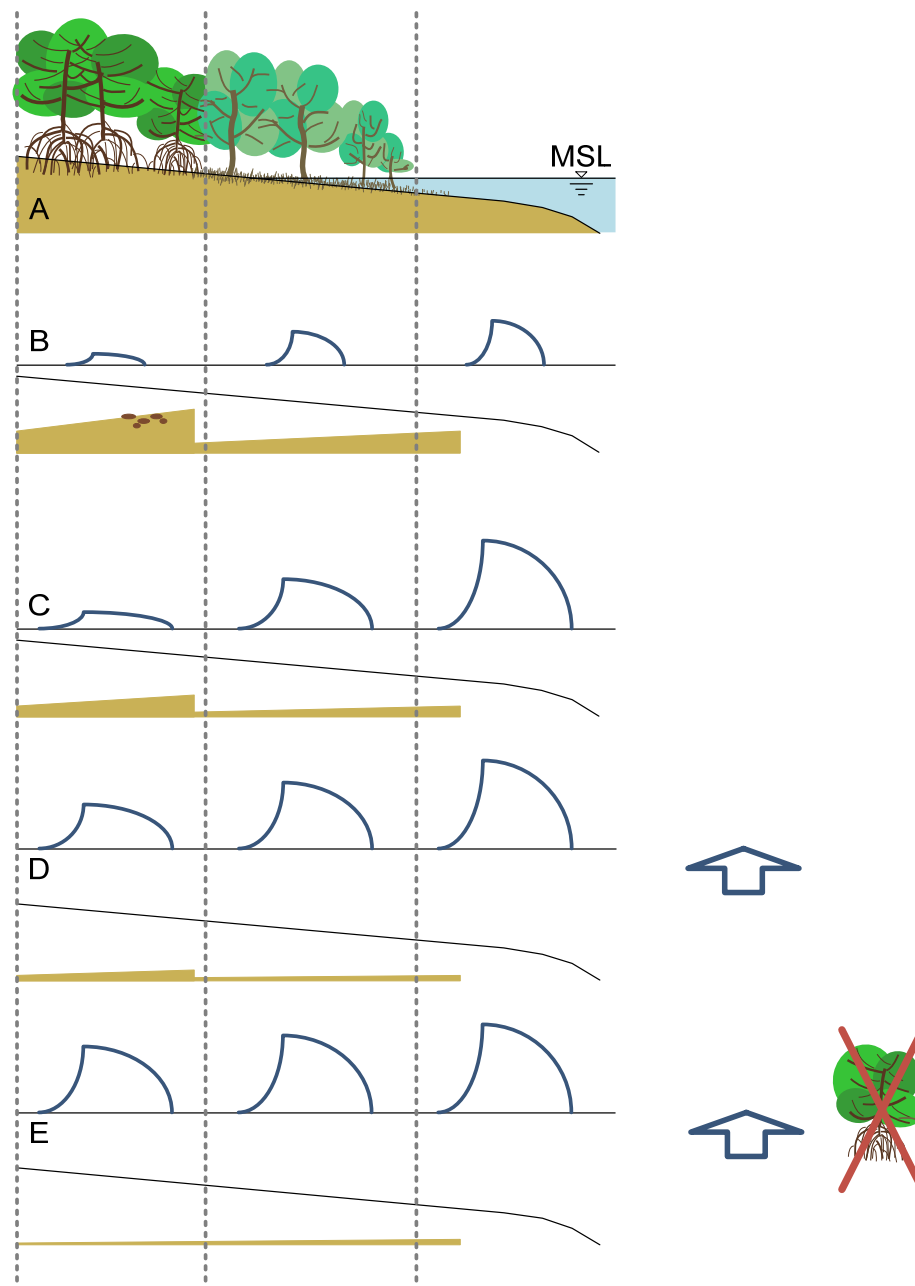
Figure II – Observed and extrapolated trends in wave attenuation and sediment deposition in (A) a mangrove dwelling a smoothly sloping intertidal area. (B) Wave attenuation and deposition rates under normal low-energy conditions. The lower plots indicate how these processes could be affected (C) during storm conditions, (D) by increased water levels, e.g. during spring tides, and (E) by combined high water levels and vegetation removal. Blue waves represent wave heights and sand coloured boxes indicate deposition patterns. Indicated zones represent (left to right): dense *Rhizophora* forest, a sparsely vegetated *Avicennia*/*Sonneratia* fringe and the mudflat.

Figuur II – Geobserveerde en geëxtrapoleerde trends in de golfdemping en sedimentdepositie in (A) mangroven in een intergetijdengebied met een kleine bodemhelling. (B) Golfdemping en depositie onder normale condities met lage golven. De figuren eronder laten zien hoe deze processen kunnen veranderen (C) tijdens een storm, (D) door een hoger waterniveau, bijv. tijdens springtij, en (E) door een gecombineerd hoger waterniveau en de afwezigheid van mangroven. De blauwe golven geven de golfhoogte weer en de zandkleurige blokken representeren het depositiepatroon. De onderscheiden zones zijn (van links naar rechts): dichte *Rhizophora* begroeiing, dunnere begroeiing van *Avicennia*/*Sonneratia* bomen aan de rand van het bos en het slik voor het bos.

Samenvatting

Mangroven zijn moerasachtige ecosystemen die voorkomen in de hogere delen van het intergetijdengebied, ongeveer tussen gemiddeld zeeniveau en het hoogste hoogwater. Mangrovebossen groeien op fijn sediment zoals silt en klei en de begroeiing bestaat uit zout-bestendige mangrovebomen en struikachtigen. Deze ecosystemen zijn te vinden in de tropen en subtropen en komen voor in kustgebieden die beperkt zijn blootgesteld aan golven en stromingen, zoals estuaria en lagunes. Dit proefschrift gaat in op de bijdrage van mangroven aan de kustveiligheid. Deze beschermende functie is het gevolg van bio-fysische interacties tussen de mangrovebegroeiing, de hydrodynamica en de sedimentdynamiek in het intergetijdengebied. Het spectrum van de bio-fysische interacties in mangroven bestrijkt tijdschalen variërend van seconden tot eeuwen en ruimteschalen die reiken van microscopisch kleine kleideeltjes tot continenten (Hoofdstuk 1). Voor het vergroten van ons begrip van de bijdrage van mangroven aan de kustveiligheid door het invangen van sediment en het dempen van golven, is een grondige kennis vereist van de bio-fysische interacties op korte tijdschalen. Dit proefschrift heeft tot doel (i) de invloed van verschillende biogeofysische kenmerken op de getijstromen door de mangroven in kaart te brengen, (ii) het effect van plotselinge veranderingen van de biogeofysische omgevingskenmerken op de getijstromen en sedimentdepositie in de mangroven te analyseren en (iii) de demping van golven in mangroven te correleren met de vegetatiedichtheden en met sedimentdepositie.

HET COMBINEREN VAN OBSERVATIES IN HET VELD EN NUMERIEKE SIMULATIES

Voor het analyseren van de bio-fysische interacties in mangroven wordt in dit proefschrift gebruik gemaakt van observaties in het veld én simulaties met een numeriek model. De velddata zijn verzameld in drie relatief onaangetaste mangrovebossen langs de Thaise Andaman-kust. Elk van deze gebieden verschilde qua blootstelling aan stromingen en golven en qua bodemprofiel (morfologie). Daardoor verschilde ook de samenstelling en dichtheid van de begroeiing sterk, zowel binnen een gebied als tussen de verschillende gebieden. In één studiegebied was het mangrovebos gelegen op een plateau met een bodemhoogte boven gemiddeld zeeniveau. Dit plateau had een steile helling aan de zeezijde en werd doorsneden door getijkreken (Figuur IA). In de twee andere gebieden nam de bodemhoogte zeer geleidelijk

toe. Voor het bos lagen uitgestrekte slikken zonder vegetatie en de mangrovebegroeiing begon op een bodemhoogte net onder gemiddeld zeeniveau (Figuur IIA). De mangroven in deze twee gebieden waren duidelijk gezoneerd, in overeenstemming met de inundatiefrequentie door het getijregime. De gemengde samenstelling van de mangroven in het eerstgenoemde gebied daarentegen was karakteristiek voor hogergelegen mangroven die minder zijn blootgesteld aan hydrodynamische activiteit.

Naast de observaties in het veld is van een van de studiegebieden een numeriek model geconstrueerd in Delft3D (Hoofdstuk 3). Dit model maakte het mogelijk om fysische parameters te variëren, waardoor omstandigheden nagebootst konden worden die niet in het veld waren waargenomen. In dit model werd de begroeiing geschematiseerd tot onbuigzame verticale cilinders, waaromheen extra wrijving en turbulentie optrad. Er is een uitgebreide kalibratie en validatie uitgevoerd van zowel een driedimensionaal model (3D) als een diepte-gemiddeld tweedimensionaal model (2DH; waarin turbulentie rondom de vegetatie niet wordt berekend). Op basis daarvan kon geconcludeerd worden dat beide modellen de observaties uit het veld accuraat reproduceerden. Het 2DH-model had daarbij 80-90% minder rekentijd nodig dan het 3D-model en daardoor was het mogelijk om een uitgebreide gevoeligheidsanalyse uit te voeren. De representatieve dieptegemiddelde kenmerken van de mangrovebegroeiing, nodig voor dit 2DH-model, kwamen overeen met de dichtheden en afmetingen op een hoogte van één-derde tot de helft van de waterdiepte in de mangroven bij het hoogste hoogwater.

DE RELATIE TUSSEN GETIJSTROMEN EN BIOGEOFYSISCHE MANGROVE KARAKTERISTIEKEN
Getijstromen in mangroven bepalen de aanvoer en de verdeling van sediment en nutriënten en zijn dus van essentieel belang voor de ontwikkeling en het behoud van mangrovekusten. In Hoofdstuk 2 wordt de vraag behandeld hoe de hydrodynamica ten gevolge van het getij in mangroven samenhangt met de specifieke topografie, de vegetatie en de blootstelling aan stromingen en golven van de verschillende gebieden. In het hogergelegen mangrovegebied doorsneden door getijkreken, werden twee getijregimes geobserveerd: *creek flow* was dominant zolang het waterpeil niet hoger kwam dan een dichte laag van mangrove wortels op de rand van het bos grenzend aan het estuarium (Figuur IB), *sheet flow* overheerste juist wanneer waterpeilen deze drempel overschreden en water direct vanuit het estuarium het bos instroomde (Figuur IC). In de lagergelegen gebieden zonder kreken werden de stromingspatronen continu gedomineerd door *sheet flow*. In tegenstelling tot de *sheet flow* in de hogergelegen mangroven, werd de *sheet flow* in de lagergelegen gebieden beïnvloed door de richting en sterkte van rivierafvoeren. Deze invloed van rivierafvoeren nam af met het kleiner worden van de waterdiepte en/of een grotere vegetatiedichtheid in de mangroven. Uiteindelijk volgde de *sheet flow* dan het door de wrijving met de mangroven veroorzaakte kustdwarse verhang van de waterspiegel.

Stroomsnelheden in de kreken waren tot een orde groter ($O(10^{-1})$m/s) dan de stroomsnelheden in de vegetatie ($O(10^{-2})$m/s), waar de stroomsnelheden steeds kleiner werden met het toenemen van de dichtheid van de begroeiing. Specifieke kenmerken van de begroeiing en het

bodemprofiel veroorzaakten een onregelmatig verticaal profiel van de horizontale snelheden. Indicatieve berekeningen van de getij-instroom toonden aan dat de *creek flow* een grote bijdrage leverde aan de totale getij-instroom in hogergelegen mangroven. Deze resultaten verschaffen empirisch inzicht in de stromingspatronen in mangrovekusten.

EFFECTEN VAN BIOGEOFYSISCHE VERANDERINGEN OP GETIJDYNAMIEK IN MANGROVEN

In Hoofdstuk 3 wordt het effect van de bio-fysische interacties op de kenmerkende patronen van getijstromen en sedimentdepositie in mangroven verder uitgewerkt. De relatieve invloed van de begroeiing en de topografie op zowel de getijstroming als de sedimentdepositie zijn in kaart gebracht. Observaties in het hogergelegen mangrovegebied toonden aan dat het beschutte gebied in het hart van het bos effectief sediment inving en vastlegde tijdens springtij (Figuur IB,C). Simulaties met het model toonden aan dat zowel de patronen in de getijstroming als de omvang en patronen van de sedimentdepositie voornamelijk veroorzaakt werden door de karakteristieke topografie van dit gebied. Modelsimulaties wezen ook uit dat het bestudeerde mangrovegebied in een stabiele toestand verkeerde, waarin de vegetatiedichtheid nauwelijks effect had op de sedimentdepositie. Daarentegen werden veranderingen in de topografie of de relatieve bodemhoogte van de mangroven gecompenseerd door een (lokaal) verhoogde of verlaagde sedimentdepositie.

Hoofdstuk 3 behandelt ook de gevoeligheid van de bio-fysische interacties van het getij in de door kreken doorsneden mangroven voor plotselinge veranderingen in de begroeiing, de relatieve bodemhoogte, de aanvoer van sediment en het landinwaartse mangroveoppervlak. De initiële reactie van het mangrovesysteem – of het adaptief vermogen – ten gevolge van deze instantane veranderingen is gesimuleerd met het dieptegemiddelde model. De invang van sediment in de mangroven bleek substantieel af te nemen met een afname van de sedimentaanvoer en met het verlies van landwaarts gelegen mangrovebossen. Deze effecten kunnen bijvoorbeeld optreden door de constructie van dammen in rivieren en de aanleg van garnalenkwekerijen in de mangroven. Hogere waterstanden in de mangroven, bijvoorbeeld door zeespiegelstijging, bleken de huidige stabiele toestand van de mangroven te verstoren: *sheet flows* door het bos namen toe (Figuur ID), en de ruimtelijk gemiddelde depositie in het bos nam sterk af wanneer deze hogere waterstanden samenvielen met een afname van de dichtheid van de begroeiing (Figuur IE). Deze resultaten onderstrepen de gevoeligheid van de effectiviteit van mangroven als *ecosystem engineers*, in termen van sedimentatie, voor veranderde omgevingsfactoren.

GOLFDEMPING EN SEDIMENTATIE IN MANGROVEN GEKWANTIFICEERD

Hoofdstuk 4 presenteert een mechanistische analyse van de verandering van golfparameters langs kustdwarse transecten door mangroven, en de samenhang tussen de geobserveerde golfdemping, de vegetatiekenmerken en de sedimentdynamiek. Deze processen zijn in het veld bestudeerd langs twee kustdwarse transecten in de studiegebieden met een geleidelijk oplopend bodemprofiel, waar de samenstelling en structuur van de mangroven uitgebreid in kaart is

gebracht. De geobserveerde golfdemping nam toe voor grotere vegetatiedichtheden (Figuur IIB) en met hogere inkomende golven (Figuur IIC). De gegeneraliseerde golfdempingsratio, afgeleid op basis van een breed scala aan golfhoogtes en waterdieptes, nam toe van 0.002 m^{-1} in de dun begroeide randen van de mangroven tot 0.012 m^{-1} in de dichte *Rhizophora* begroeiing meer landinwaarts langs de transecten. Uit de golfdempingsratio's voor specifieke condities volgde dat de golfdemping in de dichte *Rhizophora* begroeiing substantieel toenam met lagere waterstanden, doordat daarmee de volumetrische vegetatiedichtheid in het water ook sterk toenam. Dit effect werd niet waargenomen in de minder dichte *Avicennia*/*Sonneratia* begroeiing (Figuur IID,E).

De demping van de golfenergie door de mangroven bleek positief voor de sedimentdepositie langs beide transecten (Figuur IIB,C). Uit de geleidelijke afname van de korrelgrootte van het bodemmateriaal bleek tevens dat steeds fijner sediment kon neerslaan door de afnemende hydrodynamische activiteit richting de dichter begroeide, landwaartse gedeelten van de transecten. In combinatie met de resultaten van de numerieke simulaties in Hoofdstuk 3 onderbouwen deze bevindingen de positieve correlatie tussen de vegetatiedichtheid en het invangen van sediment in hydrodynamisch actieve mangroven met een bodemhoogte rond gemiddeld zeeniveau (Figuur IIE). Deze resultaten verschaffen inzicht in de kustverdedigingsfunctie van mangroven door het kwantificeren van hun bijdrage aan golfdemping en sedimentatie.

CHAPTER 1

INTRODUCTION

Mangroves fringing the Mae Nam Trang estuary, Thailand.

1.1   MANGROVES & SALT MARSHES' ECOSYSTEM SERVICES

Mangroves and saltmarshes are coastal wetland ecosystems in the upper intertidal area, characterized by halophytic (salt tolerant) vegetation. These coastal wetlands thrive best in low-energy, muddy coastal environments such as estuaries, lagoons, inlets and embayments [*Allen and Pye*, 1992; *Woodroffe*, 1992]. Mangroves are mainly restricted to the tropical and sub-tropical regions [*Duke*, 1992] and vegetation in mangroves consists of shrubs and trees reaching up to 30-40 m height under favourable conditions [*Tomlinson*, 1986]. Saltmarshes occur from the tropics through to the arctic with vegetation consisting of low-growing grasses, herbaceous plants and shrubs [*Adam*, 1990].

Thriving at the interface between land and sea, coastal wetlands offer a plethora of ecosystem services: providing direct livelihood services such as food and timber [*Spalding et al.*, 2010; *Barbier et al.*, 2011], regulating functions through mitigating water quality and carbon sequestration [*Ewel*, 1997; *Chmura et al.*, 2003], and coastal protection through wave attenuation and coastal stabilization [*Gedan et al.*, 2011; *Temmerman et al.*, 2013; *Bouma et al.*, in press]. Regarding coastal protection, on instantaneous time-scales, vegetation in mangroves and saltmarshes provides a barrier to waves and currents, causing attenuation of wave energy and modification of water flows [reviewed by e.g.: *Wolanski et al.*, 1992; *Koch et al.*, 2009; *Gedan et al.*, 2011; *Fagherazzi et al.*, 2013]. On longer, morphodynamic time-scales, these short-term bio-physical interactions mitigate coastal erosion and enhance sediment deposition, contributing to coastal stabilization [*Augustinus*, 1995; *Gedan et al.*, 2011; *Shepard et al.*, 2011; *Temmerman et al.*, 2013]. These capacities of plants to alter their abiotic environment are often referred to as ecosystem engineering [*Jones et al.*, 1994].

The value of ecosystem services provided by coastal wetlands has recently been estimated at about USD 12.000 per hectare per year [*De Groot et al.*, 2012]. Although considerable variation exists in such figures, coastal wetlands are without doubt one of the most valuable ecosystems, i.e. about five times more valuable than tropical rain forests [*Costanza et al.*, 1997; *De Groot et al.*, 2012]. Coastal protection provided by mangroves and saltmarshes contributes significantly to their total ecosystem value [*Barbier*, 2007; *Costanza et al.*, 2008; *Barbier et al.*, 2011; *De Groot et al.*, 2012]. While the attenuation of wind waves and storm surges in mangroves is well established [e.g. *Gedan et al.*, 2011], their protection from tsunamis is the subject of ongoing debate [*Kathiresan and Rajendran*, 2005; 2006; *Kerr et al.*, 2006; *Vermaat and Thampanya*, 2006]. Some studies report that mangroves have mitigated the impact of the 2004 Indian Ocean tsunami, reducing damage and saving lives in settlements separated from the sea by mangrove forests [*Danielsen et al.*, 2005; *Kathiresan and Rajendran*, 2005; *Laso Bayas et al.*, 2011]. Nevertheless, mangroves are facing a rapid decline of 1 to 2% per year [*Duke et al.*, 2007] and global models suggest that anthropogenic pressure and expected sea level rise may induce the disappearance of up to 70% of all coastal wetlands by 2080 [*Nicholls*, 2004].

According to *Duke et al.* [2007] "we face the prospect of a world deprived of the services offered by mangrove ecosystems, perhaps within the next 100 years". A better understanding,

and increased awareness, of the bio-physical linkages that determine mangrove functioning and their long-term survival will contribute to more comprehensive vulnerability assessments and enhance protection and restoration successes [*Friess et al.*, 2012]. This thesis focusses on these bio-physical interactions, addressing both coastal stabilization and wave attenuation in coastal mangroves.

1.2   A BRIEF OVERVIEW OF MANGROVE CHARACTERISTICS

1.2.1   A DEFINITION OF THE 'MANGROVE'

Mangroves are tidal forest ecosystems that thrive in sheltered saline to brackish environments, such as the intertidal parts of estuaries and lagoons. The functional and structural properties of these habitats are determined by a complex of climatic and site conditions that strongly interact with the physical environment [*Augustinus*, 1995; *Alongi*, 2009]. Vegetation in mangrove forests consists of trees and large shrubs, including ferns and a palm, which have developed special adaptations in order to survive in the intertidal zone [*Duke*, 1992; *Spalding et al.*, 2010]. Mangrove forests are also referred to as 'mangal' [*MacNae*, 1968].

1.2.2   GLOBAL MANGROVE DISTRIBUTION

Mangroves are bound to the tropics and sub-tropics due to their frost intolerance [*Tomlinson*, 1986]. Mangrove distribution correlates with the 20° C seawater isotherm in winter [*Duke*, 1992] and hence concentrates between 30° N latitude and 40° S latitude (Figure 1.1), with increasing densities towards the equator [*Spalding et al.*, 2010; *Giri et al.*, 2011]. The total area of mangroves was estimated at about 138.000 km^2 by the year 2000 [*Giri et al.*, 2011]. Six biogeographical mangrove regions have been defined, coinciding with the continental borders: western America, eastern America, western Africa, eastern Africa, Indo-Malesia and Australasia [*Duke*, 1992]. The two latter regions feature the greatest biodiversity with 51 and 47 mangrove species, respectively, out of about 70 species occurring worldwide [*Duke*, 1992; *Alongi*, 2002]. Similar patterns exist in mangrove biomass, with southeast Asian mangroves having the highest (aboveground) biomass, both in absolute sense and per unit area, accounting for almost half of the total global mangrove biomass [*Hutchison et al.*, in press].

Figure 1.1 – Global mangrove distribution in 2000. From: *Giri et al.* [2011].
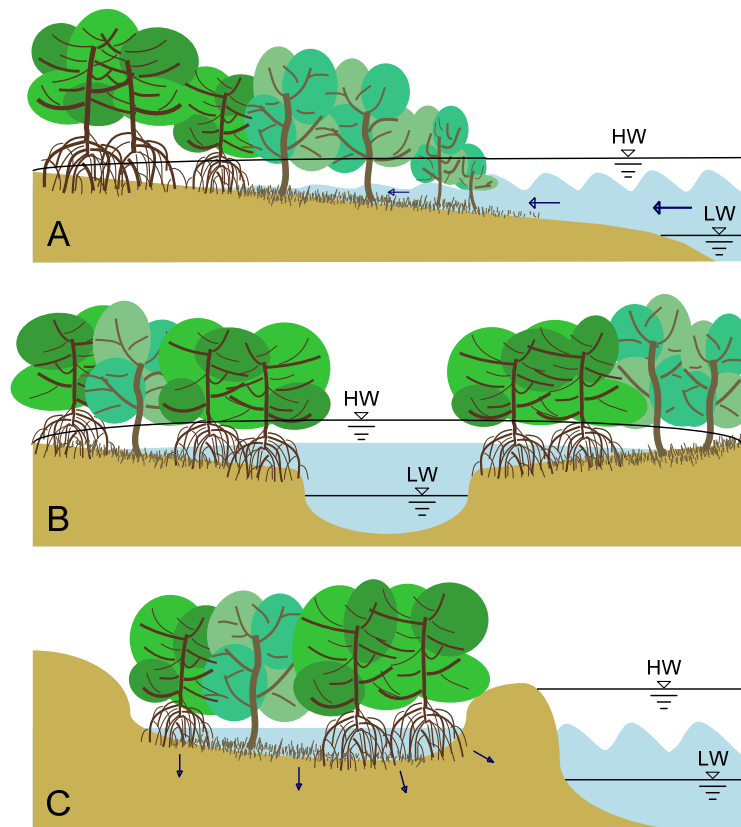
Figure 1.2 – Three main types of mangrove landforms: (A) fringing, (B) riverine and (C) basin mangroves. After: *Mazda et al.* [2007].

1.2.3 MANGROVE LANDFORMS AND GEOPHYSICAL CLASSIFICATIONS

Mangroves thrive in a variety of geographic settings and, consequently, are exposed to different physical processes. *Lugo and Snedaker* [1974] classified mangroves according to their physiognomy, recognizing six mangrove classes with distinct tidal inundation and terrestrial surface drainage attributes. This classification was aggregated by *Cintron and Novelli* [1984] to three main classes based on topographic landforms: fringing, riverine and basin mangrove forests (Figure 1.2). *Woodroffe* [1992] added a physical dimension to this classifications, differentiating between tide-dominated, river-dominated and interior mangroves.

Fringing, or tide-dominated, mangroves (Figure 1.2A) are observed at low-gradient intertidal areas of sheltered coastlines (e.g. estuaries or embayments). These mangroves are exposed to tidal action, imposing (strong) bi-directional water movements. Facing the open sea, fringing mangroves can also (incidentally) be exposed to waves. Fringing mangroves that have overgrown an island or land spit that fully inundates during high tide, form a subtype named overwash mangroves. Riverine, or river-dominated, mangroves (Figure 1.2B) are located along the banks of (tidal) rivers or creeks, for example in the deltas of large rivers. Riverine mangroves are mostly exposed to uni-directional water flows during flood tides. Basin, or interior, mangroves (Figure 1.2C) are least exposed and thrive in inland depressions. Tidal exchange in these basins is less frequent, limited to the highest tides, but slow drainage via

groundwater flows induces prolonged soil saturation [*Lugo and Snedaker*, 1974; *Woodroffe*, 1992; *Ewel et al.*, 1998; *Mazda et al.*, 2007]. This thesis focuses on fringing mangroves that face the open sea (referred to as coastal mangroves), the most dynamic mangrove landform of the abovementioned classes.

1.2.4 MANGROVES' PECULIAR ROOT SYSTEMS

In order to cope with the harsh conditions in the coastal zone, mangrove trees have some characteristic attributes: physiological mechanisms to tolerate salt, aerial roots to overcome oxygen shortage in waterlogged soils, viviparous embryos capable to establish rapidly in dynamic environments and propagules that are dispersed by the tides [*Alongi*, 2009].

Interesting from the viewpoint of bio-physical interactions in mangroves, are the above-surface aerial root systems. Four distinct root types are observed in mangrove species [*Tomlinson*, 1986; *Spalding et al.*, 2010]:

- Stilt roots are branched, looping aerial roots branching out from the main trunk of the tree, which can be detached from the forest floor, or from its lower branches (Figure 1.3A). These stilts penetrate the soil at some distance away from the tree. The branching of the roots induces a substantial increase of their number towards the forest floor, up to several hundreds of roots for a mature tree. Dense cone-shaped aboveground root networks are formed with diameters ranging up to about 10 m for one tree. Stilt roots are typical for *Rhizophora* species, but *Bruguiera* and *Ceriops* species sometimes also have small stilt roots.

Figure 1.3 – Mangrove roots: (A) stilt roots of *Rhizophora* sp., (B) pneumatophores of *Avicennia* sp., (C) knee roots of *Bruguiera* sp. and (D) buttress roots of *Xylocarpus* sp.. The red bamboo is 1 m high.

- Pneumatophores are aboveground pencil-like roots, extending from lateral sub-surface roots (Figure 1.3B). The pneumatophores can be either quite narrow or have a conical shape for *Avicennia* and *Sonneratia* species, respectively. Pneumatophores are typically less than 10 cm tall, but can get higher if inundation conditions are strenuous.
- Knee roots emerge when lateral sub-surface roots develop loops when growing away from the tree, forming knob-like or looping extensions above the soil (Figure 1.3C). Branching of these roots occurs at these knees and the height of such knees is comparable to the height of pneumatophores. Knee roots are found in *Bruguiera* and *Ceriops* species.
- Plank roots are lateral roots that are extending above the soil, following a sinuous course while growing away from the tree (Figure 1.3D). These plank roots are often the continuation of buttress roots; vertical flange-like extensions of the tree stem above the substrate. Plank roots are typical features of *Xylocarpus* and *Heritiera* species.

1.3   BIO-PHYSICAL INTERACTIONS IN COASTAL MANGROVES

Mangroves fringing (sub-)tropical coastlines form a dynamic ecosystem, where ecological processes are interacting with hydrodynamic and morphodynamic processes (Figure 1.4). A sound knowledge of processes shaping these bio-physical (mangrove-morphodynamics, mangrove-hydrodynamics) and physical (hydrodynamics-morphodynamics) interactions is indispensable (i) for understanding the effectiveness of mangroves for coastal protection and stabilization, (ii) in understanding and predicting the development of mangroves, and (iii) for unveiling the potential impacts of environmental change (e.g. sea level rise) to the mangroves.
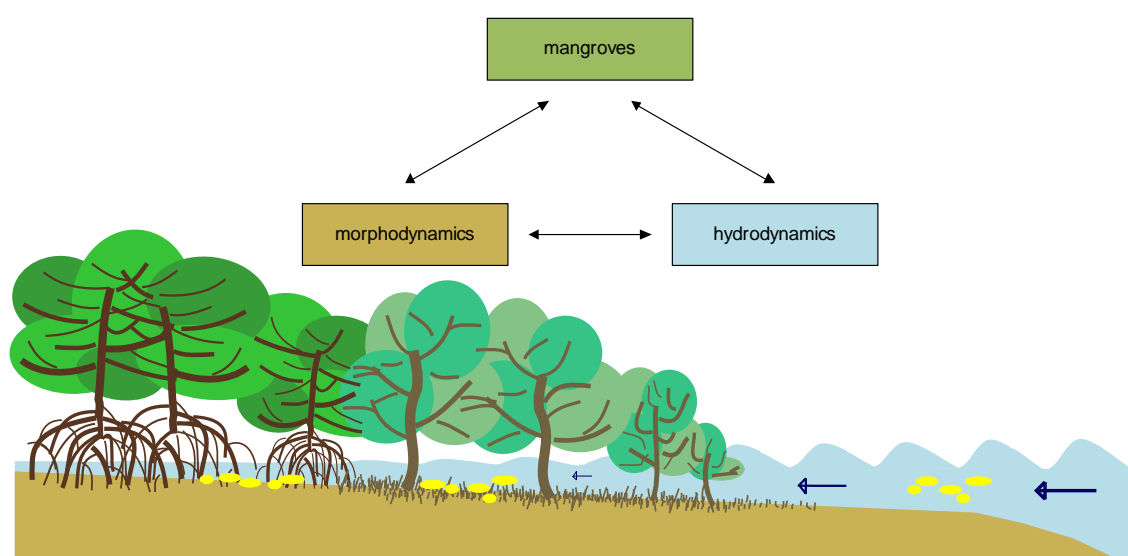
Figure 1.4 – Bio-physical interactions in coastal mangrove ecosystems.
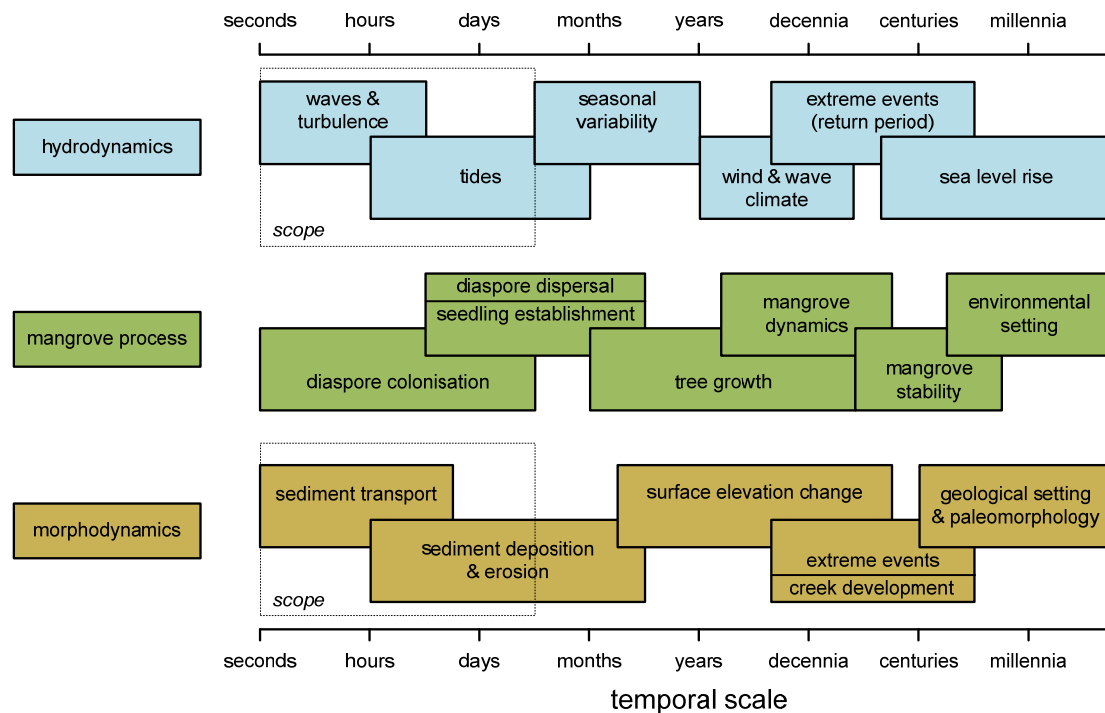
Figure 1.5 – Temporal scales of biological and physical processes in mangrove forests. The dashed boxes indicate the scope of this thesis. Prepared (in adapted form) for *Friess et al.* [2012]. Based on: *Brommer and Bochev-van der Burgh* [2009], *Cowell and Thom* [1997], *Holling* [2001], *Stive et al.* [2002], *Twilley et al.* [1999].

Each of the processes indicated in Figure 1.4 – mangrove dynamics, morphodynamics, hydrodynamics – comprises a variety of biological and physical processes, ranging from very short-term and small-scale (fast, local changes) to very long-term and large-scale (gradual or rare, regional changes). As part of the current study, these biological and physical processes have been identified and organized based on their characteristic temporal scales (Figure 1.5) and according to their characteristic spatial scales (Figure 1.6). In general, related spatial scales do increase with increasing temporal scales [see e.g. *Twilley et al.*, 1999; *Holling*, 2001; *Cowell et al.*, 2003]. Spatial scales in mangrove dynamics are typically smaller than those of the co-temporal physical processes [*Cowell and Thom*, 1997; *Stive et al.*, 2002; *Spencer and Möller*, 2013].

Hierarchy theory states that behaviour at any one scale results from higher order processes at smaller temporal and spatial scales, and is constrained by lower order processes that operate at greater temporal and spatial scales [*Gibson et al.*, 2000; *Cowell et al.*, 2003]. Consequently, processes at short temporal scales in Figure 1.5, such as waves and tidal water flows, are affected by characteristics of the lower order levels like wind climate, mangrove conditions and surface elevation. Conversely, long-term surface elevation change (i.e. coastal stability) results from higher order processes as waves, tides and sediment deposition or erosion. Different processes operating at equal temporal scales can interact directly. For example, waves directly interact both with mangrove colonisation and with suspended sediment transport. Also, extreme storm events directly affect mangrove stability and surface elevation change.
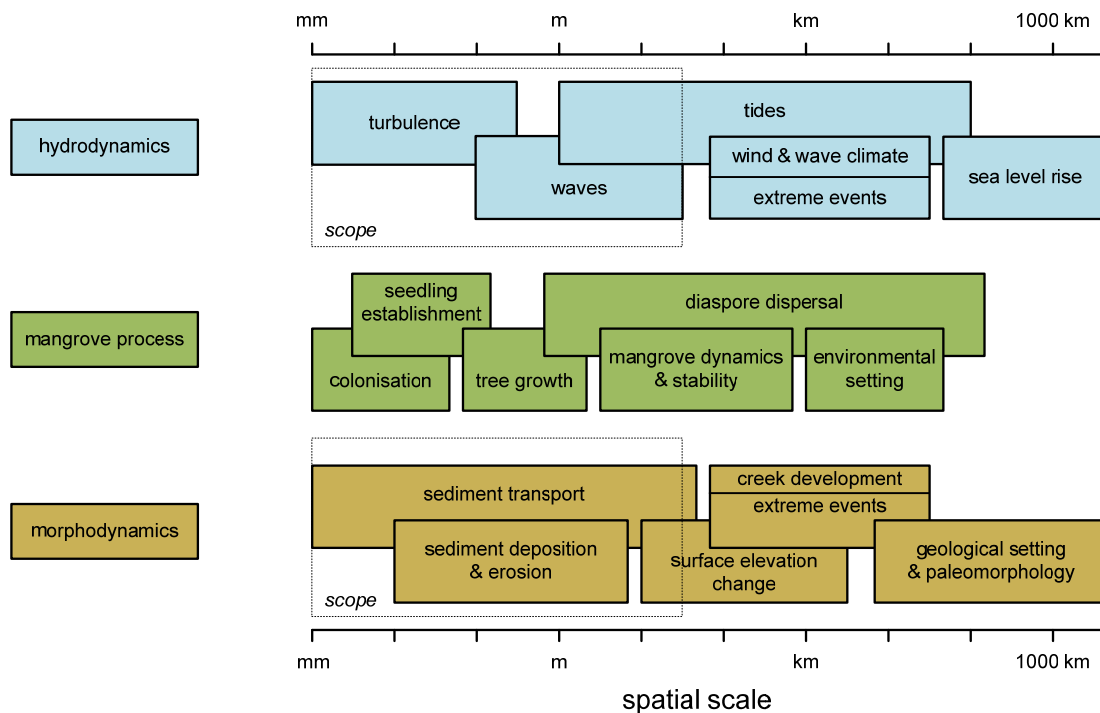
Figure 1.6 – Spatial scales of biological and physical processes in mangrove forests. The dashed boxes indicate the scope of this thesis. Based on: *Brommer and Bochev-van der Burgh* [2009], *Cowell and Thom* [1997], *Holling* [2001], *Stive et al.* [2002], *Twilley et al.* [1999].

Understanding the contribution of mangroves to coastal protection and stabilisation by mitigating long-term storm events and surface elevation change, a priori requires knowledge of the short-term processes at the basis of this long-term behaviour. This thesis focusses on these short-term processes, investigating the short-term bio-physical interactions in coastal mangroves. Short-term is defined as temporal scales ranging from seconds to weeks, limiting the scope of this thesis to bio-physical interactions regarding waves, tides, sediment transport and deposition (or erosion) rates (Figure 1.5). The spatial extent of these short-term processes ranges from millimetres up to tens (sometimes hundreds) of metres (Figure 1.6).

Short-term hydrodynamics and morphodynamics do affect colonisation and establishment of mangroves [*Balke et al.*, 2011; *Balke et al.*, 2013]. However, these short-term mangrove processes, due to their limited spatial scale (Figure 1.6), cannot significantly affect hydrodynamics or morphodynamics. Large-scale processes with temporal scales exceeding weeks, remain constant during the short-term processes under study, imposing invariable boundary conditions. According to hierarchy theory, the short-term hydrodynamic and morphodynamic processes act within the constraints imposed by the existing morphology, mangrove cover and the prevailing hydrodynamic climate.

1.4 CONTRIBUTION OF MANGROVES TO PHYSICAL PROCESSES IN THE INTERTIDAL

Since the pioneering work by *Watson* [1928], classifying mangroves according to the local tidal regime, geophysical characteristics of mangroves (e.g. tidal regime and topography) gained attention as factors significantly contributing to mangrove physiognomy [*Lugo and Snedaker*, 1974]. Initial studies inferred the land-building capacity of mangroves without much quantitative evidence [e.g. *Davis*, 1938]. This view was revised later on as mangroves were found to be opportunistic colonizers [e.g. *Thom*, 1967; *Woodroffe*, 1982]. Until the 1980's the great majority of literature focussed on mangrove ecology, while studies recognizing the physical processes in mangroves mainly remained qualitative [*Mazda et al.*, 2007]. Some pioneers in bio-physical mangrove research addressed this knowledge gap. *Mazda, Wolanski and Ridd* [2007] stated that 'as a fundamental condition for the existence of mangroves (…) it is necessary to obtain a quantitative understanding of the physical processes and hydrodynamic mechanisms that take place in these intertidal areas'. Advances on the areas of tidal dynamics, concerning flow routing and sediment deposition, and wave attenuation in coastal mangroves are briefly summarized in the following sections.

1.4.1 TIDAL DYNAMICS IN COASTAL MANGROVES

Research efforts into the bio-physical functioning of mangroves initially focussed on vegetated forest platforms (elevated above mean sea level) that are dissected by tidal creeks. Creek-forest interactions are eminent processes for the supply of water and suspended matter (sediments, organic matter etc.) to these mangroves. Pioneering field and modelling studies emphasized the tidal asymmetry in mangrove creek hydrodynamics: creek flow is generally ebb dominated due to the delayed discharge from the hydraulically rough vegetated areas [*Wolanski et al.*, 1980; *Mazda et al.*, 1995; *Furukawa et al.*, 1997]. According to model simulations, ebb tidal currents within the vegetation last longer than inflowing flood currents, while peak flow velocities inside the forest are greatest on flood tide [*Mazda et al.*, 1995]. These asymmetries result in a net input of sediments into mangrove forests [*Wattayakorn et al.*, 1990; *Wolanski et al.*, 1990; *Furukawa et al.*, 1997; *Bryce et al.*, 2003; *Capo et al.*, 2006; *Vo-Luong and Massel*, 2006; *Van Santen et al.*, 2007], while the dissecting creeks maintain depth by self-scouring during ebb tidal outflows [*Wolanski et al.*, 1980; *Mazda et al.*, 1995].

The effective trapping of sediments in mangroves is corroborated by biogeomorphological studies that monitored sediment deposition over periods ranging from several tidal cycles up to one year. These studies present increased deposition rates in the fringe zone of tidal mangroves [*Adame et al.*, 2010], a gradual reduction of deposition rates with increasing bed elevation [*Anthony*, 2004; *Stokes et al.*, 2010] and a greater facilitation of sediment deposition by prop roots than by pneumatophores [*Krauss et al.*, 2003]. These morphological studies do not present spatially explicit linkages between sedimentation and the physical processes underlying the observed deposition patterns. Only few geophysical studies combine sediment transport and/or deposition along transects through mangroves with hydrodynamic measurements, linking

sediment deposition to: the distance to the creek's edge [*Furukawa et al.*, 1997]; within-forest flow velocities, vegetation density and bed level [*Van Santen et al.*, 2007]; and bed level and wave activity in the mangroves [*Vo-Luong and Massel*, 2006].

To date, the routing of tidal water flows through the vegetated parts of fringing mangroves has only been observed implicitly, inferred from water level measurements or within-creek velocity observations [e.g. *Aucan and Ridd*, 2000; *Van Loon et al.*, 2007]. Point measurements of within-forest flow velocities [cf. *Mazda et al.*, 1997b; *Mazda et al.*, 2005; *Van Santen et al.*, 2007] are rare. These and the abovementioned studies generally lack accurate elevation data and flow velocity observations covering sufficiently large mangrove areas, leaving the routing of tidal water flows and suspended sediments unresolved. *Mazda et al.* [2007] concluded that 'difficulties involved in making direct measurements of flow patterns mean that we currently have little firm information on patterns of water circulation and sedimentation within mangrove swamps'.

Practical restrictions to mangrove field studies, due to poor accessibility and harsh conditions, impose limitations to the spatial and temporal resolution and the spatial extent of field data. Numerical modelling offers a means to study mangrove hydrodynamics at an increased spatial and temporal resolution and scale. Initially, two-dimensional depth-averaged numerical model simulations were used to study creek flows in mangroves [e.g. *Wolanski et al.*, 1980]. In these models, vegetation was represented by an adjusted roughness parameter and mangrove topography was largely simplified and mostly flat [*Wattayakorn et al.*, 1990; *Wolanski et al.*, 1990; *Mazda et al.*, 1995; *Furukawa et al.*, 1997; *Aucan and Ridd*, 2000]. Meanwhile, *Mazda et al.* [1997; 2005] developed analytical models for water flows through mangroves by parameterizing vegetation characteristics. These models elucidated the contribution of the drag coefficient and eddy viscosity to flow resistance observed in multiple field sites. More detailed mechanistic insight in bio-physical creek-forest interactions in mangroves was obtained from flume studies with dowels representing scaled mangrove trees [*Wu et al.*, 2001; *Struve et al.*, 2003]. *Wu et al.* [2001] implemented these findings in a numerical model explicitly accounting for vegetation induced drag and the blockage effect by the vegetation.

To our knowledge, none of the previous studies link spatially explicit observations or simulations of tidal-scale hydrodynamics to both (i) gradients in elevation and vegetation in mangroves and (ii) sediment transport and deposition rates throughout mangroves. For saltmarshes, the temperate climate equivalent of mangroves, these tidal-scale bio-physical interactions have already been studied in a spatially explicit context [*Leonard*, 1997; *Temmerman et al.*, 2003; *Temmerman et al.*, 2005b; *Bouma et al.*, 2007]. *Temmerman et al.* [2005b] developed a three-dimensional process-based model of a saltmarsh in Delft3D [*Lesser et al.*, 2004] and successfully simulated tidal-scale dynamics, including flow routing and sediment deposition patterns. This process-based numerical model explicitly accounts for enhanced friction losses and turbulence induced by vegetation [*Uittenbogaard*, 2003]. The striking differences in vegetation structure, height and density between the rather uniform,

dense saltmarsh grasses and the much more heterogeneous, forest-like mangrove vegetation make that the results from such saltmarsh studies cannot be inferred to mangroves.

1.4.2 WAVE DISSIPATION IN COASTAL MANGROVES

Although mangroves are situated right at the interface between land and sea, mostly in areas where any other kind of sea defence is lacking, dissipation of wave energy in coastal mangroves only started to gain scientific attention since the late nineties. Ever since, a limited number of (field) studies into wave attenuation in mangroves has been published, focussing on field sites in Vietnam, Australia and Japan (Table 1.1). These studies emphasize in unison the positive contribution of mangroves to the dissipation of wind and swell waves of limited height and period.

Table 1.1 – Overview of previous studies quantifying wave attenuation in mangroves (n.a. = not available).

Location - mangrove setting	Vegetation	Incident wave height H & period T	Wave attenuation
Tong King Delta, Vietnam - fringing mangroves [*Mazda et al.*, **1997a**]	Sparse *Kandelia candel* seedlings (1/2 year-old), planted	H = n.a. T = 5-8 s	r = 0.01-0.10 per 100 m
	Dense 2-3 year-old *Kandelia candel*, up to 0.5 m high, planted	H = n.a. T = 5-8 s	r = 0.08-0.15 per 100 m
	Dense 5-6 year-old *Kandelia candel*, up to 1 m high, planted	H = n.a. T = 5-8 s	r = 0.15-0.22 per 100 m
Vinh Quang, Vietnam - fringing mangroves [*Mazda et al.*, **2006**]	*Sonneratia* sp., 20 cm high pneumatophores, canopy starts 60 cm above bed, planted	H = 0.11-0.16 m T = 8-10 s	r = 0.002-0.006 m^{-1}
	No vegetation	H = 0.11-0.16 m T = 8-10 s	r = 0.001-0.002 m^{-1}
Can Gio, Vietnam - riverine mangroves [*Vo-Luong and Massel*, **2006**]	Mixed *Avicennia* sp. and *Rhizophora* sp.	H = 0.35-0.4 m T = - s	energy reduction factor = 0.50-0.70 over 20 m (including a cliff)
Do Son, Vietnam - fringing mangroves [*Quartel et al.*, **2007**]	Mainly *Kandelia candel* bushes and small trees	H = 0.15-0.25 m T = 4-6 s	r = 0.004-0.012 m^{-1}
	Non-vegetated beach plain	H = 0.15-0.25 m T = 4-6 s	r = 0.0005-0.002 m^{-1}
Red River Delta, Vietnam - fringing (?) mangroves [*Bao*, **2011**]	Mixed vegetation	H = 0.15-0.27 m T = n.a.	r = 0.0055-0.01 m^{-1}
Can Gio, Vietnam - fringing (?) mangroves [*Bao*, **2011**]	Mixed vegetation	$H \sim$ 0.55 m T = n.a.	r = 0.017 m^{-1}
Cocoa Creek, Australia - fringing mangroves [*Brinkman et al.*, **1997**; *Brinkman*, **2006**]	Zonation: *Rhizophora* sp. (front), *Aegiceras* sp., *Ceriops* sp. (back)	H = 0.01-0.07 m $T \sim$ 2 s	energy transmission factor = 0.45-0.80 over 160 m
Iriomote, Japan - riverine mangroves [*Brinkman et al.*, **1997**; *Brinkman*, **2006**]	*Bruguiera* sp., 20-30 cm high knee roots	H = 0.08-0.15 m $T \sim$ 2 s	energy transmission factor = 0.15-0.75 over 40 m
Oonoonba, Australia - fringing mangroves [*Brinkman*, **2006**]	Zonation: *Sonneratia* sp. (front) and *Rhizophora* sp. (back)	H = 0.04-0.25 m $T \sim$ 6 s	energy reduction factor = 0.9-1.0 over 40 m

A generic measure for expressing wave attenuation is the wave height reduction per unit distance r [m^{-1}]: $r = -(\Delta H/H)/\Delta x$. Herein, H represents the incident wave height [m] and ΔH is the reduction in wave height [m] while propagating over a distance Δx [m] through the mangroves [*McIvor et al.*, 2012b]. Observed wave reduction rates in well-developed mangroves vary from 0.002-0.01 m^{-1} (Table 1.1). Alternatively, the energy transmission factor quantifies the remaining wave energy after some propagation distance through the mangroves, which is the inverse of the energy reduction factor [*Brinkman et al.*, 1997; *Vo-Luong and Massel*, 2006]. Observed energy reduction ranges from 20% up to 100% over variable distances (Table 1.1). These wave reduction rates vary significantly with water depth and vegetation characteristics.

Wave attenuation by mangroves observed in the field has been parameterized in bulk roughness parameters, either a wave reduction rate (Table 1.1) or a bulk drag coefficient, comprising both vegetation induced drag forces and bottom friction [*Mazda et al.*, 1997a; *Quartel et al.*, 2007]. Both *Mazda et al.* [1997a] and *Quartel et al.* [2007] obtained exponentially increasing bulk drag coefficients for increasing water depths within the mangroves due to limited height of the dwarfed trees in their field sites. Conversely, *Brinkman et al.* [1997] obtained increasing transmission factors, and hence decreasing wave attenuation, for increasing water depths at two sites with, presumably, fully grown mangrove trees (Table 1.1).

Enhancing our understanding of the processes determining wave attenuation in mangroves requires mechanistic studies of the propagation of waves through mangrove vegetation. Recent advances in numerical modelling explicitly resolve vegetation induced drag forces by integrating friction forces over a composition of one or several layers of rigid vertical cylinders [*Vo-Luong and Massel*, 2008; *Suzuki et al.*, 2012]. For a reliable representation of the vegetation, this approach requires detailed, site specific information on vegetation characteristics such as stem and root diameters, vertical vegetation distribution, vegetation densities and (bulk) drag coefficients. However, due to poor vegetation data the abovementioned models were calibrated in the vegetation parameters [*Vo-Luong and Massel*, 2008; *Suzuki et al.*, 2012], raising questions regarding their general validity. Field data comprising accurate measurements of the cross-shore topography, vegetation structure, water depths and wave parameters are indispensable for further development of the abovementioned numerical models [*McIvor et al.*, 2012b; *Möller*, 2012].

Wave and vegetation parameters are changing from site to site, depending on local geophysical mangrove settings (Table 1.1). Previous studies on wave attenuation in mangroves accurately quantified wave conditions, water depths and the local topography [e.g. *Brinkman*, 2006; *Vo-Luong and Massel*, 2006; *Quartel et al.*, 2007]. Nevertheless, most studies cover a rather limited range of wave conditions, as data collection often spanned a few tides only [*Mazda et al.*, 1997a; *Brinkman*, 2006]. Moreover, vegetation characteristics lack a spatially explicit quantification in most field studies to date, as they only present either qualitative descriptions of local vegetation patterns or fairly rough quantifications of the vegetation cover [*Brinkman*, 2006; *Vo-Luong and Massel*, 2006; *Quartel et al.*, 2007].

1.5   RESEARCH OBJECTIVE

Previous sections have shown that comprehensive data sets on short-term bio-physical interactions in coastal mangroves – i.e. flow routing, sediment deposition and wave attenuation – are limited. Studies linking spatially explicit observations (or simulations) of sediment deposition rates throughout mangroves to both gradients in elevation and vegetation and to tidal-scale hydrodynamics or wave dynamics are unprecedented. Recent reviews by *Mazda et al.* [2007] and *McIvor et al.* [2012b] addressed that the lack of such data limits our understanding of tidal-scale dynamics and wave attenuation, respectively, in coastal mangroves.

This study aims to improve our understanding of these short-term bio-physical interactions in coastal mangroves, in particular with respect to their contribution to coastal stabilization and coastal safety, by (i) collecting and analysing a comprehensive set of field data, (ii) unravelling contributing processes through numerical modelling, based on the field observations, and (iii) simulating system behaviour for conditions beyond the observed field data.

1.6   RESEARCH QUESTIONS

Based on the research objective, addressing current knowledge gaps in short-term bio-physical interactions in coastal mangroves, five research questions have been identified:

Q1. How do tidal-scale hydrodynamics in coastal mangroves vary throughout different field sites with distinct biogeophysical settings, and how do these differences relate to their specific vegetation, topography and hydrodynamic exposure?

Q2. How to simulate tidal-scale hydrodynamics and sediment dynamics in coastal mangroves accurately and efficiently in Delft3D, and to what extent can the bio-physical interactions in coastal mangroves be reproduced accurately by a depth-averaged Delft3D model?

Q3. According to field observations and numerical simulations, what is the relative contribution of vegetation and topography to the tidal flow routing and to sediment deposition patterns in coastal mangroves?

Q4. What is the sensitivity of tidal-scale bio-physical interactions in coastal mangroves to changes in vegetation, sea level, sediment supply and mangrove extent beyond the biogeophysical settings observed in the field, according to model simulations?

Q5. How do wave characteristics change along cross-shore transects through coastal mangroves and how do observed – changes of – wave characteristics correlate with vegetation characteristics and sediment dynamics?

In accordance with the different components of the research objective, research questions **Q1** and **Q5** principally focus on the collection and analysis of field data. Research questions **Q2**, **Q3** and **Q4** focus on the combination of field data and numerical modelling in an attempt to simulate field observations and to obtain insight into bio-physical interactions in mangroves for conditions beyond the conditions observed.

1.7 RESEARCH APPROACH: COMBINING FIELD OBSERVATIONS AND NUMERICAL MODELLING

This study started with an extensive field campaign, lasting from November 2010 to May 2011. Data were collected at three different, rather undisturbed mangrove sites at the Andaman coast of Trang province in southern Thailand (Figure 1.7). One site comprised a slightly elevated mangrove forest dissected by tidal creeks (Figure 1.7E). Data collection at this site focussed on spatial variations in flow velocities and sediment deposition. The second and third site, constituting lower elevated mangroves without creeks, were exposed to sea and swell waves (Figure 1.7F,G). Data collection at these sites comprised the monitoring of waves along cross-shore transects, in addition to observations of flow velocities and sediment deposition. At all three sites, the topography and the vegetation cover were surveyed meticulously (Figure 1.8).

The obtained field data are used for the analysis of two direct bio-physical interactions in coastal mangroves:
- The routing of tidal water flows, and how this flow routing depends on vegetation, topography and nearshore water flows (**Q1**), is studied at all three field sites.
- Wave attenuation, and how this depends on vegetation and topographic characteristics (**Q5**), is studied along the two transects.

The processes described above focus on the direct bio-physical interactions between the mangroves and the hydrodynamics. However, indirectly, the sediment dynamics are also affected by these bio-physical interactions. The consequent deposition patterns are related to both the tidal flow routing in the elevated mangrove site dissected by tidal creeks (**Q3**) as well as to the wave climate at both transects (**Q5**).

The comprehensive analysis of the tidal routing of water and sediments through mangroves dissected by tidal creeks requires additional research in order to distinguish between the contribution of different environmental parameters to these processes. Therefore, the abovementioned Delft3D model that *Temmerman et al.* [2005b] applied to simulate tidal dynamics in saltmarshes (see Section 1.4.1), is adjusted to study tidal-scale dynamics in mangroves. In an attempt to increase model efficiency and to reduce vegetation data requirements, this model is applied both in three-dimensional (as in previous studies) and in depth-averaged mode in order to compare model accuracies (**Q2**). With an efficient depth-averaged numerical model, it is possible to study the contribution of vegetation and topography to the tidal-scale dynamics observed in the field (**Q3**). This model is used as well for analysing the initial response of the mangroves to instantaneous (anthropogenic) changes to the

biogeophysical conditions (**Q4**). These simulations provide mechanistic insight in (i) the contribution of mangroves to short-term accretion, adding to coastal stabilization, and (ii) the potential sensitivity of mangroves' stabilizing function to environmental change.
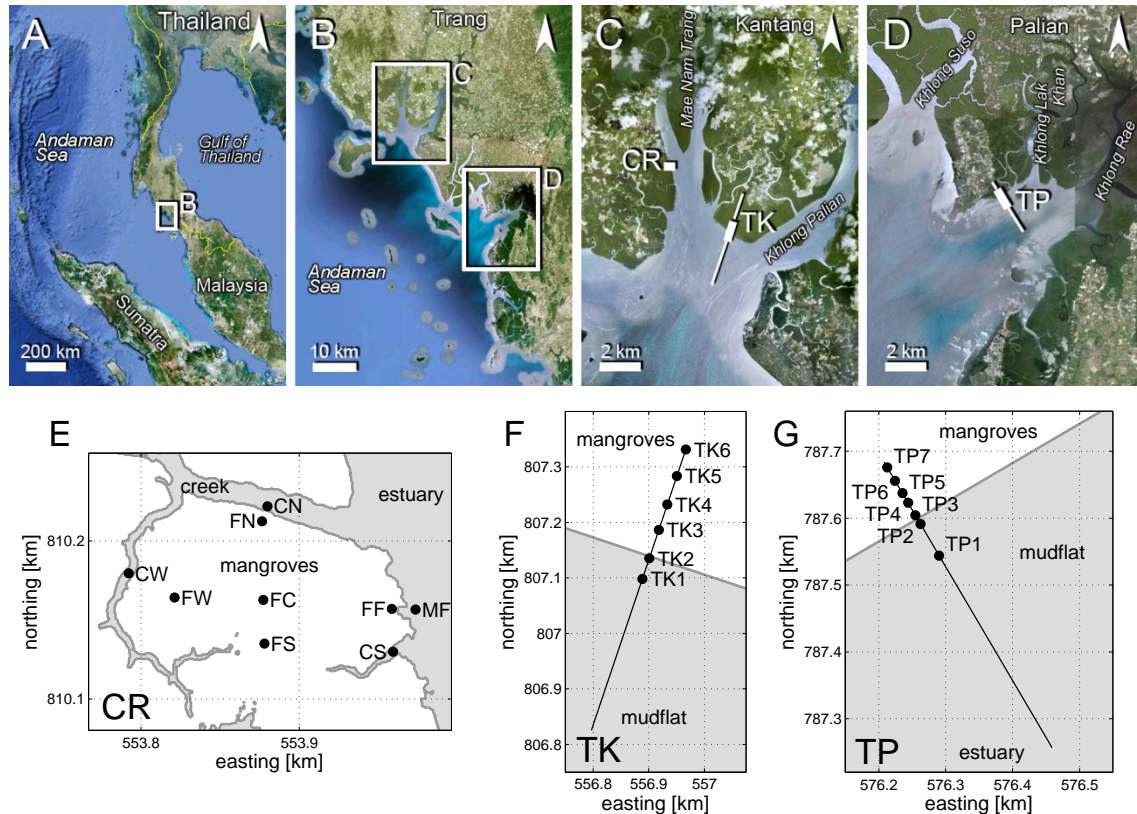
Figure 1.7 – Geography of the field sites. (A) The Andaman coast of southern Thailand. (B) The coastal areas of Trang province. (C) The estuary of the Mae Nam Trang and Khlong Palian rivers, with the position of the creek catchment 'CR' and Kantang transect 'TK'. (D) The estuary of the Khlong Lak Khan and Khlong Rae with the Palian transect 'TP' (source: Google Earth). The lower plots (E-G) present the main topography of each of the study sites.

This combined observational-numerical research approach is prerequisite to obtain mechanistic insights in the bio-physical interactions shaping tidal-scale dynamics and wave attenuation in coastal mangroves. As presented in Section 1.4, field studies so far (often) collected incomplete data on the biogeophysical settings of the mangroves such as the topography or the vegetation characteristics. First, the comprehensive spatially explicit field data collected for this study provide a solid base for quantifying and correlating the observed bio-physical interactions. Second, collecting our own field data allows us to overcome the problem of lacking calibration and validation data in developing a numerical model. This means that we can prevent numerous assumptions, which would affect the quality of the model that is developed for simulating tidal flow routing (and the model that might be developed in the future for wave attenuation). In return, an accurate model representation of the bio-physical interactions in mangroves allows for an in-depth analysis isolating the contribution of the specific biogeophysical mangrove settings to the observed tidal-scale dynamics (or wave attenuation). Also, such models are

useful aids for studying the effects of environmental changes (far) beyond the range of conditions that can be observed in the field.
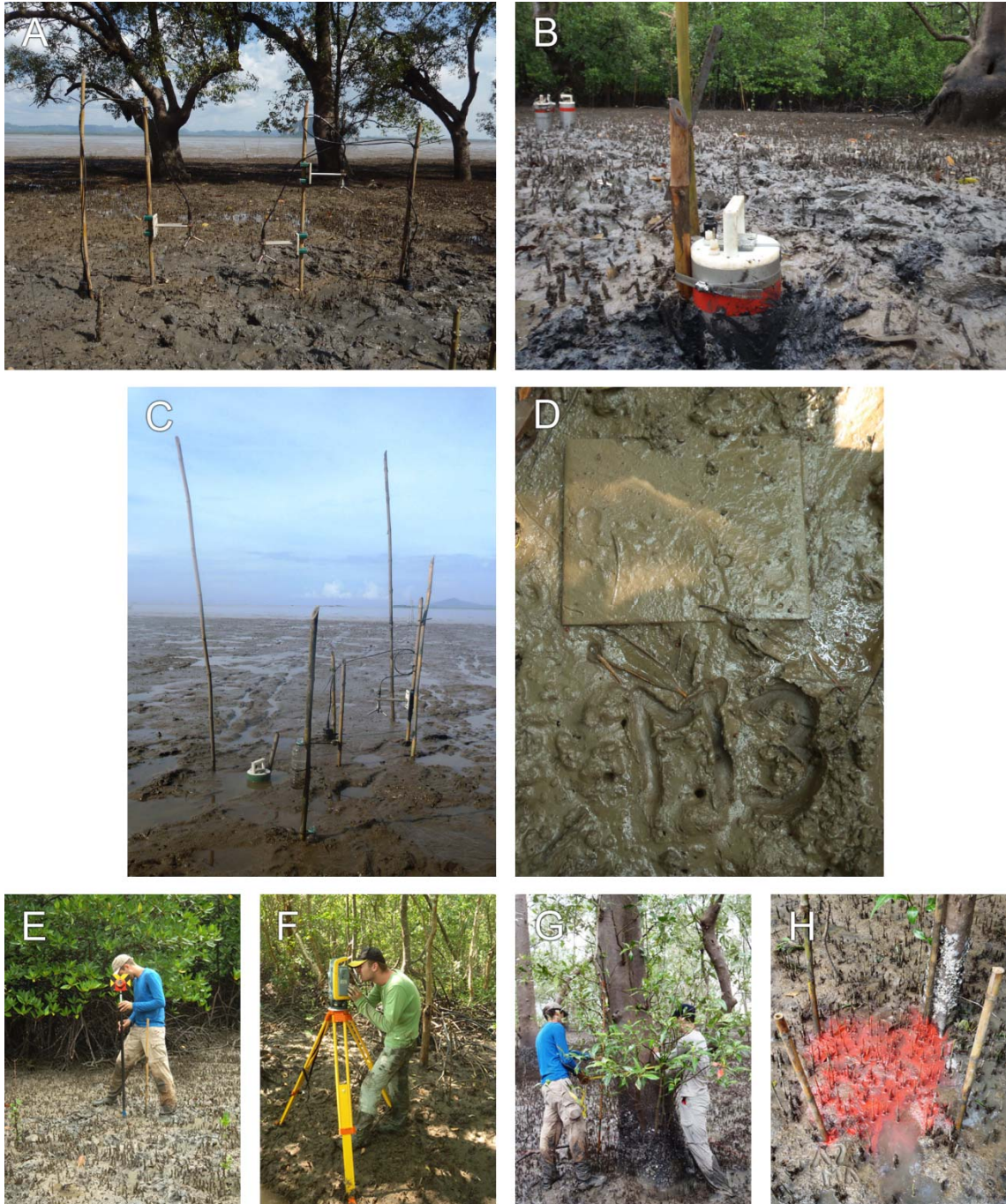
Figure 1.8 – Data collection in the field. (A) Monitoring flow velocities with Acoustic Doppler Velocimeters (Nortek). (B) Monitoring waves with MacroWave pressure sensors (Coastal Leasing). (C) Combined collection of wave, flow velocity and water level data. (D) Monitoring sediment deposition with custom made mortar covered ceramic tiles. (E,F) Topographic survey with a total station (Trimble). (G,H) Surveying vegetation structure by counting trees and measuring root and stem diameters.

1.8   THESIS OUTLINE

This thesis contains three chapters presenting the research and findings regarding the research questions introduced above. Chapter 2 is dedicated to the flow routing patterns in coastal mangroves. This chapter focusses on field observations and presents the different flow routing patterns in coastal mangroves with variable biogeophysical settings – i.e. topography, vegetation, hydrodynamic exposure (**Q1**). Chapter 3 presents a numerical model in Delft3D for simulating tidal flow routing and sediment dynamics in an elevated mangrove forest dissected by tidal creeks. The results of the three-dimensional and depth-averaged simulations are compared to the field observations (**Q2**). The depth-averaged model is applied to analyse the contribution of various biogeophysical conditions, and impacts of changes therein, to the flow routing through this mangroves forest and the consequences for sediment deposition patterns (**Q3 & Q4**). Chapter 4 addresses the propagation of waves through coastal mangroves and the cross-shore variation in vegetation properties and sediment dynamics. The reduction of wave heights and attenuation of wave energy is analysed in conjunction with vegetation characteristics, aiming at explicit relations between vegetation characteristics and wave mitigation (**Q5**). Chapter 5 concludes this thesis with a synthesis of the conclusions regarding the research questions and with some recommendations resulting from experiences in the field and the findings of this study.

CHAPTER 2

FLOW ROUTING IN MANGROVE FORESTS:
A FIELD STUDY IN TRANG PROVINCE, THAILAND[*]

The tide entering the mangroves along the Mae Nam Trang estuary, Thailand.

ABSTRACT

Flow routing in mangrove forests has great implications for the transport and distribution of sediments and nutrients and hence for mangroves' development and persistence. Whereas previous studies were limited to the creeks, supposedly feeding the surrounding mangroves, this chapter demonstrates the contribution of biogeophysical impacts on flow routing through estuarine mangroves. We present the results of a field campaign covering three relatively undisturbed mangrove sites in two estuaries in Trang province, Thailand. The sites range from a mangrove forest elevated above mean sea level with steep cliffs and incised by tidal creeks, to smoothly inclining mangroves fronted by extensive mudflats and showing a clear vegetation zonation starting below mean sea level. It is shown how flow routing through estuarine mangroves is impacted by biogeophysical factors; elevation, exposure and vegetation. Within the higher elevated mangroves, *creek flow* prevails when water levels remain below a dense vegetation layer at the mangrove fringe bordering the estuary. *Sheet flow* prevails when this threshold is exceeded and direct water exchange takes place. The low-lying sites do not feature creeks and tidal flows are typically sheet flows, being susceptible to forcing by river discharges. With decreasing water depths and/or increasing vegetation densities, the effects of this forcing are reduced and flow velocities follow the vegetation induced cross-shore water level gradients. Flow velocities within the creeks are up to an order of magnitude greater than those within the vegetation, where velocities decrease progressively with increasing vegetation densities. Particular vegetation and elevation characteristics cause irregular velocity variations along the vertical, within the vegetation as well as in the creeks. Tentative tidal flux calculations demonstrate the significant contribution of creek flow to the total tidal prism in higher elevated mangroves. By explicitly quantifying and mapping flow routing through mangrove forests, this chapter provides observational evidence for flow routing phenomena that have been postulated in previous studies.

2.1 INTRODUCTION

Mangroves form a key ecosystem along sheltered tropical and sub-tropical coastlines. Mangrove vegetation consists of salt-tolerant trees and shrubs, able to resist hydrodynamic forces [*Augustinus*, 1995]. Next to their abundant ecological functions [*Barbier et al.*, 2008; *Spalding et al.*, 2010], mangroves facilitate coastal stabilization [e.g. *Anthony*, 2004; *Van Santen et al.*, 2007; *Alongi*, 2008] and wave attenuation [e.g. *McIvor et al.*, 2012b]. Mangroves presumably contributed to coastal safety in areas affected by the 2004 Indian Ocean tsunami [*Danielsen et al.*, 2005]. Despite these vital functions, mangroves are in rapid decline. Worldwide mangrove cover declined from ~$18.8 \cdot 10^6$ ha in 1980 [*FAO*, 2007] to ~$13.8 \cdot 10^6$ ha at present [*Giri et al.*, 2011]. In order to increase awareness of the need for, and – ultimately – to promote, successful mangrove preservation, there is an urgent need to better understand the physical mechanisms that shape and maintain mangroves and determine their contribution to coastal safety.

Previous studies into flow patterns in and near mangroves mainly have focussed on the large-scale interactions between the mangrove forest and tidal rivers and creeks, or the nearshore [e.g. *Wolanski et al.*, 1980; *Wattayakorn et al.*, 1990; *Wolanski et al.*, 1990; *Mazda et al.*, 1995; *Furukawa et al.*, 1997; *Aucan and Ridd*, 2000]. This aspect gained considerable interest since flow routing, trapping and outwelling of tidal water fluxes are important for the supply of sediment and nutrients to mangroves. Many studies employ numerical models in investigating these large-scale interactions in mangrove environments [e.g. *Wolanski et al.*, 1980; *Mazda et al.*, 1995; *Furukawa et al.*, 1997; *Aucan and Ridd*, 2000; *Wu et al.*, 2001]. Data from the field are generally sparse; field campaigns usually last for a few days and often cover just one study site [*Furukawa et al.*, 1997; *Aucan and Ridd*, 2000; *Kobashi and Mazda*, 2005].

Studies into flow patterns within the vegetated parts of mangrove forests are very scarce. *Kobashi and Mazda* [2005] initiated this research by collecting flow velocity data along a transect through smoothly sloping riverine mangroves without creeks. They observed a rectification of the flow pattern along the transect: flow velocities were parallel to the river at the forest fringe but gradually turned perpendicular to the river further into the forest. *Aucan and Ridd* [2000] included the effect of creeks incising the forest in their study of the mangroves fringing Cocoa Creek in Australia. From limited visual observations, they concluded that flooding of the mangroves results from a combination of overbank (sheet) flow and creek flow through small forest channels. In contrast, ebbing was observed to largely take place through creek flow, as the very small bed level gradient in the extensive mangroves at Cocoa Creek caused the mangroves near the creek to dry first on ebb tide [*Aucan and Ridd*, 2000].

To date, flow routing within the vegetated parts of mangrove forests has only been explained by implicit observations [e.g. *Aucan and Ridd*, 2000; *Mazda et al.*, 2005; *Van Loon et al.*, 2007], due to a lack of accurate elevation data and flow velocity observations covering sufficiently large mangrove areas. *Mazda et al.* [2007] state that "difficulties involved in making direct measurements of flow patterns mean that we currently have little firm information on patterns

of water circulation and sedimentation within mangrove swamps". This chapter aims to explicitly demonstrate, with field data: (i) how flow routing and flow velocities within the studied mangrove forests are affected qualitatively by topography, exposure and vegetation, and (ii) to what extent tidal creeks contribute to water fluxes into (and out of) mangroves in a higher elevated mangrove area incised by creeks.

We carried out a field campaign in relatively undisturbed estuarine mangrove forests in Trang province, Thailand, from November 2010 to May 2011. Data collection included measurements of elevation, vegetation, water levels and flow velocities. Three sites have been studied that show pronounced differences in: (i) geophysical settings, i.e. location within the estuary and elevation with respect to the tidal range; (ii) hydrodynamic exposure imposed by tides, waves and river flows; and (iii) vegetation cover. Data collection in these three nearby mangrove sites enhanced the identification of the impact of the above mentioned biogeophysical settings on hydrodynamics, as other environmental conditions were largely constant.

This chapter is organized as follows. Section 2.2 starts with an introduction into the geographical settings of the study sites and Section 2.3 addresses the collection and processing of field data. Section 2.4 presents the results of the field study: the topography and vegetation patterns; flow routing at each of the sites; an investigation of the locally observed flow velocity profiles; and finally some explorative calculations of water fluxes along the various flow routes at the creek catchment site. The findings from this field study are discussed and contextualized in Section 2.5. Section 2.6 presents our conclusions on flow routing through mangroves.

2.2   STUDY SITES

The three study sites are located along the east coast of southern Thailand, in Trang province (Figure 2.1A-B). This area is part of the Thai Andaman coast, comprising many embayments, islands and islets offering a perfect habitat for mangroves. The Andaman coast hosts ~80% of the present $244 \cdot 10^3$ ha of Thai mangroves [FAO, 2007], and many coastal ecosystem complexes along this coast are still intact [Spalding et al., 2010]. The study sites are in relatively undisturbed conditions and remained unaffected by the 2004 Indian Ocean tsunami. This is due to the sheltering of the southern part of the Andaman Sea from incoming waves from the Indian Ocean by the tip of Sumatra (Banda Aceh) and the scattered islets.

Trang province (Figure 2.1B) comprises two estuaries: (i) one in the district of Kantang, at the confluence of the rivers Mae Nam Trang and Khlong Palian, herein referred to as the Kantang estuary (Figure 2.1C); and (ii) another in the Palian district, with the rivers Khlong Lak Khan and Khlong Rae as its tributaries, herein referred to as the Palian estuary (Figure 2.1D). Both estuaries show a pronounced difference between (i) mangroves covering areas with smooth, low gradient bed slopes and (ii) mangroves featuring a pronounced 'cliff' at the forest fringe, which is incised by tidal creeks (resembling the morphology of salt marshes [e.g. *Van der Wal et al.*, 2008]). The former mangroves are fronted by intertidal mudflats, typically extending up to

hundreds of meters into the estuary. At the cliffed areas, intertidal mudflats are typically constricted to a few tens of meters width. Due to the presence of creeks and the higher bed elevation – reducing the exposure to hydrodynamics – the cliffed areas feature greater elevation variations such as levees and mud lobster mounds. In contrast, at the smoothly sloping stretches, bed elevations are undisturbed and largely uniform in the longshore direction.
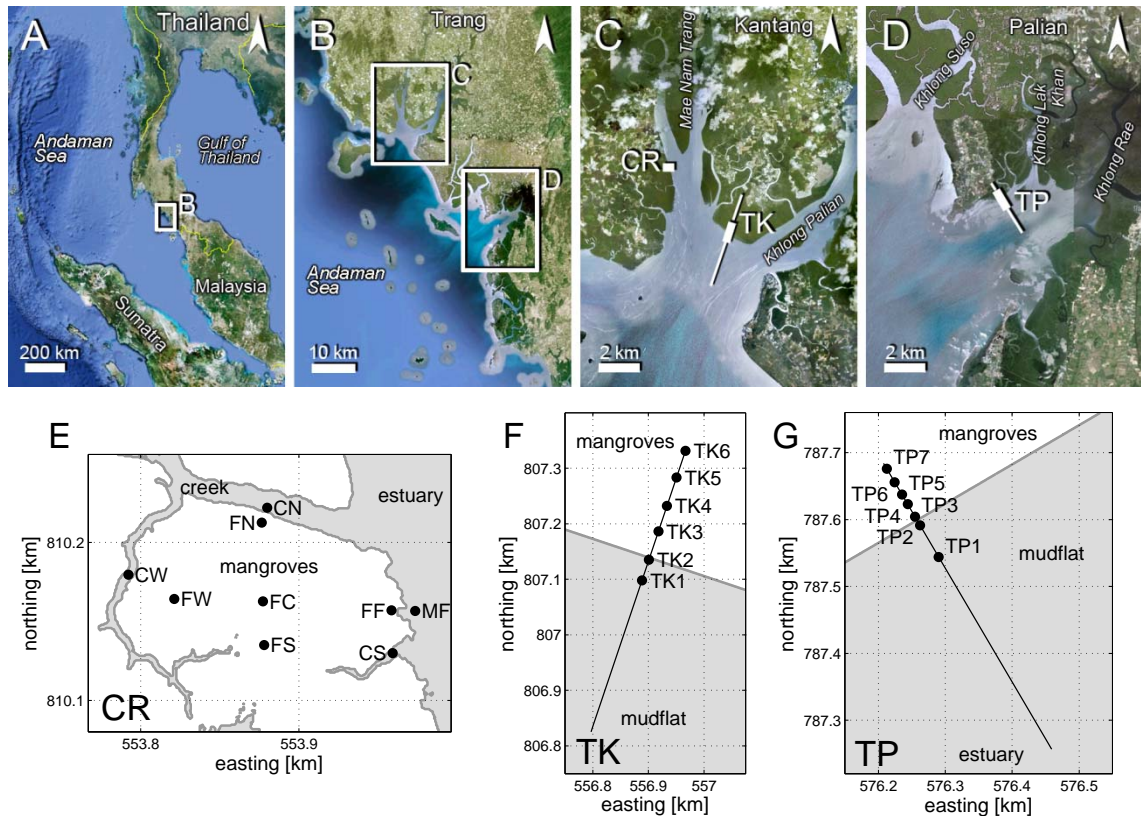
Figure 2.1 – Topography of the study areas : (A) the east coast of southern Thailand facing the Andaman Sea; (B) the coastal areas of Trang province; (C) the Kantang estuary with the position (and orientation) of the creek catchment (CR) and Kantang transect (TK) indicated by white boxes (and a white line); (D) the Palian estuary with the Palian transect (TP) indicated similarly (source: Google Earth). The lower graphs (E-G) show schematic maps of the study sites including the measurement locations (CN/CS/CW = creek north/south/west, FN = fringe north, MF = mudflat, FF = forest fringe, FC/FS/FW = forest centre/south/west). Easting and northing coordinates correspond to UTM-47N.

Two study sites are located in the Kantang estuary (Figure 2.1C). One site is part of a creek catchment (herein referred to as the creek catchment, CR) and is located on the west bank of the Mae Nam Trang, about 6 km inland in the Kantang estuary. This site has a sharp cliff at the riverbank, separating the mudflat from the forest fringe (MF and FF respectively in Figure 2.1), and is incised by pronounced creeks. These creeks are ephemeral tidal creeks with little or no discharge at low tide and do not discharge freshwater as their catchment is limited to the mangroves. The Kantang transect (TK), is located on a land spit in the middle of the Kantang estuary and has a characteristic intertidal area with a very low elevation gradient. The local coastline is oriented parallel to the coastline of the mainland and directly faces the Andaman sea. The third study site is the Palian transect (TP), which is located about 8 km inland in the Palian estuary on the west bank of the Khlong Lak Khan (Figure 2.1D). This site also features a

smoothly sloping, longshore uniform intertidal area, but the location resembles the location of the creek catchment.

TK is the most dynamic field site in terms of wave exposure (Table 2.1). TP is less exposed to waves (Table 2.1), due to its inland position and coastal orientation, but is much more affected by river discharges than TK. Its inland position and high elevation – reducing exposure to waves and river discharges and limiting tidal inundation – make CR the least dynamic site (Table 2.1). Vegetation cover of all field sites is unaffected and highly developed, showing different compositions and densities (Table 2.1).

As a result of the high spatial variability of the bed elevation of the creek catchment in both cross-shore and longshore directions, measurements in this area were carried out over a two-dimensional grid covering ~150x200 m^2 (Figure 2.1E). The longshore uniformity at the other sites, allowed for data collection along transects with a length of about 500 m perpendicular to the local coastline (Figure 2.1F,G).

The study sites are tide-dominated mangroves [*Woodroffe*, 1992] being exposed to mixed semi-diurnal tides (Figure 2.2) with a mean tidal range of 2.0 m and a maximum range of 3.6 m. Quarter diurnal overtides are negligible at the shallow study sites (Figure 2.2). The wind wave climate in this region is strongly influenced by the monsoons. Southwest monsoons generate the highest waves at the Andaman coast and last from May to October. The west coast of southern Thailand has about 2.7-4.0 m of rainfall per year, peaking in September during the southwest monsoon [*Thai Meteorological Department*, 2012]. Hence our data cover a period of fairly quiet meteorological conditions.

Mangroves surrounding the study sites are extending up to 1 km inland. Depending on the tidal amplitude, the tides reach these remote areas. The study sites are limited to the front few hundreds of meters of the mangroves, flooded by all tides and most exposed to tidal currents. This restriction was imposed by the difficult accessibility of these relatively undisturbed mangroves and limited tidal windows for fieldwork. Moreover, further extending the study sites would have reduced spatial data resolution due to time and equipment constraints.
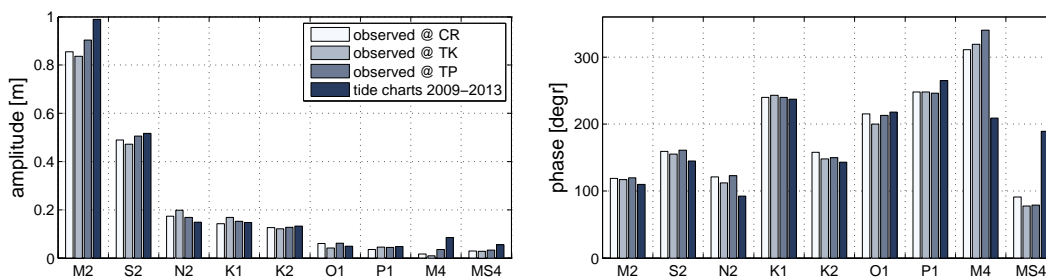
Figure 2.2 – Constituents of the tidal signal observed at the field sites (analysed from retrieved pressure data, see Table 2.2). For reference, tidal constituents retrieved from long-term data from tide charts are included [*Royal Thai Navy*, 2012].

Table 2.1 – Overview of main biogeophysical characteristics of the three field sites.

Site	Geophysical setting	Exposure	Vegetation
CR	Estuarine: high bed (0.3 to 0.9 m +MSL)[a], crab mounds (up to 2.0 m +MSL), sharp cliffs	Tides[b]: $A = 1.9$ m; $v < 0.1$ m/s Waves: not significant	Mixed: dense fringe forest, sparse inner forest
TK	Estuarine/coastal: smooth bed slope (-0.5 to 0.7 m +MSL)[a]	Tides[b]: $A = 1.9$ m; $v < 0.1$ m/s Waves[c]: $H_s = 7.4$ cm; $T_m = 4.6$ s	Zones: sparse front (Avi/Son[d]), dense back (Rhi[d])
TP	Estuarine: smooth bed slope (-0.9 to 0.5 m +MSL)[a]	Tides[b]: $A = 2.0$m; $v < 0.1$ m/s Waves[c]: $H_s = 6.9$ cm; $T_m = 3.5$ s	Zones: sparse front (Avi/Son[d]), dense back (Rhi[d])

[a] Bed levels of the vegetated zone of the study site

[b] A = maximum tidal amplitude (Figure 2.2); v = tidal flow velocity at mudflat in front of mangrove forest (Section 2.4.2)

[c] H_s = significant wave height; T_m = mean wave period (data from *Horstman et al.* [2012])

[d] Avi = *Avicennia*; Son = *Sonneratia*; Rhi = *Rhizophora* (Figure 2.4)

2.3 METHODOLOGY

2.3.1 DATA COLLECTION

TOPOGRAPHIC SURVEY

We mapped the topography of the study areas thoroughly with Trimble survey equipment (SPS 700-S6 Total Station and R-6 Real Time Kinematic GPS). For the creek catchment, ~4400 survey points were mapped with respect to a local benchmark by laser altimetry (Total Station). Survey point density was increased at greater bed level gradients. Pronounced bed elevation changes at creeks, cliffs and mud lobster mounds were surveyed along transects perpendicular to the elevation gradient. Due to the limited topographic variability at the transects, just ~100 survey points were mapped at each site, again with respect to local benchmarks and with an increasing density in steeper sloping (vegetated) parts. The local benchmarks were georeferenced with the RTK-GPS.

Accuracy of the survey data was affected by the instable muddy soil, the limited sight through the vegetation and a lack of sufficient GPS and/or reference signals. Surveying equipment was positioned on wooden planks that did not show significant subsidence during the few hours of deployment at one position. Data obtained from different positions throughout the area – which was required due to the poor sight – did not show identifiable elevation discontinuities at their interfaces. Therefore, local accuracy of the elevation data is high: $O(10^{-2})$ m. The local horizontal accuracy was reduced from $O(10^{-2})$ m along the transects to $O(10^{-1})$ m in the creek catchment due to the repetitive moving of the equipment.

VEGETATION MAPPING

Firstly, vegetation zones with characteristic species compositions and forest densities have been identified at each site. These zones were mapped along with the elevation surveys. For each zone, vegetation was surveyed in detail within representative plots of 20x20 m^2 (15x15 m^2 within the creek catchment). Within these plots, trees were identified and counted. For every

species, we measured the DBH (diameter at breast height, i.e. at 1.3 m elevation) of several representative trees in each plot and took scaled pictures of these trees for qualitative characterization of their geometry (e.g. root height, root density). Vegetation along both transects was surveyed meticulously, comprising measurements of all root and stem diameters of the representative trees at multiple elevations [*Horstman et al.*, 2012].

FLOW VELOCITY AND WATER LEVEL OBSERVATIONS

Flow velocities were monitored throughout the study sites deploying three cable probed Acoustic Doppler Velocimeters (ADVs, Nortek) at 6 MHz head frequency. The ADV probes were mounted downward looking, monitoring flow velocities in x-, y- and z-directions at 0.07 m above the bed (Figure 2.3B). This configuration was previously deployed in salt marshes [*Temmerman et al.*, 2005a; *Horstman et al.*, 2011a]. The ADVs' transmitters were located 0.23 m above the bed (Figure 2.3B), and minimum water depths of ~0.25 m were required for data collection. Probes were positioned with sufficient clearance from the vegetation, levelled and aligned to the north. Pressure sensors in the end-bells of the ADVs' battery/memory housing were installed at 0.07 m above the bed (with the housing buried, Figure 2.3). Deployment details of the ADVs are summarized in Table 2.2.

In the creek catchment, ADVs were deployed in the surrounding creeks, in front of the forest, at the forest fringes and in the inner mangrove area (Table 2.2). Along the transects, ADVs were deployed in each of the successive vegetation zones (Figure 2.4B): mudflat, sparsely vegetated forest fringe and dense back forest (Table 2.2). The three ADVs were deployed at one study site at a time. Installation took place during spring tides (some locations required spring low tide for installation) and most deployments lasted over a spring-neap tidal cycle.

ADVs were as well deployed for measuring vertical flow velocity profiles at several locations. Therefore, ADVs were simultaneously deployed at three different elevations (Figure 2.3A, see Table 2.2 for details), during a single day close to spring tide (only at TK3 this measurement was shortly after neap tide). At CN and FF, the two higher observations were located at ~0.2 and at 0.7-0.8 times the observed maximum water depths during these measurements (2.3 m at CN; 0.6 m at FF). At TK3 and TP4 these ratios were ~0.1 and 0.3-0.5 (at 1.1 m and 1.7 m maximum water depths, respectively). Inundation at FN was too shallow to collect velocity data.

Additionally, Sensus Ultra diver pressure sensors (ReefNet inc.) were deployed during the field campaign in order to obtain information on local tidal elevations and water temperatures (Table 2.2). Along with these measurements, local meteorological data (www.wunderground.com) were stored throughout the field campaign for ambient atmospheric pressures. All equipment was fixed to long (~4m) thick bamboo stakes that were driven into the substrate for ~3 m, providing a stable construction unaffected by short-term (surface) elevation changes.

Table 2.2 – Overview of equipment deployment including observed parameters, positioning, instrument settings and deployment duration.

Parameter observed	Equipment	Location (see Figure 1)	Elevation [m above local bed level]	Sampling frequency [Hz]	Samples per burst; burst interval [s]	Deployment duration per position
Flow velocities (v_x, v_y, v_z) **[m/s]**	Nortek ADV	CN, CW, CS, MF, FF FN [a], FC, FW, FS TK2, TK4, TK6 TP3, TP5, TP7	0.07 (Figure 2.3B)	16	4096; 1500	14 days (2x 14d @ CN; 3x 14d @ FC)
Flow velocities (v_x, v_y, v_z) **[m/s]**	Nortek ADV	CN, FF, FN TK3, TP4	CN: 0.07-0.50-1.50 (Figure 2.3A) FF: 0.07-0.15-0.50[a] FN: 0.07[a]-0.15[a]-0.50[a] TK3/TP4:0.07-0.15-0.50	16	4096; 450 (4096; 300 @ TK3/TP4)	1 day
Pressure [dBar]	Pressure sensor (ADV)	CN, CW, CS, MF, FF FN, FC, FW, FS TK2, TK4, TK6 TP3, TP5, TP7	0.07 (Figure 2.3B)	16	4096; 1500	14 days (2x 14d @ CN; 3x 14d @ FC)
Pressure [dBar]	Pressure sensor (ADV)	CN, FF, FN TK3, TP4	0.07 (Figure 2.3A)	16	4096; 450 (4096; 300 @ TK3/TP4)	1 day
Pressure [mBar]	Sensus Ultra diver	MF TK2, TP2	0.45	1/300	(continuous)	5 months (2 months @ TK2)
Temperature [K]	Sensus Ultra diver	MF TK2, TP2	0.45	1/300	(continuous)	5 months (2 months @ TK2)

[a] No useful data obtained due to insufficient water depths.
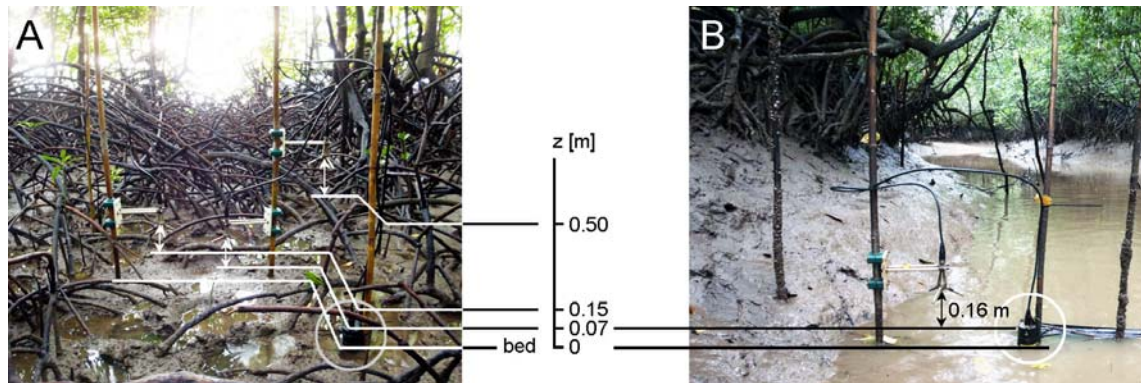
Figure 2.3 – Deployment of ADVs (A) during the collection of flow velocity profile data, here at the densely vegetated fringe of the creek catchment (FF) and (B) during a regular deployment with a single point measurement, here in the main creek at the creek catchment (CN). The end-bells of the partially buried ADV housings (encircled) contain a pressure sensor.

2.3.2   DATA PROCESSING AND ANALYSIS

COMPILING ELEVATION MAPS

Local horizontal coordinates obtained in the Total Station survey were transformed to UTM coordinates by correcting for the offset with the coordinates obtained at the RTK-GPS benchmarks. Vertical coordinates were adjusted to their elevation with respect to mean sea level (MSL). To obtain a digital elevation model (DEM) of the creek catchment CR, transformed

survey data were interpolated in ArcGIS (ordinary kriging, exponential semivariogram model) with an 0.5 m horizontal resolution. Data obtained along each of the transects were first transposed along contour lines parallel to the coast (assuming uniform longshore topography) to obtain one transect perpendicular to the coastline. The gradual elevation changes along this transect were linearly interpolated.

PRE-PROCESSING HYDRODYNAMIC DATA

Pre-processing of the ADV data consisted of filtering, averaging and data correction. To filter inaccurate data from the datasets, the mean correlation threshold for the return signals of the ADVs' receiver probes was set to 80% [*SonTek*, 1997; *Chanson et al.*, 2008]. The filtered velocity and pressure data were free of major disturbances (e.g. shipping or animal activity). The data were subsequently burst-averaged (1 burst = 256 s) to remove minor disturbances and fluctuations caused by wind and swell waves (<20 s), as they are beyond the scope of this chapter.

Water levels were calculated by correcting pressure signals of the ADVs and divers for equipment bound and atmospheric pressure (1008 +/- 5 mbar) offsets. Water depths were calculated with local gravitational acceleration (9.78 m/s^2) and a constant water density (1004 kg/m^3) that was calculated for a water temperature of 26-33 ^{o}C (observed by the Sensus Ultra divers) and a salinity of 9-13 PPT (analysed from water samples). Water levels were calculated by adding local bed elevations. Obtained long-term water level data from the divers are of good quality as proven by the resembling results of the tidal constituents analysis in Figure 2.2. The MSL was derived by comparing these long-term water level measurements with local tide charts of the *Royal Thai Navy* [2012], giving the offset between local elevations from the topographic survey and the MSL reference.

Comparison of the water levels retrieved from the ADVs' pressure sensors and the divers unveiled signal attenuation in two ADVs, which increased towards the end of the field campaign (up to 0.9 m). These errors were compensated for by inter-comparison of the tidal amplitudes observed from the different devices and tide charts and by applying resulting amplification factors. Nevertheless, information on observed water depths (and hence water level gradients) by the ADVs became about one order less accurate (from $O(10^{-2})$ to $O(10^{-1})$ m accuracy) towards the end of the field campaign.

ASSIMILATING QUASI-SYNOPTIC FLOW ROUTING MAPS

Simultaneous flow velocity monitoring was limited to three locations. In order to cover more locations at the creek catchment, repeated deployments were executed (Table 2.2). During each of the subsequent deployments, one ADV was deployed at the same observation point to obtain a benchmark. Hence in any deployment only two additional monitoring locations were covered and the nine-points data collection grid at the creek catchment (Table 2.2) required four fortnightly deployments. Three of the deployments included measurements at FC as benchmark,

while two deployments included CN (Table 2.2). Resembling observations of water levels and flow velocities at these benchmarks were selected for each subsequent deployment. Additionally, tidal and meteorological conditions during these observations have been compared [*Horstman*, in prep.]. Ultimately, for each deployment at the benchmarks, one time slot (i.e. one tidal cycle) with similar observations obtained during similar conditions was selected. With these time slots, simultaneously obtained data for the remaining grid points throughout the study area were selected from each deployment. Hence we reconstructed an area-wide quasi-synoptic dataset, comprising field data for all nine locations and observed during resembling conditions. This procedure was repeated for various high water levels.

2.4   RESULTS

2.4.1   TOPOGRAPHY AND VEGETATION

Topographic characteristics of the creek catchment are: the pronounced ~1 m high cliff at the estuarine border (indicated by a sharp colour gradient in Figure 2.4A); the creeks that incise the area and end in local depressions in the centre of the area; the steep creek banks; the high elevation of the forest floor of 0.5-0.9 m +MSL; and the mud lobster (*Thalassina anomala*) mounds up to 1.5 m high and several meters in diameter in the centre of the area (Figure 2.4A). The latter are a common feature in sheltered parts of mangrove forests [e.g. *Sivasothi*, 2000]. The transects have lower elevations with respect to the tidal range (Figure 2.4A), featuring lower and smoother elevation gradients than the creek catchment. Both transects are fronted by a wide intertidal mudflat with 1:1000-5:1000 slopes, while steeper bed slopes (5:1000-15:1000) are observed within the mangroves, due to enhanced within forest sedimentation [*Augustinus*, 1995].

The creek catchment has four distinct vegetation zones (Figure 2.4B). The forest fringe facing the Mae Nam Trang (zone CRI) is the most densely vegetated part of site CR (Table 2.3). In this zone, a single *Rhizophora* tree has several hundreds of prop roots of a few centimetres diameter at 10 cm above the bed. Higher above the bed, these roots gradually merge into larger roots and eventually into the tree trunk (Figure 2.3). This network of prop roots is densest in the lower 0.5 m above the forest floor (but locally reaches up to 2 m). Zones CRII and CRIII show a mixed tree composition (Table 2.3), comprising trees with much less extensive, height-limited (5-15 cm) root systems: pneumatophores (e.g. *Avicennia*), knee roots (e.g. *Bruguiera*) and plank roots (e.g. *Xylocarpus*). Zone CRIV contains the most mature and tallest *Rhizophora* trees of this site (Table 2.3).

Along the transects, vegetation starts at bed levels around -0.5 m +MSL, much lower than the forest floor in the creek catchment. Vegetation zonation along both transects is quite similar (Figure 2.4B): the sparsely vegetated forest front ranges from about -0.5 to 0.2 m +MSL, featuring a mix of giant *Avicennia* and *Sonneratia* trees (Table 2.3); further inland (elevation >0.2 m +MSL), *Rhizophora* trees are dominant. In zone TKII the *Rhizophora* vegetation is rather uniform, but less than half as dense as in zone TPII (Table 2.3). Beyond the inland extent

of the surveyed transects, at higher elevations, the forests gradually develop into a mixed mangrove forest with mud lobster mounds, resembling the vegetation at the creek catchment.
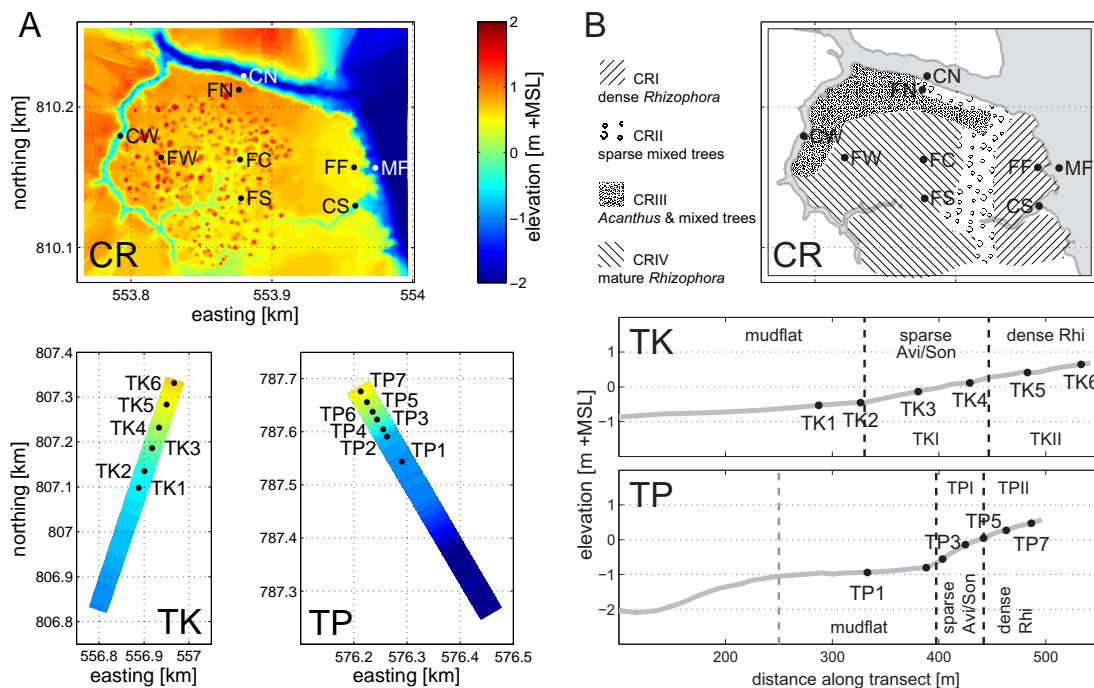
Figure 2.4 – Elevation models (A) and vegetation maps (B) of the study sites. The mudflat at TK extends further offshore (hundreds of meters), but could not be fully surveyed. Vegetation characteristics of the zones in (B) are summarized in Table 2.3. Note: TP3 is located in front of the trees, on a mudflat with a sparse *Avicennia*/*Sonneratia* pneumatophore cover.

Table 2.3 – Vegetation characteristics of the vegetation zones distinguished at the study sites, including tree densities. Zone numbers refer to the zones marked in Figure 2.4B.

Zone	Vegetation description	Tree density [trees/100 m^2]
CRI	*Rhizophora* dominated vegetation getting smaller and denser towards forest fringe with dense root network ~0.5 m high	20 (6.2 *Rhizophora*)
CRII	Mixed vegetation of *Rhizophora*, *Avicennia*, *Sonneratia*, *Bruguiera* and *Xylocarpus* trees of variable ages	19 (3.1 *Rhizophora*)
CRIII	Mixed vegetation of *Rhizophora*, *Avicennia*, *Sonneratia*, *Bruguiera* and *Xylocarpus* trees of variable ages; dense *Acanthus* understory	20 (3.6 *Rhizophora*)
CRIV	Mature/tall *Rhizophora* trees; *Acanthus* and *Acrostichum* understory	7.1 (5.3 *Rhizophora*)
TKI	Sparse, very large *Avicennia* and *Sonneratia* trees (0.2-0.9 m DBH), with smaller ones (10-25 mm DBH) in between; bed covered in pneumatophores (300-2200 per m^2)	41 (0.6 very large trees)
TKII	Homogeneous *Rhizophora* vegetation (40-225 mm DBH) with extensive stilt root systems (up to 340 roots at 0.10 m above bed)	11
TPI	Sparse, very large *Avicennia* and *Sonneratia* trees (0.4-0.9 m DBH); bed covered in pneumatophores (500-1700 per m^2)	0.8
TPII	Homogeneous *Rhizophora* vegetation (60-160 mm DBH) with extensive stilt root systems (up to 450 roots at 0.10 m above bed); many small seedlings in between (few cm's stem diameter); few *Avicennia* and *Sonneratia* trees (36-480 mm DBH)	28 (2.3 *Avi/Son*) + 73 seedlings

The above observations show that vegetation characteristics at each of the sites are resembling for equal bed elevations. This is due to the strong dependence of mangrove vegetation characteristics on local inundation frequencies [*Watson*, 1928; *Van Loon et al.*, 2007].
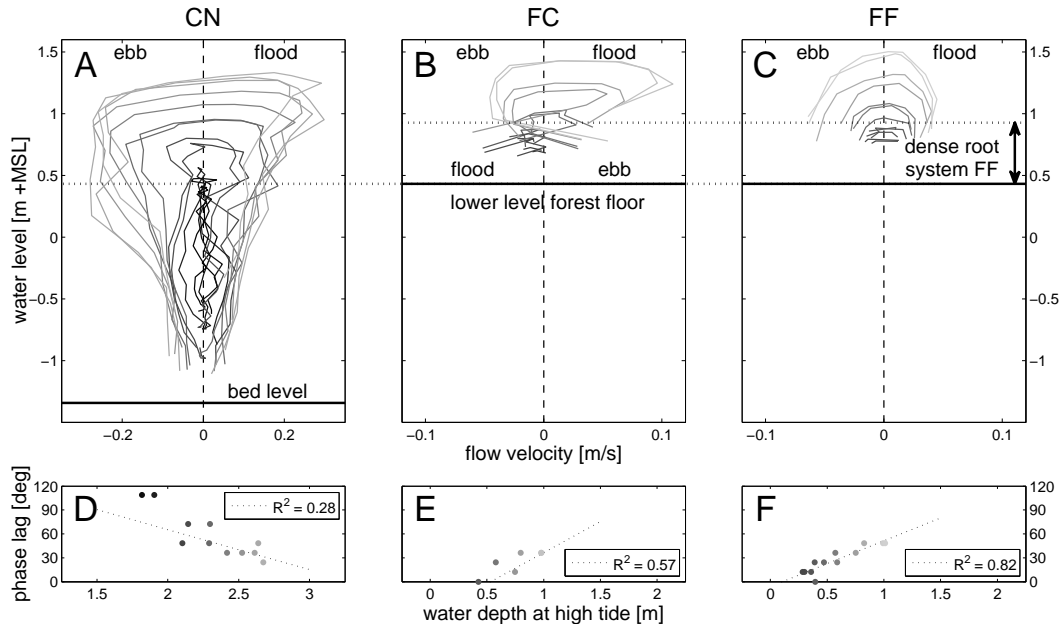
Figure 2.5 – Tidal flow velocity curves and corresponding phase lags observed in the creek catchment in the main creek at CN (A,D), in the centre at FC (B,E) and over the forest fringe at FF (C,F) for variable tidal conditions. The darkest shades denote neap tides, the brightest shades represent spring tides. Flow velocities are scalars ($V = (v_x^2 + v_y^2)^{1/2}$) with a positive (negative) sign if the major velocity component is directed westward (eastward), i.e. the prevailing flow direction of flood (ebb) tides at this site. Phase lags express the time lag between the maximum flood flow velocities and high water (plotted linear regression fits are based on all data obtained at each position, the coefficients of determination (R^2) are presented in the boxes). Note: high water levels do not correspond as data for CN are from another deployment than data for FC and FF.

2.4.2 FLOW ROUTING CHANGES OVER A TIDAL CYCLE

CREEK CATCHMENT – CREEK FLOW VS. SHEET FLOW IN HIGHER ELEVATED MANGROVES

Maximum creek flow velocities are $O(10^{-1})$ m/s and within forest flow velocities are $O(10^{-2})$ m/s (Figure 2.5). This is in line with previous studies observing an order of magnitude difference between flow velocities in mangrove creeks and the adjacent forests [*Anthony*, 2004; *Van Santen et al.*, 2007]. A distinct asymmetry is observed in the tidal flow velocities in the main creek at CN (Figure 2.5A; landward flood (seaward ebb) velocities are defined positive (negative)): a sharp flow velocity peak during flood when the water level exceeds the lowest bed elevations of the creek catchment at ~0.4 m +MSL (as observed in previous creek flow studies [*Wolanski et al.*, 1992; *Mazda et al.*, 1995; *Van Loon et al.*, 2007]), versus an extended velocity peak at ebb at slightly lower water levels than the flood peak (causing self-scouring of the creek [*Wolanski et al.*, 1992]). The phase lag, expressed as the delay between flood velocity peaks and high water, is 45° on average, showing a weak decreasing trend with increasing high water levels (i.e. increasing water depths; Figure 2.5D). When high water levels do not exceed

the lowest bed level of the study site, these velocity peaks diminish. Maximum flow velocities increase from neap to spring tide, because of the increasing tidal prism that enhances water fluxes and flow velocities.

In contrast, flows within the forest do not show a pronounced difference between inflow at flood and outflow at ebb (Figure 2.5B,C). Inflow velocities at the fringe facing the estuary (FF) are reduced significantly due to the sudden cliff and the dense vegetation. On ebb tide, water flows down the cliff, giving rise to slightly higher flow velocities. At the same time, velocities at FF increase when water levels exceed the dense root layer of the forest fringe (Figure 2.5C). Phase lags between maximum water levels and flood flow velocity peaks are reduced to 0-48°; maximum velocities occur upon flooding of FF and hence phase lags increase for greater inundation depths, as the interval between maximum flood velocity and high water increases.

Observations confirm the distinction of a *creek flow* stage and a *sheet flow* stage in the creek catchment (Figure 2.6), instigating a complex tidal flow velocity pattern at the centre of the creek catchment FC (Figure 2.5B). Each tidal inundation of the forest starts and ends with a creek flow stage (Figure 2.6): at water levels just exceeding the forest floor, water cannot flow to/from the centre of the study area directly from/to the estuary, due to a slightly elevated levee just behind the forest fringe (Figure 2.4A). This creek flow stage causes the flood velocity peak at CN once the forest starts to inundate (Figure 2.5A). When high water levels in front of the forest remain below about 0.9 m +MSL, creek flow prevails throughout the tidal cycle (Figure 2.6B). This threshold coincides with the upper limit of the dense root layer at the forest fringe (Figure 2.3 and Figure 2.5).

At the sheet flow stage, flow directions at FC (initially being negative, i.e. eastward, during the creek flow stage) turn to the west (Figure 2.5B), and water flows directly from the estuary into the forest. During the sheet flow stage, flow directions are uniform throughout the site (Figure 2.6A). This sequence reverses at ebb, moving from the sheet flow stage to the creek flow stage (Figure 2.6A). Tidal water levels exceeding this sheet flow threshold induce an enhanced velocity peak at flood tide and a prolonged maximum ebb flow velocity at FC (Figure 2.5B). Shallow water flows over the elevated bank at FN were mainly parallel to the creek flow at CN (visual observation, no hydrodynamic data could be obtained at FN).

Towards flood slack tides, flow velocities rapidly decrease throughout the study area (Figure 2.5). At high water, water is still flowing into the mangroves (Figure 2.5 and Figure 2.6) due to the negative water level gradient throughout the mangroves [e.g. *Mazda et al.*, 2005]. Flow reversal at CN (and CW) shortly lags behind the reversal of the sheet flow pattern within the forest by ~25 minutes or 12° (Figure 2.6). This is related to the limited monitoring height of 0.07 m above the bed as flow reversal near the bed can lag behind the flow reversal near the water surface in this creek (Section 2.4.3).
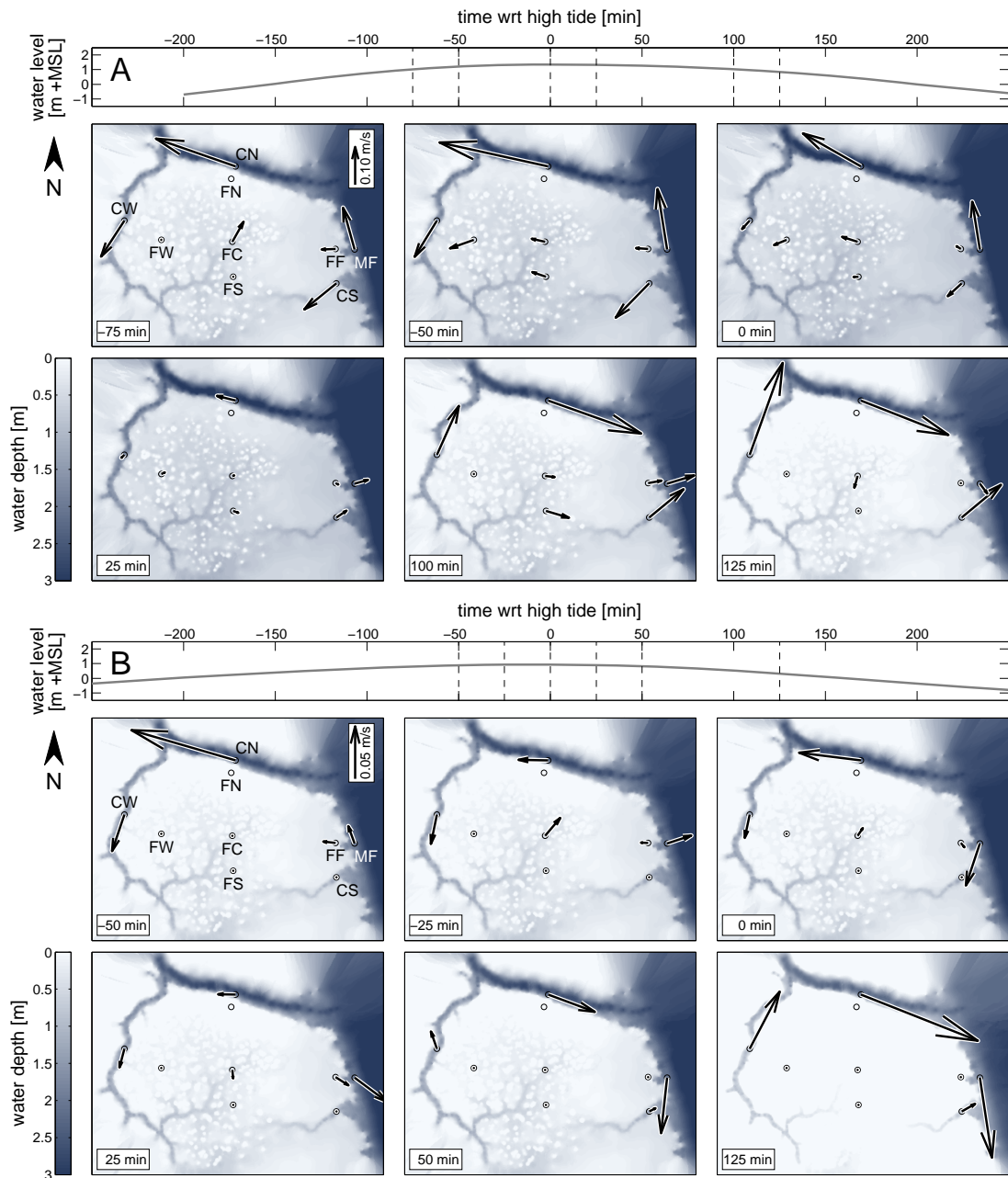
Figure 2.6 – Flow routing through the creek catchment during two different tidal cycles: the high water level in front of the forest at MF is 1.35 m +MSL in (A) and 0.93 m +MSL in (B). These high water levels are exceeded by 62% and 20% of the tides, respectively. Each subplot contains the tidal water levels as observed at MF (upper panel) and inundation maps of the creek catchment, including flow vectors, for six times indicated in the upper panel (lower panels).
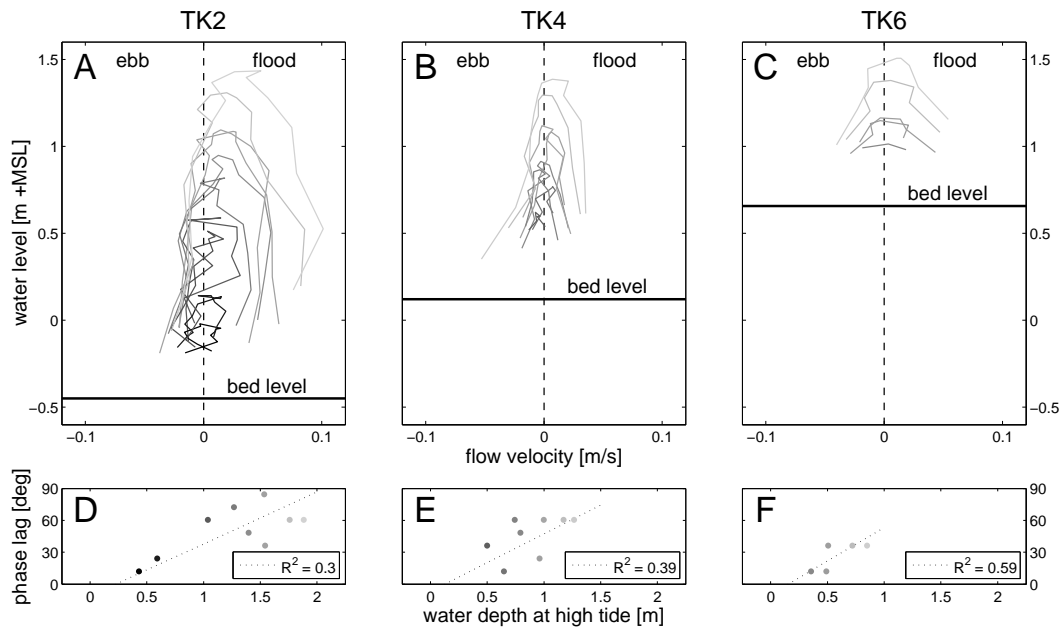
Figure 2.7 – Tidal flow velocity curves and phase lags (as in Figure 2.5) observed along the Kantang transect at TK2 (A,D), TK4 (B,E) and TK6 (C,F). The darkest and brightest shades denote neap and spring tides, respectively. Velocity scalars are assigned a positive (negative) value if their major component is directed northward (southward), i.e. the prevailing flow direction of flood (ebb) tides at this site.
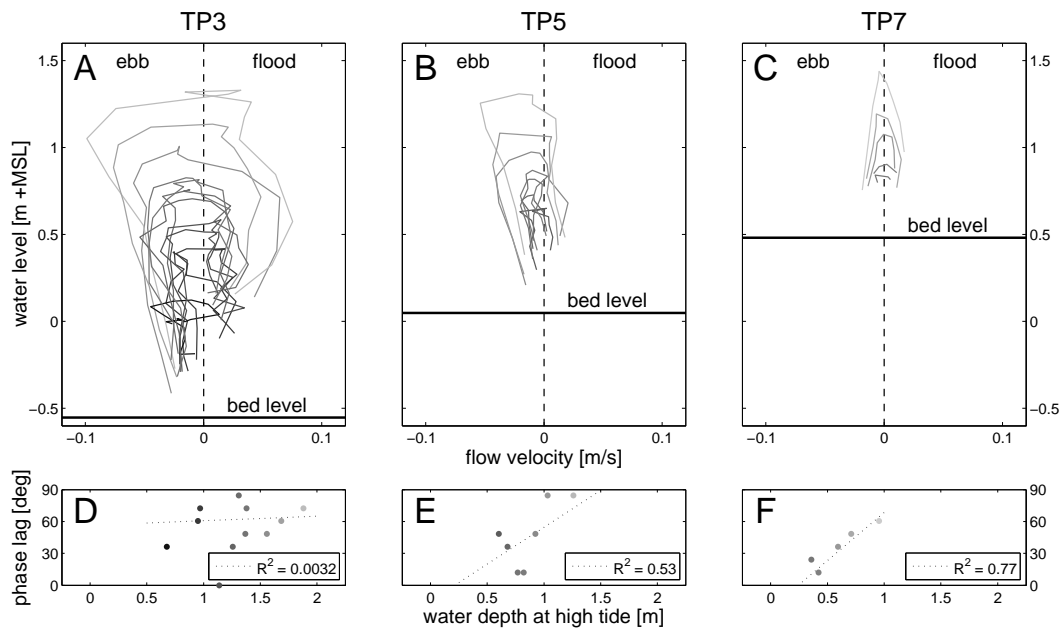
Figure 2.8 – Tidal flow velocity curves and phase lags (as in Figure 2.5) observed along the Palian transect at TP3 (A,D), TP5 (B,E) and TP7 (C,F). The darkest and brightest shades denote neap and spring tides, respectively. Velocity scalars are assigned a positive (negative) value if their major component is directed northward (southward), i.e. the prevailing flow direction of flood (ebb) tides at this site.

TRANSECTS – FLOW ROUTING IN LOW-LYING MANGROVES

Maximum flow velocities along both transects are $O(10^{-2})$ m/s only (Figure 2.7 and Figure 2.8), similar to the flow velocities within the forest at site CR. Flow velocities and phase lags decrease further into the forest, where inundation depths are decreasing and vegetation densities are greatest (Figure 2.7 and Figure 2.8). A notable difference with the tidal flow velocity curves at CR is that, although minor velocity peaks are present, flow velocities remain rather constant on flood and ebb tides. This is attributed to the smooth bed profile at both transects (Figure 2.4). Tidal flow velocity profiles at TK and TP feature a flood and ebb dominance, respectively. Subtidal flow velocities (calculated as tidal averaged velocities) at the Palian transect at TP3 are on average -0.01 m/s (i.e. ebb tidal flows are dominant) with a slightly decreasing trend from -0.015 to -0.005 m/s with increasing high water levels (Figure 2.8A). This is in line with the findings of *Huijts et al.* [2009] that residual outflows in estuarine systems are focussed over tidal shoals, while residual inflow occurs in deeper estuarine channels due to along-channel density gradients. These findings do not apply to the observations at TK though, due to the different orientation of this transect with respect to the discharging rivers Mae Nam Trang and Khlong Palian. At TK2 the subtidal velocities vary significantly with the tidal amplitude: from about -0.01 m/s at neap tides to 0.03 m/s at spring tides, inducing flood dominance. This tendency towards positive subtidal flows at spring tides is due to the increasing tidal prism that counteracts the river discharges into the estuary. At both transects, subtidal velocities diminish inside the forest.

At transect TK, the positive subtidal currents at spring tide deflect flow velocities at TK2 to the northwest (Figure 2.9A), where the Mae Nam Trang enters the estuary (Figure 2.1). At transect TP, flow velocities are mainly directed perpendicular to the transect (Figure 2.9B). Flow velocities at TP align with the main flow direction of the Khlong Lak Khan: to the northeast on flood tide and to the southwest on ebb tide. Nevertheless, flood flow velocities at TP5 are negligible, while ebb tidal velocities are $O(10^{-2})$ m/s (Figure 2.9B), giving rise to the previously mentioned subtidal velocity component.

At TK, it is only during the initial stages of ebb that the discharging current from the forest is strong enough to deflect the prevailing (subtidal) northwest current to the southeast (Figure 2.9A). Similarly, only at low water depths (and low velocities) at the onset and final stages of the forest's flooding, the velocity vectors inside the forest at TP are directed more parallel to the transect in the landward and seaward direction, respectively. At high water, when flow directions within the forest are reversing, flow velocities at TK2 are still directed inland due to the greater phase lag in the deeper water over the non-vegetated mudflat (Figure 2.7 and Figure 2.9). Velocities at TK2 are observed to reverse up to 50 minutes (24°) after the within-forest velocities. The phase lags between high water and peak flood velocities are on average 49° at TK2 and 62° at TP3 (Figure 2.7D and Figure 2.8D) and typically decline into the forest and with decreasing high water levels (i.e. decreasing inundation depths; Figure 2.7 and Figure 2.8). The latter trend is similar to the one obtained at FF (Figure 2.5F) and is again related to the occurrence of maximum velocities upon flooding, inherently inducing greater phase lags for

increasing inundation depths. At TP3, the decline of the phase lag with decreasing inundation depths is suppressed by the subtidal discharge: flood fluxes are counteracted by the negative subtidal flow and maximum flood velocities are only observed when tidal fluxes into the estuary are greatest, in this case about 2 hours prior to high water.

With reduced tidal amplitudes (neap tides, not shown), flow routing along the transects changes. Water depths on the mudflats reduce to magnitudes comparable to the within-forest water depths during spring tides. At TK this causes the subtidal velocity to decrease due to the increasing contribution of bed shear stresses and flow velocity vectors become oriented more parallel to the transect. However, at the Palian transect the subtidal velocity persists due to the dominant impact of the river. Around high water, with maximum water depth and minimum tidal forcing (due to diminishing water level gradients), flow vectors align with the discharge direction of the Khlong Lak Khan. Due to the smaller inundation depths, phase lags between flow reversal in front of and within the forest reduce at both transects and become unresolvable with the time interval of our data.
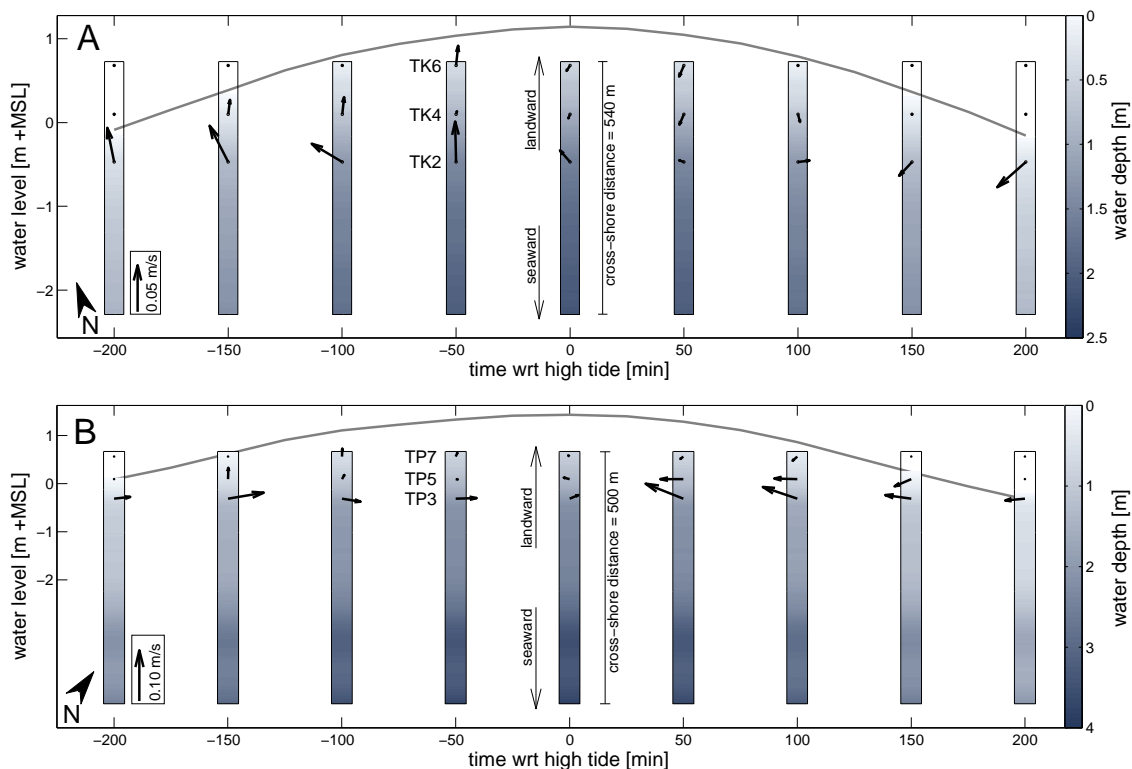
Figure 2.9 – Flow routing along the Kantang transect (A) and Palian transect (B). Both plots represent spring tide conditions. Each subplot contains a tidal water level curve, as observed at the front monitoring location (background) and inundation maps of the transects, including flow velocity vectors, at a 50-minute time interval (bars). Transects are rotated for convenience, the orientation is indicated by north arrows in the lower left corner.

2.4.3 FLOW VELOCITY PROFILES

Flow velocity variations along the vertical were obtained from simultaneous velocity measurements at three fixed elevations at the same location (Figure 2.10). At CN flow velocities at 0.50 m above the bed (V_{50}) are on average 1.53 times greater than those at 0.07 m above the bed (V_7, Table 2.4). Flow velocities at 1.50 m above the bed (V_{150}) show the same average ratio with respect to the near-bed velocity, but with a much greater variance (Table 2.4). Flow velocities nearer the water surface can be (substantially) smaller than those at 0.50 m above the bed, as in the profiles in Figure 2.10A, but can be greater as well. This decrease of flow velocities near the water surface is related to the bathymetry of the creek: (i) momentum redistribution due to secondary currents near the banks of narrow channels can instigate a velocity dip near the water surface [*Yang et al.*, 2004; *Sassi et al.*, 2011] and (ii) reduced velocities over the creek banks (located 2.3 m above the bed level of CN) induce horizontal shear and increased turbulence, reducing flow velocities in the upper parts of the creek flow [*Pestrong*, 1965]. Within-bank water flows in the creek lack the latter friction sources, but only experience friction from the (bare) creek bed and the banks.

Within the mangroves, flow velocity profiles show an increased resemblance with a logarithmic profile (Figure 2.10B). Nevertheless, velocity profiles at TP4 are not consistent over time. Velocities at 0.15 m above the bed (V_{15}) are on average a factor 2.0 greater than V_7, but this ratio is quite variable ($\sigma = 1.1$) and this uncertainty increases higher above the bed (Table 2.4). Variability of the flow velocity ratios at any location cannot be explained by changes in the local water depth (or any derivatives thereof) as correlation tests prove non-significant interdependencies. These irregular flow velocity profiles are attributed to the great variation of the vegetation density with depth (Table 2.3) and to the particular bathymetry of the creek catchment (including cliffs, levees and mud mounds).

Table 2.4 – Means (μ) and standard deviations (σ) for ratios relating flow velocities at different levels above the bed (V_n = velocity at n cm above the bed).

Location	Velocity ratio	μ	σ
CN	V_{50}/V_7	1.53	0.54
CN	V_{150}/V_7	1.53	1.24
FF	V_{15}/V_7	1.74	0.69
FF[a]	V_{50}/V_7	-	-
TK3	V_{15}/V_7	1.47	1.58
TK3	V_{50}/V_7	1.19	4.53
TP4	V_{15}/V_7	2.01	1.08
TP4	V_{50}/V_7	2.77	2.31
TK3&TP4[b]	V_{15}/V_7	1.75	1.37
TK3&TP4[b]	V_{50}/V_7	2.08	3.54

[a] No data are available for V_{50}.

[b] Combined analysis for data obtained at TK3 and TP4.
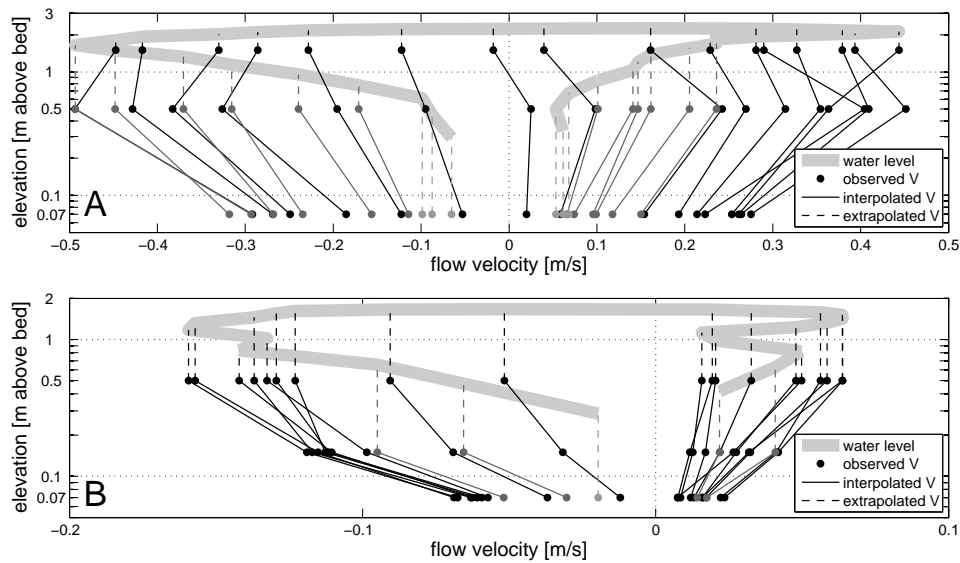
Figure 2.10 – Flow velocity profiles (15 min intervals) during spring tide in the creek catchment at CN (A) and along the Palian transect at TP4 (B). Profiles consist of linear interpolations and constant extrapolations of three (fixed) point measurements along the vertical. Positive velocities indicate incoming tides (i.e. directed westward at CN and northward at TP4).

At high tide, flow reversal near the bed lags behind the reversal in the upper part of the water column at CN (Figure 2.10A). This observation is not persistent throughout our data and is contradictory to the general observation that tidal channel flows reverse slightly earlier near the bed on ebb tide [*Huijts et al.*, 2009]. However, this finding can be explained by the phase lag in the near-bed tidal flow reversal throughout the creek catchment site. Near-bed flow velocities within the forest reverse earlier on ebb tide than within the creek at CN (Figure 2.6) and hence near-surface flow velocities in the creek reverse about concurrently with the velocities throughout the surrounding forest due to horizontal shear (as mentioned above). These opposing water currents might be caused by delayed response of water slopes throughout vegetated areas. At the onset of ebb tide, the local water level gradient in the outer band of the wide mangrove forest, where the creek catchment is located (Figure 2.1C), changes faster than the water level gradient over the entire mangrove forest. This causes the (negative) ebb tidal currents in the front of the forest to start prior to the ebb tidal currents throughout the greater area, causing the within-bank (positive) flood currents in the creek to persist a little longer.

2.4.4 WATER FLUXES AT THE CREEK CATCHMENT

Exploratory water flux calculations were executed for the creek catchment to quantify the contribution of creek flow and sheet flow to the tidal dynamics. Flow velocities throughout the water column were extrapolated from the measured velocities V_7 with the factors presented in Table 2.4. Factors derived for CN were also applied to CS and CW. The missing factor for V_{50}/V_7 at FF was substituted with the value obtained from TK3 and TP4, as the V_{15}/V_7 ratios show good resemblance. Resulting flow velocities (at 0.07/0.15/0.50 m at FF and 0.07/0.50/1.50 m at CN/CW/CS) were interpolated for intermediate elevations and assumed constant above the uppermost velocity estimation (Figure 2.10).
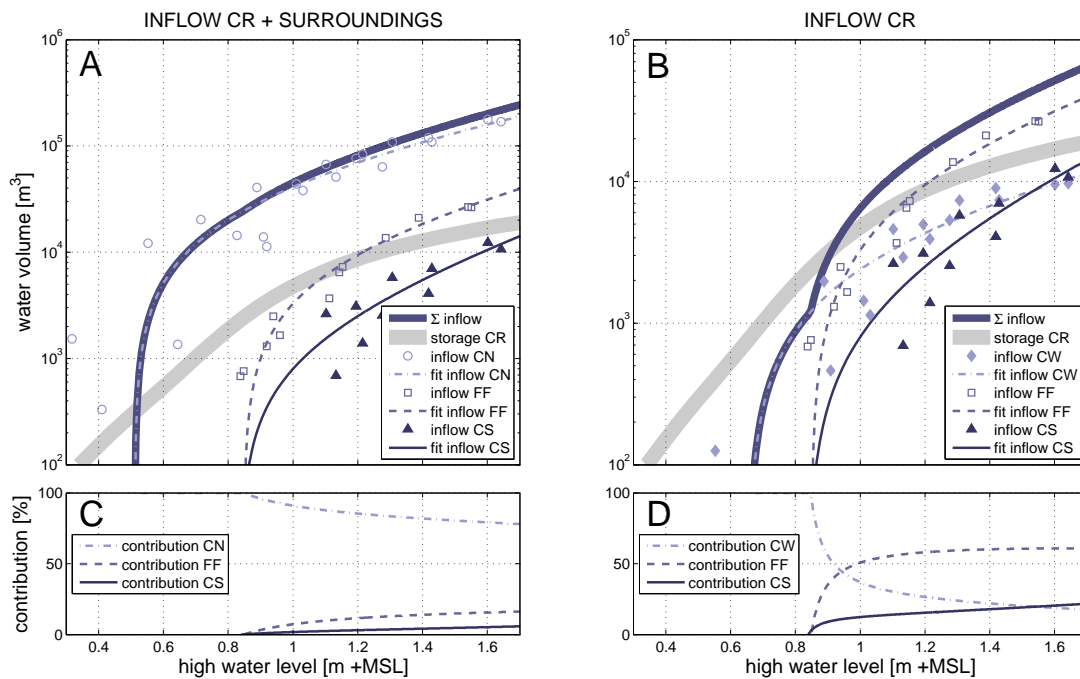
Figure 2.11 – Contribution of different flow paths to tidal inflows (volumetric and percentages) into the greater mangrove forest surrounding CR (A,C) and into the study site CR (B,D). Inflows are related to high water levels observed at MF. Lines in (A,B) represent fitted power functions (see text). The tidal prism of the study site CR has been included for reference (storage CR).

These reconstructed flow velocity profiles were applied to the wet cross-section of each of the creeks and the forest fringe. The cross-sectional area of the creeks was demarcated by the creek bed cross-sections (obtained from the DEM) and the local water level. The wet cross-section over the forest fringe was determined by the local inundation depth and the fringe length (which was limited to the study site). Obtained (time-dependent) flow velocity profiles and water levels were applied uniformly along these cross-sections and discharges were calculated accordingly. The discharges were integrated to obtain inflows during flood and outflows during ebb. These calculations have been applied to the biweekly datasets, so tidal in- and outflow volumes were calculated for variable high water levels (Figure 2.11).

Note that these tidal fluxes do not represent the full tidal prism, as no velocity data were obtained for water depths <0.25 m and hence no discharges are calculated for the initial stages of ebbing and the final stages of flooding. This will particularly affect the fluxes over the elevated forest fringe (at 0.49 m +MWL), as its inundation is limited in depth and duration. In the deep creeks (bed levels at CN, CW and CS are -1.34, -0.41 and -0.54 m +MWL, respectively), inundations are much greater and last longer, hence the relative contribution of the unresolved discharges will be much smaller. Nevertheless, increased velocity fluctuations in the sluggish neap tides reduce the accuracy of the obtained creek fluxes at low high water levels.

Resulting in-/outflow volumes for all flow paths were linked to high water levels observed at MF (as high water levels are sloping throughout the site). For each flow path, power functions were fitted (least squared error) to relate in-/outflows to the high water level (HW) at MF: *in-/outflow = a·HW^b + c* (Figure 2.11). These fits are in good agreement with the calculated data (R^2 = 0.93±0.05). Additionally, the tidal prisms of the creek catchment site (as demarcated by the creeks) were calculated (Figure 2.11) by assuming horizontal high water levels (as accurate water level data throughout the area were lacking), equal to the water levels observed at FC (which is ~0.13 m below the high water level at MF).

Water fluxes were considered at two different scales: (i) the greater creek catchment including the surrounding mangroves extending north and west of the study site, which is fed by the total inflow through creeks CN and CS and by the input over the forest fringe; and (ii) the confined area of the study site CR, which is fed by water fluxes via CS, CW and FF (the bank along the northern creek significantly blocks direct inflow from CN into the study site (Section 2.4.3)). For each area, obtained water fluxes are summarized and contributions of the different flow paths are compared (Figure 2.11). The main creek CN is the major contributor to the total observed inflows (78-100%), although the influx over the forest fringe gains importance with increasing high water levels (up to 16% of the total inflow; Figure 2.11A,C). The smaller creek CW forms the major transport route into the study site CR at neap tides when high water levels do not exceed the previously identified sheet flow threshold (~0.9 m +MSL). However, sheet flow over the forest fringe rapidly exceeds the inflow through CW for high water levels beyond this threshold (Figure 2.11B,D).

For ebb tidal fluxes (Figure 2.12) contributions of the different flow paths are largely resembling the trends in the influxes. However, the contribution of outflow over the forest fringe is smaller than its contribution to inflow for water levels just exceeding the sheet flow threshold: up to 3% and 20% for its contribution to the total outflow and the outflow of CR, respectively. The enhanced contribution of creek flow during ebb tides resembles the implicit observations by *Aucan and Ridd* [2000], as described in the introduction.

For tides with high water levels above 0.95 m +MSL, the summarized inflows into the mangroves exceed the outflows, inducing a net inflow (Figure 2.12A,B). In the greater mangrove forest, these net inflows are directly instigated by the rapidly increasing influxes through the main creek CN at higher tides (Figure 2.12A) and can be related to the decrease in phase lags we observe at CN towards the highest tides (Figure 2.5D). A zero phase lag, when maximum flow velocities and water levels coincide, generates a maximum net inflow (i.e. Stokes transport). Hence, net inflows at CN increase with increasing high water levels. With these higher high water levels, other flow paths present net inflows as well. The net outflows observed for lower high water levels suggest the presence of a fortnightly tidal pump mechanism. However, as the accuracy of the calculated tidal fluxes reduces for lower high water levels, trends in calculated fluxes render less reliable for lower high water levels and we cannot confirm the existence of the suggested tidal pump mechanism.
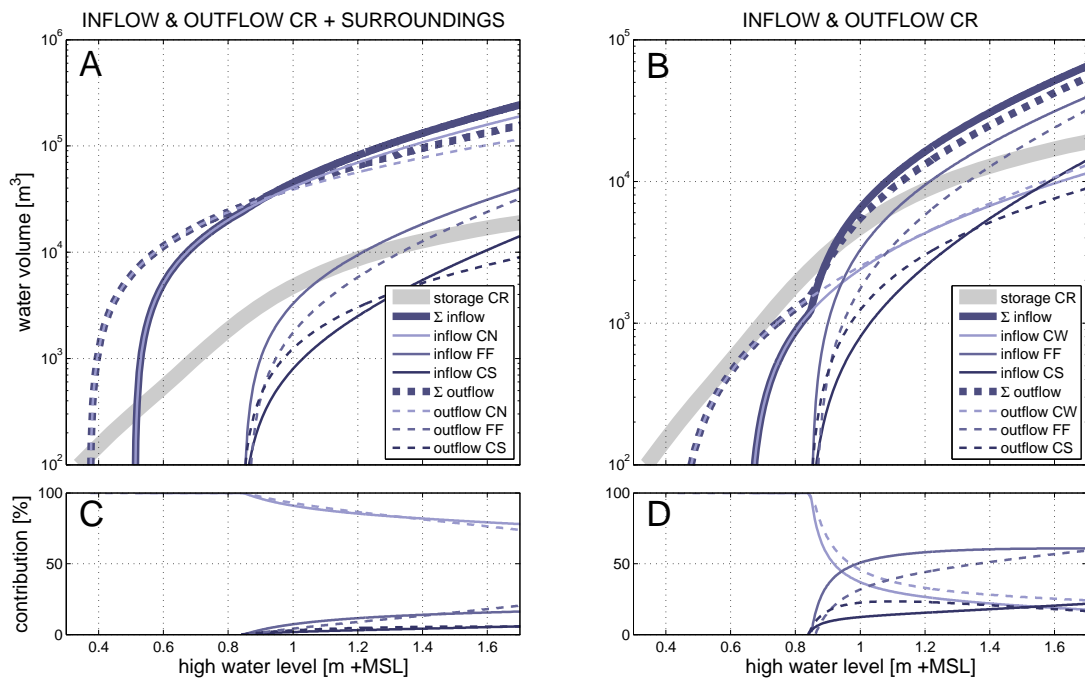
Figure 2.12 – Comparison of the contribution of different flow paths to tidal inflows and outflows (volumetric and percentages) for the greater mangrove forest surrounding CR (A,C) and for the study site CR (B,D). Plots only show the fits to the observed tidal fluxes (as in Figure 2.11).

2.5   DISCUSSION

2.5.1   BIOGEOPHYSICAL EFFECTS ON FLOW ROUTING

Observations at the different study sites, at variable tidal conditions, unveil similarities and differences between the impacts of biogeophysical parameters on flow routing patterns. Firstly, some general principles on hydrodynamics in non-vegetated estuaries and in salt marshes, the temperate climate equivalent of mangroves, are shown to hold for mangrove environments:

- Whereas tidal water levels show a principal semi-diurnal component at all study sites (Figure 2.2), velocity signals contain a significant quarter diurnal component (e.g. Figure 2.5) as velocities are subsequently increasing and decreasing on a single tidal flank [*Blauw et al.*, 2012]. A full wavelet analysis was not possible because of the discontinuity of the data [*Torrence and Compo*, 1998]. However, wavelet analysis on padded velocity signals indicated that the contribution of quarter diurnal harmonics equals the contribution by semi-diurnal constituents in flow velocities at CN, TK2 and TP3 [*Horstman*, in prep.]).

- Phase lags between peak flood velocities and high water levels are on average 45° for the deep creek (CN) to 49-62° at the lowest elevated stations along the transects (TK2 and TP3). Within the forest, phase lags decline due to decreasing inundation depths and increasing shear stresses. A similar trend was observed in salt marshes by *Mariotti and Fagherazzi* [2012].

65

- Flow reversal at CN and TK2 generally lags up to 24° behind the onset of ebb tidal currents within the shallower, vegetated parts of the mangroves (Figure 2.6, Figure 2.9). *Li and Valle-Levinson* [1999] presented analytical proof for this, showing that the flow in deeper channels lags behind the flow velocities over adjacent shoals by ~30° in narrow non-vegetated estuaries.

Secondly, three trends are observed throughout different parts of the study sites, relating hydrodynamics to specific biogeophysical settings:

- At low-lying (w.r.t. MSL) locations in front of the mangroves, at TK2 and TP3, flow directions and velocities strongly correlate with the estuarine flow patterns in front of the transects (Figure 2.9), as imposed by the combination of river discharges and tidal dynamics. Flow velocities seaward of TK2 are lower than those in front of TP3 due to the extensive shallow mudflat in front of TK (Figure 2.1), causing a weaker longshore forcing of the flow vectors at TK. In general, flow velocities at TK are about two times smaller than at TP (Figure 2.7 vs. Figure 2.8).

- At sparsely vegetated locations, flow directions and velocities are susceptible to the prevailing flow outside the vegetation. Flow directions at the sparsely vegetated, low-lying forest front at TP5 and higher elevated creek bank at FN (Figure 2.4B, TPI/CRII in Table 2.3) are mainly parallel to the flow directions at the Khlong Lak Khan and the main creek, respectively (Figure 2.9 and Section 2.4.2). The weaker forcing at the Kantang transect is not affecting the flow velocities or directions inside the forest at TK4 (Figure 2.9), where vegetation is as well more dense than at TP5 (TKI/TPI in Table 2.3).

- At higher elevated (w.r.t. MSL) and densely vegetated areas, flow velocities are rapidly decreasing and become perpendicularly oriented to the flow in open water. The very high vegetation density at the estuarine forest fringe of the creek catchment at FF (Figure 2.4B, CRI in Table 2.3) impedes the flow velocity component parallel to the estuarine water flow: velocities at FF are mainly perpendicular to the shoreline (Figure 2.6). The same is observed along the transects (Figure 2.9), where vegetation densities increase significantly towards the densely vegetated back forest (TKII/TPII in Table 2.3). The cross-shore flow component in the dense vegetation is instigated by the prevailing water level gradient, generated by the combination of relatively fast tidal water level changes on open water (i.e. estuary, river or creek) and the dense vegetation resisting this water movement [*Wolanski et al.*, 1980; *Mazda et al.*, 1995]. This also occurs when water levels in the sparsely vegetated forest fringes are decreasing and dense covers of pneumatophores (i.e. short pencil roots) start to contribute significantly to the imposed friction (Figure 2.9).

Additional bed roughness induced by topographic features such as the creek banks, the low levee in the creek catchment and the mud lobster mounds, could not be distinguished from the vegetation induced roughness. When the entire creek catchment is flooded (sheet flow stage in Figure 2.6A), flow velocities throughout the mangroves are of the same magnitude, irrespective

of the local topography. Hence, although topographic features play a major role in the flow routing at site CR (see 2.5.2), there seems to be a minor effect on actual flow velocities during full inundation of the forest.

2.5.2   CREEK FLOW VS. SHEET FLOW

While *sheet flow* prevails at the gradually inclining transects of TK and TP (Figure 2.9), flow routing in the higher elevated creek catchment is the result of an interplay between *creek flow* and *sheet flow* (as described for salt marshes by *Temmerman et al.* [2005a]). Within the forest, slightly elevated levees along the forest fringe (FF) and the main creeks (CN) inhabit direct inflow at the initial stages of flooding and the final stages of ebbing, forcing the in-/outflow through the creeks; the creek flow stage (cf. Figure 2.6). The onset of the sheet flow stage is further restricted by the dense root networks covering the forest fringe (FF), obstructing direct inflows from the estuary for water levels below 0.9 m +MSL (Figure 2.6, Figure 2.11).

The effects of this sheet flow threshold are observed in the fluxes (Figure 2.11), but near-bed flow velocities over the forest fringe do not increase during the sheet flow stage (Figure 2.5B). The great near-bed vegetation densities at FF (Figure 2.4B, CRI in Table 2.3) induce significant vertical shear and near-bed velocities will be significantly lower than velocities above the dense vegetation layer [*Bouma et al.*, 2007]. Nevertheless, the presence of the sheet flow threshold is corroborated by the changing direction of the flow velocities in the centre of the study site at FC (Figure 2.5B). Contrary to the data at FF, the flow velocity profiles at FC do show a peak at flood tide as water levels exceed 0.9 m +MSL. This velocity peak can even exceed the maximum flood velocities observed at FF (Figure 2.5B,C), because of the reduced vegetation density at FC (CRIV in Table 2.3), reducing vertical shear.

The creeks remain (by far) the main contributor to total tidal fluxes into (and out of) the mangroves (Figure 2.11C), as within-creek water depths are greater and bottom friction in the creeks is negligible compared to shear stresses within the forest vegetation. This is contrary to the increase of the sheet flow contribution in salt marshes to volumes equalling the creek flow contribution at spring high water levels [*Temmerman et al.*, 2005a]. This difference is attributed to the favourable sheet flow conditions over the low and rather uniform salt marsh vegetation – compared to the much higher and variable mangrove vegetation – at increasing water levels.

2.5.3   CALCULATION OF WATER FLUXES

The present study shows that vertical shear in the horizontal velocities is substantial, both in the creeks and within the forest (Table 2.4), due to depth-dependent vegetation densities and pronounced elevation gradients. For within-forest velocities, the contribution of vertical shear was identified by *Wolanski et al.* [1980] to increase velocities by a factor 1.3 from 0.3 m to 1 m above the bed. This is comparable to the increase we obtained (Table 2.4). Observed flow velocities within the creek CN are on average rather constant for the upper part of the water column (Figure 2.10A), resembling previous observations in a mangrove creek by *Woodroffe*

[1985]. However, near-surface flow velocities at CN show a substantial variance (Table 2.4). *Sassi et al.* [2011] obtained detailed information on spatial and temporal velocity variations in a tidal river (~400 m wide) and observed a near-surface velocity dip that was increasing towards the riverbanks. Little is known about these near-surface velocity variations in narrow tidal creeks (*O*(1-10) m wide) incising intertidal areas. The observed near-surface velocity dip of the creek flow (Figure 2.10A) has previously been observed for within-bank creek flows near the sides of tidal channels by *Bayliss-Smith* [1979] and for overbank flow conditions by *Pestrong* [1965]. However, based on our flow velocity profile data, we cannot resolve the contribution of the suggested processes – near-bank secondary currents and horizontal shear with slow overbank flows – to these near-surface velocity variations. Nevertheless, it is evident that neither the constant velocity profile applied by *Temmerman et al.* [2005a], nor the logarithmic velocity profile deployed by *Bryce et al.* [2003], both considering salt marsh creeks, represent our observations.

By explicitly taking account of the vertical shear in the horizontal velocities, a major source of uncertainty in the calculation of tidal fluxes is significantly reduced. Studies into tidal fluxes in salt marsh creeks found that spatial variations in flow velocities and the use of only one sampling location leads to errors in the calculated water fluxes of 5-15% [*Kjerfve and Wolaver*, 1988; *Suk et al.*, 1999; *Temmerman et al.*, 2005a]. If the fluxes in Figure 2.11 were calculated by applying V_7 to the entire water column instead, calculated creek fluxes would even have been only 60-80% of the presented fluxes.

Unfortunately, water level observations became increasingly inaccurate during the field campaign (see Section 2.3.2) and the corrected water levels still show negative deviations of 10-15% of the local water depth (negative, because inaccuracies were caused by dampened pressure signals). Additionally, within-creek velocity profiles were only obtained at CN and lateral variations of flow velocities along the creek cross-section were not resolved. The latter were also not accounted for in previous studies. In summary, presented creek fluxes are presumably as accurate as in previous studies, since inaccurate water level observations cancel the positive effect of the increased vertical velocity resolution. This accuracy only applies to the tidal phases that were covered by our velocity measurements (water depths >0.25 m).

Concerning the estimation of tidal fluxes over the vegetated forest fringe, no previous work has shown how to cope effectively with the inherent spatial velocity variations. The logarithmic flow profile, representing turbulent flows over 'flat' beds, is not applicable for water flowing through the densely vegetated forest fringe (cf. Figure 2.10B). At the other hand, fluxes over the forest fringe of CR would have been up to 40% smaller if only V_7 was applied to the entire water column. Although the bed level is rather constant along the forest fringe (Figure 2.4A), vegetation density and structure are quite variable (Figure 2.3) and will cause local deviations of the obtained flow velocity profiles. In order to improve accuracy of the sheet flow estimates, spatial variability in the flow profiles – horizontal as well as vertical, since no velocity data

were obtained for V_{50} at FF and velocities at water depths <0.25 m were not covered either – should be resolved.

2.5.4 POTENTIAL GENERALITY OF OBSERVED PHENOMENA

The three study sites represent two distinct topographies for mangrove areas: (i) a higher elevated forest with bed levels above MSL, surrounded by cliffs and incised by creeks at CR; and (ii) a smoothly inclining forest starting below MSL, fronted by extensive mudflats at TK and TP. Bed elevations in the latter areas are gradually increasing towards the back forest and creeks do not occur. These study sites do represent the main features that are observed throughout the local mangrove forests – and in many estuarine and coastal mangroves in Southeast Asia – as introduced in Section 2.2. The flow routing within the greater forests surrounding our study sites are supposed to be reminiscent of the dynamics at the study sites. This is corroborated by the fact that the greater mangrove forest shows a generic upscaling: nearby creeks extending further into the mangroves are wider and deeper at their confluence with the estuary as they facilitate a greater tidal prism; and the forest floor just shows a greater increase in elevation over the entire width of the mangrove forests.

Due to the characteristic zonation of mangroves [*Watson*, 1928; *Van Loon et al.*, 2007], vegetation is largely resembling that at other relatively undisturbed mangrove forests with comparable topographic features. Nevertheless, vegetation densities will depend on developmental stage and local exposure. Comparable exposure characteristics are expected at other mangrove sites however, as most mangroves thrive at sheltered intertidal positions without significant wave exposure, as in the present study. Concerning the forcing by river-fed estuarine discharges in front of the mangroves, different conditions were covered within the present study. The limited effects of this forcing on the flow routing at CR will also be observed in other elevated, creek-incised mangrove forests. Other gently sloping estuarine/coastal mangrove sites in the region either directly facing the open sea or bordering a river, face a forcing comparable to TK and TP, respectively, and will resemble flow routing observed at these transects.

All velocity data presented in this chapter are based on point measurements, simultaneously obtained at different positions and elevations. Data collection procedures were carefully maintained throughout the field campaign, to ascertain that all velocity data were obtained under resembling conditions (e.g. fixed heights, away from vegetation, full spring-neap tidal cycles; see Table 2.2). This way, we collected a consistent set of data suited for the analysis of the qualitative trends presented in this chapter. In order to obtain detailed knowledge on the quantitative impact of variable biogeophysical settings on flow routing, these processes need to be studied at a much greater spatial and temporal resolution. Based on the present field data, we will develop a numerical model in order to obtain this increased resolution (see Chapter 3). Herewith, we will study the sensitivity of the mangrove hydrodynamics to changes in bathymetry, vegetation cover and hydrodynamic exposure independently, in order to isolate the effects of each of these factors. This will also show how our observations from the field could be generalized to other sites with (slightly) different conditions.

2.6   CONCLUSIONS

Particular differences in flow routing are observed between (i) a higher elevated mangrove forest (above MSL) that is fronted by a steep cliff and incised by pronounced creeks and (ii) gradually inclining sites with a very small bed slope, where mangrove vegetation starts below MSL and is fronted by extensive mudflats. The former areas display two stages during flooding (and ebbing): a *creek flow* stage, when water is supplied to (discharged from) the mangroves mainly through the creeks; and a *sheet flow* stage, when inflow (outflow) over the densely vegetated forest fringe, imposing a sheet flow threshold, occurs and flow velocities throughout the area turn perpendicular to the local coastline. The characteristic topography of the higher elevated mangroves gives rise to marked velocity fluctuations within the ephemeral tidal creeks, where flow velocities ($O(10^{-1})$ m/s) are up to an order of magnitude greater than in the surrounding forest. Tidal water flows at the low-lying transects ($O(10^{-2})$ m/s) lack these morphology induced velocity patterns, but instead are much more exposed to estuarine currents giving rise to longshore subtidal velocity components. At all sites, flow velocities are observed to decrease significantly when bed levels increase and mangrove vegetation becomes denser. Friction imposed by the dense forest vegetation counteracts longshore velocity components and flow velocities are mainly observed along cross-shore water level gradients within the mangroves. High water at the lower, non-vegetated parts of the transects and in the deep creek lags behind flood tidal velocity peak with about 40-60° (about 1.5-2 hrs). These phase lags reduce with increasing bed elevation and vegetation density. Additionally, tidal flow reversal at these low-elevation positions are shown to lag (up to 50 minutes) the onset of ebb tidal flow velocities within the elevated, vegetated parts of the study sites.

Due to the vegetation and characteristic bathymetry, observed flow velocity profiles in the mangroves and in a creek deviate substantially from the regular logarithmic velocity profiles. Especially near-surface velocities in the creek are found to be affected by both wall effects at the steep creek banks and flow deceleration due to horizontal shear with the relatively slow flow velocities through the surrounding mangroves. Tidal fluxes have been calculated with the observed variations of the velocity profiles. For the higher elevated mangroves incised by creeks, these fluxes indicate a predominant contribution by the creeks to the tidal flooding and ebbing of the mangroves. Direct inflow over the forest fringe gains share once water levels exceed the sheet flow threshold, but remains much smaller than the inflow through the creeks. Calculated fluxes through the main creek suggest a fortnightly tidal pump with net tidal inflows into the mangroves during the highest tides, which might be instigated by the decreasing phase lags in this creek with increasing high water levels.

This chapter explicitly quantified and mapped flow routing in mangrove swamps, and related flow routing characteristics, in a qualitative sense, to three biogeophysical factors: elevation, exposure and vegetation. The field sites differ substantially in these biogeophysical conditions and thereby, observed tidal dynamics are supposedly representative for many mangrove sites. Quantification and high-resolution analysis of the (separate) impacts of these conditions on tidal dynamics in mangroves will be facilitated by a numerical model that is presented in Chapter 3.

CHAPTER 3

TIDAL-SCALE FLOW ROUTING AND SEDIMENTATION
IN MANGROVE FORESTS:
COMBINING FIELD DATA AND NUMERICAL MODELLING[†]

Monitoring tidal water flows in dense Rhizophora vegetation fringing the Mae Nam Trang estuary, Thailand.

ABSTRACT

Tidal-scale bio-physical interactions establish particular flow routing and sedimentation patterns in coastal mangroves. Sluggish water flows through the mangrove vegetation and enhanced sediment deposition are essential to maintain these valuable ecosystems, thereby enabling their contribution to coastal protection and stabilization. To improve our understanding of these bio-physical interactions, we combine spatially explicit observations of tidal-scale flow routing and sediment deposition in coastal mangroves with numerical simulations. Field observations were obtained in an elevated mangrove stand dissected by tidal creeks, located in the Trang river estuary at the Thai Andaman coast. An accurate and efficient depth-averaged process-based numerical model of this field site was developed in Delft3D.

The creeks form the major pathway for the tidal inflow during the lower tides, while the sheltered interior of the forest is an effective sediment sink during the higher tides. A numerical sensitivity analysis of the initial response – or adaptive capacity – of the studied mangrove system to instantaneous environmental changes uncovers a stable state. Deposition rates are rather independent of the vegetation density, while counteracting adjustments of the topography and relative elevation. Sediment trapping efficiency strongly reduces with diminishing sediment inputs and mangrove area losses. Deeper inundations of the mangroves are in favour of flow routing through the forest and spatially averaged deposition rates drop markedly when this coincides with decreasing vegetation densities. These results clearly indicate the sensitivity of mangroves' ecosystem engineering ability – in terms of sedimentation – to climate change and anthropogenic threats.

3.1   INTRODUCTION

Mangrove forests consist of salt-tolerant trees and shrubs that thrive in intertidal areas of relatively sheltered tropical and sub-tropical coastlines (e.g. estuaries and lagoons). This vegetation has a substantial above ground biomass, consisting of (aerial) roots, stems and canopy, that significantly interacts with tidal and riverine water flows [*Wolanski et al.*, 1980; *Furukawa et al.*, 1997; *Mazda et al.*, 2005]. Mangroves also support coastal stability: directly, by trapping and stabilizing sediments with their root systems; and indirectly, by reducing hydrodynamic exposure of the substrate [*Krauss et al.*, 2003; *Van Santen et al.*, 2007]. These bio-physical interactions are typical features of biogeomorphic systems that are created by ecosystem engineers – organisms changing their abiotic environment [*Jones et al.*, 1994; 1997]. Knowledge on the bio-physical functioning of mangroves is key to understanding mangroves' persistence in view of global climate change effects and anthropogenic threats. Such resilience issues comprise mangrove adaptation to increased water levels caused by sea level rise [*Alongi*, 2008; *Webb et al.*, 2013], reduced tidal prism due to the conversion of mangrove forests to aqua- or agriculture or for other purposes [*Mazda et al.*, 1995; *Thampanya et al.*, 2006; *Winterwerp et al.*, 2013], changes in mangrove cover induced by (natural) dynamics of mangrove composition and structure [*Dahdouh-Guebas et al.*, 2000] or sediment starvation due to river damming [*Thampanya et al.*, 2006].

Studies on the bio-physical functioning of mangroves, describing the movement of water and suspended matter (sediments, organic matter etc.) through mangrove systems, initially focussed on creek-forest interactions. These studies emphasized the tidal asymmetry in mangrove creek hydrodynamics: creek flow is generally ebb dominated due to the delayed discharge from the hydraulically rough vegetated areas [*Wolanski et al.*, 1980; *Mazda et al.*, 1995; *Furukawa et al.*, 1997]. Within the mangroves, vegetation induced friction significantly decelerates tidal currents [e.g. *Mazda et al.*, 1995]. These processes result in a net input of sediments into mangroves' vegetated areas [*Wattayakorn et al.*, 1990; *Bryce et al.*, 2003; *Vo-Luong and Massel*, 2006] while the dissecting creeks maintain depth by self-scouring through enhanced ebb tidal outflows [*Wolanski et al.*, 1980; *Mazda et al.*, 1995].

For a mechanistic understanding of the tidal routing of water and sediments through mangroves, additional research is required distinguishing between the contribution of different environmental settings to these processes. The abovementioned field data provide a solid base for identifying the bio-physical interactions in mangroves. Accurate model representations of these bio-physical interactions allow for an in-depth analysis isolating the contribution of specific biogeophysical mangrove settings to the tidal-scale dynamics.

The first numerical, depth-averaged models of mangroves were used to study creek flow in mangroves. These models simulated vegetation induced friction through an adjusted roughness factor and the modelled topography was greatly simplified and mostly flat [*Wolanski et al.*, 1980; *Wattayakorn et al.*, 1990; *Mazda et al.*, 1995; *Furukawa et al.*, 1997; *Aucan and Ridd*, 2000]. Meanwhile, *Mazda et al.* [1995; 1997; 2005] derived analytical models for water flows

through mangrove vegetation, parameterizing vegetation by the frontal plant area, vegetation volume and representative vegetation length scale. The latter parameterization represents the void space in between the mangrove vegetation within a control volume, divided by the total projected area of the obstacles in that control volume [*Mazda et al.*, 1997b]. This length scale varies greatly with vegetation species, vegetation density and tidal elevation and was used to parameterize the drag coefficient and the coefficient of dynamic eddy viscosity [*Mazda et al.*, 2005].

More detailed mechanistic insight in bio-physical interactions in mangroves was obtained from flume experiments with dowels as scaled mangrove trees, studying creek-forest interactions [*Wu et al.*, 2001; *Struve et al.*, 2003]. From their findings, *Wu et al.* [2001] developed a numerical model explicitly accounting for vegetation induced drag and the blockage effect by the vegetation, both computed directly from structural mangrove characteristics. Yet, none of the numerical models simulating flow routing in mangroves takes account of the depth dependency of the vegetation characteristics, nor of the local topography.

For salt marshes – the temperate climate equivalent of mangroves – the bio-physical interactions between vegetation and tidal-scale dynamics have been studied in a spatially explicit sense, through field, flume and modelling experiments [*Leonard*, 1997; *Temmerman et al.*, 2005b; *Bouma et al.*, 2007]. These studies provided insights in the tidal flow patterns through salt marsh areas or, at a smaller scale, through salt marsh vegetation and the consequent sediment deposition patterns. *Temmerman et al.* [2005b] applied the Delft3D modelling suite [*Lesser et al.*, 2004] to simulate tidal-scale flow routing and deposition patterns in a salt marsh. This process-based numerical model explicitly accounted for vegetation induced drag and turbulence. For these computations, the vegetation was modelled as (multiple layers of) rigid vertical cylinders with particular (spatially varying) diameters and densities. The strikingly different vegetation structure of the rather uniform, dense and height limited marsh vegetation and the much more heterogeneous, larger, but (often) sparser mangrove vegetation means that the results from such marsh studies cannot be used to infer the outcomes for mangroves. Calibration and validation of this model for a mangrove environment requires spatially explicit empirical data of the tidal-scale hydrodynamics and sedimentation in mangrove forests, as well as detailed bathymetric information and vegetation characteristics.

Previously, we presented an observational study of the flow routing in three estuarine mangrove sites in southern Thailand (Chapter 2). Specific aspects of the biogeophysical settings of these sites (topography, vegetation density, hydrodynamic exposure) and their impact on the tidal-scale flow routing were analysed from observed flow velocities and directions. Within a mangrove site elevated above mean sea level and dissected by tidal creeks, two distinct flow regimes were observed: *creek flow* prevailed when water levels remained below a dense vegetation layer at the mangrove fringe bordering the estuary, while *sheet flow* prevailed when this threshold was exceeded and direct inflow over the forest fringe was facilitated. Sheet flow

directions at this site were unaffected by estuarine currents and sheet flows followed the vegetation induced cross-shore water level gradients.

In this chapter we aim to: (i) analyse the implications of the tidal flow routing for the deposition rates and patterns in a mangrove system dissected by tidal creeks, and to (ii) explore the initial response of both the flow routing and the deposition patterns to instantaneous changes of the biogeophysical settings of the mangroves, by using a combined observational-numerical approach. These aims are addressed using a numerical model (Delft3D) combined with field measurements collected at a mangrove site along the Thai Andaman coast. This approach is required to simulate the (isolated) variation of variable biogeophysical settings, comprising changes of the topography, vegetation, relative elevation, sediment supply and mangrove extent. The sensitivity analysis enhances our understanding of the contribution of these biogeophysical settings to the bio-physical interactions observed in the studied mangrove site by showing the initial system response to instantaneous changes in any of these parameters.

3.2 FIELD OBSERVATIONS

3.2.1 FIELD SITE

Field data for this study were collected from November 2010 to May 2011 in an estuary in the district of Kantang in Trang province, Southern Thailand (Figure 3.1B). The study site ($7^{o}19'45''$N; $99^{o}29'17''$E) is located on the west bank of the estuary of the river Mae Nam Trang, approximately 6 km inland from the main coast and 2 km upstream of the confluence of the rivers Mae Nam Trang and Khlong Palian.

The studied mangrove site is tide-dominated [*Woodroffe*, 1992], exposed to mixed semi-diurnal tides with a mean tidal range of 2.0 m and a spring tidal range of 3.6 m. Wave exposure is very limited due to the sheltered location of the study site. Mangrove vegetation is in pristine condition and highly developed. The mangroves extend up to 1.5 km inland (Figure 3.1C), where they are partly converted into aquaculture ponds. The study site is located at the estuarine front of the mangroves and stretches a few hundreds of meters inland (Figure 3.1D). This area is flooded by most tides and significantly exposed to tidal currents.

3.2.2 FIELD DATA

TOPOGRAPHY

The intertidal part of the study site was mapped accurately through a high-resolution total station survey. Topographic data were interpolated in ArcGIS (ordinary kriging with exponential semivariogram; Figure 3.1D). Local vertical accuracy of the elevation data was $O(10^{-2})$ m, while the horizontal accuracy was reduced to $O(10^{-1})$ m due to the repetitive moving of surveying equipment required to cover the entire study site (Section 2.3.1). Subtidal bed levels were obtained through echosoundings along a cross-shore transect originating at N0, resolving a 7:100 cross-shore bed slope for the estuarine river bed [*Horstman*, in prep.].
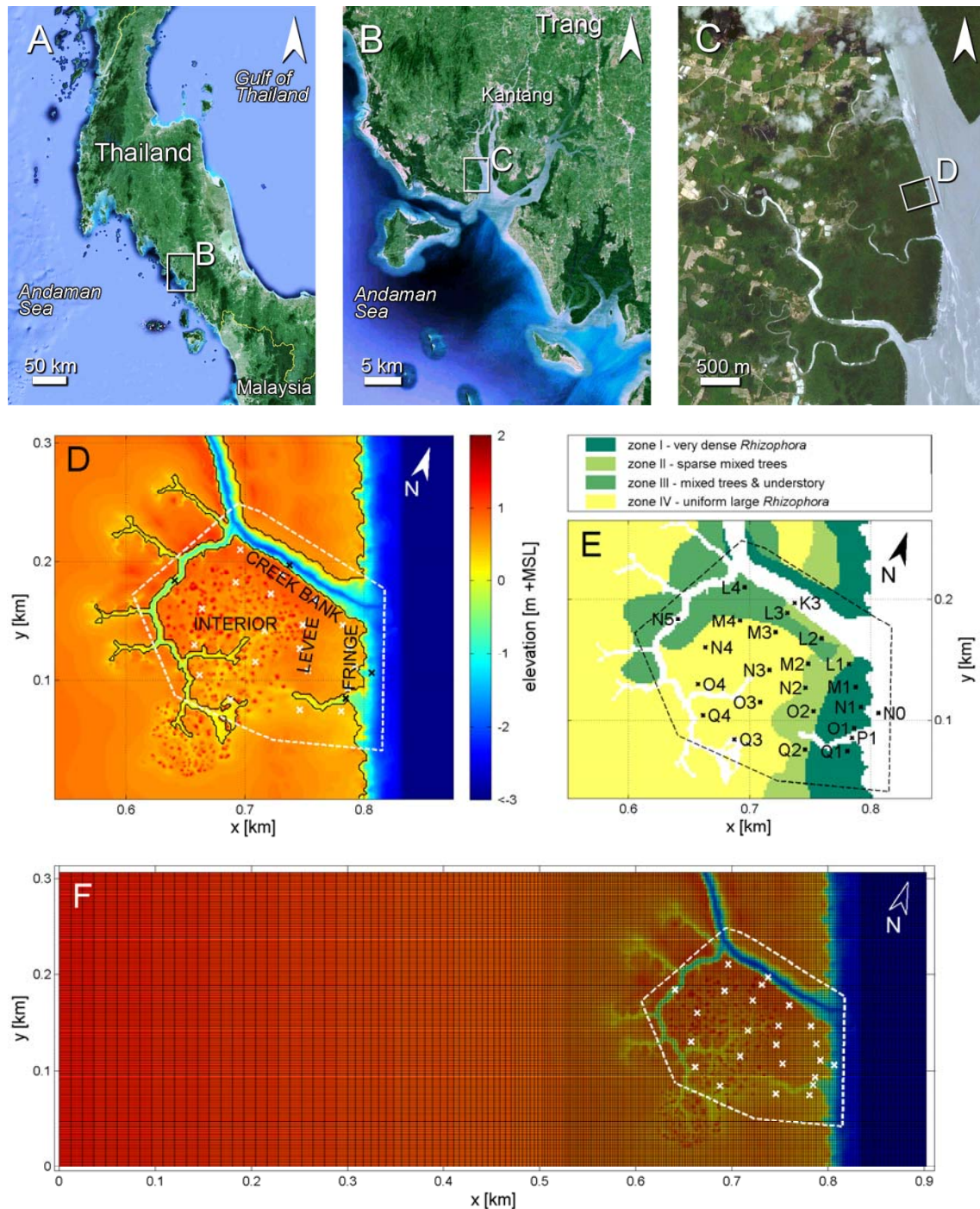
Figure 3.1 – (A) The convoluted Andaman coast of Southern Thailand. (B) The Mae Nam Trang estuary, Trang province. (C) Mangrove forests covering the west bank of the lower Mae Nam Trang river, where the study site is located. (D) Topographic map of the study site, demarcated by the dashed white line. The locations of (field) data collection are marked (x), contours of creeks and cliffs are plotted in black and particular zones of the study site are indicated (creek bank, fringe, levee, interior). (E) The vegetation cover, including codes of the data collection points. Details of the vegetation composition in the four vegetation zones are summarized in Table 3.1. (F) The model domain for the numerical simulations in Delft3D. The rectilinear model grid is plotted on top of the extended topography of the study site and its surroundings.

The study site features an elevated mangrove platform, elevated 0.3-0.9 m +MSL (Mean Sea Level), fronted by a sharp cliff separating the mangrove forest from the mudflat (i.e. the mangrove-mudflat edge). The platform is dissected by pronounced tidal creeks (Figure 3.1D). These creeks are ephemeral, lacking (fresh)water inputs from the inland area, as their catchment is limited to the mangroves. Mud mounds created by mud lobsters (*Thalassina*) are common in the less-exposed parts of the study site and are up to 1.5 m high and several meters in diameter. Levees with elevations slightly higher than the surrounding forest floor were observed just inland of the estuarine forest fringe and at the creek banks (Figure 3.1D). Micro-topographic variations ($O(10^{-3}-10^{-2})$ m) due to e.g. burrowing crabs or vegetational uplift are omnipresent throughout the area, but remained unresolved in the elevation survey.

VEGETATION COVER

Vegetation at the study site generally comprises four mangrove tree genera and one mangrove shrub: *Rhizophora*, *Bruguiera*, *Xylocarpus*, *Avicennia* and *Acanthus*, respectively. Each of these trees features distinct root systems: stilt roots, knee roots, plank roots and pneumatophores (pencil roots), respectively (see Table 3.1). Four vegetation zones were identified (Figure 3.1E): the exposed forest fringe accommodating a dense tree mixture dominated by *Rhizophora* trees with great root density (Figure 3.1E, zone I); the lower elevated interior of the study site, rather uniformly covered with older, taller *Rhizophora* trees with extensive root systems (zone IV); and the levees behind the forest fringe (zone II) and the elevated creek banks (zone III), overgrown with a sparser tree assemblage. The higher elevated parts of the forest floor in zone III and the mud mounds are covered with *Acanthus* (and few *Acrostichum*) shrubs. This vegetation zonation correlates with hydrodynamic exposure and inundation frequencies and is typically observed in southeast Asian mangroves with bed elevations towards the higher limit of the tidal range [*Watson*, 1928; *Van Loon et al.*, 2007].

Within each vegetation zone, a representative plot (15x15 m^2) was surveyed and trees were identified and counted. Average stem diameters at multiple levels above the bed were collected for representative trees in each plot/zone (Table 3.1). For the *Rhizophora* vegetation, some of the results were obtained from comprehensive vegetation studies in surrounding field sites [see *Horstman*, in prep.]. Near-bed root structures extending <10 cm above the forest floor (e.g. pneumatophores) were not quantified at this site.

FLOW ROUTING & WATER LEVELS

Three Acoustic Doppler Velocimeters (ADVs, Nortek) were used to monitor flow velocities at 0.07 m above the bed (16 Hz, 256 s per burst, 25 min burst interval) and water depths. These data were collected at nine locations (Figure 3.1E: K3, L3, N3, N0, N1, N4, N5, O3, P1) during four bi-weekly surveys, each covering a full spring-neap tidal cycle. Each survey comprised one benchmark location (overlapping with previous surveys) to allow for the selection of data obtained under similar hydrodynamic conditions. Additionally, the three ADVs were deployed

simultaneously, first at K3 and later at N1 to collect velocity profile information (1 day at each position, 7.5 min burst interval). Processing of the ADV data is discussed in Section 2.3.2.

Tidal inflow (and outflow) through the creeks and over the forest fringe was calculated by combining the obtained flow velocity profiles, the bi-weekly observations of near bed velocities, concurrent water levels (obtained by the ADV's pressure sensors) and topographic data. Resulting discharge-time series for bi-weekly periods (Figure A.1A and B) revealed the relation of the tidal discharge and the tidal excursion, both for the creek flow and for the sheet flow over the forest fringe (Figure 2.11 and Figure 2.12). Errors in the obtained tidal discharges, based on a single point measurement, were 5-15 % (Section 2.3.2).

Tidal water levels were additionally monitored throughout the field campaign by a pressure sensor (Sensus Ultra diver, Reefnet Inc.) positioned at N0. Obtained time-series of intermittent water level observations allowed for the reconstruction of a continuous tidal signal (using *Codiga's* [2011] UTide software; Figure 3.2). Joint analysis of the tidal signal and multiple years of tide charts for this area resolved the MSL datum (Section 2.3.2).

Table 3.1 – Vegetation composition and structure for the four vegetation zones mapped in Figure 3.1E. For each tree and shrub type, the number N [-] of individuals in a 15x15 m^2 survey plot is indicated (1x1m^2 for *Acanthus*), along with the diameter d [mm] of the tree trunk at multiple elevations z [m] above the forest floor. For the stilt root networks of *Rhizophora* trees, the number n [-] and average diameter of all elements were measured at multiple elevations. The final column presents the standard diameter d_s [mm] and the representative number of standard elements n_s [-] for the vegetation density per unit area ($N_s = 1$ m^{-2}; see Section 3.3.2).

Zone	*Rhizophora* N	$n(z) \cdot d(z)$ 0.1 m	0.5 m	1.0 m	2.0 m	*Bruguiera* N	$d(z)$ 0.1 m	0.5 m	1.0 m	2.0 m	*Xylocarpus* N	$d(z)$ 0.1 m	0.5 m	1.0 m	2.0 m	*Avicennia* N	$d(z)$ 0.1 m	0.5 m	1.0 m	2.0 m	*Acanthus* N	$d(z)$ 0.1 m	0.5 m	1.0 m	Standardized N_s	$n_s(z) \cdot d_s(z)$ 0.1 m	0.5 m	1.0 m	2.0 m
I	14	342·26	100·31	21·45	2·155	11	680	204	187	162	12	516	206	189	163	7	119	102	94	81	0	-	-	-	1/m²	24·26	7.0·31	1.8·45	0.25·155
II	7	168·23	76·24	42·24	9·36	15	400	120	110	95	12	675	270	248	214	8	308	264	242	209	0	-	-	-	1/m²	8.4·23	3.7·24	2.5·24	1.0·36
III	8	310·27	115·23	50·30	13·47	5	120	36	33	29	17	405	162	149	128	14	73	62	57	49	25/m²	7	7	0	1/m²	45·27	43·23	2.3·30	0.8·47
IV	12	342·26	100·31	21·45	2·155	0	-	-	-	-	3	390	156	143	124	1	73	62	57	49	0	-	-	-	1/m²	18·26	5.4·31	1.2·45	0.1·155
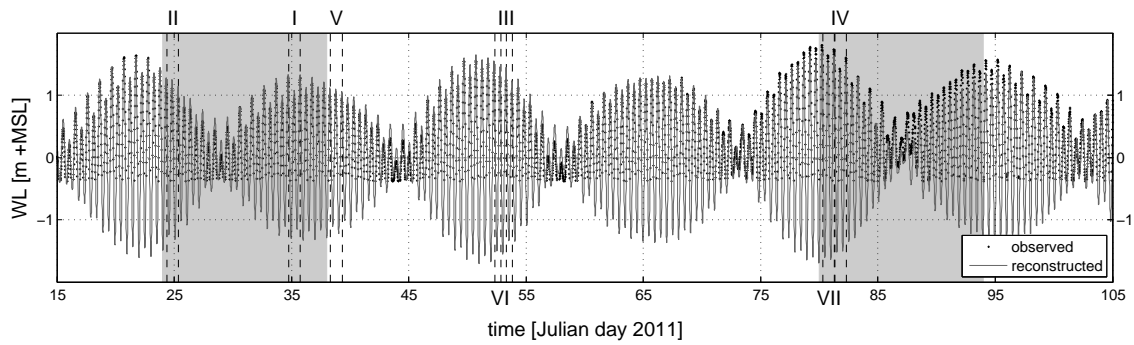
Figure 3.2 – Field observations and reconstruction of the tidal signal. Observed tidal water levels (at N0), only covering the upper half of the tidal signal, show good correspondence with the tidal signal reconstructed with tidal component analysis. Torrential rainfall in the period from day 85 to 95, causing severe flooding, gave rise to the increased observed high water levels that are not represented by the reconstructed tidal signal. Roman numerals indicate the simulation periods for the numerical model; shaded areas were used for creek discharge standardization (Appendix A).

SEDIMENT DYNAMICS

The suspended sediment concentration (SSC) was derived from the backscatter intensity of the ADV observations [c.f. *Salehi and Strom*, 2011]. SSC calibration of the ADVs in a controlled environment, with bed material from the field, produced a good correlation between SSC and the signal-to-noise ratio (SNR [dB]) of the ADVs: $\log(SSC) = 0.189 \cdot SNR - 5.89$ ($R^2 = 0.94$), with SSC in mg/l [*Horstman*, in prep.]. Observed SNR data were processed similarly to the flow velocity data and converted to SSCs afterwards. The tidal maxima of the observed SSCs in front of the study site (at N0) increased significantly with increasing high water levels (Figure 3.3).

Sediment deposition was monitored with sediment traps: 0.20x0.25 m^2 ceramic tiles covered with a smooth layer of mortar to mimic the forest floor. These tiles were carefully levelled with the forest floor. Sediment traps were deployed at the monitoring locations on the vegetated platform (Figure 3.1E) during four periods of two tides (~24 hrs). Deposited sediments were rinsed, filtered (0.7 μm Whatman GF/F filters) and dried for 24 hrs at 105° C before weighing.
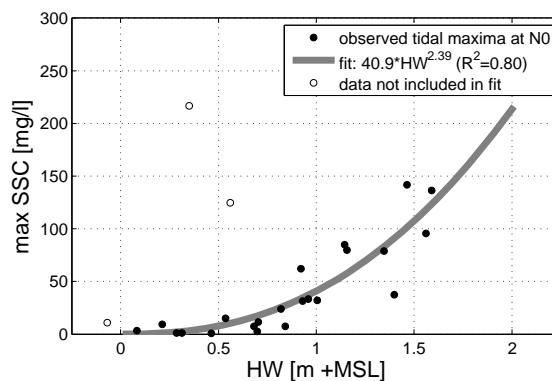
Figure 3.3 – Tidal maxima of the suspended sediment concentrations (SSC) on the mudflat in front of the study site at N0. Observations span a full spring-neap tidal cycle covering a range of tidal high water levels (HW). The fitted line represents the empirical relation between the maximum SSC and the tidal HW (outliers, probably due to occasional disturbances, were excluded).

Sediment samples of the bed's top layer were collected at all monitoring locations and were analysed for grain size distributions (Malvern) and organic contents (ashing). The bed material is a cohesive sandy mud with mean grain size d_{50} = 66.5(±12) µm and dry bulk density ρ_{dry} = 1285(±32) kg/m³ (spatial averages ±standard deviations). This substrate is at the upper limit of the mud range, but is still cohesive by the observed high contents of silt (49±6%) and organic matter (12±2%).

3.3   MODEL DEVELOPMENT

3.3.1   MODEL DESCRIPTION

The Delft3D software is widely applied for simulating flow hydrodynamics, sediment dynamics, morphological processes and biotic impacts in shallow water environments [e.g. *Hibma et al.*, 2003; *Temmerman et al.*, 2005b; *Hu et al.*, 2009; *Van Leeuwen et al.*, 2010]. The process-based Delft3D-FLOW module solves the three-dimensional (3D) or two-dimensional (depth-averaged, 2DH) unsteady shallow water equations. The hydrodynamic model applies horizontal momentum equations, the hydrostatic pressure relation (i.e. the reduced vertical momentum equation under the shallow water assumption), the continuity equation, the advection-diffusion equation and a turbulence closure model (for an extensive description, see *Lesser et al.* [2004] and *Deltares* [2014]). Transport and deposition of sediments are computed simultaneously with the hydrodynamics, facilitating direct feedback between hydro- and morphodynamics [*Lesser et al.*, 2004].

Recently, Delft3D was extended with modules to resolve the additional flow resistance by subtidal and intertidal vegetation [*Uittenbogaard*, 2003; *Baptist*, 2005]. *Uittenbogaard* [2003] developed a one-dimensional vertical (1DV) momentum equation and turbulence closures accounting for the effects of vegetation, which is represented as a collection of rigid vertical cylinders. These procedures were implemented in Delft3D as the directional point model (DPM). The 3D application of the DPM, simulating depth-variations in flow and turbulence through vegetation fields, has been calibrated and validated successfully for tidal dynamics in intertidal and subtidal ecosystems [*Temmerman et al.*, 2005b; *Bouma et al.*, 2007; *Borsje et al.*, in press]. In this section, some main features of Delft3D are discussed regarding the 3D implementation of the DPM, the computation of sediment dynamics, and the depth-averaged simulation of these processes.

3D MODEL INCLUDING VEGETATION EFFECTS
The 3D implementation of the DPM extends the momentum equation with a depth-dependent vegetation induced friction force $F(z)$ [N/m³] following from the (summarized) flow drag around the vegetation elements:

$$F(z) = \frac{1}{2} \rho_w C_D n(z) D(z) |u(z)| u(z) \tag{3.1}$$

Wherein ρ_w is the water density [kg/m^3]; C_D represents the (cylindrical) drag coefficient [-]; $n(z)$ indicates the depth-distribution of the number of cylindrical elements per unit area [m^{-2}] with depth-dependent diameter $D(z)$ [m]; and $u(z)$ is the horizontal velocity [m/s] at elevation z [m]. Momentum exchange is limited by the porosity of the vegetation $(1-A_p(z))$, obtained from the cross-sectional area of the vegetation per unit area $A_p(z)$ [-]:

$$A_p(z) = \frac{1}{4}\pi D^2(z)n(z) \tag{3.2}$$

In the present model, initially developed for 1DV simulations, spatial variations of the vegetation porosity only affect vertical momentum exchange [*Baptist*, 2005]. In addition, vegetation effects enter the momentum equation through the eddy viscosity v [m^2/s] which is resolved by the k-ε turbulence closure. This closure is adapted to account for (i) the vegetation induced turbulence generation and dissipation and (ii) the reduced horizontal area $(1-A_p(z))$ for turbulent diffusion [*Uittenbogaard*, 2003].

Simultaneously, Delft3D resolves suspended sediment transport through an advection-diffusion formulation [*Deltares*, 2014]:

$$\frac{\partial c}{\partial t} + \frac{\partial uc}{\partial x} + \frac{\partial vc}{\partial y} + \frac{\partial(w-w_s)c}{\partial z} = \frac{\partial}{\partial x}\left(D_H\frac{\partial c}{\partial x}\right) + \frac{\partial}{\partial y}\left(D_H\frac{\partial c}{\partial y}\right) + \frac{\partial}{\partial z}\left(D_V\frac{\partial c}{\partial z}\right) \tag{3.3}$$

Wherein c represents the SSC [kg/m^3]; u, v and w are the velocity components in x, y and z directions, respectively [m/s]; w_s is the sediment's settling velocity [m/s]; and D_H and D_V represent the horizontal and vertical eddy diffusivities [m^2/s]. For cohesive sediments, erosion (E_r) and deposition rates (D_r) [kg/m^2/s] are computed with the Partheniades-Krone equations [*Partheniades*, 1965]:

$$D_r = w_s c_b\left(1 - \frac{\tau_b}{\tau_{cr,d}}\right) \qquad\qquad for\ \tau_b < \tau_{cr,d} \quad \left(else\ D_r = 0\right) \tag{3.4}$$

$$E_r = M\left(\frac{\tau_b}{\tau_{cr,e}} - 1\right) \qquad\qquad for\ \tau_b > \tau_{cr,e} \quad \left(else\ E_r = 0\right) \tag{3.5}$$

Wherein c_b is the near-bed sediment concentration [kg/m^3]; τ_b is the bed shear stress [N/m^2] resolved by the hydrodynamics module; $\tau_{cr,d}$ and $\tau_{cr,e}$ are the critical bed shear stresses for the facilitation of deposition and the initiation of erosion, respectively [N/m^2]; and M represents the erodibility of the bed material [kg/m^2/s]. Finally, the morphological change (i.e. net deposition) is calculated by subtracting the time-integrated deposition and erosion rates.

2DH MODEL INCLUDING VEGETATION EFFECTS

Alternatively, Delft3D can simulate the impacts of vegetation (or other biota) on hydrodynamics and sediment dynamics in a depth-averaged (2DH) mode [cf. *Van Leeuwen et al.*, 2010]. This model does not resolve vertical variations of the hydrodynamics or sediment transport, which means that all vertical derivatives (e.g. the last terms of the l.h.s and r.h.s of eq.(3.3)) reduce to zero. This seems suitable for the highly turbulent, well mixed conditions in a mangrove system

featuring its greatest variability in the horizontal plane: deep creeks dissecting an elevated platform covered with tall vegetation. Two 2DH vegetation representations are available in Delft3D: a direct method, implementing the (depth-averaged) DPM; and an indirect approximation, based on adapted (decreased) Chézy roughness values [*Baptist et al.*, 2007]. Here we adopted the depth-averaged DPM method, based on its favourable results in a comparative analysis for a mangrove environment [*Horstman et al.*, 2013].

Implementing the DPM in 2DH mode imposes some model reductions with respect to its 3D implementation. First, depth-averaged vegetation characteristics are required. Second, (vegetation impacts in) vertical momentum exchange and turbulent processes remain unresolved. Hence, vegetation effects are limited to the vegetation induced friction force (eq. (3.1)), which is now computed with the depth-averaged horizontal velocity $\bar{u}$ [m/s]. Third, suspended sediment transport is obtained from the depth-averaged advection-diffusion equation. Erosion and deposition rates (eq. (3.4) and (3.5)) consequently follow from the resulting depth-averaged SSC instead of the near-bed SSC. Last, the bed-shear stress is resolved from the depth-averaged flow velocity by assuming a standard (i.e. logarithmic) velocity profile along the vertical [*Deltares*, 2014].

3.3.2 MODEL SETUP

TOPOGRAPHY & VEGETATION COVER

The present study implements a Cartesian rectilinear grid for the horizontal model discretization and, for the 3D simulations, a boundary fitted σ-grid with eight equally distributed depth layers (of time-varying thickness) for the vertical discretization. The model domain extents at least 50 m beyond the boundaries of the study site (Figure 3.1F), limiting the impact of boundary effects within the study site. Moreover, the model domain extends 600 m further inland in order to represent the storage capacity of the extensive inland mangrove. This area is limited by an assumed divide between the area inundating from the study site and the area flooding via a creek south of the study site, dissecting the back of the up to 1.5 km wide mangrove fringe (see Figure 3.1C). Grid cells measure 2x2 m at the main area of interest (Figure 3.1F). Away from this area, grid sizes gradually increase to 2x12 m at the landward model boundary and 2x4 m at the estuarine boundary.

The topography of the field site was projected on the rectilinear model grid (Figure 3.1F). Bed levels were averaged within each grid cell, except for the creeks (all parts lower than 0.60 m +MSL) where the minimum observed elevation of each grid cell was selected to maintain continuous flow paths. Based on visual observations in the field, bed levels and patterns within the field site were extended to its surroundings. The subtidal part of the model domain has a 7:100 bed slope, as obtained from the echosounding (Section 3.2.2). Bed level gradients of the inland extension were derived from the high spring tidal water levels reaching the terrestrial boundary of the mangroves located ~1.5 km inland (Figure 3.1C), presenting a mild average cross-shore bed slope of 1:1250.

Vegetation characteristics were standardized to densities per unit area, with one representative stem diameter per zone for proper representation in the DPM (Table 3.1). The diameter of the *Rhizophora* roots, being the dominant vegetation elements, was set as the standard vegetation diameter (d_s). All other vegetation elements were expressed in d_s. A representative number of roots n_s per unit area ($N_s = 1$ m^{-2}) with diameter d_s was calculated from the frontal area of the vegetation ($N \cdot n \cdot d = N_s \cdot n_s \cdot d_s$). Depth-dependent standardized vegetation characteristics were assigned according to the vegetation zones shown in Figure 3.1E (inland of x = 0.5 km vegetation was changed to zone III type). The drag coefficient (C_D) of the vegetation elements was set to unity (following findings of *Nepf and Vivoni* [2000] for emergent vegetation). For the standardized vegetation representation of the *Acanthus* shrubs, featuring significant foliage within the water column, the frontal surface of each individual shrub was set at five times its single stem diameter (Table 3.1).

BOUNDARY CONDITIONS & MODEL PARAMETERS

The model domain contains two open boundaries: the estuarine (eastern) boundary and the intersection of a creek with the northern boundary (Figure 3.1F). The latter boundary was required as the limited field data did not allow us to model the entire catchment of this creek. Within the estuarine part of the model domain, longshore riverine and tidal water flows were neglected, as they were found to have negligible impact on the tidal water flows into/within the mangrove forest (Chapter 2). Tidal water levels at the estuarine boundary were imposed according to the tidal signal obtained at N0 (Figure 3.2) and were characterized by the water level at high tide (HW; Table 3.2).

A generic boundary condition was developed for the creek in- and outflow at the second open model boundary, based on a parameterization of the observed creek discharges at K3 (see Appendix A). This parameterization delivered three non-dimensional discharge curves that only require HW as input for selection and for scaling with the maximum tidal discharge and tidal discharge duration. Test runs of the model without discharge boundary condition for the creek computed creek discharges at K3 that were only about 30% of the observed discharges. In order to simulate representative creek discharges at K3, 70% of the parameterized discharge at K3 was assigned as a discharge boundary condition to the creek. Consequently, this boundary condition did not require direct input of observational data, enabling the simulation of tidal conditions for which no data were obtained at K3.

Simulation of the tidal sediment dynamics required the definition of sediment concentrations at the open model boundaries. Based on the observed correlation between HW and SSC in front of the study site (Figure 3.3), the SSC boundary condition for the estuarine model boundary was set to a fixed value obtained with the (average) high water level of each pair of simulated tides (Table 3.2). The SSC boundary condition for the imposed creek discharge was found of minor importance, as it does not supply sediments to the study area, and was set to a fixed value of 40 mg/l.

Table 3.2 – Model parameters used for model calibration and validation. The roman numerals with the tidal conditions (HW) refer to the simulated periods indicated in Figure 3.2. Shaded cells mark the parameters that were varied for model calibration.

Parameter	Variable	Field observation	Model calibration hydrodynamics		Model validation hydrodynamics		Model calibration sediment dyn.		Model validation sediment dyn.	
			3D	2DH	3D	2DH	3D	2DH	3D	2DH
$Z(x,y)$	topography	Figure 3.1F	Figure 3.1F	Figure 3.1F	Figure 3.1F	Figure 3.1F	Figure 3.1F	Figure 3.1F	Figure 3.1F	Figure 3.1F
$C_b(x,y)$ [s/m$^{1/3}$]	Manning bed roughness	not available	0.005: 0.005·0.05	0.030	0.030	0.030	0.030	0.030	0.030	0.030
$n_s(x,y,z)$; $d_s(x,y,z)$	vegetation elements (3D)	Table 3.1 Figure 3.1E	Table 3.1 all layers	-	Table 3.1 all layers	-	Table 3.1 all layers	-	Table 3.1 all layers	-
$n_s(x,y)$; $d_s(x,y)$	vegetation elements (2DH)	Table 3.1 Figure 3.1E	-	Table 3.1 0.1;0.3;0.5;0.75;1 m	-	Table 3.1 0.5 m	-	Table 3.1 0.5 m	-	Table 3.1 0.5 m
$HW(x,y)$ [m]	boundary condition: water level at high tide	Figure 3.2	I - 1.27;0.96	I - 1.27;0.96	III - 1.30;1.24 IV - 1.76;1.42	III - 1.30;1.24 IV - 1.76;1.42	II - 1.17;1.11	II - 1.17;1.11	V - 1.01;1.01 VI - 1.37;1.31 VII - 1.81;1.65	V - 1.01;1.01 VI - 1.37;1.31 VII - 1.81;1.65
$c(x,y)$ [mg/l]	boundary condition: SSC	Figure 3.3	-	-	-	-	60	60	V - 40 VI - 80 VII - 150	V - 40 VI - 80 VII - 150
$Q(t)$ [m^3/s]	boundary condition: creek discharge	Figure A.1	$0.7 \cdot Q_{K3,ST}$	$0.7 \cdot Q_{K3,ST}$	$0.7 \cdot Q_{K3,ST}$	$0.7 \cdot Q_{K3,ST}$	$0.7 \cdot Q_{K3,ST}$	$0.7 \cdot Q_{K3,ST}$	$0.7 \cdot Q_{K3,ST}$	$0.7 \cdot Q_{K3,ST}$
$v_H(x,y)$ [m^2/s]	eddy viscosity (deep water)	not available	$1 \cdot 10^{-3}$ (0.1)	$1.1 \cdot 10^{-3}$ (0.1)	$1 \cdot 10^{-3}$ (0.1)	$1.1 \cdot 10^{-3}$ (0.1)	$1 \cdot 10^{-3}$ (0.1)	$1.1 \cdot 10^{-3}$ (0.1)	$1 \cdot 10^{-3}$ (0.1)	$1.1 \cdot 10^{-3}$ (0.1)
w_s [mm/s]	settling velocity	not available	-	-	-	-	0.1;0.1;1	0.1	0.1	0.1
$\tau_{b,cr}$ [N/m^2]	critical bed shear stress	0.10-0.15	-	-	-	-	0.05;0.05: 0.30	0.05;0.05: 0.30	0.10	0.15

An overview of relevant model variables and boundary conditions, including field observations of these variables (if available), is provided in Table 3.2. Sediment characteristics were modelled in accordance with the average sediment characteristics obtained from the field (Table 3.2). A fixed bed was implemented in the model, omitting erosion of the present topography. Nevertheless, (computed) fresh deposits could be re-entrained as the critical bed shear stress for deposition and erosion was assumed uniform. The 3D model was run with a constant horizontal eddy viscosity ($1 \cdot 10^{-3}$ m^2/s), reducing computation times with respect to model runs including a horizontal large eddy simulation module to compute this parameter [*Deltares*, 2014]. The 3D model runs resolved that the dispersion by vertical turbulence added about one-tenth to the horizontal viscosity. Consequently, the horizontal eddy viscosity was set to a constant value of $1.1 \cdot 10^{-3}$ m^2/s for the 2DH model runs (Table 3.2). In the deeper parts of the estuary the viscosity was raised to 0.1 m^2/s to suppress model instabilities.

3.3.3 MODEL CALIBRATION AND VALIDATION

CALIBRATION - RESOLVING UNKNOWN MODEL PARAMETERS

The 3D model required calibration of parameters for which no (or uncertain) information was obtained from the field: the hydraulic bed roughness, relevant to the simulated hydrodynamics; and the sediment settling velocity and critical bed shear stress, both input to the morphodynamic computations. The calibration results of the 3D model were implemented in the 2DH model. Due to depth-averaging, this model required additional calibration. The 2DH model was calibrated with the depth-averaged vegetation representation and the critical bed shear stress. The former was required for accurate simulation of the depth-averaged hydrodynamics. Calibration of the critical bed shear stress was needed in order to compensate for the slight overestimation of bed shear stresses by the 2DH model that cannot resolve enhanced velocity reductions due to greater near-bed vegetation densities.

The calibration parameters were varied systematically over their potential ranges, as summarized in Table 3.2. With the calibration runs we sought for best agreement with the local flow velocities and deposition rates obtained from the field. Each of the calibration runs simulated a period of 24 hours, comprising approximately two tides (periods I and II in Figure 3.2). The accuracy of the computed velocities and deposition rates (SIM) with respect to the reference velocities and deposition rates (REF), either being the field observations or the 3D model results, was expressed through the Nash-Sutcliffe model accuracy MA [*Nash and Sutcliffe*, 1970]:

$$MA = 1 - \frac{\sum (SIM - REF)^2}{\sum (REF - \overline{REF})^2} \qquad (3.6)$$

Overbars indicate time averaged values in case of velocities, or spatial averages in case of sediment deposition. Unit value of the model accuracy (MA = 1) represents perfect correspondence between either the computed and observed data or the results of the 2DH and 3D models. If MA ≤ 0, the model has no predictive capacity in addition to the average of the

reference data, i.e. the model has no skill. This model accuracy parameter is equivalent to the Brier skill score (BSS) that is frequently applied to assess the performance of morphological models [e.g. *Sutherland et al.*, 2004]. For the morphodynamic simulations, we applied their qualification for the (unmodified) BSS: MA > 0.5 indicates an excellent model skill; 0.2 < MA < 0.5 represents a good model skill; 0.1 < MA < 0.2 means the model's skill is reasonably/fair; and 0 < MA < 0.1 indicates poor model skill.

For the calibration of the 3D hydrodynamic model in the hydraulic bed roughness, the computed and observed velocities in the main creek at K3 and in the forest's centre at N3 were compared. Velocity data from the field were retrieved at 0.07 m above the bed. Hence, the 3D model results, obtained at time-varying σ-layers, were interpolated (linearly) to compute velocities at the same elevation. Best agreement was obtained for a Manning's roughness coefficient of $0.030 \text{ s/m}^{1/3}$ (MA = 0.96 and 0.30 for K3 and N3, respectively; Table 3.3), a value similar to previously applied roughness coefficients in mangrove creeks [*Wolanski et al.*, 1990; *Furukawa et al.*, 1997] and common for small, non-vegetated natural streams in cohesive soils [*Chow*, 1959]. Figure 3.4 shows that computed velocities, discharges and water levels generally agree well with the field observations.

Best correspondence between 3D computed and observed deposition rates was obtained for a settling velocity of 0.1 mm/s and a critical bed shear stress of 0.10 N/m^2 for erosion as well as deposition (MA = 0.38; Table 3.3). This settling velocity is at the lower end of the 0.1-0.5 mm/s settling velocity range previously used for mangrove sediments [e.g. *Furukawa et al.*, 1997; *Winterwerp et al.*, 2005]. The obtained critical bed shear stress is common for unconsolidated, muddy intertidal sediments [e.g. *Widdows et al.*, 2007].

The parameters resolved from the calibration of the 3D model were subsequently implemented in the 2DH model. 2DH computed velocities were compared to depth-averaged velocity estimates from the field data. From the limited velocity profile measurements at K3 and N1, it was derived that $\bar{u} \approx 1.3 \cdot u_{0.07}$ (with a standard deviation of $\pm 0.5 \cdot u_{0.07}$), where $u_{0.07}$ is the observed velocity at 0.07 m above the bed. In the calibration of the 2DH hydrodynamics model, the vegetation characteristics at 0.50 m above the bed returned best resemblance of the computed depth-averaged velocities with estimates of the observed depth-averaged velocities at K3 in the main creek and at N3 in the forest (Table 3.3). The 2DH computed velocities and discharges were similar to the 3D model results (Figure 3.4), indicating comparable performance of the 2DH and the 3D models.

Table 3.3 – Model accuracies of the calibration of the 3D and 2DH models.

	Calibrated 3D model vs. field data (MA)	Calibrated 2DH model vs. field data (MA)	Calibrated 2DH model vs. 3D simulation (MA)
Velocities at K3 (period I)	0.96	0.94	0.99
Velocities at N3 (period I)	0.30	0.33	0.95
Deposition at all stations (period II)	0.38	0.33	0.91
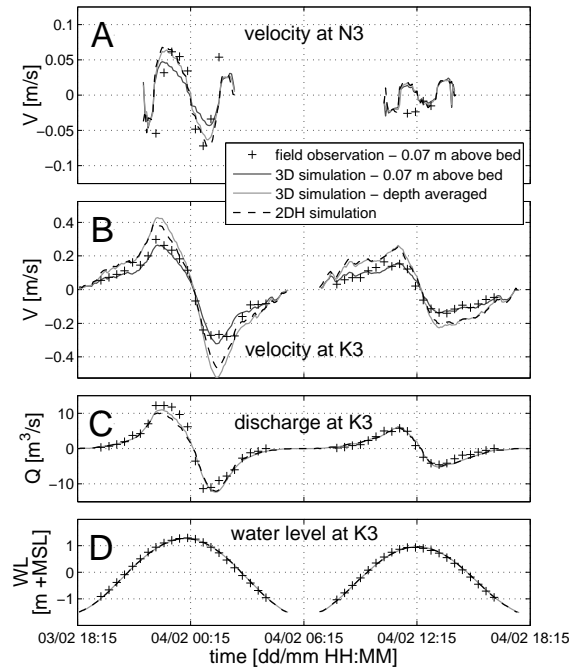
Figure 3.4 – (A) Flow velocities at N3, (B) flow velocities at K3, (C) discharges at K3 and (D) concurrent water levels at K3. Positive velocities and discharges are directed westward (i.e. the main flood direction). Each panel presents field observations and simulation results by both the 3D and 2DH models. The velocity plots include field data obtained at 0.07 m elevation; velocities at 0.07 m and depth-averaged velocities obtained from the 3D model; and depth-averaged velocities from the 2DH model.

Finally, best accuracy of the 2DH computed deposition rates was obtained with a critical bed shear stress of 0.15 N/m^2 (MA = 0.33; Table 3.3). This critical bed shear stress is only slightly higher than the calibrated value for the 3D model and is still within the common range for unconsolidated, muddy sediments [*Widdows et al.*, 2007]. Additionally, as well as for the hydrodynamics, the predicted deposition rates by the 2DH model were very similar to the 3D model.

VALIDATION I – MODEL PERFORMANCE FOR VARIABLE CONDITIONS
After the model was calibrated, additional model runs were executed to validate the models' skill in predicting hydro- and sediment dynamics under different conditions. The validation simulations each comprised different periods of two subsequent tides (periods III-VII in Figure 3.2) with different tidal and consequently different SSC boundary conditions (Table 3.2). The individual quality of each of the validation simulations was assessed similar to the assessment of the calibration runs.

Validation of the hydrodynamic model comprised two other days during which velocities have been observed within the forest (at N3, N4 and O3; period III) and in the creeks (at K3, N5 and P1; period IV). Obtained model accuracies for the velocities computed by both the 3D model and the 2DH model were generally reasonable. Obtained model accuracies for the predicted velocities within the forest were reasonable to good (MA = 0.14-0.58; Table 3.4), while

predicted velocities within the creeks were generally good (MA = 0.19-0.55). Computed depth-averaged velocities by both models were resembling (MA = 0.78-0.99; Table 3.4).

Model accuracies for the point-wise comparison of the deposition rates for the individual validation runs were lower than for the calibration runs (some below zero; Table 3.4). Nevertheless, a joint analysis of all validation runs returned good agreement between the predicted and observed deposition rates, for both the 3D and the 2DH models (Table 3.4). Only predictions for period VI are rather poor, because excessive deposition rates were measured at the fringe and levee (Figure 3.6C; HW = 1.34 m +MSL). Moreover, a combined analysis of all deposition predictions by the calibration and validation runs showed that both the 3D and the 2DH models computed spatially explicit deposition rates (point-wise comparison) over a range of conditions with less than a factor two difference from the observed deposition rates (MA = 0.48 and 0.53, respectively; Figure 3.5A,C).

VALIDATION II – COMPARING AGGREGATE MODEL RESULTS AND FIELD OBSERVATIONS
The foregoing comparison of computed and predicted point-velocities does not reveal the contribution of different flow routes into the mangroves. These flow routes are relevant since they map the main supply routes of water and waterborne materials into the mangroves. The three major flow routes of the study site are: creek flow through the main creek at the north of the study site (referred to as CN), wherein data were collected at K3; creek flow through the smaller creek at the south of the study site (referred to as CS), with data collection at P1; and direct inflow – or sheet flow – over the forest fringe (FF), with data collection at N1. Computed tidal inflows and outflows along these flow paths were compared to the tidal discharges that were calculated from the field data.

Similarly, a point-by-point comparison of observed and computed deposition rates does not reveal (differences in) spatial patterns in the deposition rates. Moreover, this point-wise comparison is quite sensitive to local variations (and errors) in observed deposition rates induced by the highly non-uniform mangrove environment. Hence, the observed and computed deposition rates were aggregated according to the four distinct zones within the study site (Figure 3.1D): the estuarine forest fringe (comprising L1, M1, N1, O1, Q1), the creek bank (L2, L3, L4), the levee directly behind the forest fringe (M2, N2, O2, Q2), and the forest's interior (M3, M4, N3, N4, O3, O4, Q3, Q4).

Table 3.4 – Model accuracies of the validation of the 3D and 2DH models. Accuracies are presented for every monitoring position (velocities) or simulation period (deposition, between brackets). Aggregate deposition accuracies follow from a joint analysis of the validation runs.

	3D simulations vs. field data (MA)	2DH simulations vs. field data (MA)	2DH simulations vs. 3D simulations (MA)
Velocities at O3/N3/N4 (period III)	0.58/0.53/0.14	0.24/0.28/0.36	0.96/0.94/0.91
Velocities at N5/K3/P1 (period IV)	0.48/0.38/0.55	0.36/0.19/0.28	0.78/0.99/0.97
Deposition at all stations (periods V/VI/VII)	0.44 (-0.47/-0.17/0.13)	0.50 (-0.25/-0.16/0.25)	0.89 (0.94/0.88/0.74)
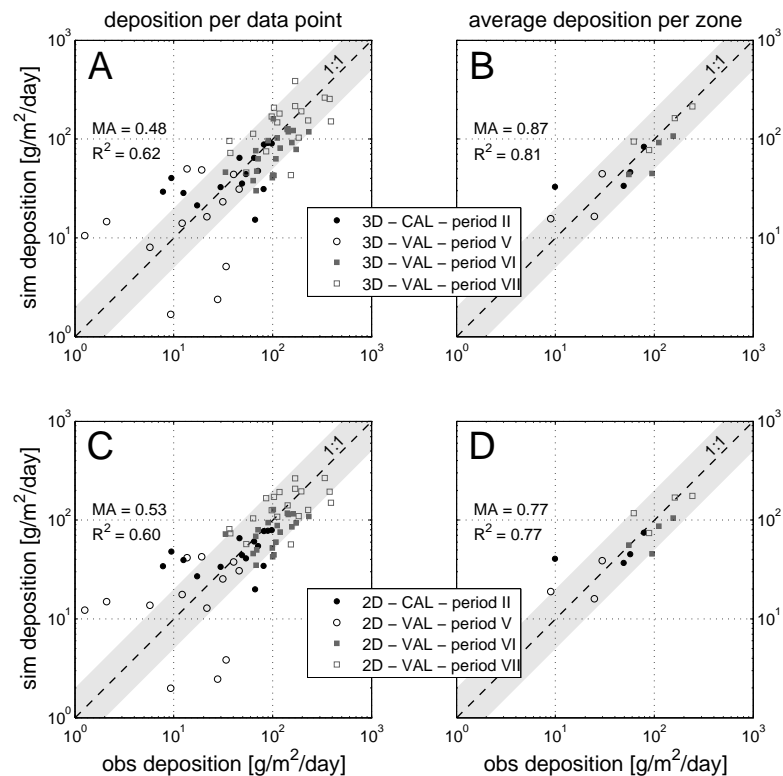
Figure 3.5 – Comparison of observed (obs) and computed (sim) sediment deposition rates. (A,B) Simulation results are obtained with the 3D and (C,D) with the 2DH model runs for the calibration and validation of the morphodynamic simulations. (A,C) Computed and observed deposition rates are compared for single observations and (B,D) for averaged deposition rates for the different topographic zones. Periods refer to the (simulated) tidal conditions as presented in Table 3.2 and shaded areas indicate a factor two difference between observed and computed deposition rates.

It was found that the tidal inflows via the creeks and the forest fringe for all 3D calibration and validation runs showed reasonable to good correspondence with the field data (Figure 3.6A). Especially, inflow through the northern creek (CN) and over the forest fringe (FF) were reproduced very well (MA > 0.8; Table 3.5). Subsequent comparison of the computed and observed deposition rates per zone (Figure 3.5B) showed that the 3D model accurately (reasonably-excellent) predicted the average deposition in each of the zones over a range of tidal conditions (Table 3.5).

Computed tidal inflows via the creeks and over the forest fringe obtained from the 2DH calibration and validation runs are almost equal to the tidal inflows computed with the 3D model (Figure 3.6A), resulting in similar model accuracies for the predicted inflow per flow route (Table 3.5). The aggregated deposition rates predicted by the 2DH model also compared well with the field data, except at the creek bank, and only showed minor deviations with respect to the 3D computed deposition rates (Table 3.5, Figure 3.6C).

These aggregate comparisons show that (i) both calibrated models predict flow routing and deposition patterns very well over a range of tidal conditions and (ii) the calibrated 2DH model performs comparable to the calibrated 3D model. Concluding, the highly turbulent, well mixed

89

conditions within the mangroves, that show major biogeophysical variations in the horizontal direction, allow for a depth-averaged numerical simulation. Results for observed and computed tidal outflows were similar and are not presented.

Table 3.5 – Model accuracies of the aggregate results of the calibration and validation runs presented in Figure 3.6 (dep = deposition).

	3D simulations vs. field data (MA)	2DH simulations vs. field data (MA)	2DH simulations vs. 3D simulations (MA)
Inflow creek north (CN)	0.88	0.87	0.97
Inflow forest fringe (FF)	0.84	0.71	0.96
Inflow creek south (CS)	0.21	0.27	1.00
Dep forest fringe (FRI)	0.79	0.78	0.98
Dep creek bank (CRB)	0.39	-0.40	0.82
Dep levee (LEV)	0.39	0.39	0.98
Dep interior (INT)	0.95	0.81	0.94
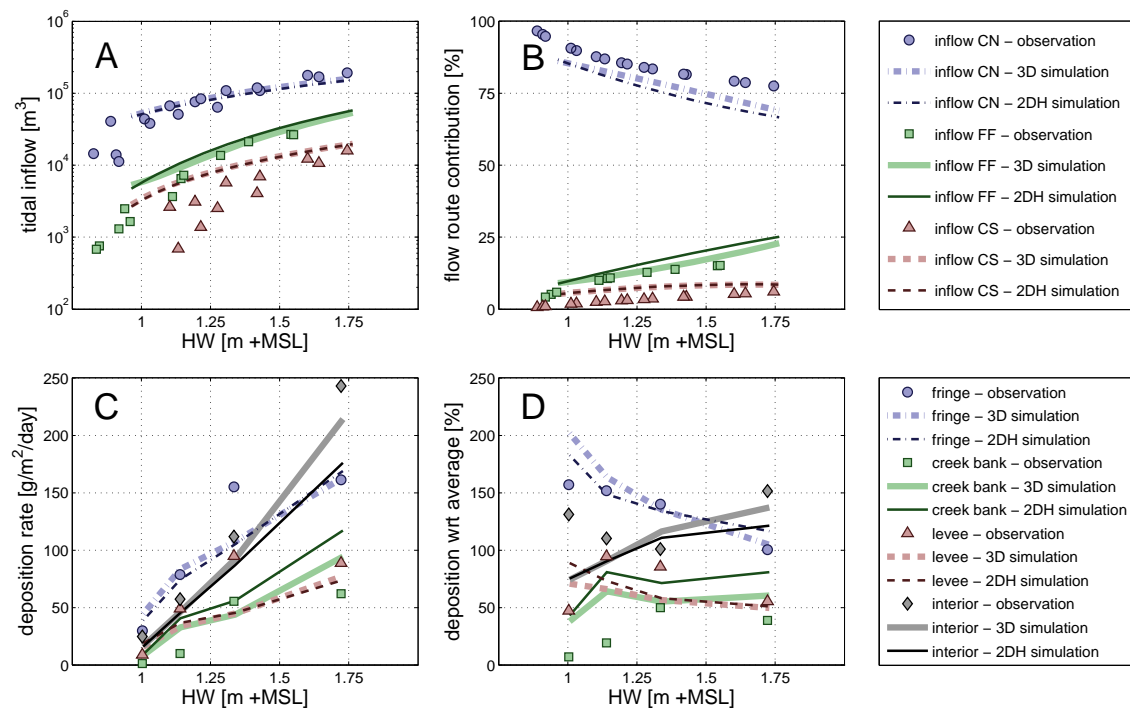
Figure 3.6 – Observed and computed tidal-scale flow routing and sediment deposition for a range of tidal conditions: (A) the total inflow through the creeks at K3 (CN) and P1 (CS) and over the forest fringe of the study site into the mangroves; (B) the relative contribution of inflow through the creeks with respect to the total inflow; (C) the average sediment deposition per topographic zone; (D) the relative distribution of the sediment deposition with respect to the spatial average.

3.4 UNDERSTANDING TIDAL DYNAMICS IN MANGROVES

In order to improve our understanding of the routing of water and sediments in an elevated mangrove stand dissected by tidal creeks, this section first elaborates on the simulation results obtained from the calibration and validation of the models. This analysis concerns the present situation of the mangroves. Subsequently, the validated 2DH model is applied to study the contribution of several environmental parameters to the tidal-scale dynamics within the mangroves and the initial response of the system to instantaneous changes of these conditions.

3.4.1 PRESENT STATE FLOW ROUTING AND DEPOSITION PATTERNS

Both observations and simulations consistently show the flow velocities in the creeks to be an order of magnitude greater than the flow velocities through the mangrove vegetation (Figure 3.7). Characteristic velocity peaks were observed within the creeks when water levels exceed the forest floor on flood tide, while prolonged ebb tidal velocity peaks were observed in the creeks for a greater range of water depths (Figure 3.8), resembling previous field observations [e.g. *Wolanski*, 1992; *Mazda et al.*, 1995; *Van Santen et al.*, 2007].

Flow routing maps for spring tidal conditions, reconstructed from the field data (Figure 3.7A) and obtained with the 3D model (Figure 3.7B) reveal a similar characteristic sequence of flooding and drying. It was found that the creeks form the major flow route into and out of the mangroves during the initial stages of flood and the final stages of ebb, when water levels are below the very dense root layer covering the forest floor at the estuarine fringe of the study site (reaching up to 0.9 m +MSL). This is named the *creek flow* stage. In turn, the *sheet flow* stage corresponds to higher water levels, facilitating direct in- and outflow over the forest fringe (50-100 minutes to high tide in Figure 3.7). Nevertheless, creek inflows were found to remain dominant during the sheet flow stage with flow velocities in the creek of $O(10^{-1})$ m/s while those through the vegetation were only $O(10^{-2})$ m/s (Figure 3.4).

With the increase of tidal high water levels during spring tides, the tidal prism (i.e. the total inflow during flood) of the study site increases (Figure 3.6A). The relative contribution to the tidal prism by the creeks is slightly decreasing with increasing HW (Figure 3.6B). The contribution of the sheet flow over the forest fringe increases up to about 20-25% of the total inflow for both the field observations and model simulations. This is due to the increase of flow velocities through the forest with increasing water levels, as vegetation densities decrease with height and the relative impact of the abundant near-bed roughness elements is reduced.

The field observations revealed a clear trend of increasing diurnal deposition rates within the forest for increasing HW, which was quite well reproduced by the different calibration and validation runs of the 2DH model (Figure 3.6C). The greater tidal prism with increasing HW enhances flow velocities and hence transport of suspended sediments into the mangroves, facilitating increased deposition rates. Apparently, the ebb tidal flow velocities are insufficient to resuspend and export the deposited sediments, irrespective of the HW-related tidal prism.

This observation does not apply to the creeks, where ebb tidal velocity peaks tend to increase in strength and duration (Figure 3.4B and Figure 3.8), enhancing the self-scouring mechanism of the creeks for increasing tidal amplitudes [cf. *Mazda et al.*, 1995; Chapter 3 of this thesis]. However, no deposition (nor erosion) data were obtained in the creeks and self-scouring of the creeks was not computed, as erosion of the present topography was not included in the model.
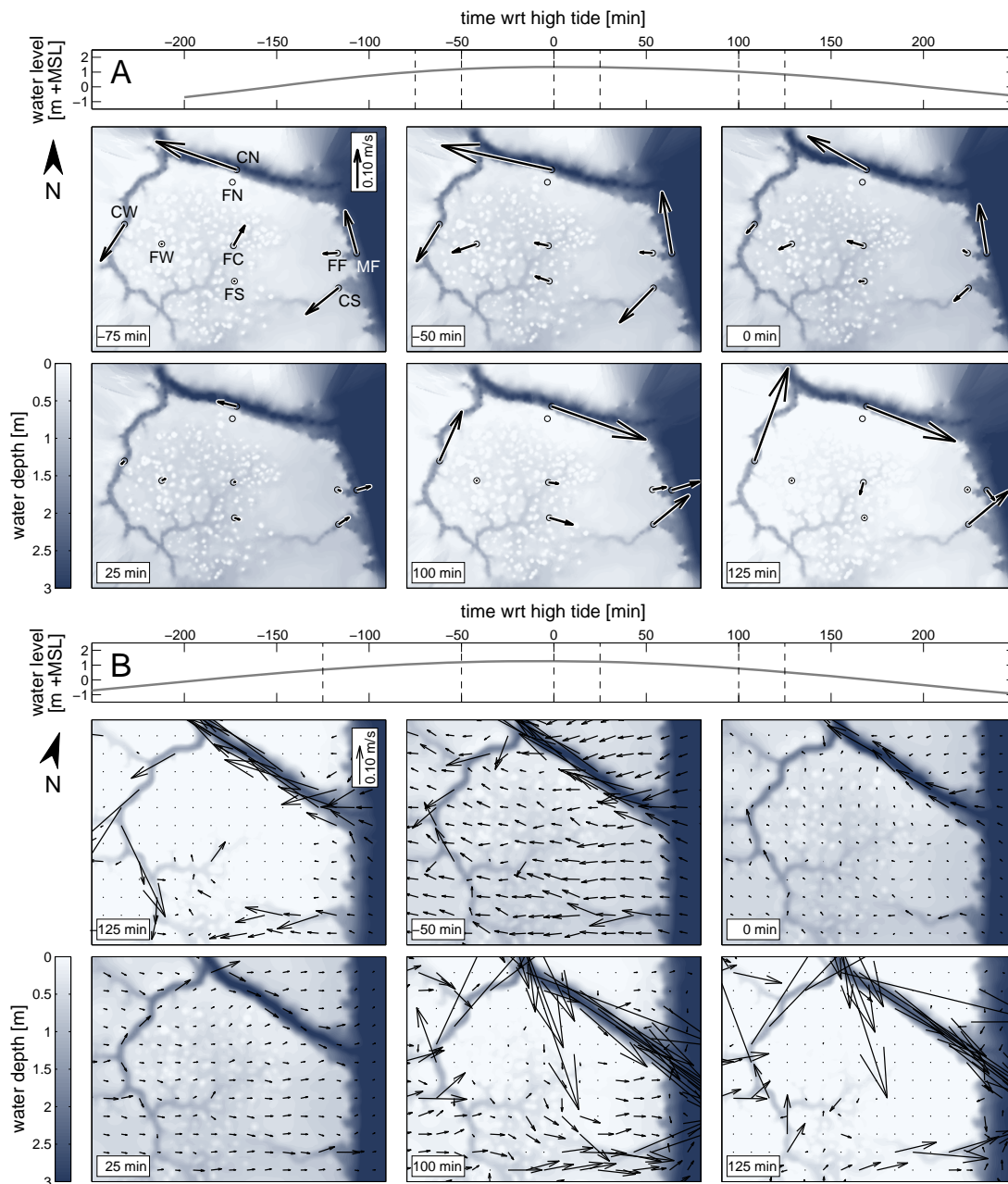
Figure 3.7 – Comparison of tidal flow routing (A) observed in the field and (B) computed with the 3D model. Both panels show velocities at 0.07 m above the bed observed/computed during the tidal cycle with high tide at February 4, 00:00 AM (period I in Figure 3.2). Due to the required assimilation of the observed flow routing map from various observation periods, water levels (and hence flow velocities) are not completely similar (HW is 1.35 and 1.27 m +MSL in (A) and (B), respectively).

Observed and computed diurnal sediment deposition rates for the four zones within the forest show an increasing trend (Figure 3.6C). Diurnal deposition rates in the forest's interior increase about 2-3 times faster with increasing HW than deposition rates throughout the other zones. These findings corroborate that the low-lying centre of the study site functions as a sediment sink, whereas increasing flow velocities for greater HW apparently limit the sediment deposition (or even facilitate erosion) at the more exposed fringe and levee of the forest. Consequently, the relative deposition in the forest's interior is above average (>100%) and increases for greater HW, while relative deposition rates in the other zones are mainly decreasing for greater HW (Figure 3.6D). It should be noted that the distribution of deposits in the model simulations with lower high water levels deviates from the field observations: relative deposition rates in the forest's interior are underestimated while relative deposition rates at the creek bank are significantly overestimated for HW < 1.25 m +MSL (Figure 3.6D).
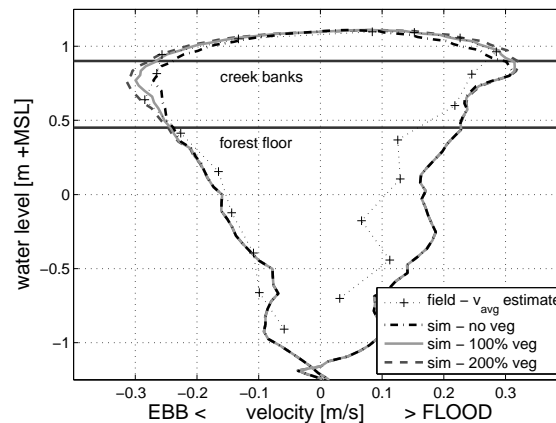
Figure 3.8 – Stage-velocity curves plotting the observed and (2DH) computed depth-averaged horizontal velocities at K3. Simulation results show the effect of increasing vegetation densities or the lack of vegetation with respect to the present situation (100% veg).

3.4.2 SENSITIVITY OF TIDAL DYNAMICS TO BIOGEOPHYSICAL SETTINGS

The successfully calibrated and validated 2DH model was applied to analyse the initial response of the tidal-scale dynamics within the mangroves to instantaneous changes of five environmental parameters: (i) topography, (ii) vegetation density, (iii) relative elevation, (iv) sediment supply and (v) mangrove area loss. These parameters were systematically varied across a range of conditions (Table 3.6) and each of these conditions was simulated for a period of 24 hours (~two subsequent tides). Every scenario was simulated with the tidal conditions of period II, which represented the mean tidal range (Table 3.2). For each of these runs, resulting flow routing and deposition pattern parameters were calculated (cf. Figure 3.6). Figure 3.10 summarizes the sensitivity of the mangrove system to each of the simulated parameter changes.

Table 3.6 – Overview of the parameter variations for the sensitivity analysis. The different scenarios comprise: changes to the study site's topography (BED), the vegetation density (VEG), the relative elevation of the site with respect to mean sea level (MSL), the concentration of suspended sediments in the tidal water supply (SED) and the loss of mangrove area due to land-use changes (CON).

Parameter	Variable	Standard value	Sensitivity analysis (2DH)				
			BED	VEG	MSL	SED	CON
$Z(x,y)$	topography	Figure 3.1F	Figure 3.9	Figure 3.1F	Figure 3.1F	Figure 3.1F	Figure 3.1F inland area loss of 0:120:600m
$n_s(x,y)$; $d_s(x,y)$	vegetation elements (2DH)	Table 3.1 0.5 m	Table 3.1 0.5 m	$(0:0.2:2)\cdot n$ Table 3.1 0.5m	Table 3.1 0.5 m	Table 3.1 0.5 m	Table 3.1 0.5 m
$HW(x,y)$ [m]	boundary condition: water level at high tide	-	1.17;1.11	1.17;1.11	0.67:0.1:1.67 0.61:0.1:1.61	1.17;1.11	1.17;1.11
$c(x,y)$ [mg/l]	boundary condition: SSC	-	60	60	60	10:10:100	60
$Q(t)$ [m³/s]	boundary condition: creek discharge	$0.7\cdot Q_{K3,ST}$	$0.7\cdot Q_{K3,ST}$	$0.7\cdot Q_{K3,ST}$	$0.7\cdot Q_{K3,ST}$	$0.7\cdot Q_{K3,ST}$	$(1:0.2:0)\cdot$ $0.7\cdot Q_{K3,ST}$

TOPOGRAPHY

To analyse the contribution of the distinctive topography of the forest floor within the study site to the observed tidal dynamics, simulations were run for a topography void of mud lobster mounds (but still featuring levees and creek banks; Figure 3.9B) and a topography with a uniform, smoothly sloping forest platform (Figure 3.9C). It was found that flow routing through the creeks slightly reduces when the topography of the forest floor is smoothened, while the sheet flow over the forest fringe gradually increases from 12.5% to 19% of the total inflow (Figure 3.10A,F). Maximum flow velocities within the creeks and in the forest are hardly affected by the removal of the mounds. When the banks and levees are removed as well, maximum flow velocities in the creek reduce by about 10-20%, while maximum shallow-water flow velocities within the forest (at N3) increase by up to about 45% at flood and 95% at ebb.
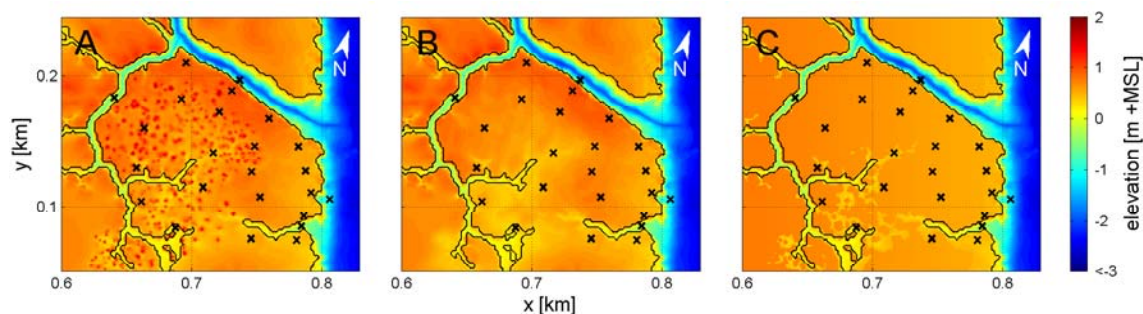
Figure 3.9 – Topographic adjustments to the study site: (A) the original topography; (B) mud lobster mounds are removed from the initial topography; (C) mud mounds and levees are replaced by a gently sloping forest platform dissected by the creeks.

Average deposition rates increase with reduced topographic variations and the deposition pattern changes (Figure 3.10K,P). When only the mud mounds are removed, deposition remains unaffected at the fringe, levee and creek bank, but deposition in the interior increases with almost 30%. This is presumably caused by the fact that, due to the removal of the mud mounds, fluxes of water and sediments to this area are enhanced, while the creek banks and the levee maintain their sediment trapping capacity (as flow velocities remain unaffected). When the banks and levees are removed as well, deposition in the forest's interior decreases again, due to increasing flow velocities. At the position of the formerly elevated zones (creek bank, levee and fringe) the deposition increases under these conditions (up to 55%), due to reduced exposure of the (lower elevated) bed and enhanced influxes of water and sediments caused by the greater water depths.
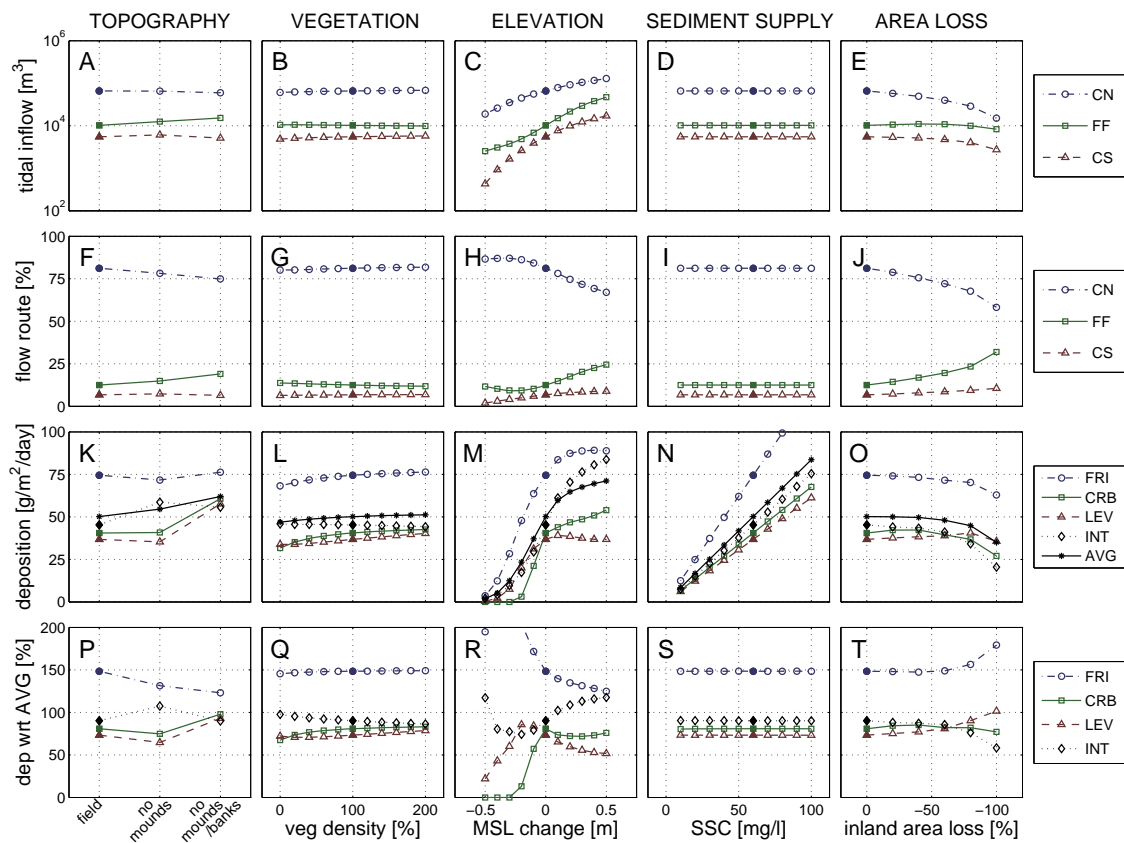
Figure 3.10 – The initial effects of instantaneous changes of biogeophysical settings on flow routing and sediment deposition. The upper row of panels shows the initial effect of (A) a changing topography, (B) vegetation density changes, (C) relative elevation change, (D) changing sediment supply and (E) mangrove conversion on the total tidal inflow through the northern creek (CN), the southern creek (CS) and over the forest fringe (FF). The second row of panels (F-J) displays the relative contribution of the different flow routes to the total inflow for the simulated conditions. The third row (K-O) presents the initial effect of the same scenarios on the spatially averaged net deposition rates per zone: the forest fringe (FRI), the creek bank (CRB), the levee (LEV) and the forest's interior (INT). These plots also show the average deposition throughout the study site (AVG). The bottom row (P-T) shows the relative deposition in each of these zones with respect to the average deposition. Filled symbols represent simulation results for the present conditions, open symbols represent hypothetical conditions.

VEGETATION DENSITY

Simulations with the original bathymetry combined with variable vegetation densities, showed that the vegetation hardly affects the flow routing (Figure 3.10B,G). Relative inflow over the forest fringe only reduces by a few percent with vegetation densities increasing from 0 to 200% of the present density. Apparently, vegetation blockage of the water flow is always very minor due to the relatively open vegetation structure. Nevertheless, the resulting increase in flow routing through the creeks enhanced the maximum creek flow velocities at K3 with 15-20% (Figure 3.8), mostly on ebb tide as a result of the increasing delay of discharges into and out of the mangroves, contributing to a cross-shore water level gradient. Although this effect will certainly affect the self-scouring of the creeks, the deposition pattern within the forest remains largely unaffected by these changes (Figure 3.10L,Q). Predicted average deposition rates throughout the study site only increase with about 10% over the full range of simulated vegetation densities. This increase is caused by greater flow blockage at the forest fringe and creek bank, enhancing local deposition rates (Figure 3.10L). Conversely, deposition rates in the forest's interior gradually decrease with increasing vegetation densities blocking the supply of sediments to this zone.

RELATIVE ELEVATION

The effect of the relative elevation of the forest floor with respect to mean sea level was simulated by varying the mean sea level with -0.5 to +0.5 m, while maintaining the tidal amplitudes (Table 3.6). With the corresponding variation of HW, discharge boundary conditions for the northern creek were also adjusted (Figure 3.2). Increased sea levels affect the distribution of the (increased) tidal prism over the flow routes into the forest, reducing the contribution by the inflow through the northern creek by 14% while increasing the sheet flow over the forest fringe (Figure 3.10C,H). Conversely, for an increased relative elevation of the forest (negative MSL change), the tidal prism decreases and the contribution of creek flow shows a minor increase with respect to the present situation. This is explained by the relative reduction of both vegetation friction (vegetation density decreases with elevation) and bed friction with greater water depths, allowing for increasing flow velocities and discharges over the forest fringe into the forest.

The relative elevation of the forest with respect to MSL appears very important for the deposition rates and spatial distribution thereof. When the relative elevation of the forest instantaneously increases by 0.5 m, deposition rates throughout the forest drop to zero (Figure 3.10M). A lower elevation of the forest with respect to mean sea level enhances (water and) sediment fluxes into the mangroves. This gives rise to increasing deposition rates (Figure 3.10M), except at the levee that is exposed to the increased sheet flow over the forest fringe (Figure 3.10C). Increasing sea levels are mainly in favour of deposition in the sheltered interior of the forest (Figure 3.10R), as the direct sediment supply to this area increases with an increasing share of inflow over the forest fringe, while near-bed velocities remain low due to the topography and vegetation. Relative deposition in the other zones decreases (Figure 3.10R) due to increased exposure by the enhanced creek and sheet flows.

SEDIMENT SUPPLY

Sensitivity of the system to sudden changes of the sediment availability was simulated by varying the SSC boundary condition (Table 3.6). Inherently, these variations only affect the sediment dynamics, as any effects of a changing sediment load on the hydraulic parameters (e.g. density and viscosity) were omitted. Changing SSC in the estuarine water directly affects the sediment fluxes into the study site, and modulates deposition rates throughout the study site proportionally (Figure 3.10N). Changes in the distribution of the deposition throughout the study site are negligible (Figure 3.10S).

MANGROVE AREA LOSS

One of the driving forces of the tidal flow routing is the tidal prism, which is imposed by the landward extent and morphology of the mangroves. Reduction of the tidal prism was simulated by simultaneously decreasing the inland extent of the intertidal area west of the study site (by raising bed levels to 3 m +MSL) and reducing the imposed creek flow boundary condition at the northern model boundary. Both the intertidal area and the imposed creek discharge were reduced by steps of 20% (Table 3.6). Loss of mangrove area inherently reduces tidal inflows, mainly the creek flows (Figure 3.10E). Consequently, sheet flow increasingly contributes to the tidal prism when the mangrove area is reduced (Figure 3.10J). From the model results it also follows that, for the particular conditions of this study site, conversion of up to about 50% of the inland mangrove area does not significantly affect deposition rates (Figure 3.10O). This is explained by the fact that this remote area faces limited inundation depths during flood tide, adding little to the tidal prism (Figure 3.10E).

Due to the greater reduction of tidal inflows (volumes and velocities) with an increasing loss of inland mangrove area, sediment inputs and deposition rates decrease throughout the forest (Figure 3.10O). With a reduced input of sediments, a greater share of the sediment influx deposits in the outer bands of the mangroves (fringe and levee), further reducing the sediment supply to the mangrove's interior. Distribution of the sediment deposition changes correspondingly in favour of the forest fringe and levee, both increasing with about 30%, while the relative deposition in the forest's interior reduces with about 30% (Figure 3.10T). Additionally, the decreasing creek flows affect the self-scouring mechanism of the creeks, as computed maximum flow velocities at K3 reduce by about 70-80%, instigating enhanced accretion of the creeks.

3.4.3   THE ROLE OF VEGETATION IN LOWER ELEVATED MANGROVES

The dominance of the impact of the topography over the impact of (changing) vegetation densities in the present situation is instigated by the high elevation of the forest platform with respect to mean sea level. When similar variations were imposed on an area that is located 0.5 m lower with respect to MSL, the impact of increasing vegetation densities became much more pronounced (Figure 3.11).
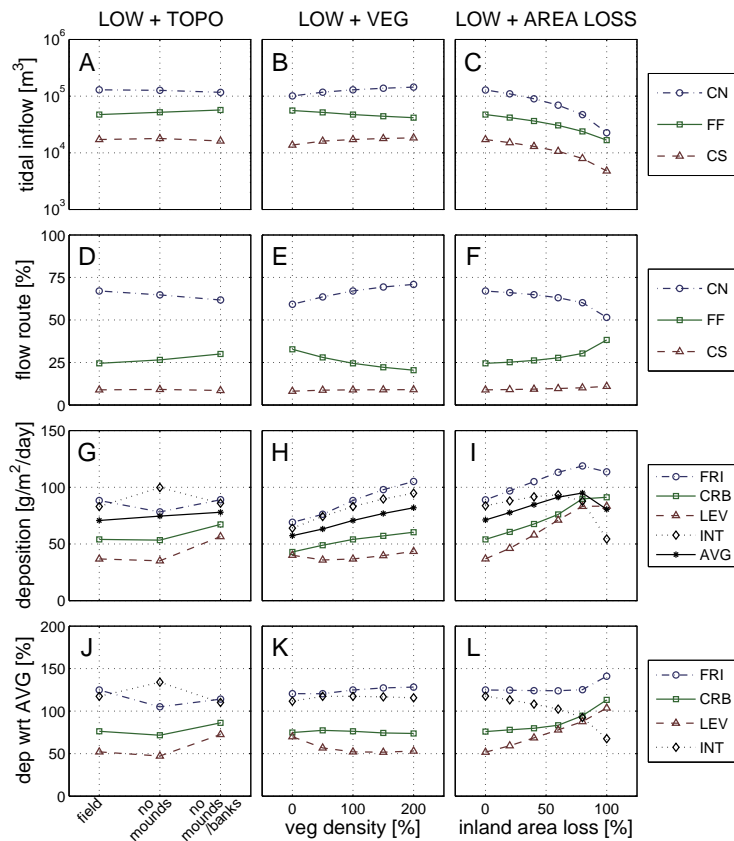
Figure 3.11 – The initial effects of instantaneous changes of biogeophysical settings on flow routing and sediment deposition, when the relative elevation of the forest floor is decreased by 0.5 m. Effects are mapped for: (left) a changing topography, (centre) variable vegetation density and (right) reduction of the inland mangrove area loss. Plotted flow routing and deposition characteristics are similar to Figure 3.10 (note the increased scale of the deposition plots).

The tidal prism of the lower elevated mangrove forest is greater (Figure 3.11A-C) and the flow routing shows a similar dependence of the vegetation density and of the simulated topography (Figure 3.11D-E). A reduction of the vegetation density from 100% to a cleared site, causes a significant shift of inflow through the creeks (-8%) to sheet flow over the forest fringe (+9%). More importantly, with an increased inundation depth of the forest deposition rates are much more sensitive to the vegetation density than to the topography (Figure 3.11G-H), due to the greater influxes of water and sediments. Vegetation clearance would reduce deposition rates by about 20%, except at the levee. On contrary, a vegetation cover twice as dense as the present cover would induce 10-20% higher deposition rates throughout the lowered study site (Figure 3.11H). Under these conditions, changes to the topography only cause an increase of 5-10% of the spatially averaged deposition rates (Figure 3.11G).

Additional runs with the lower elevated mangroves for a gradually decreasing extent of the inland mangrove forest present some (upfront) counterintuitive results, showing increasing deposition rates within the study site (Figure 3.11I). This increase is caused by the reduced (sheet) flow velocities through the study site when the inland mangrove area is excluded from tidal inundation, while sufficient suspended sediments are supplied to feed the enhanced

deposition. However, the converted mangrove area is excluded from deposition in this scenario. According to the cumulative sediment fluxes during the simulated period, the net sediment flux into the study site (through the creeks and over the fringe) halves for a complete removal of the inland mangroves (from 1.2 to about 0.6 m³).

3.5   DISCUSSION

3.5.1   STABILITY OF MANGROVES WITH RESPECT TO CHANGING ENVIRONMENTAL CONDITIONS

The effective trapping of sediments in mangroves was previously corroborated by biogeomorphological studies that monitored sediment deposition over periods ranging from several tidal cycles up to one year. These studies linked deposition rates with e.g. mangrove zonation [*Adame et al.*, 2010], bed elevation [*Anthony*, 2004; *Stokes et al.*, 2010] and root types [*Krauss et al.*, 2003]. Yet, these studies did not explain spatially explicit linkages between the physical processes – sedimentation and flow routing – on one hand, and the biogeomorphological settings on the other hand. Nevertheless, these spatially explicit linkages are key to understand the bio-physical interactions in, and hence the maintenance of, coastal mangroves.

The range of simulations for the analysis of the initial response of the mangrove system to variable biogeophysical settings provides evidence that the mangrove system is stable in its current configuration. First, removal of slight elevations such as the creek banks and the levee behind the forest fringe, induces increased deposition rates (up to 55% higher) at exactly these locations (Figure 3.10K,P). Second, instantaneous changes of the vegetation density do not (significantly) affect the tidal dynamics in the study site (Figure 3.10B,L). Third, a sudden change of the relative elevation (lowering of the forest floor or rising sea level) causes a positive feedback for the deposition rates throughout the study site: generally, deposition rates reduce (with about 20%) when inundation depths decrease (with 0.1 m) and vice versa (with 100% vegetation density; Figure 3.10M). However, this adaptive capacity is limited as the increase of the deposition rates slows down for increasing inundation depths (Figure 3.10M). This limitation is (partly) imposed by the sediment supply, which is directly related with the SSC concentration of the water entering the forest (Figure 3.10N) and the total tidal water exchange that, as well, depends on the inland extent of the mangroves (Figure 3.10O).

The stability of the mangrove system changes when the relative elevation of the forest would have been 0.5 m lower, i.e. inundation depths are greater due to either a lower elevation of the forest floor or an (instantaneously) increased sea level. For this altered elevation, the computed initial impacts of changing biogeophysical settings increase and the effect of vegetation changes exceeds the impact of the mangrove's topography (Figure 3.11G,H). The initial response of the system, or its adaptive capacity, becomes dependent of the vegetation density with greater vegetation densities facilitating faster adjustment of the morphology (Figure 3.11H). A reduction of the inland extent of the mangroves would also increase local deposition rates

(Figure 3.11I), provided the sediment supply is sufficient. For reduced suspended sediment concentrations in the tidal inflow, this increase of deposition rates within the study site will be limited. Either way, total sediment trapping by the partly converted mangroves is reduced, presumable affecting the adaptive capacity of the coastal zone.

Given the previous findings, the sediment trapping capacity of the mangroves is affected when great parts of the inland extending mangrove area are converted for coastal development, aqua- or agriculture, oil palm or timber plantations [*Polidoro et al.*, 2010; *Winterwerp et al.*, 2013] and when suspended sediment import reduces e.g. due to river damming [*Thampanya et al.*, 2006]. Additionally, with 0.5 m deeper inundations, deposition rates become susceptible to reduced vegetation densities, e.g. due to logging [*Ellison and Farnsworth*, 1996; *Alongi and De Carvalho*, 2008]. These findings address the initial response of the system to the impacts of sudden land-use changes and sea level rise, adding to the knowledge base for understanding the trends observed in previous studies addressing mangrove resilience [e.g. *Thampanya et al.*, 2006; *Alongi*, 2008; *Webb et al.*, 2013]. These results are a clear indicator for the sensitivity of mangroves' ecosystem engineering function to climate change and anthropogenic threats.

3.5.2 DEPTH-AVERAGED NUMERICAL MODELLING OF MANGROVE DYNAMICS

The present study started with a 3D process-based model, that was previously validated for the simulation of tidal dynamics in salt marshes [*Temmerman et al.*, 2005b; *Bouma et al.*, 2007]. Simulating tidal dynamics in a mangrove environment, featuring much greater variability in vegetation structure and variability than salt marshes, was proven to be successful with the obtained validation results (Table 3.5). Alternatively, post-calibration results of the depth averaged model showed good correspondence with the simulation results of the 3D model and, hence, with the field observations. Meanwhile, computation times were reduced by a factor 5-10 (i.e. 80-90%) compared to the 3D model, which had only eight depth layers. Consequently, the 2DH model proved to be an efficient, i.e. accurate and less demanding, alternative to the 3D model.

The 2DH model required a depth-averaged vegetation representation. The calibration of this model resolved that vegetation densities at 50 cm above the forest floor represented the depth-averaged impact of the mangrove vegetation. With sediment deposition rates validated successfully for the different topographic zones (Table 3.5), each with particular vegetation types (Figure 3.1D,E), it is concluded that this vegetation representation is accurate for different types of vegetation. As the forest floor was elevated 0.3-0.9 m above MSL, maximum inundation depths within the forest were 0.9-1.5 m for the highest simulated spring tides (Table 3.2). These findings corroborate that the vegetation density at one-half to one-third of the maximum inundation depth at spring tide is representative for similar modelling studies of other mangrove areas. Consequently, it would suffice to map vegetation characteristics at a single elevation. Given the great horizontal and vertical variability in mangrove vegetation and the harsh conditions in the field, this greatly reduces field labour.

Notwithstanding the depth-averaged approach, the model requires an accurate topography. It was established that the tidal dynamics at the study site were greatly topography-induced. The omission of mud mounds and banks from the modelled topography causes a slight shift in flow routing patterns, while predicted deposition rates vary up to 30% with respect to a run with the high-resolution topography (Figure 3.10K). This finding emphasizes the need to use high-resolution topographic data when simulating tidal dynamics in mangroves. To our knowledge, however, previous studies simulating tidal dynamics in mangroves implemented a highly schematized, smoothly inclining forest floor [*Wolanski et al.*, 1980; *Wolanski et al.*, 1990; *Mazda et al.*, 1995; *Wu et al.*, 2001]. Additionally, the relative elevation of the forest floor with respect to the tidal range was found to be a major contributor to the tidal dynamics in the mangroves (Figure 3.10C,M). Consequently, the topographic data need reference to a tidal datum, which was shown to be accurately retrieved via basic long-term (>month) monitoring of tidal water levels (Figure 3.2).

3.5.3   THE ROLE OF MANGROVES AS ECOSYSTEM ENGINEERS

Ecosystem engineers are organisms that are capable of changing their abiotic environment, often mitigating their habitat in favour of their own survival [*Jones et al.*, 1994; 1997]. Mangroves were shown to own such traits by facilitating and enhancing sediment deposition rates. These deposition rates were observed to correlate positively with the inundation depth (Figure 3.6C, Figure 3.10M, Figure 3.11). This initial system response presumably supports the maintenance of a suitable elevation of the forest floor with respect to mean sea level. Corresponding long-term trends have been observed from geomorphological studies of mangrove deposits [e.g. *Ellison and Stoddart*, 1991; *McKee*, 2011].

Another important ecosystem engineering trait of mangroves is the stabilization of their silty soils by binding sediments and limiting sediment exposure to hydrodynamic forces [e.g. *Spenceley*, 1977; *Krauss et al.*, 2003]. *Thampanya et al.* [2006] demonstrated that mangrove dominated coasts in Southern Thailand exhibit less erosion than non-vegetated areas, corroborating the coastal stabilization by mangrove vegetation. This stabilizing effect by mangrove vegetation is just partially represented in this work. The model only accounted for the erosion of the fresh deposits and did not include erosion due to wave action (as the study site was not significantly exposed to waves). Erosion of the existing morphology was not included in the model. Inclusion of this process would require a critical erosion shear stress for the compacted forest floor with its abundant biological constituents (roots, microbial mats etc.). Although the effects of mangrove characteristics, and related biological components, on sediment accretion and elevation change have been studied before [*Krauss et al.*, 2003; *McKee*, 2011], no direct relationships have been provided yet for these processes.

The next challenge is to simulate the resulting evolution of mangroves over longer (decadal) time spans, for example to reconstruct the development of present mangrove topography or to predict the future development of mangrove sites. Such an evolutionary model requires the inclusion of the abovementioned erosive processes that also give rise to the formation of tidal

creeks. These erosive processes have been studied in great detail for salt marshes [e.g. *Fagherazzi et al.*, 2012] and can, given the similarities in biogeophysical system settings, probably be translated to mangrove environments. The collection of accurate long-term data on surface elevation changes in mangroves [cf. *Webb et al.*, 2013] is prerequisite for the calibration and validation of these evolutionary models.

Additionally, long-term modelling requires the inclusion of vegetation dynamics, taking account of colonization, growth and mortality of the mangroves. Vegetation dynamics in mangroves were previously parameterized by *Van Maanen et al.* [2011] for their idealized simulation of long-term morphodynamic evolution of a tidal basin, including mangrove dynamics. Recent mechanistic studies by *Balke et al.* [2011; 2013], focussed on the colonization by and establishment of mangrove seedlings on exposed mudflats. Enhanced understanding of the short-term biophysical interactions in mangroves, from the present model, and of the establishment thresholds for mangroves, will bridge the gap between the previous idealized model [*Van Maanen et al.*, 2011] and a process-based long-term biophysical mangrove evolution model simulating the long-term functioning of mangroves as ecosystem engineers.

3.6   CONCLUSIONS

In the field site, an elevated mangrove stand dissected by tidal creeks, tidal flow routing comprised a creek flow stage – during which tidal in-/outflows were funnelled through the creeks – and a sheet flow stage – when water flowed directly from the estuary into the mangroves. Observed deposition rates increased for higher high tides, due to the enhanced tidal prism and the consequent import of sediments. Deposition of the imported sediments increased fastest in the interior of the mangrove forest, that was least exposed to the faster sheet flows during spring tides. For an increase of the tidal prism, the deposition rates in the interior increased most, confirming its sediment trapping function.

A sensitivity analysis with the calibrated and validated depth-averaged numerical model showed the initial system response to instantaneous changes of the topography, vegetation density, relative elevation, sediment supply and mangrove. The tidal-scale flow routing and sediment deposition – rates and pattern – are found to be greatly bathymetry induced, mostly depending on the characteristic topography of the field site and its high elevation with respect to mean sea level. Model simulations provide evidence that the studied mangrove site is stable in its current configuration, with vegetation densities hardly affecting deposition rates. Moreover, the deposition rates change in concordance with the removal of topographic features or changes of the relative elevation: deposition increases at the locations of removed creek banks and levees and deposition also increases when inundation depths increase (and vice versa). The supply of suspended sediments and the extent of the mangrove forest are prerequisites for these ecosystem engineering traits.

The significant of the vegetation density gains importance for greater inundation depths, enhancing sheet flows through the mangrove vegetation. The computed initial response of the system shows deposition rates to increase or decrease with up to 20% for, respectively, double the vegetation density or an area void of mangrove vegetation. Again, this increased deposition requires sufficient suspended sediment concentrations in the tidal fluxes as deposition rates were found to change proportionally to this parameter.

By simulating the initial response – or adaptive capacity – of the mangroves to reduced sediment supply and reduced mangrove area, the present findings show a decreasing sedimentation due the impacts of e.g. river damming and mangrove conversion for e.g. aqua- or agriculture. With deeper inundations, reduced vegetation densities cause the mangroves' sediment trapping to diminish as well, addressing the potential impacts of future sea level rise and vegetation loss due to e.g. logging. These results are a clear indicator for the sensitivity of mangroves' ecosystem engineering ability, in terms of sedimentation, to climate change and anthropogenic threats.

CHAPTER 4

WAVE ATTENUATION IN MANGROVES:
A QUANTITATIVE APPROACH TO FIELD OBSERVATIONS[‡]

Avicennia and Sonneratia trees facing storm conditions at the Mae Nam Trang estuary, Thailand.

ABSTRACT

Coastal mangroves, dwelling at the interface between land and sea, provide an important contribution to coastal safety by attenuating incident waves and by trapping and stabilizing sediments. This chapter focusses on mechanistic relations between vegetation densities, wave attenuation rates, sediment characteristics and sedimentation rates in mangroves. These processes were studied along two cross-shore transects through mangroves fringing two estuaries in the southern Andaman region of Thailand. Vegetation composition and structure were mapped profoundly, resolving submerged vegetation densities of up to 32 volume-‰, depending on the water depth. Wave attenuation rates increased substantially for increasing vegetation densities. Generalized wave attenuation rates (r), based on fits to the observed attenuation for a range of incident wave heights and water depths, increased from 0.002 m^{-1} in the sparsely vegetated forest fringes with *Avicennia* and *Sonneratia* species, up to 0.012 m^{-1} in the dense *Rhizophora* vegetation in the back of the forests. Attenuation rates for single data bursts resolved that decreasing water depths, and consequently increasing volumetric vegetation densities, induced wave attenuation rates to increase substantially in the dense *Rhizophora* vegetation while such an effect was absent in the sparser *Avicennia*/*Sonneratia* vegetation. Wave attenuation in the mangroves also facilitated enhanced deposition and a gradual fining of the bed material.

These findings corroborate the coastal defence function of mangroves by quantifying their contribution to wave attenuation and sediment trapping. The explicit linking of these properties to vegetation composition and structure facilitates mechanistic modelling studies into the coastal defence capacities of mangroves.

4.1 INTRODUCTION

Mangroves form a key-ecosystem in the intertidal area of tropical and sub-tropical coastlines. Mangrove vegetation, consisting of trees and shrubs, copes with the harsh conditions in the intertidal: salinity, tidal flooding and waves. Forming an evident barrier between land and sea, mostly in areas where any other kind of sea defence is lacking, mangroves contribute to wave attenuation [*Vo-Luong and Massel*, 2006; *Quartel et al.*, 2007] and to coastal stabilization [*Augustinus*, 1995; *Anthony*, 2004; *Van Santen et al.*, 2007; *Alongi*, 2008]. Mangroves are even said to have saved lives and properties during the Indian Ocean tsunami in 2004 [*Danielsen et al.*, 2005; *Kathiresan and Rajendran*, 2005], though the exact contribution of mangrove vegetation is disputed [*Kerr et al.*, 2006]. Despite these invaluable regulating services, mangroves are in rapid decline [*FAO*, 2007; *Spalding et al.*, 2010]. Hence, there is an urgent need to unravel the physical contribution of mangroves to coastal safety in order to increase awareness of the need for mangrove preservation.

Unravelling dissipation of wave energy in coastal mangroves by field and laboratory studies has only gained attention since the late nineties [*Alongi*, 2009]. Due to the inaccessibility of (natural) mangrove forests, a limited number of field studies has been executed in mangroves in Vietnam, Australia and Japan (Table 4.1). These studies emphasize in unison the positive contribution of mangroves to the dissipation of wind and swell waves of limited height and period. Nevertheless, observed wave reduction rates show significant variation with water depth and vegetation characteristics (Table 4.1).

Wave attenuation by mangroves observed in the field has previously been parameterized by calculating bulk roughness parameters, either a wave attenuation rate (Table 4.1) or a bulk drag coefficient, comprising both vegetation induced drag forces and bottom friction [*Mazda et al.*, 1997a; *Quartel et al.*, 2007]. Both *Mazda et al.* [1997a] and *Quartel et al.* [2007] obtained exponentially increasing bulk drag coefficients for increasing water depths within the mangroves due to limited height of the dwarfed trees in their field sites. Conversely, *Brinkman et al.* [1997] obtained increasing transmission factors, hence decreasing wave attenuation, for increasing water depths at two sites with taller mangrove vegetation (Table 4.1).

Enhancing understanding of the contributing processes determining wave attenuation in mangroves requires mechanistic studies of the propagation of waves through vegetation. Recent advances in numerical modelling explicitly resolve vegetation induced drag forces by integrating friction forces over a composition of one or several layers of rigid vertical cylinders [*Vo-Luong and Massel*, 2008; *Suzuki et al.*, 2012]. For a reliable representation of the vegetation, this approach compels detailed, site specific information on vegetation characteristics such as stem and root diameters, vertical vegetation distribution, vegetation densities and (bulk) drag coefficients. However, due to poor vegetation data the abovementioned models were calibrated in the vegetation parameters [*Vo-Luong and Massel*, 2008; *Suzuki et al.*, 2012], raising questions regarding their general validity.

Table 4.1 – Overview of previous studies into wave attenuation in mangroves. Wave attenuation is quantified by the ratio of the wave height reduction (ΔH) and the incident wave height (ΔH) per distance (Δx): $r = \Delta H/(H \cdot \Delta x)$ (n.a. = not available).

Location - mangrove setting	Vegetation	Incident wave height H & period T	Wave attenuation
Tong King Delta, Vietnam - fringing mangroves [*Mazda et al.*, **1997a**]	Sparse *Kandelia candel* seedlings (1/2 year-old), planted	H = n.a. T = 5-8 s	r = 0.01-0.10 per 100 m
	Dense 2-3 year-old *Kandelia candel*, up to 0.5 m high, planted	H = n.a. T = 5-8 s	r = 0.08-0.15 per 100 m
	Dense 5-6 year-old *Kandelia candel*, up to 1 m high, planted	H = n.a. T = 5-8 s	r = 0.15-0.22 per 100 m
Vinh Quang, Vietnam - fringing mangroves [*Mazda et al.*, **2006**]	*Sonneratia* sp., 20 cm high pneumatophores, canopy starts 60 cm above bed, planted	H = 0.11-0.16 m T = 8-10 s	r = 0.002-0.006 m^{-1}
	No vegetation	H = 0.11-0.16 m T = 8-10 s	r = 0.001-0.002 m^{-1}
Can Gio, Vietnam - riverine mangroves [*Vo-Luong and Massel*, **2006**]	Mixed *Avicennia* sp. and *Rhizophora* sp.	H = 0.35-0.4 m T = n.a.	energy reduction factor = 0.50-0.70 over 20 m (including a cliff)
Do Son, Vietnam - fringing mangroves [*Quartel et al.*, **2007**]	Mainly *Kandelia candel* bushes and small trees	H = 0.15-0.25 m T = 4-6 s	r = 0.004-0.012 m^{-1}
	Non-vegetated beach plain	H = 0.15-0.25 m T = 4-6 s	r = 0.0005-0.002 m^{-1}
Red River Delta, Vietnam - fringing (?) mangroves [*Bao*, **2011**]	Mixed vegetation	H = 0.15-0.27 m T = n.a.	r = 0.0055-0.01 m^{-1}
Can Gio, Vietnam - fringing (?) mangroves [*Bao*, **2011**]	Mixed vegetation	$H \sim$ 0.55 m T = n.a.	r = 0.017 m^{-1}
Cocoa Creek, Australia - fringing mangroves [*Brinkman et al.*, **1997**; *Brinkman*, **2006**]	Zonation: *Rhizophora* sp. (front), *Aegiceras* sp., *Ceriops* sp. (back)	H = 0.01-0.07 m $T \sim$ 2 s	energy transmission factor = 0.45-0.80 over 160 m
Iriomote, Japan - riverine mangroves [*Brinkman et al.*, **1997**; *Brinkman*, **2006**]	*Bruguiera* sp., 20-30 cm high knee roots	H = 0.08-0.15 m $T \sim$ 2 s	energy transmission factor = 0.15-0.75 over 40 m
Oonoonba, Australia - fringing mangroves [*Brinkman*, **2006**]	Zonation: *Sonneratia* sp. (front) and *Rhizophora* sp. (back)	H = 0.04-0.25 m $T \sim$ 6 s	energy reduction factor = 0.9-1.0 over 40 m

Hence, field data comprising accurate measurements of both hydrodynamics (wave heights, water depths and, if possible, flow velocities) and vegetation parameters is indispensable for further development of the abovementioned numerical models [*McIvor et al.*, 2012b; *Möller*, 2012]. Both are changing from site to site, depending on local geography, wave climate and vegetation characteristics. Although wave attenuation studies accurately quantified hydrodynamic conditions, often only a very limited range of conditions is covered as data collection often spans a few tides only [*Mazda et al.*, 1997a; *Brinkman*, 2006]. Vegetation characteristics were poorly represented yet by either qualitative descriptions of local vegetation

patterns or fairly rough quantifications of the vegetation cover [*Brinkman*, 2006; *Vo-Luong and Massel*, 2006; *Quartel et al.*, 2007]. *Mazda et al.* [1997b] made an exceptional effort by identifying detailed vegetation parameters and quantifying the volume of submerged mangrove biomass. This concept will be deployed in the present study.

This chapter addresses the explicit correlations between vegetation densities, wave attenuation, sediment characteristics and sedimentation rates in mangroves. We aim to correlate wave attenuation with the volume-percentage of submerged mangrove biomass for variable vegetation compositions and densities, pursuing an explicit relation between the mangrove density and the wave attenuation capacity of mangroves. Along with these bio-physical interactions, we aim to link the attenuated hydrodynamic conditions to sediment properties and deposition rates within mangroves. These correlations will be based upon the results of a comprehensive field campaign combining measurements of the hydrodynamics and sediment dynamics at multiple locations along two cross-shore transects trough mangrove fringes, with the collection of detailed topographic and vegetation data.

4.2   STUDY SITES

The study sites are located at the east coast of southern Thailand, in Trang Province (Figure 4.1A,B). This area is part of the convoluted Thai Andaman coast, consisting of many embayments, islands and islets offering a perfect habitat to mangroves. The Andaman coast hosts about 80% of the 244,000 hectare of Thai mangroves [FAO, 2007]. Although the Thai Andaman coast was severely struck by the 2004 Indian Ocean tsunami, the study sites remained unaffected. The tip of Sumatra (Banda Aceh) and the many islets shelter the southern part of the Andaman Sea and the study sites, respectively, from incoming waves from the Indian Ocean.

Two cross-shore transects were defined for this study. One transect was located in the district of Kantang, in the estuary of the rivers Mae Nam Trang and Khlong Palian, herein referred to as the Kantang estuary (Figure 4.1C). The other transect was situated in the district of Palian, in the estuary with the rivers Khlong Lak Khan and Khlong Rae as its tributaries, herein referred to as the Palian estuary (Figure 4.1D). The Kantang transect was directed southwest towards the Andaman Sea (Figure 4.1C) while the Palian transect was directed towards the southeast across the Palian River estuary (Figure 4.1D). These cross-shore transects were in line with the prevailing direction of wave propagation in the shallow coastal waters. We focussed on the front few 100's of meters of the rather extensive mangrove forests in both estuaries as attenuation of hydrodynamic energy largely occurs in the front of the forest.

Both transects featured a gradually sloping forest floor with average slopes of 3.3(±2.6):1000 and 6.0(±7.6):1000 (± standard deviations) for the Kantang and Palian transect, respectively (Figure 4.2). The sparsely vegetated forest front at both transects was dominated by trees of *Avicennia* sp. and *Sonneratia* sp. (Figure 4.2) and the forest floor was covered in a dense layer of pneumatophores (pencil roots) of these trees. The densely vegetated back forest at both

transects was dominated by *Rhizophora* sp. instead, with their dense networks of stilt roots. Due to the difference in bed slopes and the inundation induced zonation of mangrove vegetation [*Watson*, 1928; *Van Loon et al.*, 2007], the vegetation zones were narrower along the Palian transect than along the Kantang transect. Additionally, greater vegetation densities were observed in the Palian back forest.

The study sites were tide dominated [*Woodroffe*, 1992], exposed to a mixed semi-diurnal tide with a mean tidal range of 2.0 m and a maximum range of 3.6 m (Section 2.2). The wind wave climate in this region is strongly influenced by the monsoons. Southwest monsoons generate the highest waves at the Andaman coast and prevail from May to October. Northeast monsoon prevails from October to February. The present data have been collected from December 2010 to May 2011 and hence mainly cover the relatively quiet conditions of the northeast monsoon. However, during the last week of March 2011, the Andaman coast was struck by severe storms giving rise to increased wave heights at the coasts and causing severe floods inland. Additionally, wave exposure of the two transects varied due to the different orientations with respect to the Andaman Sea (Figure 4.1C,D).

4.3   DATA COLLECTION AND PROCESSING

4.3.1   ELEVATION SURVEY

We mapped the topography of the study sites thoroughly with Trimble survey equipment (SPS 700-S6 Total Station and R-6 Real Time Kinematic GPS). At each transect about 100 survey points were mapped with respect to local benchmarks. Survey point density was increased in steeper sloping (vegetated) parts of the transects. The local benchmark at each transect was georeferenced with the RTK-GPS. The elevation of the transects with respect to mean sea level was obtained from an analysis of locally obtained tidal water level data (Section 4.3.3). These data were processed to cross-shore transect profiles (Section 2.4.1).
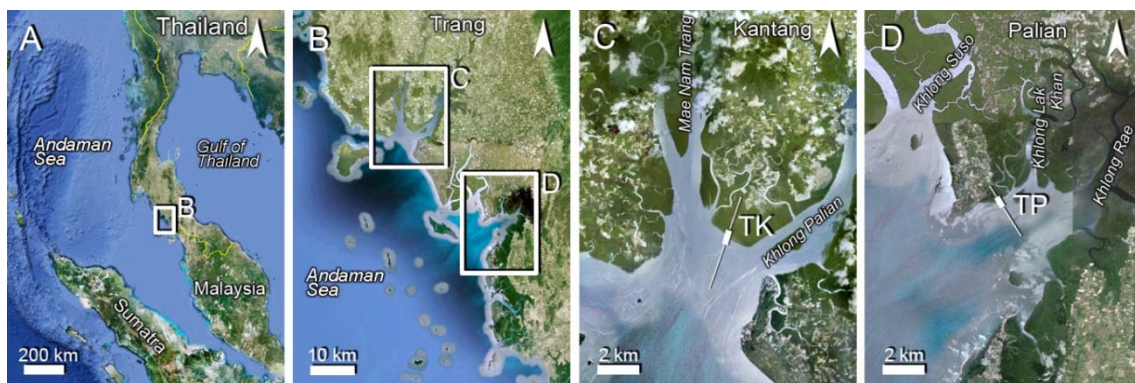
Figure 4.1 – Topography of the study sites. (A) The east coast of southern Thailand facing the Andaman Sea. (B) The coastal areas of Trang province. (C) The Kantang estuary with the position of the Kantang transect (TK) indicated by a box; the line indicates the orientation of the transect. (D) The Palian estuary with the Palian transect (TP) indicated similarly (source: Google Earth).
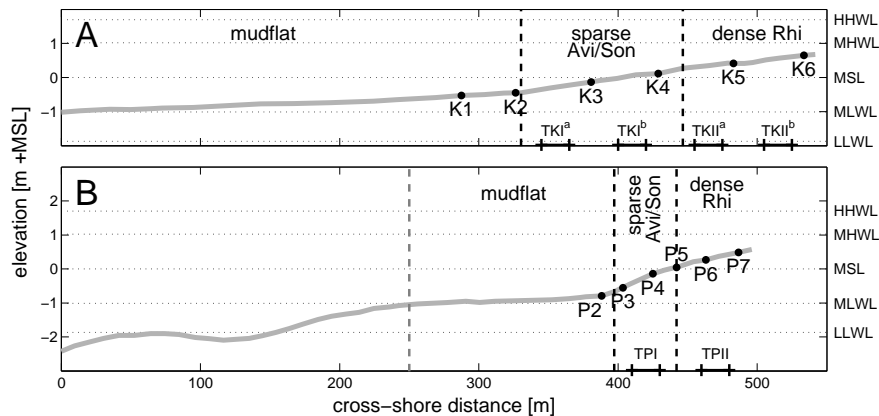
Figure 4.2 – Elevation of the cross-shore transects including instrument positions at (A) the Kantang transect and (B) the Palian transect. Distinct vegetation zones along the transects are demarcated by dashed lines (Avi/Son = *Avicennia*/*Sonneratia*; Rhi = *Rhizophora*). Vegetation survey plot positions are indicated at the bottom of each graph and characteristic tidal water levels are indicated at the right (HHWL = highest high water level; MHWL = mean high water level; MLWL = mean low water level; LLWL = lowest low water level).

4.3.2   VEGETATION SURVEY

Vegetation cover at the wave transects was mapped by quantifying all vegetation elements within a total of six vegetation plots of 20x20 m^2 along both transects. These plots were distributed over the different vegetation zones along both transects and according to the spacing and vegetation variability, one or two plots were assigned per zone (Figure 4.1C,D). The vegetation survey method slightly differed for the plots within the sparsely vegetated front forest and the plots within the densely vegetated back forest.

In the forest fringe zone (plots TKI[a,b] and TPI in Figure 4.2), where *Avicennia* and *Sonneratia* species were predominant (Figure 4.4B), trees were classified according to their size. The trunk or stem diameter was measured at breast height (i.e. 1.50 m) or, when the tree was too small, at one third of the height of the sapling. These stem diameters were categorized in five groups: 0-10 mm, 10-25 mm, 25-100 mm, 100-200 mm and >200 mm. Per category, one representative tree was selected of which the stem diameter was measured at 0.1 m, 0.5 m, 1.0 m, 1.5 m and 2.0 m above the bed. Diameters of branches at these elevations, if any, were included as well. *Rhizophora* vegetation in the forest fringe was rather sparse and those trees present were quite similar and small. All *Rhizophora* trees in the plots were counted and diameters of all roots, stems and branches of one representative tree were measured at 0.1 m, 0.5 m, 1.0 m and 2.0 m above the bed.

In the densely vegetated back forest (plots TKII[a,b] and TPII in Figure 4.2), *Rhizophora* sp. was predominant (Figure 4.4C). In the back forest plots, all trees were counted and root characteristics were measured for a small, an average and a large tree (*Rhizophora* tree sizes were much more variable than in the forest fringe). Detailed characterization of these trees was

performed similar to the method for the forest fringe; diameters of all roots, stems and branches of these representative trees were measured at 0.1 m, 0.5 m, 1.0 m and 2.0 m above the bed. *Avicennia* and *Sonneratia* trees in the back forest were treated the same as the *Rhizophora* trees. Their total number was counted, and the same measures were taken for representative samples.

Seedlings (i.e. single stemmed tree saplings) were only encountered in plot TPII and these were counted separately, along with the diameter of one average seedling sample. For remaining stems of dead trees, the average height and diameter was included as well. Additionally, three subplots of 0.5x0.5 m^2 (or 1x1 m^2, depending on pneumatophore densities) were allocated within each vegetation plot, representing a sparse, average and dense pneumatophore cover. In each subplot, the total number of pneumatophores was counted. Height and diameter of the pneumatophores was measured for 20 randomly chosen pneumatophores per subplot.

All obtained vegetation characteristics were merged into a single vegetation parameter expressing the different vegetation densities along the transects. Vegetation data were first transformed into the total horizontal coverage of vegetation elements within each of the vegetation plots at different levels above the bed. Subsequently, the volume of vegetation within the water column was calculated by integrating the (depth-dependent) horizontal vegetation coverage over depth. These vegetation volumes were expressed as relative vegetation volumes (volume-‰) compared to the total submerged volume, similar to the volumetric vegetation parameter deployed by *Mazda et al.* [1997b].

4.3.3 HYDRODYNAMIC DATA COLLECTION

Six high frequency pressure sensors (MacroWave, Coastal Leasing Inc.) were deployed for collecting wave data along the transects. These sensors are robust and the internal memory and battery housing facilitates autonomous data collection for periods of up to several weeks, depending on sampling frequency and battery quality. Sampling rates of the pressure sensors were set to 10 Hz, with burst lengths of 2^{12} samples (~7 minutes) at intervals of 20 minutes. Data collection by all sensors was started simultaneously for every deployment. In order to start data collection at shallow water depths, the instruments were buried with the sensors levelled at 5-7 cm above the bed (Figure 4.3).

The wave sensors were deployed at six positions along each of the wave transects (Figure 4.2). Two sensors were located at the subsequent interfaces between the mudflat, the sparsely vegetated forest fringe and the densely vegetated back forest (Figure 4.3). The four remaining sensors were located within these specific zones: one on the mudflat in front of the forest, one in the sparsely vegetated forest fringe and two within the densely vegetated back forest (Figure 4.2). Following the different topography of the sites, distances between the instrument locations were about 50 m along the Kantang transect (Figure 4.2A) and about 20 m at the Palian transect (Figure 4.2B).
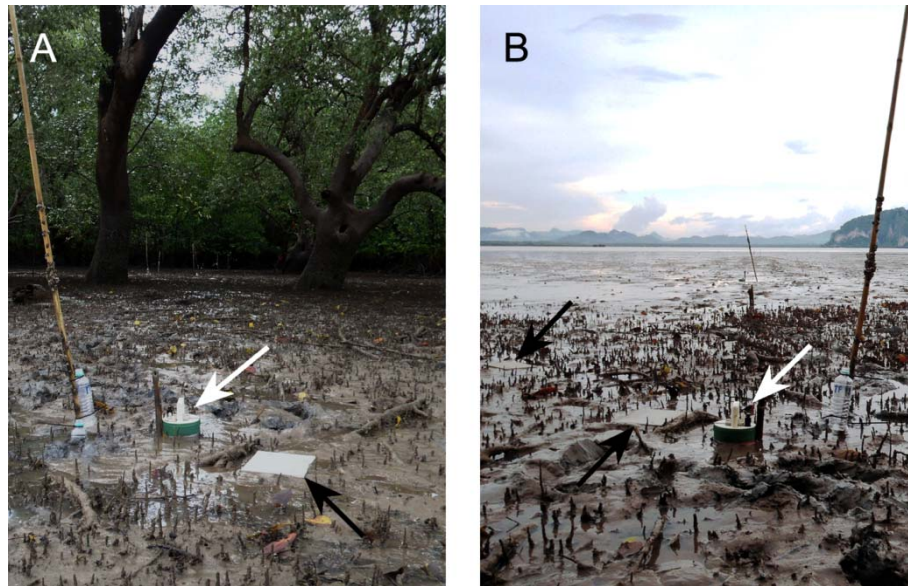
Figure 4.3 – Simultaneous deployment of wave sensors (white arrows) and sediment traps (black arrows) at the Palian transect, position P3. (A) A view towards the forest: the sparse *Avicennia* and *Sonneratia* vegetation landward op P3, and the dense *Rhizophora* forest in the back. (B) A view towards the estuary: P3 was located at the edge of the mangrove vegetation, with the mudflat in front of it.

Wave sensors were deployed three times along each of the transects and single deployments lasted for periods of 2 to 6 weeks. Deployments at the Kantang transects lasted from 26 January to 5 March, from 7 March to 20 March and from 24 March to 14 April 2011. At the Palian transect, instrument deployments lasted from 25 November to 5 December 2010, from 8 December 2010 to 19 January 2011 and from 17 April to 2 May 2011. Due to poor battery performance and technical issues, some sensors stopped data collection prematurely. Hence, collected data sets are gapped in time and space.

Next to these high-frequency wave sensors, low-frequency pressure (and temperature) loggers (Sensus Ultra, ReefNet Inc.) were deployed continuously during the field campaign. These sensors collected pressure data with a sampling interval of 5 minutes, monitoring tidal water levels. These loggers were positioned at K2 along the Kantang transect and between P2 and P3 at the Palian transect (Figure 4.2).

4.3.4   SEDIMENT DATA COLLECTION

Sediment deposition was monitored with sediment traps. The traps were made of 0.20x0.25 m^2 ceramic tiles, covered in a smooth layer of mortar to mimic the forest floor. These tiles were carefully levelled with the forest floor (Figure 4.3). Sediment traps were deployed during one single deployment at each transect. Two traps were deployed at each monitoring position along the transects during low spring tide (7 March at Kantang, 19 April at Palian). One trap of each pair was collected after a period of one or two tides (~12/24 hrs), the other trap was collected after a full spring-neap tidal cycle (20 March at Kantang, 2 May at Palian). Diurnal sediment

trapping during neap tidal conditions rendered inaccurate results as parts of the transects remained submerged at low tide.

Deposited sediments were rinsed, filtered (0.7 μm Whatman GF/F filters) and dried for 24 hrs at 105° C before weighing [*Horstman et al.*, 2011b]. Additionally, sediment samples of the (undisturbed) top layer of the bed were collected at all monitoring positions for the analysis of grain size distributions (Malvern) and organic matter content (ashing).

4.3.5   PROCESSING HYDRODYNAMIC DATA

Obtained pressure data from the wave sensors were corrected for the atmospheric pressure, preliminary to the conversion into water depths. From meteorological data for the period of the field campaign it was derived that the average atmospheric pressure was 1008 hPa. Diurnal fluctuations of the atmospheric pressure (±5 hPa) were irrelevant on the short time scale of waves. For the conversion to water depths, the specific gravity was calculated from the site specific gravitational acceleration and water density: 9.78 m/s^2 and 1004 kg/m^3 respectively. This density was calculated for a water temperature varying between 26° and 33° C (observed by the Sensus Ultra loggers) and a salinity of 9-13 PPT (obtained from water samples).

Spectral analysis was executed according to *Hegge and Masselink's* [1996] method deploying Fourier analysis to calculate wave energy density spectra from observed water depth fluctuations for each burst (see Appendix B). From these energy density spectra, we derived the significant wave height H_s [m], root-mean-square wave height H_{rms} [m], mean wave period T_m [s] and total wave energy E_{tot} [J/m^2] for every burst of wave data. Subsequently, data bursts were selected for time spans during which the entire transect was flooded. This selection was due to assimilate coherent datasets of wave characteristics at the subsequent monitoring positions along each transect, obtained simultaneously and for similar conditions (e.g. incoming wave height).

4.4   RESULTS

4.4.1   VEGETATION DENSITY

High-resolution vegetation data (see Appendix C) were transformed into vegetation cover rates, expressing the relative vegetation coverage of the horizontal surface at a certain elevation (in per milles (‰), Figure 4.4A). This vegetation coverage varied for each of the vegetation plots. In general, the vegetation coverage dropped suddenly above the pneumatophore layer in the forest fringe (the *Avicennia* zones), while vegetation coverage in the back forest (the *Rhizophora* zone) showed a more gradual decrease with increasing elevation.
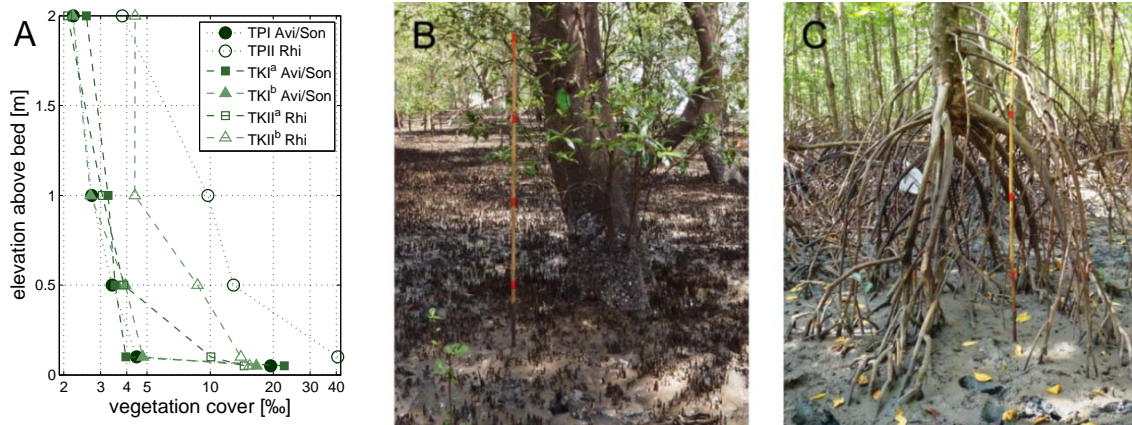
Figure 4.4 – Variation of the vegetation cover with elevation above the forest floor. (A) Horizontal vegetation coverage [‰] significantly reduces with increasing elevation above the forest floor; note the logarithmic horizontal axis. (B) Characteristic vegetation in the *Avicennia/Sonneratia* zone (TKI[b]). (C) Characteristic vegetation in the *Rhizophora* zone (TKII[b]). The red tapes on the bamboo in (B) and (C) are 0.50 m apart and start at 0.50 m above the bed.

At 5 cm above the bed (i.e. the mean height of the pneumatophores), vegetation coverage in the *Avicennia* plots was quite high (17-23‰, Figure 4.4A) due to the dense cover of pneumatophores varying from 300 up to 2200 pneumatophores/m^2 (Appendix C). Above this dense layer of pneumatophores, vegetation coverage suddenly decreased to less than 5‰, since at these levels vegetation mainly consisted of a few tree stems (Figure 4.4B). For the *Rhizophora* plots, the near bed vegetation density was of the same order, although the coverage showed greater variability (15-41‰). The decrease of vegetation coverage with increasing elevation was much more gradual in this zone than in the forest fringe due to the characteristic architecture of these trees. The stilt roots of the *Rhizophora* trees branched off into a dense network of roots (up to 460 roots for a single large tree) with a typical diameter of only a few centimetres close to the bed (Figure 4.4C, Appendix C).

The horizontal vegetation coverage was integrated over the water depth to obtain the volumetric vegetation density (expressed as volume-‰). For the Palian transect, vegetation densities in the forest fringe were significantly smaller than in the back of the forest with volumetric densities of 4.3‰ and 20‰, respectively, for a water depth of 1 m. For the Kantang transect, for a water depth of 1 m, volumetric vegetation densities within both plots in the *Avicennia* zone were 4.5‰, while the density was 5.8‰ and 9.3‰ for the front and back plots within the *Rhizophora* zone, respectively. The increase in vegetation density along the Kantang transect was much less pronounced and did not correlate as much to the predominant vegetation type as along the Palian transect, due to the sparser *Rhizophora* cover at the Kantang transect.

4.4.2 WAVE CLIMATE

Averaged wave energy density spectra at the monitored cross-shore positions are plotted in Figure 4.5 for each deployment (periods with spectra for less than six positions are due to malfunctioning sensors). Presented wave data cover a wide range of tidal conditions (Figure

4.5I), nevertheless neap tides are poorly represented in the data as water levels remained too low to flood the entire transects. Data of the last deployment at Kantang and the middle deployment at Palian were separated in a high-energy period (Figure 4.5D and F, respectively) and a period with moderate wave conditions (Figure 4.5C and G, respectively). The obtained spectra highlight some distinct differences in the wave climates faced at both transects and during the different periods.

In general, the observed wave energy was low during the first three periods of data collection (Figure 4.5A,E,G) , except for a few days early December (Figure 4.5F) when wind directions turned onshore (southwest) instead of the usual offshore (northeast) wind direction for this time of the year [*Thai Meteorological Department*, 2012]. These periods coincided with the northeast monsoon period, lasting until February. Wave energy tended to increase during the subsequent deployments (Figure 4.5B,C,D,H), upon the arrival of the southwest monsoon, starting in May. The most energetic conditions were observed in the March/April deployment at the Kantang transect (Figure 4.5D), when the area was hit by severe storms.

The wave spectra for the Kantang transect were mostly uni-modal with wave periods mainly varying between either 6-11 s for the January/February deployment (Figure 4.5A) and 11-19 s for the data collected in March and April (Figure 4.5B-D). The wave spectra for the Palian transect, on the other hand, were less consistent. The spectra for the December and April/May deployments along this transect were bi-modal, with peaks at periods between 3-5 s and 6-11 s for the former deployment (Figure 4.5F) and at periods between 6-10 s and 11-19 s for the latter deployment (Figure 4.5H). The Kantang transect was typically exposed to (longer) swell waves (10-20 s) during the deployments in March and April, while the wave climate at the Palian transect was mostly dominated by shorter sea waves. Although, at Palian the contribution of swell waves also increased at the onset of the southwest monsoon.

Maximum energy densities along the Kantang transect were up to twice as high as the maxima along the Palian transect, indicating that the Kantang transect was exposed to higher waves. Together with the different modalities of the spectra, these characteristics were induced by the orientation of the transects. The Kantang transect was directly exposed to swell waves from the Andaman Sea and hence incident waves were at the lower end of the frequency spectrum for wind waves. The Palian transect, on the other hand, was oriented towards an estuary with a short fetch, limiting the period and height of the incident waves.

Energy density levels in the subsequent sensors along the transects generally decreased for frequencies >0.1 Hz during all deployments. It even appears that some energy was transferred from relatively short waves (>0.1 Hz) to waves longer than 10 s during the March measurements at the Kantang transect (Figure 4.5B) and during the April/May measurements at the Palian transect (Figure 4.5H): energy densities in the 0.05-0.1 Hz frequency range were slightly increasing towards the back of the forest, while energy densities at larger frequencies were decreasing towards the back of the forest.
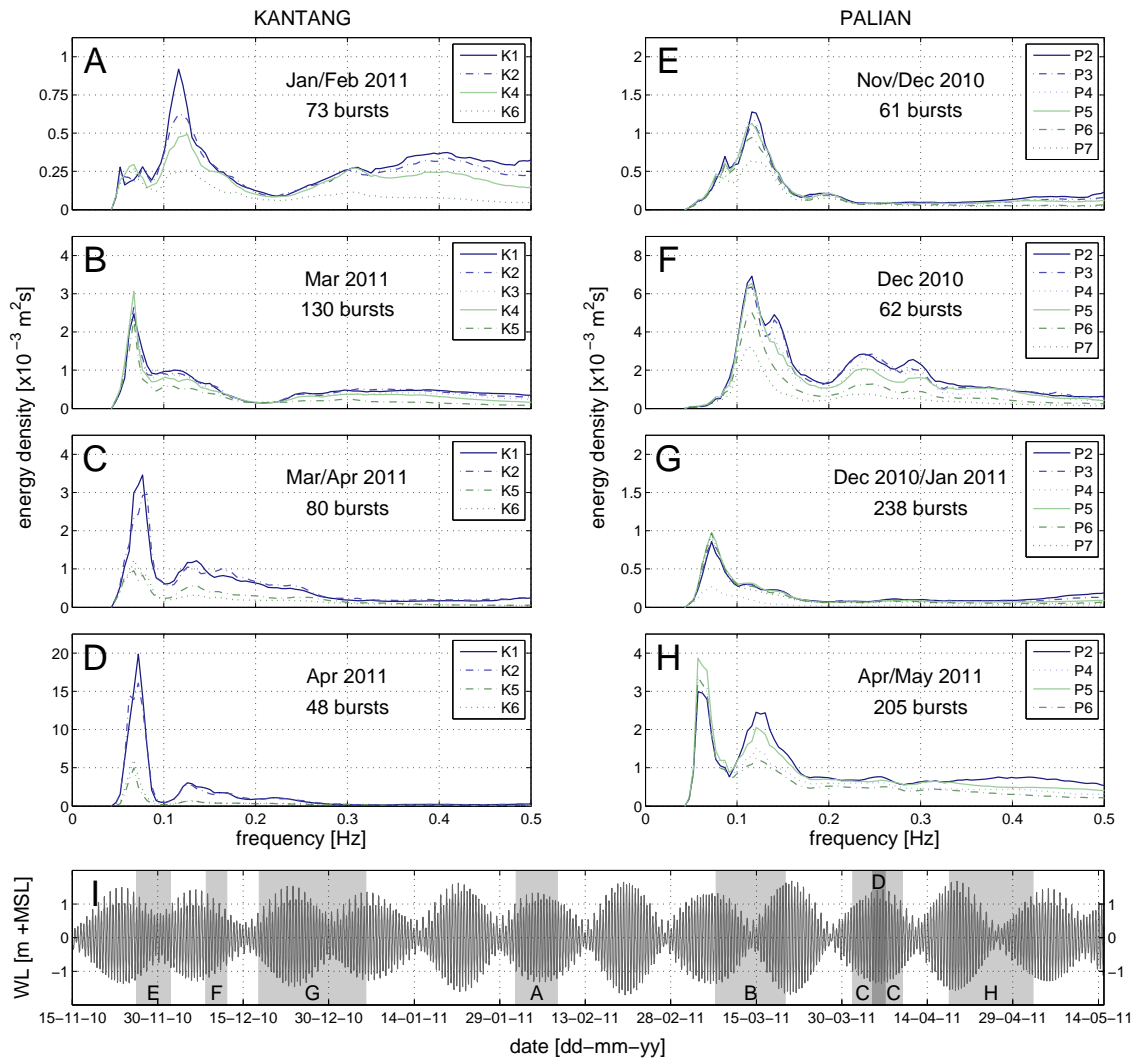
Figure 4.5 – Averaged wave energy density spectra of simultaneously obtained wave data during full inundation of the cross-shore transects (A-D) at Kantang and (E-H) at Palian, each for four different periods. (I) Tidal conditions during the field campaign. The shaded areas in panel I represent the data collection periods of the spectra in panels A-H. Sensor positions (K1-K6 and P2-P7) refer to the numbering in Figure 4.2.

4.4.3 CROSS-SHORE CHANGES IN WAVE PROPERTIES

Changes of the wave characteristics along the transects were obtained from the wave energy density spectra for each data series as differentiated before (Figure 4.6). Typical incident waves at both transects (at T1 and P2) did not exceed 15 cm in height. No significant correlation was obtained between the water depths and the wave heights at T1 and P2 (Pearson's $R = 0.05$ ($p = 0.36$) and $R = 0.01$ ($p = 0.77$), respectively), hence depth-limitations were insignificant to the incident shallow waves.

Between the first and last sensors (K1-K6), mean significant wave heights gradually decreased from 5.5-10.6 cm to 2.9-5.8 cm at the Kantang transect (-42 to -47%; Figure 4.6A). During the March deployment, wave height decreased from 6.7 to 4.6 cm (-31%) between K1 and K5 only.

117

The increasing wave heights in the subsequent deployments coincide with the increase of the wave energy density spectra for the respective data series (Figure 4.5A,B,C,D). Mean significant wave heights along the Palian transect decreased from 4.4-11.3 cm to 3.0-6.5 cm between the first and last sensors (-30 to -43%; Figure 4.6I). A lower reduction, from 8.4 to 6.6 cm (-22%), was obtained between P2 and P6 during the last data series.

While the significant wave heights decreased along both transects, mean wave periods were slightly increasing towards the back of the forest. Mean wave periods changed from 2.9-6.4 s to 4.1-5.7 s and from 2.8-4.1 s to 4.8-5.0 s along the Kantang and Palian transects, respectively (Figure 4.6B,J). Shorter waves (i.e. frequencies >0.1 Hz) lost more energy when propagating into the forest than the longer waves (<0.1 Hz), as was observed from the wave energy density spectra (Figure 4.5). Hence, shorter waves got attenuated more effectively when propagating into the forest, as opposed to the longer-period swell waves that hardly got attenuated, increasing the mean wave periods.

Due to the quadratic relation between wave height and wave energy, total wave energy decreased more pronouncedly along the transects than the wave heights. Along the Kantang transect 68-74% of the total incident energy (2.0-7.2 J/m^2) was dissipated over the 246 m stretch between the first and last sensor (Figure 4.6C). During the March deployment, 53% of the incident energy (2.9 J/m^2) was attenuated between K1 and K5 (196 m apart). At Palian, 52-71% of the mean incident total wave energy (1.3-9.4 J/m^2) was attenuated between the first and last sensor, which were only 98 m apart (Figure 4.6K). During the final data collection period, 41% of the incident energy (5.0 J/m^2) was attenuated between P2 and P6 (only 75 m apart).

The attenuation of wave energy was merely caused by drag and friction forces induced by the mangrove vegetation and bed roughness. Observed wave heights were ranging up to about 15% of the simultaneously measured water depths (Figure 4.6D,L). Wave breaking occurs for wave heights exceeding 60-83% of the water depth [*Battjes and Stive*, 1985]. Hence, wave breaking could not have contributed significantly to the wave energy losses along the transects.

When severe storms hit the Kantang transect, only three wave sensors collected proper data. Wave data for March 27 and 28 (2011) are plotted in Figure 4.7, without selecting those bursts for which all three sensors were inundated. Significant wave heights exceeded 30 cm during the most extreme conditions. Mean significant wave heights decreased from 15.3 to 6.5 cm (-58%) between K2 and K4 (Figure 4.7A), which were 102 m apart and only had the sparse vegetation fringe in between. Consequently, 81% of the incident wave energy (15.4 J/m^2) was attenuated between these two stations (Figure 4.7C). As wave heights ranged up to 40% of the water depth (Figure 4.7D), wave breaking was observed (this was visually observed in the field), but still to a limited extent. Hence, even during storm conditions, the vegetation and bottom induced drag and friction forces were the major drivers for wave attenuation.
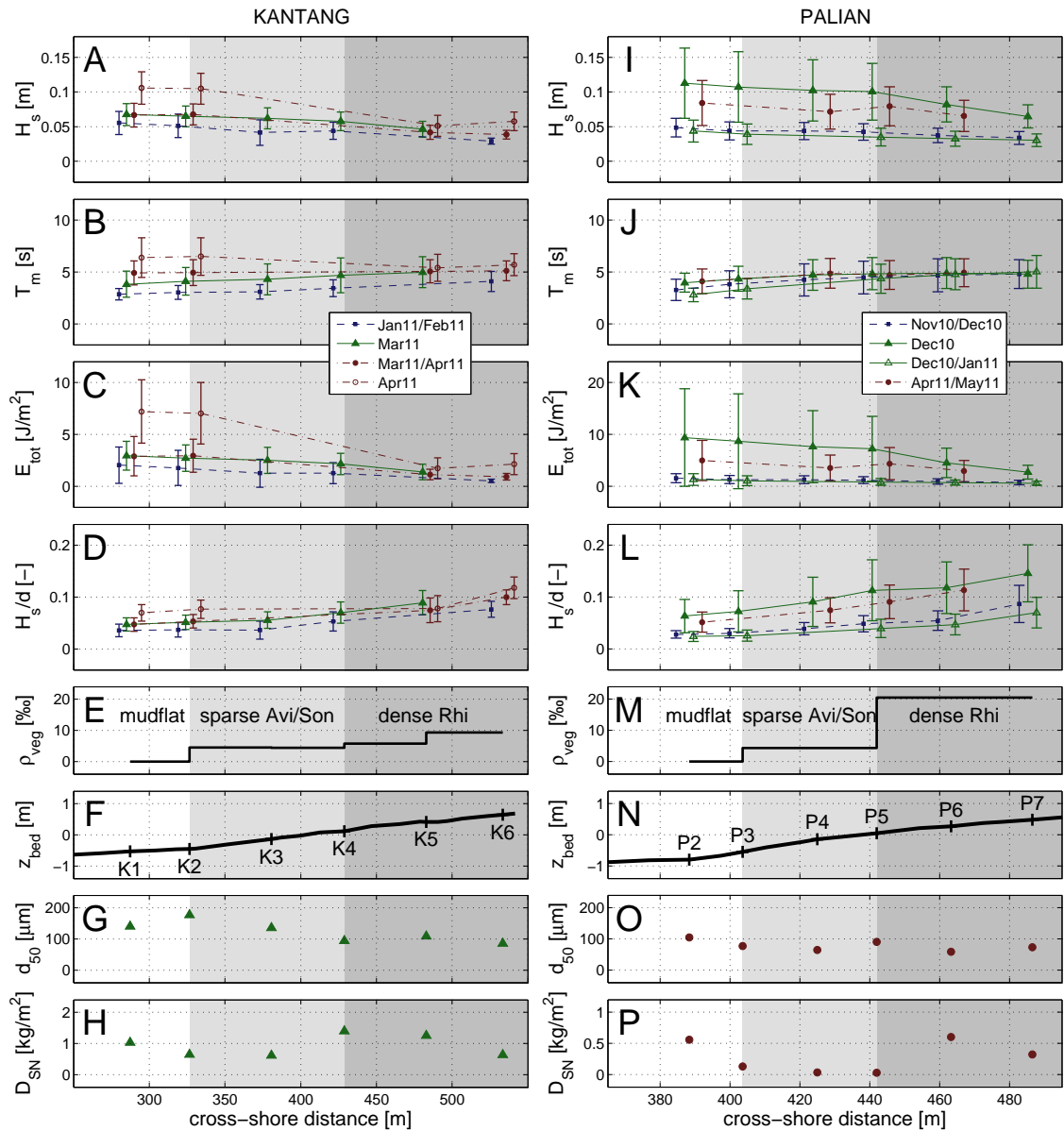
Figure 4.6 – Biogeophysical conditions along the transects: (A,I) significant wave heights H_s [m]; (B,J) mean wave periods T_m [s]; (C,K) total wave energy E_{tot} [J/m^2]; (D,L) wave heights divided by water depths H_s/d [-]; (E,M) vegetation densities ρ_{veg} within 1 m above the forest floor [volume-‰]; (F,N) elevation z_{bed} [m +MSL]; (G,O) mean grain size of the top soil layer d_{50} [µm]; and (H,P) net sediment deposition during a full spring-neap tidal cycle D_{SN} [kg/m^2], each for the Kantang and Palian transect, respectively. Plots of the wave characteristics present mean observed values, with error bars indicating the standard deviation. Data comprise four different periods for each transect. Note that horizontal offsets in the upper panels are just for visibility, monitoring positions were equal for all periods.

Within the first data series for the Kantang transect, average significant wave heights increase by 6% between K3 and K4 (Figure 4.6A). Similarly, within the last data series for the Palian transect, an 11% increase of the average significant wave height is observed between P4 and P5 (Figure 4.6I). These observations coincide with the sudden increase of the vegetation density just behind K4 and P5 (Figure 4.6E,M), possibly causing wave reflection at the edge of the dense *Rhizophora* vegetation [cf. *Massel et al.*, 1999; *Méndez et al.*, 1999]. During storm

conditions (Figure 4.7), this same phenomenon is even observed in front of the sparse vegetation of the *Avicennia* zone at the Kantang transect, when the wave height shows a local increase of about 8%.
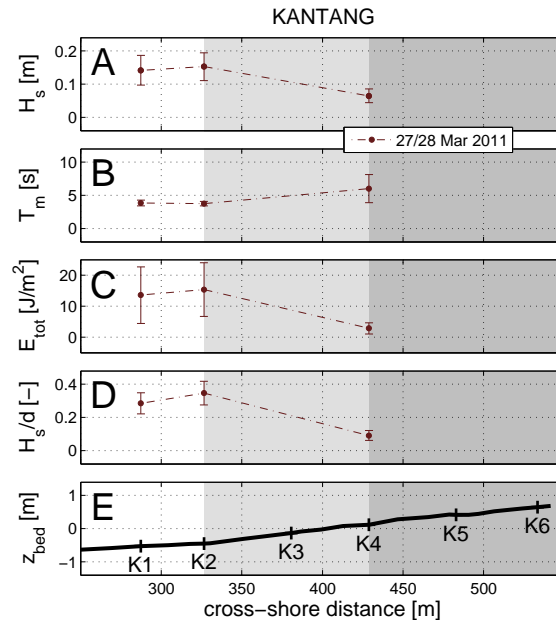
Figure 4.7 – Wave characteristics along the Kantang transect (same as Figure 4.6) for a two-day storm period.

4.4.4 SEDIMENT CHARACTERISTICS AND CROSS-SHORE DEPOSITION PATTERNS

The bed material at both transects consists of a sandy mud, containing on average 34(±7)% (±standard deviation) and 45(±6)% silts (<63 μm) at the Kantang and Palian transect, respectively. The soils contained 10(±1)% and 10(±3)% organic material at the respective transects. At the Kantang transect, mean grain sizes (d_{50}) gradually decreased towards the back of the forest, from 177 to 86 μm (Figure 4.6G). At the Palian transect, fining of the sediments towards the back of the forest (105-58 μm) was interrupted at P5, where grain sizes were somewhat greater (90 μm) than those at the two seaward and landward monitoring positions (Figure 4.6O). This local coarsening was in concordance with the slight increase in hydrodynamic activity observed around P5 (Figure 4.6K). Sediment grain sizes of soil samples of the top layer of the forest floor were generally coarser at positions with increased hydrodynamic activity (Figure 4.8; Pearson's $R = 0.67$ ($p = 0.018$) for the correlation indicated by the fitted trend).

Sediment deposition was correlated with the significant wave heights observed for the duration of the trapping experiments. For this comparison, we did not filter the wave data for concurrent observations along the entire transects. Deposition starts at the onset of flooding of any of the monitoring locations, so all wave dynamics (all bursts) at any location were included. Deposition rates observed during spring tide, for one tidal inundation at Kantang (0.05-0.26 kg/m^2) and for two tidal inundations at Palian (0.10-0.35 kg/m^2), poorly correlated with the

observed significant wave heights (Figure 4.9A). Notably, variations in the observed wave heights were really small these days.

Maximum deposition rates during a full spring-neap tidal cycle (~14 days) were only up to 5 times greater than those obtained during a single spring tide, with deposition rates of 0.61-1.4 kg/m^2 and 0.03-0.60 kg/m^2 at Kantang and Palian, respectively (Figure 4.6H,P). Overall, spring-neap tidal deposition rates rapidly reduced with a minor increase in mean observed significant wave heights (Figure 4.9B; $R = -0.84$ ($p < 0.01$) for the correlation indicated by the fitted trend). Along both transects, deposition rates decreased from the mudflat into the sparsely vegetated forest front (Figure 4.6H,P). Subsequently, in the dense vegetation of the *Rhizophora* zones deposition rates increased, but again decreased towards the back of the forest (Figure 4.6H,P).
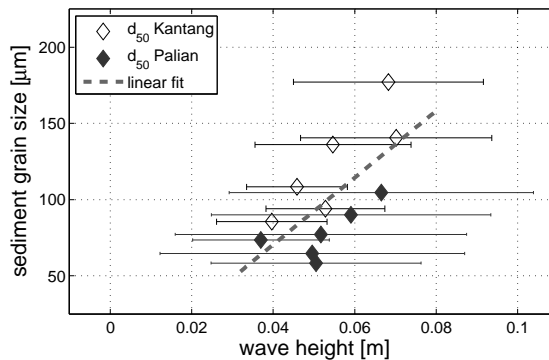
Figure 4.8 – Mean sediment grain sizes d_{50} [μm] along the transects versus the observed significant wave heights H_s [m]. Plotted error bars indicate means ± standard deviations of the observed wave heights during all three deployment periods at each transect.
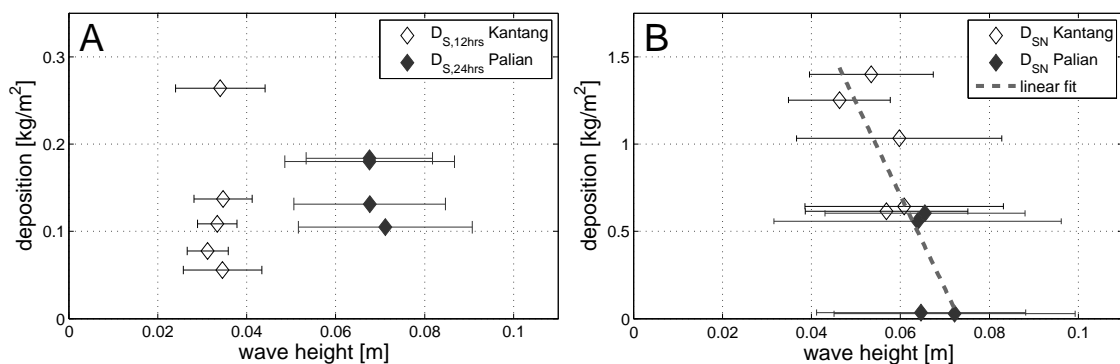
Figure 4.9 – Sediment deposition rates [kg/m^2] observed (A) during one/two spring tidal cycles (12/24 hrs) at Kantang and Palian, respectively, and (B) during a full biweekly spring-neap tidal cycle, also at Kantang and Palian. Plotted error bars indicate means ± standard deviations of the significant wave heights H_s [m] during the respective sediment trapping periods (all bursts included).

4.4.5   LINKING WAVE ATTENUATION TO VEGETATION DENSITIES

Together with the decrease of wave height and energy along both transects, deviations around the mean observed values also decreased into the forest (Figure 4.6A,C,I,K). Higher-than-average wave heights and energies were reduced more effectively, while lower wave heights and energies were attenuated less effectively than the mean observed values. Hence, the attenuating capacity of mangroves did not only depend on the vegetation induced drag and friction forces and the bed friction, but also on the wave conditions: with increasing wave heights and greater incident wave energies, the attenuation increased as well. This trend was corroborated by the increased wave attenuation during storm conditions (Figure 4.7A,C) with respect to regular conditions (Figure 4.6A,C) along the Kantang transect.

For both transects, wave attenuation analyses comprised data collected during the first two deployments, spanning the first two data series for Kantang (Figure 4.5A-B) and the first three data series for Palian (Figure 4.5E-G). These series contained data for most monitoring positions along both transects. Wave height losses were studied over the distinct vegetation zones at each transect: mudflat, sparsely vegetated forest front, densely vegetated back forest. Per data burst, the decrease of the wave height for each zone ($\Delta H = H_{x1} - H_{x2}$ [m]) was standardized to the wave height loss per unit distance ($\Delta H/\Delta x$ [-]) by dividing with the distance between the front most monitoring position (x_1) and the last position (x_2) within any vegetation zone ($\Delta x = x_2 - x_1$ [m]). This standardized wave attenuation correlated well with the incident wave height at the first sensor in any of the zones (H_{x1}; Figure 4.10).

Standardized wave attenuation correlated rather poorly with the incident wave heights at the mudflats with correlation coefficients (R) of 0.21 and 0.17 ($p<0.01$) for the Kantang and Palian transect, respectively (Figure 4.10A,D). Within the mangroves, this correlation strongly improved for increasing vegetation densities: correlation coefficients were 0.52 and 0.58 ($p<<0.001$) in the *Avicennia* zones at Kantang and Palian, respectively (Figure 4.10B,E), while they further increased to 0.66 and 0.91 ($p<<0.001$) for the *Rhizophora* zones of the respective transects (Figure 4.10C,F).

According to previous work, the rate of wave attenuation per unit length in the direction of wave propagation is defined by [*Mazda et al.*, 2006]:

$$r = \frac{\Delta H}{H} \frac{1}{\Delta x} \tag{4.1}$$

Wherein r [m^{-1}] is the wave attenuation rate and H represents the wave height at the sea side monitoring position (H_{x1}). Equation (4.1) was rewritten into a the derivative representing the linear increase of the wave attenuation for increasing incident wave heights:

$$r = \frac{d(\Delta H / \Delta x)}{dH} \tag{4.2}$$
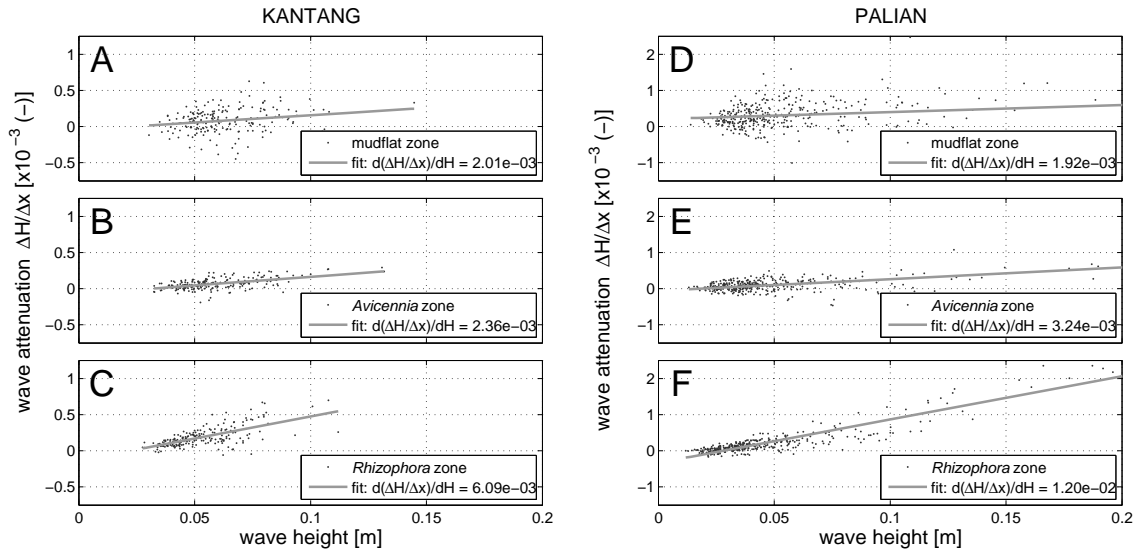
Figure 4.10 – Correlation between the incident significant wave height H_s [m] and the wave attenuation, expressed as wave height loss per unit distance $\Delta H/\Delta x$ [-]. Results comprise the respective vegetation zones: (A,D) mudflats, (B,E) sparsely vegetated *Avicennia*/*Sonneratia* zones at the forest front and (C,F) denser vegetated *Rhizophora* zones further inland, for the Kantang and Palian transects, respectively.

From the results in Figure 4.10, generalized wave attenuation rates were obtained for all vegetation zones, each covering a range of incident wave heights and water depths. These rates increased for the greater vegetation densities towards the back of both transects (Table 4.2). Consequently, the wave attenuation rates correlated significantly ($R = 0.98$ ($p<0.001$); Figure 4.11) with the volumetric vegetation densities within 1 m above the forest floor (Figure 4.6E,M). The best fit of the wave attenuation rate with respect to the vegetation density (ρ_{veg}) in volume-‰ resulted in the following expression:

$$r = 5.1 \cdot 10^{-4} \cdot \rho_{veg} + 1.5 \cdot 10^{-3} \qquad (4.3)$$

This expression quantifies the incline of the attenuating capacity of mangrove vegetation with increasing vegetation densities. Roughly, the generalized attenuation rate increased by about 0.005 m^{-1} with a 10‰ increase of the volumetric vegetation density within 1 m above the forest floor. Nevertheless, even on the mud flats, where no vegetation was present, waves were attenuated and the wave attenuation rate was positive, represented by the offset of equation (4.3).

Table 4.2 – Obtained wave attenuation rates r and calculated shoaling coefficients K_s, both per unit distance.

	KANTANG		PALIAN	
	r [m^{-1}]	$1-K_s$ [m^{-1}]	r [m^{-1}]	$1-K_s$ [m^{-1}]
mudflat zones	$2.0 \cdot 10^{-3}$	$1.0 \cdot 10^{-4}$	$1.9 \cdot 10^{-3}$	$2.7 \cdot 10^{-3}$
***Avicennia* zones**	$2.4 \cdot 10^{-3}$	$-4.9 \cdot 10^{-4}$	$3.2 \cdot 10^{-3}$	$-9.9 \cdot 10^{-4}$
***Rhizophora* zones**	$6.1 \cdot 10^{-3}$	$-1.6 \cdot 10^{-3}$	$1.2 \cdot 10^{-2}$	$-3.1 \cdot 10^{-3}$
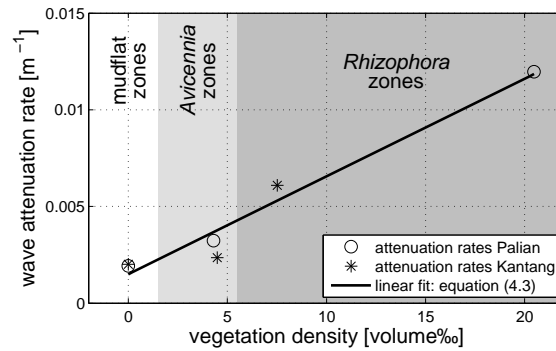
Figure 4.11 – Wave attenuation rates r [m^{-1}] for the subsequent vegetation zones at each transect correlate significantly with the volumetric vegetation density within 1 m above the forest floor ρ_{veg} [volume-‰] of each zone.

Alternatively, wave height attenuation was calculated for each individual data burst directly from equation (4.1). Concurrent volumetric vegetation volumes within the water column were obtained for every single burst by integrating the relative volume of vegetation elements below the average water level between any pair of monitoring positions. Consequently, a much greater range of vegetation densities was obtained than those plotted in Figure 4.11, as the volumetric vegetation densities varied with the water depth (cf. Figure 4.4A). Accordingly, a range of wave attenuation rates was obtained from the individual data bursts (cf. Figure 4.6A,I). Data were binned in vegetation density intervals of 1‰ and the mean wave attenuation (and standard deviation) was computed for every bin (Figure 4.12).

The single-burst trends of the wave attenuation with respect to the submerged vegetation densities (Figure 4.12), obviously, were similar to the trends of the generic wave attenatuion rates obtained per vegetation zone (Figure 4.11). Additionally, these data indicated how the wave attenuation within each vegetation zone changes with variable water depths and the consequent changes of the relative volume of submerged vegetation. At the Kantang transect, r ranged from about 0.001 m^{-1} in the *Avicennia* zone, to values increasing from 0.002 to 0.005 m^{-1} in the *Rhizophora* zone (Figure 4.12A). Variations in the vegetation density within the *Avicennia* zone were rather small, hence no real variation in the wave reduction was obtained. At the Palian transect, within the *Avicennia* zone again no real variation in the wave attenuation (r = 0.002 m^{-1}) was obtained. However, variability of the vegetation densities in the dense *Rhizophora* zone was substantial and wave attenuation increased from 0.001 to 0.007 m^{-1} for an increase of the vegetation density from 19 to 32‰.

Due to the decrease of vegetation densties at increasing elevations (Figure 4.4), higher water depths induced decreasing vegetation densities and, consequently, reduced wave attenuation rates (Figure 4.13). Due to the limited vertical variability of the vegetation structure in the *Avicennia* zones once the pneumatophores were flooded (Figure 4.4A), wave attenuation rates were rather indipendent of the water depth (r = 0.001-0.002 m^{-1}; Figure 4.13A,B). The slight increase of wave attenuation rates in these zones could have been caused by submergence of the lower canopies with the highest tides. Conversely, the gradual decrease of the number of roots

with increasing elevations in the *Rhizophora* zones caused the wave attenuation to drop progressively for increasing water depths (r = 0.006 to 0.001-0.002 m^{-1}; Figure 4.13A,B).
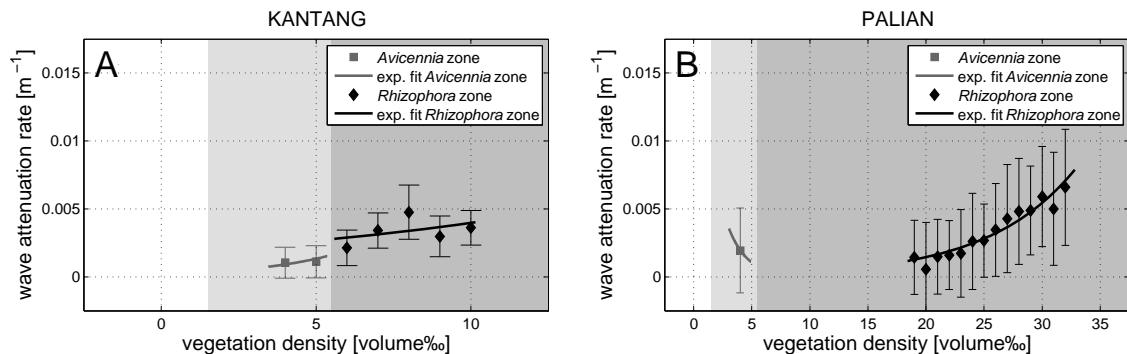
Figure 4.12 – Wave attenuation rates r [m^{-1}] tend to increase with the relative volume of submerged vegetation ρ_{veg} [volume-‰] at both the (A) Kantang and (B) Palian transect. (Error bars indicate mean ± the standard deviation.)
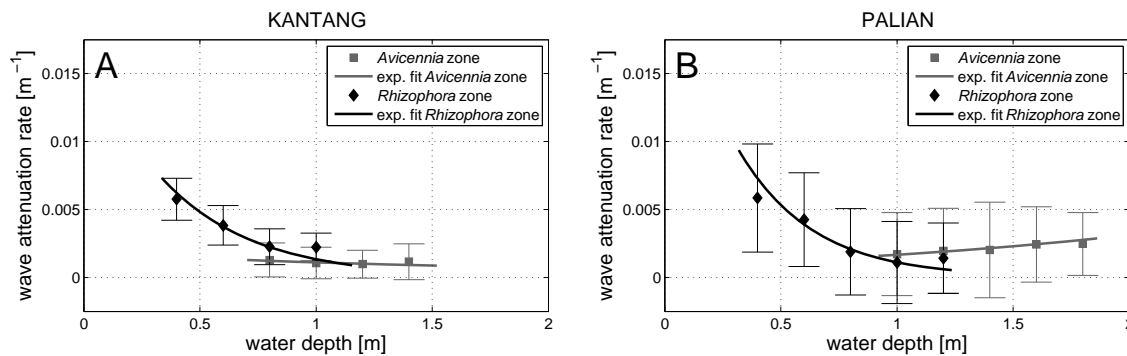
Figure 4.13 – Wave attenuation rates r [m^{-1}] correlate with the concurrent water depths [m] at the (A) Kantang and (B) Palian transect. (Error bars indicate mean ± the standard deviation.)

4.5   DISCUSSION

Brinkman [2006] observed reductions of total wave energy at three different mangrove sites (Cocoa, Oonoonba, Iriomote) of 64%, 95% and 71% along transects of respectively 260 m, 40 m and 40 m in length. Along with these findings, significant wave heights were found to decrease by 50%, 75% and 54% along the respective transects (Table 4.1). The latter two reduction rates of both wave energy and height are quite high compared to the energy reduction (41-74%; Figure 4.6C,K) and wave height attenuation (22-47%; Figure 4.6A,I) obtained in the present work. Nevertheless, obtained wave attenuation rates (r = 0.002-0.012 m^{-1}; Figure 4.11) compare well with previous observations by e.g. *Mazda et al.* [2006] for a transect along the Vinh Quang coast, Vietnam: 0.001-0.004 m^{-1}; and *Quartel et al.* [2007] at their Red River site: 0.004-0.012 m^{-1} (Table 4.1).

At the same time, *Quartel et al.* [2007] obtained increasing wave attenuation rates for increasing water depths within the mangroves, while *Mazda et al.* [1997a] found the wave attenuation to be rather constant with variable water depths. These findings are in contrast with the significant

decrease of the wave attenuation with increasing water depth observed in the present study, in particular in the dense *Rhizophora* vegetation (Figure 4.13). This contrasting behaviour is instigated by the limited height of the dwarfed trees in the field sites of the former studies, while vegetation in the present study was highly developed with trees up to about 20 m high.

The variability in previously and currently obtained wave attenuation data underlines the susceptibility of mangroves' attenuating capacity to variations in both hydrodynamic conditions (incident wave energy, water depth) and vegetation characteristics. Consequently, detailed information on both hydrodynamic conditions and vegetation characteristics is imperative for a mechanistic understanding of the vegetation induced wave attenuation in mangroves. Rough vegetation parameters, such as the number of trees, tree height and leaf cover [e.g. *Quartel et al.*, 2007; *Bao*, 2011] are inadequate for developing explicit relations for the wave attenuation in mangroves of arbitrary constituency (in terms of species composition and tree structure) under variable hydrodynamic conditions. Instead, the volume of submerged vegetation, as adopted in the present study, is a comprehensive characterization of the vegetation structure [*Mazda et al.*, 1997b], facilitating the development of such generic relations (sensu equation (4.3)).

Wave data presented in this chapter were collected with robust, autonomous pressure gauges. Comparison of the water depths obtained simultaneously with high-frequency wave sensors (MacroWave) and low-frequency pressure loggers (Sensus Ultra) rendered perfect near-unity correlations. This finding confirms the accuracy of the data retrieved with the wave sensors for the water depths observed in the field. The resolution of the wave sensors was ~0.7 cm (0.01 psi), limiting the detection of waves of a few centimetres in height (<1-3 cm; Figure 4.10). The few negative wave attenuation values in Figure 4.10 could be due to the limited resolution of the equipment. However, no proof was found for structural errors in the obtained wave data and these negative attenuation values could also be induced by local wind effects (mainly in front of the forest) or wave reflection at steep gradients in the vegetation density.

Sudden cross-shore changes in the vegetation density might have induced locally increasing wave heights due to wave reflection [*Massel et al.*, 1999; *Méndez et al.*, 1999]. This was noted in some of the data collected at the transition from the sparsely vegetated *Avicennia* zone to the much denser *Rhizophora* vegetation at both transects (Figure 4.6A,I), further corroborating the need for detailed mapping of (spatial changes of) vegetation characteristics. The observed wave reflection (6-11%) is similar to the 0.07 reflection coefficient computed by *Massel et al.* [1999] for an artificial mangrove fringe. For increased wave heights and periods during a storm, wave heights even showed a minor increase (8%) at the relatively sparse vegetation fringe of the *Avicennia* zone at the Kantang transect (Figure 4.7). Hence, along with the increasing attenuating capacity of mangrove vegetation (Figure 4.10), wave reflection might increase for higher incident waves. The latter is similar to the enhanced reflection of higher waves at submerged permeable structures [*Ting et al.*, 2004].

In addition to the attenuation and reflection of waves, wave shoaling is an important phenomenon in shallow coastal waters [*Van Rijn*, 2008]. Based on the observed water depths and wave characteristics, computed shoaling coefficients range between 1.00049 and 1.0031 per unit distance. When subtracting the shoaling coefficient from unit value, the rate of change of the wave height due to shoaling is obtained, allowing easy comparison with the measured wave reduction rates (Table 4.2). The resulting negative shoaling rates identify an increasing wave height within each of the vegetated zones. Shoaling rates are greater for the steeper slopes of the Palian transect (Figure 4.2). The computed increase of the wave heights due to shoaling is about 20-30% of the measured wave reduction within the mangrove vegetation (Table 4.2). Consequently, gross attenuation of wave heights by the mangrove vegetation is expected to be 20-30% greater than the presented wave attenuation rates (e.g. Figure 4.11).

This chapter focusses on the net contribution of mangrove ecosystems to wave attenuation. The mangrove ecosystem includes the characteristic slopes, causing an increase of the wave heights due to shoaling, and the typical bed composition that causes wave reduction through the bed roughness. Quantifying the exact contribution of vegetation, shoaling and bottom friction to the observed attenuation rates is difficult since the different processes and their effects on e.g. the wave period and wave energy flux cannot be isolated from the field data. In addition, one should take into account the effects of viscous friction and percolation [*Möller et al.*, 1999]. The present study unifies all these effects in a net wave attenuation rate, similar to previous studies that presented bulk friction factors representing all or most wave modulating processes [*Quartel et al.*, 2007; *Paul and Amos*, 2011].

Structural complexity and density of the mangroves was observed to increase towards the back of both transects, dwelled by *Rhizophora* species. The densest vegetation was observed at the least exposed Palian transect. Greater hydrodynamic stresses limited the vegetation density at the Kantang transect, as the structure and composition of mangroves are closely linked to and limited by the geophysical settings of their habitat [e.g. *Thom*, 1967; *Woodroffe*, 1992]. In general, ecosystems with the greatest wave-attenuating capacity are difficult to obtain in (relatively) high energy environments [*Bouma et al.*, in press]. Nevertheless, hydrodynamic conditions are ameliorated by the mangroves and denser vegetation structures are facilitated with increasing distances from the forest fringe, as observed at the landward extents of both transects (where mangroves extended several hundreds of meters further inland). This constraint emphasizes the beneficial effects of wider mangrove ecosystems in terms of coastal protection.

Observed sediment characteristics and bi-weekly deposition rates were also found to correlate negatively with the wave exposure of the mangrove sites (Figure 4.8, Figure 4.9). Amelioration of the wave energy by mangroves facilitates the trapping of sediments [*Van Santen et al.*, 2007; *Winterwerp et al.*, 2013]. Cross-shore increases in vegetation density, giving rise to increased wave attenuation, facilitate the progressive deposition and trapping of finer materials. This was confirmed by the gradual decrease of the mean grain size of the bed material along the studied transects (Figure 4.6G,O). Consequently, in the shelter of the dense *Rhizophora* trees, allowing

for the deposition of finer sediment fractions, deposition suddenly increased (Figure 4.6H,P). However, further into the forest, deposition reduced again due to the limited supply of suspended sediments. Additionally, local increases of the wave energy, for instance due to wave reflection, reduced deposition rates while a coarsening of the bed material was observed (Figure 4.6O,P).

The results of this study address the (significant) contribution of coastal mangroves to wave attenuation and sediment trapping. Although the observed substantial wave attenuation at the bare mudflats as well, probably due to fluid mud effects [e.g. *Elgar and Raubenheimer*, 2008], we emphasize that mangroves are important stabilizers of these extensive mudflats: mangroves enhance sediment trapping and consolidation while reducing erosion [*Anthony and Gratiot*, 2012; *Winterwerp et al.*, 2013]. To further study the bio-physical interactions in mangroves that induce their attenuating capacity, mechanistic modelling studies are required that explicitly take account of peculiar vegetation characteristics such as the numbers and diameters of roots, stems and branches and their vertical variation. Such models would be (easily) transferrable to other study sites, provided basic information on both the vegetation and the hydrodynamics (and the bathymetry) is known.

4.6   CONCLUSIONS

This chapter presented field data concerning wave attenuation and sediment dynamics along two cross-shore transects in coastal mangroves in Southern Thailand. Collection of wave data in combination with detailed vegetation measurements, was unprecedented and is of great importance to the further development of knowledge on the attenuation of waves in mangrove vegetation.

The detailed characterization of the vegetation cover at the field sites emphasizes the variability of mangrove vegetation structure in both the vertical and the horizontal direction. Vegetation densities are strongly dependent of the dominant vegetation type as *Rhizophora* stilt root systems are much more extended than the pneumatophores of *Avicennia* and *Sonneratia* species. Volumetric vegetation densities within one meter above the forest floor were found to be 4.3-4.5‰ in the *Avicennia* zones along both transects. Vegetation densities in the *Rhizophora* zones were (much) higher: 5.8-9.3‰ at the Kantang transect and 20‰ at the Palian transect, which were even higher (up to 32‰) for water depths <1 m.

Mean observed significant wave heights decreased (on average) by 42-47% along the Kantang transect which was 246 m long, and with 30-43% along the Palian transect which was only 98 m long. Over the same distances, total wave energy (on average) decreased with 68-74% and 52-71% along these transects, respectively. For increased wave heights during storm conditions, we observed a maximum wave energy reduction of 79% over 141 m, while significant wave heights were reduced up to 54%. Wave attenuation was mainly restricted to the short wind

waves (<10 s), since swell waves (10-20 s) tended to remain their energy or even gained energy by the attenuation of the shorter waves.

Wave attenuation was found to correlate significantly with the incident wave height for the different vegetation zones. The generalized wave attenuation rates, obtained by the gradient of the relation between wave height reduction and incident wave height, ranged between 0.002-0.012 m^{-1}. These rates showed a significant positive correlation with the volumetric vegetation density. In addition, single burst attenuation rates showed that decreasing water depths, and consequently increasing volumetric vegetation densities, induced wave attenuation rates to increase substantially from 0.001 to 0.007 m^{-1} in dense *Rhizophora* vegetation. Reduced wave attenuation capacity was observed in sparser *Avicennia*/*Sonneratia* vegetation, in terms of the volumetric vegetation density, where wave attenuation rates were rather independent of the water depth.

Reductions of the wave energy by the mangroves were found to facilitate greater bi-weekly deposition rates along both transects. Reduced hydrodynamic activity towards the, consequently, denser vegetated back of the mangrove forests allowed for the deposition of finer sediments, as confirmed by the gradual fining of the bed material. A local reduction of the deposition rate and increase of the mean grain size was observed at the interface between the sparsely vegetated forest fringe and the dense *Rhizophora* vegetation, where wave reflection supposedly gave rise to a local increase of the wave energy.

The findings of this chapter corroborate the coastal defence function of mangroves and provide a starting point for mechanistic modelling studies into the attenuating capacities of mangroves.

CHAPTER 5

SYNTHESIS

Returning to the boat after another day in the field, yet again a little wiser.

5.1   CONCLUSIONS

The research presented in this thesis aimed to enhance our understanding of the short-term bio-physical interactions in coastal mangroves, in particular with respect to their contribution to coastal stabilization and coastal safety. Five research questions were identified, focussing on: (i) the impact of biogeophysical settings on tidal water flows and sediment deposition patterns in coastal mangroves; (ii) the consequences of changing biogeophysical settings for the flow routing and sediment deposition patterns in coastal mangroves; and (iii) the relation between biogeophysical characteristics and the attenuation of waves in coastal mangroves. Conclusions regarding each of the research questions are recapitulated below.

Q1.   How do tidal-scale hydrodynamics in coastal mangroves vary throughout different field sites with distinct biogeophysical settings, and how do these differences relate to their specific vegetation, topography and hydrodynamic exposure?

By explicitly quantifying and mapping flow routing through three mangrove sites in southern Thailand, Chapter 2 provided observational evidence for flow routing phenomena in coastal mangroves. These flow routing patterns were linked, in a qualitative sense, to three biogeophysical factors: topography, hydrodynamic exposure and vegetation. Particular differences in flow routing were observed between (i) a higher elevated mangrove forest (above mean sea level) that was fronted by a steep cliff and dissected by pronounced ephemeral tidal creeks and (ii) gradually inclining sites with a very small bed slope, where mangrove vegetation started below mean sea level and was fronted by extensive mudflats. Vegetation in the latter sites was clearly zonated, with sparse landmark trees of *Avicennia* and *Sonneratia* species in front and dense, tall *Rhizophora* vegetation at the back, in accordance with tidal inundation regimes. Vegetation at the former site was dense as well, with a mixed composition of trees and shrubs, typical for less exposed mangroves.

Within the higher elevated mangrove forest dissected by tidal creeks, *creek flow* prevailed when water levels remained below the dense vegetation layer at the mangrove fringe bordering the estuary. *Sheet flow* prevailed when this threshold was exceeded and water flows were directed straight into the forest from the estuary (or vice versa). Flow velocities within the creeks were up to an order of magnitude greater ($O(10^{-1})$ m/s) than those within the vegetation ($O(10^{-2})$ m/s), where velocities decreased progressively with increasing vegetation densities. Tidal water flows at the low-lying transects lacked these morphology induced flow routing patterns and sheet flows prevailed throughout the tidal cycle. Flow routing at these transects was much more exposed to and affected by estuarine river discharges, giving rise to longshore subtidal velocity components within the mangroves. With decreasing water depths and/or increasing vegetation densities, the effects of this directional forcing were reduced at the low-lying sites and flow velocities followed the vegetation induced cross-shore water level gradients instead.

The characteristic vegetation structure and particular topography of the creeks were found to cause irregular velocity variations along the vertical, imposing velocity profiles noncompliant

with standard logarithmic flow velocity profiles, within the forest as well as in the creeks. Global tidal flux calculations, taking account of the observed variations of the velocity profiles, demonstrated the significant contribution of creek flow to the total tidal prism of the mangrove site dissected by tidal creeks. In addition, calculated fluxes through the main creek at this site suggested a fortnightly tidal pump with net tidal inflows into the mangroves during the highest tides. This finding was corroborated by decreasing phase lags between high water and maximum tidal flow velocities, that were observed in this creek for increasing high water levels.

Q2. How to simulate tidal-scale hydrodynamics and sediment dynamics in coastal mangroves accurately and efficiently in Delft3D, and to what extent can the bio-physical interactions in coastal mangroves be reproduced accurately by a depth-averaged Delft3D model?

Chapter 3 presented the first attempt to combine spatially explicit observations of tidal-scale flow routing and sediment deposition in coastal mangroves with a high-resolution process-based numerical model. The established three-dimensional Delft3D model combines hydrodynamic and morphodynamic computations and explicitly accounts for vegetation imposed drag forces and turbulence effects. This model was deployed to simulate tidal dynamics in a mangrove site dissected by tidal creeks. After calibration of the three-dimensional model in the bed roughness (hydrodynamics) and in the sediments' settling velocity and critical bed shear stress (morphodynamics), simulated tidal flow routing and sediment dynamics compared well with the observed dynamics in the field.

The three-dimensional model was subsequently reduced to a depth-averaged model, inspired by the dominance of the horizontal heterogeneity of the studied mangrove site, instigated by the contrast of the deep tidal creeks and the densely vegetated platform. The depth-averaged model was calibrated to obtain representative depth-averaged vegetation characteristics and an adjusted critical bed shear stress, compensating for the non-resolved vertical variations in both vegetation and flow velocities. Vegetation properties at 0.5 m above the bed (i.e. one-half to one-third of the maximum tidal inundation depth) provided a good depth-averaged representation of the complex mangrove vegetation. Simulation results of the calibrated depth-averaged model reproduced the results of the three-dimensional model and showed similar agreement with the field data. Computation times of this model were 80-90% shorter than for the three-dimensional model. Hence, the depth-averaged model was an efficient yet accurate tool for simulating tidal-scale flow routing and sediment dynamics in these mangroves.

Q3. According to field observations and numerical simulations, what is the relative contribution of vegetation and topography to the tidal flow routing and to sediment deposition patterns in coastal mangroves?

Spatial explicit observations from the field and simulations with the validated depth-averaged model were combined to study the contribution of local vegetation and topography to tidal-scale

flow routing and sediment deposition patterns in in a mangrove site dissected by tidal creeks. In Chapter 3, the model simulations consistently showed the flow velocities in the creeks to be an order of magnitude greater than the flow velocities over the forest platform, consistent with the field observations (Chapter 2). The creeks were found to remain a major conduit of water into the mangroves, regardless of the tidal conditions. Observed and simulated deposition rates increased most at the sheltered interior of the mangrove forest for increasing high tide water levels (25-240 $g/m^2/day$), emphasizing the favourable sediment trapping function of this zone compared to the more exposed forest fringe (30-160 $g/m^2/day$), levee behind the forest fringe (9-90 $g/m^2/day$) and creek bank (1-60 $g/m^2/day$).

The tidal-scale flow routing and sediment deposition (rates and pattern) were found to be greatly bathymetry induced, mostly depending on the characteristic topography of the field site and its high elevation with respect to mean sea level. This followed from the persistence of the characteristic hydrodynamic patterns, even with simulations for the total clearance of the mangrove vegetation. Moreover, simulated deposition rates changed in concordance with the removal of topographic features or changes of the relative elevation: deposition increased (up to 55%) at the locations of removed creek banks and levees, whereas deposition increased (with about 20%) throughout the study site when inundation depths increased (with 0.1 m) and vice versa. On the other hand, simulations for increasing vegetation densities (0-200%) only slightly enhanced the deposition at the outer fringes of the study site (with about 10%), while deposition in the forest's interior marginally reduced due to the increased sheet flow reduction by the denser vegetation.

Q4. What is the sensitivity of tidal-scale bio-physical interactions in coastal mangroves to changes in vegetation, sea level, sediment supply and mangrove extent beyond the biogeophysical settings observed in the field, according to model simulations?

In Chapter 3, the depth-averaged numerical model was used to conduct a sensitivity analysis into the initial impacts of changing biogeophysical conditions to the tidal-scale dynamics at the elevated mangrove site dissected by tidal creeks. The simulated initial responses of this mangrove system to instantaneous changes of biogeophysical conditions can also be regarded as a proxy for the system's adaptive capacity to cope with environmental change.

Model results corroborated that the studied mangrove system was in a stable state, constituted by the bio-physical interactions that were tightly connected to the in situ topography, tidal hydrodynamics and vegetation characteristics. Deposition rates were rather insensitive to changes of the vegetation density, while counteracting adjustments of the topography and relative elevation (see **Q3**). Nevertheless, external conditions such as the supply of suspended sediments and the extent of the mangrove forest, were pivotal in the stability of the studied mangrove system. Model results showed sedimentation to reduce proportionally with reductions of the supply of suspended sediments in the tidal fluxes, e.g. due to river damming. Sediment

trapping also reduced (up to 30%) when tidal fluxes decreased due to the conversion of inland mangrove areas, e.g. for aquaculture, agriculture or coastal development.

Instantaneous changes of the inundation depth of the mangroves, addressing the potential effects of sea level rise, were predicted to disturb the present stable state of the mangrove system: sheet flow through the forest increased, enhancing flow velocities through the mangroves at the cost of creek flow velocities. Next to limiting sediment deposition within the forest, the self-scouring capacity of the tidal creeks would be reduced, causing them to silt up. On the long run, this might limit tidal inputs of water and sediments through the creeks, consequently reducing sediment supply to, and accretion in the back mangroves.

The simulated contribution of mangrove vegetation to tidal dynamics gained importance for increased inundation depths (MSL +0.5 m). Enhanced sheet flows increased the vegetation induced friction losses for this scenario, increasing the sensitivity of deposition rates to changes in mangrove density. Moreover, the simulated initial response of the area exposed to increased inundation depths showed deposition rates to decrease (with up to 20%) when no mangrove vegetation would be present, e.g. through logging. Deteriorating vegetation densities will additionally reduce the sediment stabilizing capacity of the mangroves, increasing soil erodibility, but that process was beyond the scope of this study. These insights contribute to our understanding of the sensitivity of mangroves' ecosystem engineering function, in terms of sedimentation and coastal stabilization, to changing biogeophysical settings.

Q5. How do wave characteristics change along cross-shore transects through coastal mangroves and how do observed – changes of – wave characteristics correlate with vegetation characteristics and sediment dynamics?

Wave attenuation has been studied along two contrasting transects in Chapter 4. These transects featured different elevation and vegetation characteristics and different orientations with respect to the Andaman Sea. Along the Kantang transect, which was mostly exposed to swell waves, the density of the vegetation within 1 m above the forest floor increased from 4.5 to 9.3 volume-‰ in inland direction and 68-74% of the incident wave energy was attenuated over a distance of 246 m. Along the Palian transect, mostly exposed to shorter sea waves instead, vegetation increased from 4.3 to 20 volume-‰ in inland direction and 52-71% of the incident wave energy was attenuated along this 98 m transect. The data showed a preferential attenuation of shorter (sea) waves and energy transfer from shorter to longer wave lengths was observed occasionally. Minor wave reflection was observed at the interface between contrasting vegetation zones, where vegetation densities suddenly increased.

Wave height reductions correlated well with incident wave heights, when wave attenuation was analysed per vegetation zone. Generalized wave attenuation rates were obtained from the gradients of the relation between the wave height reduction and incident wave height for each vegetation zone. These generalized wave attenuation rates covered a range of incident wave

heights and water depths and ranged between 0.002 m^{-1} and 0.012 m^{-1}, increasing by about 0.005 m^{-1} with a 10‰ increase of the volumetric vegetation density within one meter above the forest floor. Attenuation rates for specific conditions, following from individual short data bursts, resolved that vegetation densities over the full water depth ranged up to 32 volume-‰. Decreasing water depths, and consequently increasing volumetric vegetation densities, induced wave attenuation rates to increase substantially in dense *Rhizophora* vegetation. Reduced wave attenuation capacity was observed in sparser *Avicennia*/*Sonneratia* vegetation, where wave attenuation rates were rather independent of the water depth.

Attenuation of the wave energy by the mangroves was found to facilitate increased deposition rates along both transects. Reduced hydrodynamic activity towards the, consequently, denser vegetated back of the mangrove forests allowed for the deposition of finer sediments. This was confirmed by a gradual fining of the bed material along the transects. A local reduction of the deposition rate and increase of the mean grain size was observed at the interface between the sparsely vegetated forest fringe and the dense *Rhizophora* vegetation, where occasional wave reflection supposedly gave rise to a local increase of the wave energy. Together with the conclusions of Chapter 3, these findings corroborate the positive correlation between vegetation density and sediment trapping in exposed mangroves with elevations around mean sea level.

CONCLUDING

This thesis addressed the contribution of short-term bio-physical interactions in coastal mangroves to coastal stabilization and coastal safety. Mangrove morphology and vegetation were found to play a pivotal role in tidal-scale flow routing and sediment dynamics. The contribution of mangrove vegetation to sediment trapping, and hence coastal stabilization, was found to gain importance for deeper inundating sites, while sediment supply and mangrove extent were important prerequisites to maintain sediment deposition. Additionally, vegetation density directly correlated with the wave attenuating capacity of mangroves. In turn, ameliorated wave conditions within the mangroves facilitated enhanced sediment deposition.

The obtained results emphasize the coastal defence function of mangroves by quantifying their contribution to sediment trapping and wave attenuation. Our simulations also confirmed the sensitivity of the short-term bio-physical interactions in mangrove ecosystems to environmental changes affecting their biogeophysical settings. These findings contribute to our understanding of the regulating services provided by mangroves and the sensitivity of these ecosystems to anthropogenic threats.

5.2 RECOMMENDATIONS

No matter their positive contribution to coastal safety and stabilization, mangroves are in rapid decline [*FAO*, 2007]. Following from this thesis, knowledge of the bio-physical interactions in mangroves is key to a better understanding of the protective function of mangroves and of their sensitivity to anthropogenic threats. Further enhancing this understanding might help to raise awareness of the important regulating ecosystem services provided by mangroves, strengthening the urge for mangrove conservation. Based on the findings of this thesis, a number of recommendations and suggestions for future research are summarized. These recommendations focus on (i) modelling bio-physical interactions in mangroves, (ii) collection of field data for these models, (iii) the coastal defence function of mangroves and, more general, on (iv) mangrove conservation.

MODELLING MANGROVE DYNAMICS

R1. Representative depth-averaged vegetation characteristics

For simulating bio-physical interactions in coastal mangroves, applying a simple and fast depth-averaged model in the process-based Delft3D software can be as accurate as a fully suited three-dimensional model, provided representative vegetation characteristics are schematized (Chapter 3). From the depth-averaged model simulations it followed that the vegetation characteristics at one-half to one-third of the maximum tidal inundation depth can be assumed representative for simulations of the tidal-scale dynamics in a densely vegetated mangrove stand. This finding could be generalized by repeating similar experiments for mangrove vegetation with a different composition and structure.

R2. Generalizing the depth-averaged numerical model

The depth-averaged numerical model proved useful for studying the initial tidal-scale effects of changing biogeophysical conditions to the bio-physical interactions in mangroves, by varying model settings beyond the conditions that were observed in the field (Chapter 3). This numerical modelling study concerned a single mangrove site, relatively high elevated and dissected by tidal creeks, that had adapted to its particular biogeophysical settings. The initial response of these mangroves to changing environmental conditions might differ from responses by different mangrove systems that have developed in, and hence adapted to, different biogeophysical settings, such as the more exposed study sites that had lower elevations and were not dissected by tidal creeks. The model presented in Chapter 3 could easily be applied to different mangrove sites for studying bio-physical interactions in mangroves in various biogeophysical settings. For more exposed sites, the model would greatly benefit from an inclusion of (the effects of) wave action, given the observed correlation between wave attenuation and sediment deposition (Chapter 4). By simulating tidal-scale bio-physical interactions in mangroves for a wide range of field conditions, such efforts would generalize and improve our understanding of mangroves' sensitivity to changing environmental conditions.

R3.   Simulating long-term mangrove development

The calibrated and validated depth-averaged model in Delft3D efficiently simulated tidal-scale processes. The next challenge is to extend the model to simulate longer-term bio-physical interactions in mangroves. While the tidal-scale processes will remain the same, morphodynamics and vegetation dynamics cannot be assumed constant over time spans of months to years (Figure 1.5). These ecomorphological processes can conveniently be accounted for through parameterizations of the vegetation dynamics and morphodynamics. Data and/or models are available for the parameterization of mangrove establishment [*Balke*, 2013; *Balke et al.*, 2013], mangrove growth and mortality [*Jimenez et al.*, 1985; *Berger and Hildenbrandt*, 2000; *Kitaya et al.*, 2002], organic matter accumulation contributing to surface elevation change [*McKee*, 2011], soil erosion processes [*Kirwan and Murray*, 2007; *Mariotti and Fagherazzi*, 2010] and sub-surface elevation changes due to compaction and subsidence [*Krauss et al.*, 2010; *McKee*, 2011]. Given the slow evolution of the morphology and the vegetation compared to tidal-scale hydrodynamics and sediment dynamics, computed ecomorphological changes due to these short-term dynamics can be extrapolated to ecomorphological time scales (e.g. months-years), assuming that hydrodynamics and sediment dynamics remain unaltered [*Roelvink*, 2006]. The resulting model could simulate landscape-scale ecosystem engineering in mangroves (e.g. colonization by mangroves, evolution of creeks and surface elevation change) over time spans of multiple decades and at a high spatial resolution (O(1) m), sensu previous studies into the evolution of salt-marshes [e.g. *D'Alpaos et al.*, 2007; *Temmerman et al.*, 2007; *Fagherazzi et al.*, 2012]. Previously, *Van Maanen et al.* [2011] developed an idealized model of the long-term morphodynamic evolution of a tidal basin with dynamic mangrove vegetation, that accounts for vegetation drag (approximated from submerged vegetation volumes) through the bed roughness. Extension of the present model would add a process-based component to these numerical simulations of mangrove evolution, by improving parameterizations for mangrove establishment and by explicitly accounting for vegetation induced drag forces.

DATA COLLECTION IN MANGROVES

R4.   Mapping mangrove topography

The present study emphasized the great importance of mangrove topography for tidal-scale hydrodynamics and sediment dynamics (Chapter 3). Consequently, high-resolution topographic data are key to accurate model simulations. Variations in bed elevation can be subtle, such as the creek banks and levees that were only slightly elevated (~0.1 m) with respect to the surrounding forest floor, but that extended over a wide area. On the other hand, spatial elevation changes can be extreme but very local, such as the pronounced mud lobster mounds (~1 m high) faced in higher elevated mangroves [*Sivasothi*, 2000]. Additionally, steep cliffs (up to about 1 m high) occur at the forest fringe and at the creek banks of elevated mangroves. These spatial variations require a high-resolution topographic survey. For the present study, we successfully deployed a total station to obtain topographic data of the field sites at a horizontal accuracy of O(10^{-1}) m and a vertical accuracy of O(10^{-2}) m (Chapter 2). When deploying such equipment in mangroves, it is important to create a network of fixed benchmarks while moving the equipment around to overcome the lack of clear sight through the vegetation. Obviously, the equipment

also needs a solid basis preventing it to sink in the soft mangrove mud. These surveys provide essential information to simulate and understand tidal-scale hydrodynamics and sediment dynamics in mangroves.

R5. Determining the tidal elevation benchmark

The elevation of the mangrove forest with respect to mean sea level is essential both for the physical processes (e.g. flow routing and sediment deposition; Chapter 2 and 3) and for the composition and structure of the mangrove vegetation [cf. *Watson*, 1928; *Van Loon et al.*, 2007]. Resolving the elevation of a mangrove site with respect to a vertical datum can be troublesome. At the remote mangrove areas that were studied for this thesis, differential global positioning techniques (dGPS) could not resolve the forest's elevation with respect to a local datum due to lacking nearby reference stations. However, the local mean sea level could be resolved from tidal water level data. These data were collected with low-cost pressure sensors that were deployed in the lower intertidal area at every site for several months (Chapter 2). Proper benchmarking allowed us to tie our topographic data to the local mean sea level datum. This method offers a simple (and cheap) solution to resolve the vertical datum (i.e. mean sea level) at any coastal mangrove site, while at the same time monitoring the tidal climate. These data can also provide tidal boundary conditions for numerical simulations.

R6. Mapping spatially explicit vegetation data

The rates of both wave attenuation and sediment deposition in mangroves were found to depend strongly on vegetation composition and structure, next to the hydrodynamic conditions. Spatially explicit information on vegetation composition, density and numbers and diameters of vegetation elements was essential in the analysis of these bio-physical interactions in Chapter 3 and 4. For the numerical model, these data were a prerequisite to resolve vegetation induced drag forces (and turbulence). Such detailed information on the vegetation structure was generally lacking in preceding studies. Vegetation characteristics were poorly represented by either qualitative descriptions of local vegetation patterns or fairly rough quantifications of the vegetation cover [*Brinkman*, 2006; *Vo-Luong and Massel*, 2006; *Quartel et al.*, 2007]. For future field studies in mangroves, it is recommended to include the acquisition of spatially explicit data of the vegetation structure, as presented in Chapter 3 and 4, to facilitate the quantitative analysis of the bio-physical interactions in mangroves and to serve process-based numerical modelling thereof.

R7. Generalizing the depth-averaged vegetation representation

The calibration of the depth-averaged numerical model in Chapter 3 confirmed that the vegetation characteristics at one-half to one-third of the maximum tidal inundation depth can be assumed representative for simulating the tidal-scale dynamics in mangroves. For different types of mangrove vegetation, this representative vegetation height might deviate. Moreover, climatic conditions strongly affect tree phenology in mangroves [*Tomlinson*, 1986]: at higher latitudes mangrove vegetation faces increased temperature stress and remains smaller than the well-developed climax vegetation at the present study sites. Consequently, additional studies are

required to resolve the level of the representative, depth-averaged vegetation density (cf. recommendation 1). Once this level is obtained for different mangrove covers, the present study underlines that, to explicitly account for vegetation induced drag forces in a numerical model, it suffices to collect data on mangrove structure at a single height. This significantly reduces vegetation survey efforts, compared to mapping vegetation structure at multiple elevations, as single trees can have up to several hundreds of prop roots.

ECO-SYSTEM BASED COASTAL PROTECTION

R8. Enhancing our understanding of wave attenuation in mangroves

The present study confirmed the effective attenuation of waves in mangroves, in line with previous observations (reviewed by *McIvor et al.* [2012b]). An explicit relation was developed, expressing the wave attenuation rate in mangroves as a function of the volumetric vegetation density (Chapter 4). These results were obtained from observations of waves with limited height only (generally <0.10 m). Previous studies were also limited to incident wave heights generally lower than 0.30 m (Table 1.1). Although mangroves thrive in sheltered coastal zones, they might incidentally be exposed to extreme events such as tropical storms or tsunamis. Concerning tsunamis, for example, there is observational evidence that mangroves have contributed to the safety of coastal areas [e.g. *Danielsen et al.*, 2005; *Kathiresan and Rajendran*, 2005; *Alongi*, 2008]. Though, the contribution of mangrove vegetation to the amelioration of the impact of tsunamis is disputed [*Kathiresan and Rajendran*, 2005; 2006; *Kerr et al.*, 2006; *Vermaat and Thampanya*, 2006]. The role of mangroves in the mitigation of tsunami waves is not fully understood yet, and is fundamentally different from their effect on short-period (storm) waves [*Alongi*, 2008; *Lacambra et al.*, 2013]. However, field observations of wave attenuation in mangroves during storm events are also missing yet [*Granek and Ruttenberg*, 2007]. Such observations are prerequisite for validating mechanistic modelling studies into the attenuating capacities of mangroves for increased wave heights [*Lacambra et al.*, 2013]. Hence, additional field data are required to enhance our mechanistic understanding of the coastal defence function of mangroves [cf. *Bouma et al.*, in press].

R9. Mangroves as coastal bioshields

Field observations have shown the positive contribution of mangrove vegetation to sediment trapping, facilitated by the reduction of sheet flow velocities (Chapter 3) and the amelioration of wave heights in mangroves (Chapter 4). Numerical simulations predicted increased deposition rates for greater inundation depths of the mangroves, which was confirmed by field observations (Chapter 3). These sediment trapping mechanisms provide mangrove ecosystems with a natural resilience to overcome erosion (e.g. due to storms) or deeper inundation (e.g. due to sea level rise). Accumulation of organic matter and vegetation dynamics further add to the resilience of mangroves [*Sherman et al.*, 2000; *McKee*, 2011]. In the face of global climate changes, causing sea level rise [*Rahmstorf*, 2007] and increased frequencies and intensities of storms [*Young et al.*, 2011], this resilience provides mangroves with a restoring capacity battling these disturbances [*Alongi*, 2008]. Consequently, in suitable locations, mangroves can be a sustainable alternative for, or complement to traditional coastal defences (e.g. dikes and

dams) that require continuous maintenance and upgrading [*Temmerman et al.*, 2013]. Numerical simulations in Chapter 3 showed that, in order to maintain the sediment trapping capacity of mangroves at increasing inundation depths, it is key to maintain mangroves' vegetation density and their inland extent.

MANGROVE CONSERVATION

R10. Improving mangrove restoration success

To date, mangrove restoration efforts often proved unsuccessful due to poor understanding of physical thresholds to mangrove establishment [e.g. *Lewis*, 2005; *Primavera and Esteban*, 2008]. Poor survival rates are often caused by selection of inappropriate restoration sites [*Erftemeijer and Lewis III*, 2000; *Primavera and Esteban*, 2008]. The limiting role of (excessive) hydrodynamics to mangrove establishment was studied within the present mangrove research program [*Friess et al.*, 2012; *Balke*, 2013]. This study elaborates on bio-physical interactions in climax mangrove vegetation, adding to our understanding of the interplay between biogeophysical mangrove settings and tidal-scale flow routing and deposition patterns (Chapter 2 and 3). This knowledge might provide indications on the suitability (or limitations) of the biogeophysical settings of dedicated restoration sites [*Lewis*, 2005; *Winterwerp et al.*, 2013], thereby hopefully contributing to the success of future mangrove restoration efforts.

R11. Scientific support for mangrove conservation

From the numerical model analyses in Chapter 3, it followed that a mangroves' present state is closely tied to the biogeophysical conditions of the mangrove site. Consequently, changing environmental conditions, due to anthropogenic activities such as river damming, mangrove conversion or timber harvesting [*Ellison and Farnsworth*, 1996; *Thampanya et al.*, 2006; *FAO*, 2007; *Polidoro et al.*, 2010; *Winterwerp et al.*, 2013], in addition to the consequences of (human induced) climate change, such as sea level rise [*Rahmstorf*, 2007], form an increasing threat to the bio-physical balance in mangrove ecosystems. Elaborating on the initial effects of such changes to the tidal-scale dynamics in mangroves (Chapter 3), it is recommended to simulate the long-term effects of such changes (cf. recommendation 3). These long-term analyses will provide valuable knowledge contributing to our understanding and awareness of the (potential) long-term impact of anthropogenic activities on these highly valuable ecosystems. Moreover, by enhancing our understanding (of the sensitivity) of the long-term development of mangroves, such models provide invaluable information on how to effectively protect mangroves against the potential consequences of anthropogenic threats.

Mangrove logging near Pulau Kukup, Malaysia.

REFERENCES

Adam, P. (1990). *Saltmarsh ecology*. Cambridge studies in ecology. Cambridge University Press, Cambridge, UK.

Adame, M.F., D. Neil, S.F. Wright & C.E. Lovelock (2010). Sedimentation within and among mangrove forests along a gradient of geomorphological settings. *Estuarine, Coastal and Shelf Science*, 86(1), 21-30.

Allen, J.R.L. & K. Pye (1992). Coastal saltmarshes: their nature and importance. In: J.R.L. Allen and K. Pye (Eds.), *Saltmarshes: morphodynamics, conservation and engineering significance*. Cambridge University Press, Cambridge, 1-18.

Alongi, D.M. (2002). Present state and future of the world's mangrove forests. *Environmental Conservation*, 29(3), 331-349.

Alongi, D.M. (2008). Mangrove forests: Resilience, protection from tsunamis, and responses to global climate change. *Estuarine, Coastal and Shelf Science*, 76(1), 1-13.

Alongi, D.M. (2009). *The energetics of mangrove forests*. Springer, Netherlands.

Alongi, D.M. & N.A. De Carvalho (2008). The effect of small-scale logging on stand characteristics and soil biogeochemistry in mangrove forests of Timor Leste. *Forest Ecology and Management*, 255(3–4), 1359-1366.

Anthony, E.J. (2004). Sediment dynamics and morphological stability of estuarine mangrove swamps in Sherbro Bay, West Africa. *Marine Geology*, 208(2-4), 207-224.

Anthony, E.J. & N. Gratiot (2012). Coastal engineering and large-scale mangrove destruction in Guyana, South America: Averting an environmental catastrophe in the making. *Ecological Engineering*, 47, 268-273.

Aucan, J. & P.V. Ridd (2000). Tidal asymmetry in creeks surrounded by saltflats and mangroves with small swamp slopes. *Wetlands Ecology and Management*, 8(4), 223-232.

Augustinus, P.G.E.F. (1995). Geomorphology and sedimentology of mangroves. In: G.M.E. Perillo (Ed.), *Developments in Sedimentology*. Elsevier, 333-357.

Balke, T. (2013). *Establishment of biogeomorphic ecosystems*. PhD thesis, Radboud University Nijmegen, Nijmegen, The Netherlands.

Balke, T., T.J. Bouma, E.M. Horstman, E.L. Webb, P.L.A. Erftemeijer & P.M.J. Herman (2011). Windows of opportunity: thresholds to mangrove seedling establishment on tidal flats. *Marine Ecology-Progress Series*, 440, 1-9.

Balke, T., T.J. Bouma, P.M.J. Herman, E.M. Horstman, C. Sudtongkong & E.L. Webb (2013). Cross-shore gradients of physical disturbance in mangroves: implications for seedling establishment. *Biogeosciences*, 10(8), 5411-5419.

Bao, T.Q. (2011). Effect of mangrove forest structures on wave attenuation in coastal Vietnam. *Oceanologia*, 53(3), 807-818.

Baptist, M.J. (2005). *Modelling floodplain biogeomorphology*. PhD thesis, Delft University of Technology, Delft, The Netherlands.

Baptist, M.J., V. Babovic, J. Rodríguez Uthurburu, M. Keijzer, R.E. Uittenbogaard, A. Mynett & A. Verwey (2007). On inducing equations for vegetation resistance. *Journal of Hydraulic Research*, 45(4), 435-450.

Barbier, E.B. (2007). Valuing ecosystem services as productive inputs. *Economic Policy*, 22(49), 177-229.

Barbier, E.B., S.D. Hacker, C. Kennedy, E.W. Koch, A.C. Stier & B.R. Silliman (2011). The value of estuarine and coastal ecosystem services. *Ecological Monographs*, 81(2), 169-193.

Barbier, E.B., E.W. Koch, B.R. Silliman, S.D. Hacker, E. Wolanski, J.H. Primavera, E.F. Granek, S. Polasky, S. Aswani, L.A. Cramer, D.M. Storms, C.J. Kennedy, D. Bael, C.V. Kappel, G.M.E. Perillo & D.J. Reed (2008). Coastal ecosystem-based management with nonlinear ecological functions and values. *Science*, 319(5861), 321-323.

Battjes, J.A. & M.J.F. Stive (1985). Calibration and verification of a dissipation model for random breaking waves. *Journal of Geophysical Research: Oceans*, 90(C5), 9159-9167.

Bayliss-Smith, T.P., R. Healey, R. Lailey, T. Spencer & D.R. Stoddart (1979). Tidal flows in salt marsh creeks. *Estuarine and Coastal Marine Science*, 9(3), 235-255.

Berger, U. & H. Hildenbrandt (2000). A new approach to spatially explicit modelling of forest dynamics: spacing, ageing and neighbourhood competition of mangrove trees. *Ecological Modelling*, 132(3), 287-302.

Blauw, A.N., E. Benincà, R.W.P.M. Laane, N. Greenwood & J. Huisman (2012). Dancing with the tides: Fluctuations of coastal phytoplankton orchestrated by different oscillatory modes of the tidal cycle. *PLoS ONE*, 7(11), e49319.

Borsje, B.W., T.J. Bouma, M. Rabaut, P.M.J. Herman & S.J.M.H. Hulscher (in press). Formation and erosion of biogeomorphological structures: A model study on the tube-building polychaete *Lanice conchilega*. *Limnology and Oceanography*.

Bouma, T.J., L.A. Van Duren, S. Temmerman, T. Claverie, A. Blanco-Garcia, T. Ysebaert & P.M.J. Herman (2007). Spatial flow and sedimentation patterns within patches of epibenthic structures: Combining field, flume and modelling experiments. *Continental Shelf Research*, 27, 1020-1045.

Bouma, T.J., et al. (in press). Identifying knowledge gaps hampering application of intertidal habitats in coastal protection: Opportunities & steps to take. *Coastal Engineering*.

Brinkman, R.M. (2006). *Wave attenuation in mangrove forests: an investigation through field and theoretical studies*. PhD thesis, James Cook University, Townsville, Australia.

146

Brinkman, R.M., S.R. Massel, P.V. Ridd & K. Furukawa (1997). Surface wave attenuation in mangrove forests, *Pacific Coasts and Ports '97*, 7-11 September, Christchurch, New Zealand (pp. 941-946), Centre for Advanced Engineering, University of Canterbury.

Brommer, M.B. & L.M. Bochev-van der Burgh (2009). Sustainable coastal zone management: A concept for forecasting long-term and large-scale coastal evolution. *Journal of Coastal Research*, 25(1), 181-188.

Bryce, S., P. Larcombe & P.V. Ridd (2003). Hydrodynamic and geomorphological controls on suspended sediment transport in mangrove creek systems, a case study: Cocoa Creek, Townsville, Australia. *Estuarine, Coastal and Shelf Science*, 56, 415-431.

Capo, S., A. Sottolichio, I. Brenon, P. Castaing & L. Ferry (2006). Morphology, hydrography and sediment dynamics in a mangrove estuary: The Konkoure Estuary, Guinea. *Marine Geology*, 230, 199-215.

CERC (1984). *Shore protection manual*, U.S. Army Corps of Engineers, Washington DC.

Chanson, H., M. Trevethan & S. Aoki (2008). Acoustic Doppler velocimetry (ADV) in small estuary: Field experience and signal post-processing. *Flow Measurement and Instrumentation*, 19(5), 307-313.

Chmura, G.L., S.C. Anisfeld, D.R. Cahoon & J.C. Lynch (2003). Global carbon sequestration in tidal, saline wetland soils. *Global Biogeochemical Cycles*, 17(4), 1111.

Chow, V.T. (1959). *Open-channel hydraulics*. McGraw-Hill civil engineering series. McGraw-Hill, New York.

Cintron, G. & Y. Schaeffer-Novelli (1984). Methods for studying mangrove structure. In: S.C. Snedaker (Ed.), *The mangrove ecosystem: research methods.* Monographs on Oceanographic Methodology. UNESCO, Paris, 91-113.

Codiga, D.L. (2011). *Unified tidal analysis and prediction using the UTide Matlab functions*, Graduate School of Oceanography, University of Rhode Island, Narragansett, RI, USA.

Costanza, R., O. Pérez-Maqueo, M.L. Martinez, P. Sutton, S.J. Anderson & K. Mulder (2008). The value of coastal wetlands for hurricane protection. *AMBIO: A Journal of the Human Environment*, 37(4), 241-248.

Costanza, R., R. d'Arge, R. de Groot, S. Farber, M. Grasso, B. Hannon, K. Limburg, S. Naeem, R.V. O'Neill, J. Paruelo, R.G. Raskin, P. Sutton & M. van den Belt (1997). The value of the world's ecosystem services and natural capital. *Nature*, 387(6630), 253-260.

Cowell, P.J. & B.G. Thom (1997). Morphodynamics of coastal evolution. In: R.W.G. Carter and C.D. Woodroffe (Eds.), *Coastal evolution; Late Quaternary shoreline morphodynamics.* Cambridge University Press, Cambridge, 33-86.

Cowell, P.J., M.J.F. Stive, A.W. Niedoroda, H.J. de Vriend, D.J.P. Swift, G.M. Kaminsky & M. Capobianco (2003). The coastal-tract (part 1): a conceptual approach to aggregated modeling of low-order coastal change. *Journal of Coastal Research*, 19(4), 812-827.

D'Alpaos, A., S. Lanzoni, M. Marani & A. Rinaldo (2007). Landscape evolution in tidal embayments: Modeling the interplay of erosion, sedimentation, and vegetation dynamics. *Journal of Geophysical Research*, 112(F1), F01008.

Dahdouh-Guebas, F., A. Verheyden, W. De Genst, S. Hettiarachchi & N. Koedam (2000). Four decade vegetation dynamics in Sri Lankan mangroves as detected from sequential aerial photography: A case study in Galle. *Bulletin of Marine Science*, 67(2), 741-759.

Danielsen, F., M.K. Sørensen, M.F. Olwig, V. Selvam, F. Parish, N.D. Burgess, T. Hiraishi, V.M. Karunagaran, M.S. Rasmussen, L.B. Hansen, A. Quarto & N. Suryadiputra (2005). The Asian Tsunami: A protective role for coastal vegetation. *Science*, 310(5748), 643.

Davis, J.H.J. (1938). Mangroves, makers of land. *Nature Magazine*, 31(11), 551-553.

De Groot, R., L. Brander, S. van der Ploeg, R. Costanza, F. Bernard, L. Braat, M. Christie, N. Crossman, A. Ghermandi, L. Hein, S. Hussain, P. Kumar, A. McVittie, R. Portela, L.C. Rodriguez, P. ten Brink & P. van Beukering (2012). Global estimates of the value of ecosystems and their services in monetary units. *Ecosystem Services*, 1(1), 50-61.

Deltares (2014). *User manual Delft3D-FLOW*, Deltares, Delft.

Duke, N.C. (1992). Mangrove floristics and biogeography. In: A.I. Robertson and D.M. Alongi (Eds.), *Tropical mangrove ecosystems*. American Geophysical Union, Washington DC, 63-100.

Duke, N.C., J.-O. Meynecke, S. Dittmann, A.M. Ellison, K. Anger, U. Berger, S. Cannicci, K. Diele, K.C. Ewel, C.D. Field, N. Koedam, S.Y. Lee, C. Marchand, I. Nordhaus & F. Dahdouh-Guebas (2007). A world without mangroves? *Science*, 317(5834), 41-42.

Elgar, S. & B. Raubenheimer (2008). Wave dissipation by muddy seafloors. *Geophysical Research Letters*, 35(7), L07611.

Ellison, A.M. & E.J. Farnsworth (1996). Anthropogenic disturbance of Caribbean mangrove ecosystems: Past impacts, present trends, and future predictions. *Biotropica*, 28(4a), 549-565.

Ellison, J.C. & D.R. Stoddart (1991). Mangrove ecosystem collapse during predicted sea-level rise: holocene analogues and implications. *Journal of Coastal Research*, 7(1), 151-165.

Erftemeijer, P.L.A. & R.R. Lewis III (2000). Planting mangroves on intertidal mudflats: habitat restoration or habitat conversion?, *ECOTONE VIII Seminar "Enhancing Coastal Ecosystems Restoration for the 21st Century"*, 23-28 May 1999, Ranong, Thailand (pp. 156-165). Royal Forestry Department of Thailand, Bangkok, Thailand.

Ewel, K.C. (1997). Water quality improvement by wetlands. In: G.C. Daily (Ed.), *Nature's services. Societal dependence on natural ecosystems*. Island Press, Washington DC, 329-344.

Ewel, K.C., J.A. Bourgeois, T.G. Cole & S. Zheng (1998). Variation in environmental characteristics and vegetation in high-rainfall mangrove forests, Kosrae, Micronesia. *Global Ecology and Biogeography Letters*, 7(1), 49-56.

Fagherazzi, S., P.L. Wiberg, S. Temmerman, E. Struyf, Y. Zhao & P. Raymond (2013). Fluxes of water, sediments, and biogeochemical compounds in salt marshes. *Ecological Processes*, 2(1), 3.

Fagherazzi, S., M.L. Kirwan, S.M. Mudd, G.R. Guntenspergen, S. Temmerman, A. D'Alpaos, J. Van De Koppel, J.M. Rybczyk, E. Reyes, C. Craft & J. Clough (2012). Numerical models of salt marsh evolution: Ecological, geomorphic, and climatic factors. *Reviews of Geophysics*, 50(RG1002), 1-28.

FAO (2007). *The world's mangroves, 1980-2005*. FAO Forestry Paper. Food and Agriculture Organization of the United Nations, Rome.

Friess, D.A., K.W. Krauss, E.M. Horstman, T. Balke, T.J. Bouma, D. Galli & E.L. Webb (2012). Are all intertidal wetlands naturally created equal? Bottlenecks, thresholds and knowledge gaps to mangrove and saltmarsh ecosystems. *Biological Reviews*, 87(2), 346-366.

Furukawa, K., E. Wolanski & H. Mueller (1997). Currents and sediment transport in mangrove forests. *Estuarine, Coastal and Shelf Science*, 44(3), 301-310.

Gedan, K.B., M.L. Kirwan, E. Wolanski, E.B. Barbier & B.R. Silliman (2011). The present and future role of coastal wetland vegetation in protecting shorelines: answering recent challenges to the paradigm. *Climatic Change*, 106(1), 7-29.

Gibson, C.C., E. Ostrom & T.-K. Ahn (2000). The concept of scale and the human dimensions of global change: a survey. *Ecological Economics*, 32(2), 217-239.

Giri, C., E. Ochieng, L.L. Tieszen, Z. Zhu, A. Singh, T. Loveland, J. Masek & N. Duke (2011). Status and distribution of mangrove forests of the world using earth observation satellite data. *Global Ecology and Biogeography*, 20(1), 154-159.

Granek, E.F. & B.I. Ruttenberg (2007). Protective capacity of mangroves during tropical storms: a case study from 'Wilma' and 'Gamma' in Belize. *Marine Ecology Progress Series*, 343, 101-105.

Hegge, B.J. & G. Masselink (1996). Spectral analysis of geomorphic time series: auto-spectrum. *Earth Surface Processes and Landforms*, 21(11), 1021-1040.

Hibma, A., H.J. de Vriend & M.J.F. Stive (2003). Numerical modelling of shoal pattern formation in well-mixed elongated estuaries. *Estuarine, Coastal and Shelf Science*, 57(5–6), 981-991.

Holling, C.S. (2001). Understanding the complexity of economic, ecological and social systems. *Ecosystems*, 4(5), 390-405.

Horstman, E.M. (in prep.). *Data report: Field campaign Trang, Thailand; November 2010 - May 2011*, University of Twente, Enschede, The Netherlands.

Horstman, E.M., C.M. Dohmen-Janssen & S.J.M.H. Hulscher (2013). Modeling tidal dynamics in a mangrove creek catchment in Delft3D. In: P. Bonneton and T. Garlan (Eds.), *Extended abstracts of Coastal Dynamics 2013*, 24-28 June 2013, Arcachon, France (pp. 833-844). SHOM, Brest, France.

Horstman, E.M., T. Balke, T.J. Bouma, C.M. Dohmen-Janssen & S.J.M.H. Hulscher (2011a). Optimizing methods to measure hydrodynamics in coastal wetlands: evaluating the use and positioning of ADV, ADCP and HR-ADCP. In: J. McKee-Smith and P. Lynett (Eds.), *Proceedings of 32nd International Conference on Coastal Engineering*, Shanghai (pp. 1-11). Coastal Engineering Research Council, Shanghai.

Horstman, E.M., M. Siemerink, T. Balke, C.M. Dohmen-Janssen, T.J. Bouma & S.J.M.H. Hulscher (2011b). Sediment dynamics in a mangrove creek catchment in Trang, Thailand. In: X. Shao, Z. Wang and G. Wang (Eds.), *Proceedings of the 7th IAHR Symposium on River, Coastal and Estuarine Morphodynamics*, 6-8 September 2011, Beijing (pp. 675-685). Tsinghua University Press, Beijing.

Horstman, E.M., C.M. Dohmen-Janssen, P. Narra, N.J.F. Van den Berg, M. Siemerink, T. Balke, T.J. Bouma & S.J.M.H. Hulscher (2012). Wave attenuation in mangrove forests; field data obtained in Trang, Thailand. In: J. McKee-Smith and P. Lynett (Eds.), *Proceedings of 33rd International Conference on Coastal Engineering*, Santander, Spain. Coastal Engineering Research Council, Santander.

Hu, K., P. Ding, Z. Wang & S. Yang (2009). A 2D/3D hydrodynamic and sediment transport model for the Yangtze Estuary, China. *Journal of Marine Systems*, 77(1–2), 114-136.

Huijts, K.M.H., H.M. Schuttelaars, H.E. de Swart & C.T. Friedrichs (2009). Analytical study of the transverse distribution of along-channel and transverse residual flows in tidal estuaries. *Continental Shelf Research*, 29, 89-100.

Hutchison, J., A. Manica, R. Swetnam, A. Balmford & M. Spalding (in press). Predicting global patterns in mangrove forest biomass. *Conservation Letters*.

Jimenez, J.A., A.E. Lugo & G. Cintron (1985). Tree mortality in mangrove forests. *Biotropica*, 17(3), 177-185.

Jones, C.G., J.H. Lawton & M. Shachak (1994). Organisms as ecosystem engineers. *Oikos*, 69, 373-386.

Jones, C.G., J.H. Lawton & M. Shachak (1997). Positive and negative effects of organisms as physical ecosystem engineers. *Ecology*, 78(7), 1946-1957.

Kathiresan, K. & N. Rajendran (2005). Coastal mangrove forests mitigated tsunami. *Estuarine, Coastal and Shelf Science*, 65(3), 601-606.

Kathiresan, K. & N. Rajendran (2006). Reply to 'Comments of Kerr et al. on "Coastal mangrove forests mitigated tsunami"' [Estuar. Coast. Shelf Sci. 65 (2005) 601–606]. *Estuarine, Coastal and Shelf Science*, 67(3), 542.

Kerr, A.M., A.H. Baird & S.J. Campbell (2006). Comments on "Coastal mangrove forests mitigated tsunami" by K. Kathiresan and N. Rajendran [Estuar. Coast. Shelf Sci. 65 (2005) 601–606]. *Estuarine, Coastal and Shelf Science*, 67(3), 539-541.

Kirwan, M.L. & A.B. Murray (2007). A coupled geomorphic and ecological model of tidal marsh evolution. *Proceedings of the National Academy of Sciences*, 104(15), 6118-6122.

Kitaya, Y., V. Jintana, S. Piriyayotha, D. Jaijing, K. Yabuki, S. Izutani, A. Nishimiya & M. Iwasaki (2002). Early growth of seven mangrove species planted at different elevations in a Thai estuary. *Trees*, 16(2-3), 150-154.

Kjerfve, B. & T.G. Wolaver (1988). Sampling optimization for studies of tidal transport in estuaries, *American Fisheries Society Symposium 3* (pp. 26-33).

Kobashi, D. & Y. Mazda (2005). Tidal flow in riverine-type mangroves. *Wetlands Ecology and Management*, 13(6), 615-619.

Koch, E.W., E.B. Barbier, B.R. Silliman, D.J. Reed, G.M.E. Perillo, S.D. Hacker, E.F. Granek, J.H. Primavera, N. Muthiga, S. Polasky, B.S. Halpern, C.J. Kennedy, C.V. Kappel & E. Wolanski (2009). Non-linearity in ecosystem services: temporal and spatial variability in coastal protection. *Frontiers in Ecology and the Environment*, 7(1), 29-37.

Krauss, K.W., J.A. Allen & D.R. Cahoon (2003). Differential rates of vertical accretion and elevation change among aerial root types in Micronesian mangrove forests. *Estuarine, Coastal and Shelf Science*, 56(2), 251-259.

Krauss, K.W., D.R. Cahoon, J.A. Allen, K.C. Ewel, J.C. Lynch & N. Cormier (2010). Surface elevation change and susceptibility of different mangrove zones to sea-level rise on pacific high islands of Micronesia. *Ecosystems*, 13(1), 129-143.

Lacambra, C., D.A. Friess, T. Spencer & I. Möller (2013). Bioshields: Mangrove ecosystems as resilient natural coastal defences. In: F.G. Renaud, K. Sudmeier-Rieux and M. Estrella (Eds.), *The role of ecosystems in disaster risk reduction*. United Nations University Press.

Laso Bayas, J.C., C. Marohn, G. Dercon, S. Dewi, H.P. Piepho, L. Joshi, M. van Noordwijk & G. Cadisch (2011). Influence of coastal vegetation on the 2004 tsunami wave impact in west Aceh. *Proceedings of the National Academy of Sciences*, 108(46), 18612-18617.

Leonard, L.A. (1997). Controls of sediment transport and deposition in an incised mainland marsh basin, southeastern North Carolina. *Wetlands*, 17(2), 263-274.

Lesser, G.R., J.A. Roelvink, J.A.T.M. van Kester & G.S. Stelling (2004). Development and validation of a three-dimensional morphological model. *Coastal Engineering*, 51(8–9), 883-915.

Lewis, R.R. (2005). Ecological engineering for successful management and restoration of mangrove forests. *Ecological Engineering*, 24(4), 403-418.

Li, C. & A. Valle-Levinson (1999). A two-dimensional analytic tidal model for a narrow estuary of arbitrary lateral depth variation: The intratidal motion. *Journal of Geophysical Research: Oceans*, 104(C10), 23525-23543.

Lugo, A.E. & S.C. Snedaker (1974). The ecology of mangroves. *Annual Review of Ecology and Systematics*, 5, 39-64.

MacNae, W. (1968). A general account of the fauna and flora of mangrove swamps and forests in the Indo-West-Pacific region. In: S.R. Frederick and Y. Maurice (Eds.), *Advances in Marine Biology*. Academic Press, 73-270.

Mariotti, G. & S. Fagherazzi (2010). A numerical model for the coupled long-term evolution of salt marshes and tidal flats. *Journal of Geophysical Research: Earth Surface*, 115(F1), F01004.

Mariotti, G. & S. Fagherazzi (2012). Channels-tidal flat sediment exchange: The channel spillover mechanism. *Journal of Geophysical Research: Oceans*, 117(C3), C03032.

Massel, S.R., K. Furukawa & R.M. Brinkman (1999). Surface wave propagation in mangrove forests. *Fluid Dynamics Research*, 24(4), 219-249.

Mazda, Y., N. Kanazawa & E. Wolanski (1995). Tidal asymmetry in mangrove creeks. *Hydrobiologia*, 295(1), 51-58.

Mazda, Y., D. Kobashi & S. Okada (2005). Tidal-scale hydrodynamics within mangrove swamps. *Wetlands Ecology and Management*, 13(6), 647-655.

Mazda, Y., E. Wolanski & P.V. Ridd (2007). *The role of physical processes in mangrove environments: manual for the preservation and utilization of mangrove ecosystems*. Terrapub, Tokyo.

Mazda, Y., M. Magi, M. Kogo & P.N. Hong (1997a). Mangroves as a coastal protection from waves in the Tong King delta, Vietnam. *Mangroves and Salt Marshes*, 1(2), 127-135.

Mazda, Y., M. Magi, Y. Ikeda, T. Kurokawa & T. Asano (2006). Wave reduction in a mangrove forest dominated by *Sonneratia* sp. *Wetlands Ecology and Management*, 14(4), 365-378.

Mazda, Y., E. Wolanski, B. King, A. Sase, D. Ohtsuka & M. Magi (1997b). Drag force due to vegetation in mangrove swamps. *Mangroves and Salt Marshes*, 1(3), 193-199.

McIvor, A.L., T. Spencer, I. Möller & M. Spalding (2012a). *Storm surge reduction by mangroves*, Cambridge Coastal Research Unit, Cambridge.

McIvor, A.L., I. Möller, T. Spencer & M. Spalding (2012b). *Reduction of wind and swell waves by mangroves*, Cambridge Coastal Research Unit, Cambridge.

McKee, K.L. (2011). Biophysical controls on accretion and elevation change in Caribbean mangrove ecosystems. *Estuarine, Coastal and Shelf Science*, 91(4), 475-483.

Méndez, F.J., I.J. Losada & M.A. Losada (1999). Hydrodynamics induced by wind waves in a vegetation field. *Journal of Geophysical Research: Oceans*, 104(C8), 18383-18396.

Möller, I. (2012). Bio-physical linkages in coastal wetlands – implications for coastal protection. In: W.M. Kranenburg, E.M. Horstman and K.M. Wijnberg (Eds.), *NCK-days 2012; Crossing borders in coastal research*, Enschede, The Netherlands (pp. 51-60). University of Twente.

Möller, I., T. Spencer, J.R. French, D.J. Leggett & M. Dixon (1999). Wave transformation over salt marshes: A field and numerical modelling study from North Norfolk, England. *Estuarine, Coastal and Shelf Science*, 49(3), 411-426.

Nash, J.E. & J.V. Sutcliffe (1970). River flow forecasting through conceptual models part I — A discussion of principles. *Journal of Hydrology*, 10(3), 282-290.

Nepf, H.M. & E.R. Vivoni (2000). Flow structure in depth-limited, vegetated flow. *Journal of Geophysical Research*, 105(C12), 28547-28557.

Nicholls, R.J. (2004). Coastal flooding and wetland loss in the 21st century: changes under the SRES climate and socio-economic scenarios. *Global Environmental Change*, 14(1), 69-86.

Partheniades, E. (1965). Erosion and deposition of cohesive soils. *Journal of the Hydraulics Division, American Society of Civil Engineers*, 91, 105-139.

Paul, M. & C.L. Amos (2011). Spatial and seasonal variation in wave attenuation over Zostera noltii. *Journal of Geophysical Research: Oceans*, 116(C8), C08019.

Pestrong, R. (1965). *The development of drainage patterns on tidal marshes*, Stanford University School of Earth Sciences, Stanford.

Polidoro, B.A., et al. (2010). The loss of species: Mangrove extinction risk and geographic areas of global concern. *PLoS ONE*, 5(4), e10095.

Primavera, J.H. & J.M.A. Esteban (2008). A review of mangrove rehabilitation in the Philippines: successes, failures and future prospects. *Wetlands Ecology and Management*, 16(5), 345-358.

Quartel, S., A. Kroon, P.G.E.F. Augustinus, P. Van Santen & N.H. Tri (2007). Wave attenuation in coastal mangroves in the Red River Delta, Vietnam. *Journal of Asian Earth Sciences*, 29(4), 576-584.

Rahmstorf, S. (2007). A semi-empirical approach to projecting future sea-level rise. *Science*, 315(5810), 368-370.

Roelvink, J.A. (2006). Coastal morphodynamic evolution techniques. *Coastal Engineering*, 53(2–3), 277-287.

Royal Thai Navy (2012). Pak Nam Trang tide tables. Nautical chart and publication services, Hydrographic Department.

Salehi, M. & K. Strom (2011). Using velocimeter signal to noise ratio as a surrogate measure of suspended mud concentration. *Continental Shelf Research*, 31, 1020-1032.

Sassi, M.G., A.J.F. Hoitink, B. Vermeulen & Hidayat (2011). Discharge estimation from H-ADCP measurements in a tidal river subject to sidewall effects and a mobile bed. *Water Resources Research*, 47(6), W06504.

Shepard, C.C., C.M. Crain & M.W. Beck (2011). The protective role of coastal marshes: a systematic review and meta-analysis. *PLoS ONE*, 6(11), e27374.

Sherman, R.E., T.J. Fahey & J.J. Battles (2000). Small-scale disturbance and regeneration dynamics in a neotropical mangrove forest. *Journal of Ecology*, 88(1), 165-178.

Sivasothi, N. (2000). Niche preferences of tree-climbing crabs in Singapore mangroves. *Crustaceana*, 73, 25-38.

SonTek (1997). *Pulse coherent Doppler processing and the ADV correlation coefficient*, SonTek, San Diego.

Spalding, M., M. Kainuma & L. Collins (2010). *World Atlas of Mangroves*. Earthscan, London, UK.

Spenceley, A.P. (1977). The role of pneumatophores in sedimentary processes. *Marine Geology*, 24(2), M31-M37.

Spencer, T. & I. Möller (2013). Mangrove systems. In: J.F. Shroder (Ed.), *Treatise on Geomorphology*. Academic Press, San Diego, 360-391.

Stive, M.J.F., S.G.J. Aarninkhof, L. Hamm, H. Hanson, M. Larson, K.M. Wijnberg, R.J. Nicholls & M. Capobianco (2002). Variability of shore and shoreline evolution. *Coastal Engineering*, 47(2), 211-235.

Stokes, D.J., T.R. Healy & P.J. Cooke (2010). Expansion dynamics of monospecific, temperate mangroves and sedimentation in two embayments of a barrier-enclosed lagoon, Tauranga Harbour, New Zealand. *Journal of Coastal Research*, 26(1), 113-122.

Struve, J., R.A. Falconer & Y. Wu (2003). Influence of model mangrove trees on the hydrodynamics in a flume. *Estuarine, Coastal and Shelf Science*, 58(1), 163-171.

Suk, N.S., Q. Guo & N.P. Psuty (1999). Suspended solids flux between salt marsh and adjacent bay: a long-term continuous measurement. *Estuarine, Coastal and Shelf Science*, 49(1), 61-81.

Sutherland, J., A.H. Peet & R.L. Soulsby (2004). Evaluating the performance of morphological models. *Coastal Engineering*, 51(8–9), 917-939.

Suzuki, T., M. Zijlema, B. Burger, M.C. Meijer & S. Narayan (2012). Wave dissipation by vegetation with layer schematization in SWAN. *Coastal Engineering*, 59(1), 64-71.

Temmerman, S., G. Govers, S. Wartel & P. Meire (2003). Spatial and temporal factors controlling short-term sedimentation in a salt and freshwater tidal marsh, scheldt estuary, Belgium, SW Netherlands. *Earth Surface Processes and Landforms*, 28(7), 739-755.

Temmerman, S., T.J. Bouma, G. Govers & D. Lauwaet (2005a). Flow paths of water and sediment in a tidal marsh: Relations with marsh developmental stage and tidal inundation height. *Estuaries*, 28(3), 338-352.

Temmerman, S., T.J. Bouma, G. Govers, Z.B. Wang, M.B. De Vries & P.M.J. Herman (2005b). Impact of vegetation on flow routing and sedimentation patterns: Three-dimensional modeling for a tidal marsh. *Journal of Geophysical Research*, 110, F04019.

Temmerman, S., T.J. Bouma, J. Van de Koppel, D.D. Van der Wal, M.B. De Vries & P.M.J. Herman (2007). Vegetation causes channel erosion in a tidal landscape. *Geology*, 35(7), 631-634.

Temmerman, S., P. Meire, T.J. Bouma, P.M.J. Herman, T. Ysebaert & H.J. De Vriend (2013). Ecosystem-based coastal defence in the face of global change. *Nature*, 504(7478), 79-83.

Thai Meteorological Department (2012). *The climate of Thailand*, Climatological Group, Meteorological Development Bureau, Thai Meteorological Department, Bangkok, Thailand.

Thampanya, U., J.E. Vermaat, S. Sinsakul & N. Panapitukkul (2006). Coastal erosion and mangrove progradation of Southern Thailand. *Estuarine, Coastal and Shelf Science*, 68(1-2), 75-85.

Thom, B.G. (1967). Mangrove ecology and deltaic geomorphology: Tabasco, Mexico. *Journal of Ecology*, 55(2), 301-343.

Ting, C.L., M.C. Lin & C.Y. Cheng (2004). Porosity effects on non-breaking surface waves over permeable submerged breakwaters. *Coastal Engineering*, 50(4), 213-224.

Tomlinson, P.B. (1986). *The botany of mangroves*. Cambridge tropical biology series. Cambridge University Press, Cambridge, UK.

Torrence, C. & G.P. Compo (1998). A practical guide to wavelet analysis. *Bulletin of the American Meteorological Society*, 79(1), 61-78.

Twilley, R.R., V.H. Rivera-Monroy, R. Chen & L. Botero (1999). Adapting an ecological mangrove model to simulate trajectories in restoration ecology. *Marine Pollution Bulletin*, 37(8–12), 404-419.

Uittenbogaard, R.E. (2003), Modelling turbulence in vegetated aquatic flows. Paper presented at: *International Workshop on RIParian FORest Vegetated Channels: Hydraulic, Morphological and Ecological Aspects*, 20-22 February 2003, Trento, Italy.

Van der Wal, D., A. Wielemaker-Van den Dool & P.M.J. Herman (2008). Spatial patterns, rates and mechanisms of saltmarsh cycles (Westerschelde, The Netherlands). *Estuarine, Coastal and Shelf Science*, 76(2), 357-368.

Van Leeuwen, B., D.C.M. Augustijn, B.K. van Wesenbeeck, S.J.M.H. Hulscher & M.B. de Vries (2010). Modeling the influence of a young mussel bed on fine sediment dynamics on an intertidal flat in the Wadden Sea. *Ecological Engineering*, 36(2), 145-153.

Van Loon, A.F., R. Dijksma & M.E.F. Van Mensvoort (2007). Hydrological classification in mangrove areas: a case study in Can Gio, Vietnam. *Aquatic Botany*, 87(1), 80-82.

Van Maanen, B., G. Coco & K.R. Bryan (2011). The effects of mangroves on the morphological response of tidal embayments to sea level rise. In: X. Shao, Z. Wang and G. Wang (Eds.), *Proceedings of the 7th IAHR Symposium on River, Coastal and Estuarine Morphodynamics*, Beijing (pp. 657-667). Tsinghua University Press, Beijing.

Van Rijn, L.C. (2008). *Principles of fluid flow and surface waves in rivers, estuaries, seas and oceans*. Aqua Publications, The Netherlands.

Van Santen, P., P.G.E.F. Augustinus, B.M. Janssen-Stelder, S. Quartel & N.H. Tri (2007). Sedimentation in an estuarine mangrove system. *Journal of Asian Earth Sciences*, 29(4), 566-575.

Vermaat, J.E. & U. Thampanya (2006). Mangroves mitigate tsunami damage: A further response. *Estuarine, Coastal and Shelf Science*, 69(1-2), 1-3.

Vo-Luong, H.P. & S.R. Massel (2006). Experiments on wave motion and suspended sediment concentration at Nang Hai, Can Gio mangrove forest, Southern Vietnam. *Oceanologia*, 48(1), 23-40.

Vo-Luong, H.P. & S.R. Massel (2008). Energy dissipation in non-uniform mangrove forests of arbitrary depth. *Journal of Marine Systems*, 74, 603-622.

Watson, J.G. (1928). *Mangrove forests of the Malay Peninsula*. Malayan Forest Records No. 6. Federated Malay States Government, Kuala Lumpur.

Wattayakorn, G., E. Wolanski & B. Kjerfve (1990). Mixing, trapping and outwelling in the Klong Ngao mangrove swamp, Thailand. *Estuarine, Coastal and Shelf Science*, 31(5), 667-688.

Webb, E.L., D.A. Friess, K.W. Krauss, D.R. Cahoon, G.R. Guntenspergen & J. Phelps (2013). A global standard for monitoring coastal wetland vulnerability to accelerated sea-level rise. *Nature Clim. Change*, 3(5), 458-465.

Widdows, J., P.L. Friend, A.J. Bale, M.D. Brinsley, N.D. Pope & C.E.L. Thompson (2007). Inter-comparison between five devices for determining erodability of intertidal sediments. *Continental Shelf Research*, 27, 1174-1189.

Winterwerp, J.C., W.G. Borst & M.B. de Vries (2005). Pilot study on the erosion and rehabilitation of a mangrove mud coast. *Journal of Coastal Research*, 21(2), 223-230.

Winterwerp, J.C., P.L.A. Erftemeijer, N. Suryadiputra, P. Eijk & L. Zhang (2013). Defining eco-morphodynamic requirements for rehabilitating eroding mangrove-mud coasts. *Wetlands*, 33(3), 515-526.

Wolanski, E. (1992). Hydrodynamics of mangrove swamps and their coastal waters. *Hydrobiologia*, 247, 141-161.

Wolanski, E., M. Jones & J.S. Bunt (1980). Hydrodynamics of a tidal creek-mangrove swamp system. *Marine and Freshwater Research*, 31(4), 431-450.

Wolanski, E., Y. Mazda & P. Ridd (1992). Mangrove hydrodynamics. In: A.I. Robertson and D.M. Alongi (Eds.), *Tropical mangrove ecosystems*. American Geophysical Union, Washington DC, 43-62.

Wolanski, E., Y. Mazda, B. King & S. Gay (1990). Dynamics, flushing and trapping in Hinchinbrook channel, a giant mangrove swamp, Australia. *Estuarine, Coastal and Shelf Science*, 31(5), 555-579.

Woodroffe, C.D. (1982). Geomorphology and development of mangrove swamps, Grand Cayman Island, West Indies. *Bulletin of Marine Science*, 32(2), 381-398.

Woodroffe, C.D. (1985). Studies of a mangrove basin, Tuff Crater, New Zealand: II. Comparison of volumetric and velocity-area methods of estimating tidal flux. *Estuarine, Coastal and Shelf Science*, 20(4), 431-445.

Woodroffe, C.D. (1992). Mangrove sediments and geomorphology. In: A.I. Robertson and D.M. Alongi (Eds.), *Tropical mangrove ecosystems*. American Geophysical Union, Washington DC, 7-41.

Wu, Y., R.A. Falconer & J. Struve (2001). Mathematical modelling of tidal currents in mangrove forests. *Environmental Modelling & Software*, 16(1), 19-29.

Yang, S., S. Tan & S. Lim (2004). Velocity distribution and dip-phenomenon in smooth uniform open channel flows. *Journal of Hydraulic Engineering*, 130(12), 1179-1186.

Young, I.R., S. Zieger & A.V. Babanin (2011). Global trends in wind speed and wave height. *Science*, 332(6028), 451-455.

REFERENCES

APPENDICES

APPENDIX A – CREEK DISCHARGE STANDARDIZATION

Four weeks of tidal discharge time-series for the creek at K3 (Figure A.1A and B) were centred around high water (t_{HW} = 0 hrs). The observed tidal discharge curves were normalized by (i) dividing the discharge by the maximum discharge Q_{max} [m^3/s] observed during each tide and (ii) dividing the time by the time the observation point was inundated $T_{flooded}$ [hrs], as a proxy for creek discharge duration (Figure A.1C). The normalization parameter Q_{max} showed consistent correlation with HW (R^2 = 0.97; Figure A.1D) while the relation between $T_{flooded}$ and HW featured three tidal regimes (Figure A.1E). The non-dimensional discharge curves were averaged per tidal regime, finally returning three parameterized non-dimensional discharge curves for the discharge through the main creek at K3 (Figure A.1C). Reconstruction of the observed discharges from these non-dimensional curves with the observed high water levels proved to be sufficiently accurate (Nash-Sutcliffe model accuracy = 0.83; Figure A.1A and B).
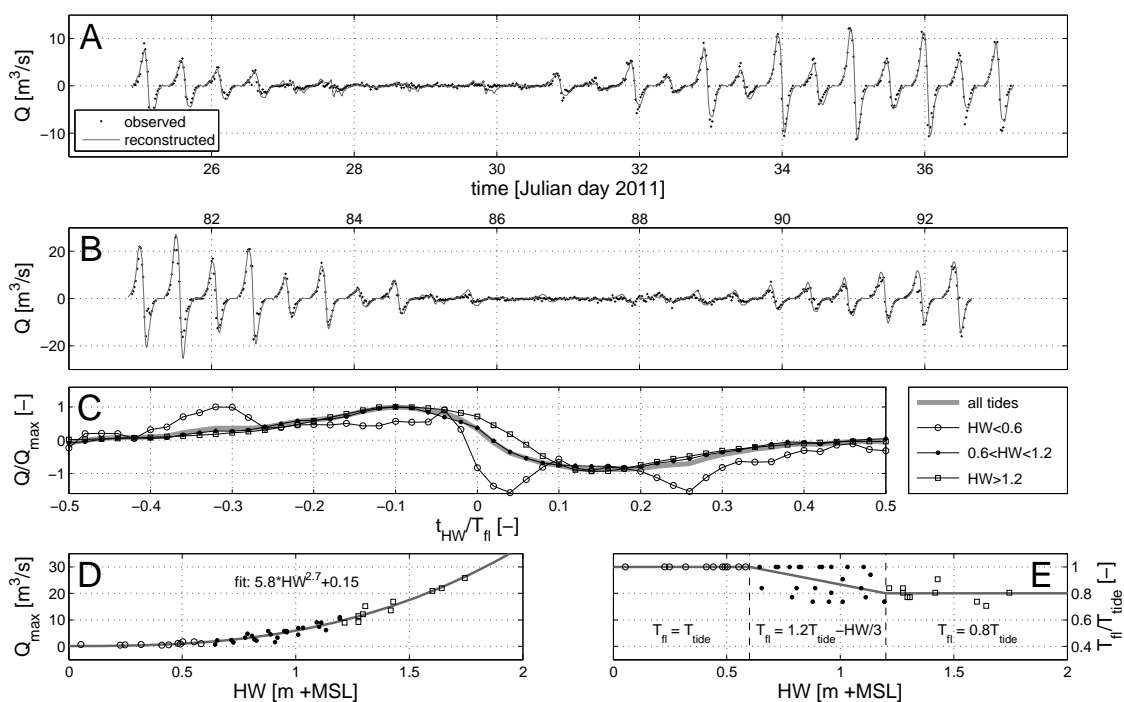
Figure A.1: Field observations and reconstruction of creek discharges at K3. (A,B) Observed discharges (calculated from observed velocities, water depths and topography) through the main creek at K3 for the periods shaded in (Figure 3.2). Reconstructed discharge curves are obtained from the normalized discharges by applying the parameterizations shown in (D) and (E) to the normalized discharge curves in (C). The observed high water level is the single input parameter for this reconstruction. (C) Normalization of the tidal discharge at K3 according to three tidal regimes: discharge is normalized by the maximum tidal discharge Q_{max} [m^3/s], time with respect to high water t_{HW} [hrs] is normalized by the time of inundation T_{fl} [hrs]. (D) The empirical relation between the maximum tidal discharge and the water level at high tide HW. (E) Inundation times (as a coefficient of the duration of a tidal cycle T_{tide}) are constant for the highest and lowest tides, but vary for intermediate HW.

APPENDIX B – SPECTRAL ANALYSIS

For the spectral analysis of the obtained water level time series we followed the six-step method presented by *Hegge and Masselink* [1996]:

1.   De-trending the signal to overcome within-burst tidal water level fluctuations.

2.   Applying a Hann-taper w for preventing leakage of spectral density from large peaks:

$$w(n) = 0.5\left(1 - \cos\frac{2 \cdot \pi \cdot n}{N-1}\right) \qquad for\ n = 1,2...,N \tag{B.1}$$

Wherein N is the length of the data series (i.e. 4096).

3.   Running an FFT procedure to calculate the Fourier coefficients $X(m)$ of the observed water depth time series $x(n)$ of length N. Each coefficient relates to a frequency interval $f(m)$:

$$X(m) = \sum_{n=1}^{N} x(n) \cdot e^{-2\pi i(m-1)(n-1)/N} \qquad for\ m = 1,...,N \tag{B.2}$$

$$f(m) = m \cdot f_s / N \qquad for\ m = 1,...,N \tag{B.3}$$

With f_s representing the sampling frequency (i.e. 10 Hz).

4.   Calculating the pressure response factor K_p in order to take into account the attenuation of the wave signal towards the bed. This factor depends on the water depth and wave length and hence can only be calculated after the FFT has been executed. Assuming linear wave theory K_p [-] can be calculated as [*CERC*, 1984]:

$$K_p(m) = \frac{\cosh(k(m) \cdot z)}{\cosh(k(m) \cdot d)} \qquad for\ m = 1,...,N \tag{B.4}$$

With the wave number $k = 2\pi/L$ [m^{-1}] calculated for each frequency interval $f(m)$ of the Fourier coefficients. The water depth d [m] and the elevation of the sensor above the bed z [m] are assumed constant within each burst.

5.   Calculating the one-sided periodogram P [m^{2}s], expressing the spectral density as a function of the wave frequency in interval m. The one-sided periodogram follows from the Fourier coefficients. Only the first half ($1 \leq N \leq (N/2+1)$) of the Fourier coefficients is taken into account, as the second half consists of complex conjugates:

$$P(m) = \frac{\left| X(m) \cdot K_p(m)^{-1} \right|^2}{f_s N} \qquad for \; m = 1, \frac{N}{2} + 1$$

$$P(m) = \frac{2 \cdot \left| X(m) \cdot K_p(m)^{-1} \right|^2}{f_s N} \qquad for \; m = 2,..., \frac{N}{2}$$

(B.5)

6.   Applying a correction factor C to take into account the effect of the taper in step 2 and calculating the energy density spectrum S:

$$C = \frac{N}{\sum_{n=1}^{N} w(n)^2}$$

(B.6)

$$S(f(m)) = C \cdot P(m) \qquad with \; m = 1,..., N/2$$

(B.7)

With $f(m)$ the frequency [Hz] of the mth component of the energy density spectrum S [m²s].

The results of this procedure were used to derive significant wave heights (H_s [m]), root-mean-square wave heights (H_{rms} [m]), mean wave periods (T_m [s]) and total wave energy (E_{tot} [J/m²]) for every burst of wave data:

$$E_{tot} = \sum_{m=1}^{N/2} S(f_m) \cdot \Delta f \cdot \rho g$$

(B.8)

$$H_s = 4\sqrt{m_0}$$

(B.9)

$$H_{rms} = 2\sqrt{2 \cdot m_0}$$

(B.10)

$$T_m = m_0 / m_1$$

(B.11)

Wherein Δf represents the frequency bandwidth of the spectrum (i.e. f_s/N [Hz]) and m_0 and m_1 are the 0th and 1st spectral moments of the energy density spectrum:

$$m_a = \sum_{m=1}^{N/2} S(f_m) \cdot f_m^{\,a} \cdot \Delta f \qquad with \; a = 0,1$$

(B.12)

APPENDIX C – VEGETATION DATA

C.1 VEGETATION PARAMETERS TRANSECT KANTANG

Table C.1 – Vegetation composition and structure of the vegetation zones mapped along the Kantang transect (Figure 4.2). For each tree type, the number N of individuals in a 20x20 m^2 survey plot is indicated, along with the diameter d [mm] of the tree trunk at multiple elevations z [m] above the forest floor. For the stilt root networks of *Rhizophora* trees, the number n and average diameter d [mm] of all elements are presented. For the pneumatophore cover of the forest floor, the number of pneumatophores N in three different 1x1 m^2 survey plots is presented, along with the average height h [mm] and diameter d [mm] of the pneumatophores in each plot.

Vegetation type	Category	TKI[a]		d(z)				TKI[b]		d(z) or n(z)·d(z)				TKII[a]		d(z) or n(z)·d(z)				TKII[b]		d(z) or n(z)·d(z)			
		N	$h;d$	0.1 m	0.5 m	1.0 m	2.0 m	N	$h;d$	0.1 m	0.5 m	1.0 m	2.0 m	N	$h;d$	0.1 m	0.5 m	1.0 m	2.0 m	N	$h;d$	0.1 m	0.5 m	1.0 m	2.0 m
Pneumatophores[1] S	S	392	50; 4.8	-	-	-	-	312	55; 6.6	-	-	-	-	28	37; 5.2	-	-	-	-	0	-	-	-	-	-
M	M	724	44; 4.5	-	-	-	-	452	35; 5.5	-	-	-	-	213	36; 5.2	-	-	-	-	39	14; 5.7	-	-	-	-
L	L	2172	82; 5.5	-	-	-	-	588	62; 6.0	-	-	-	-	519	46; 4.5	-	-	-	-	107	24; 6.9	-	-	-	-
Avicennia/Sonneratia[2] XS	XS	78	-	7	6	2	-	55	-	9	5	3	-	0	-	-	-	-	-	0	-	-	-	-	-
S	S	70	-	23	17	13	-	35	-	22	17	14	-	0	-	-	-	-	-	0	-	-	-	-	-
M	M	31	-	65	60	45	38	27	-	86	75	71	64	0	-	-	-	-	-	1	-	71	67	57	57
L	L	9	-	170	130	122	104	9	-	230	210	200	169	0	-	-	-	-	-	0	-	-	-	-	-
XL	XL	2	-	1220	1190	1140	975	3	-	722	610	550	520	1	-	460	390	370	340	0	-	-	-	-	-

Table continues on next page.

Table C.1 – Continued.

Vegetation type	Category	TKIᵃ						TKIᵇ						TKIIᵃ						TKIIᵇ					
		N	$h; d$	$d(z)$				N	$h; d$	$d(z)$ or $n(z) \cdot d(z)$				N	$h; d$	$d(z)$ or $n(z) \cdot d(z)$				N	$h; d$	$d(z)$ or $n(z) \cdot d(z)$			
				0.1 m	0.5 m	1.0 m	2.0 m			0.1 m	0.5 m	1.0 m	2.0 m			0.1 m	0.5 m	1.0 m	2.0 m			0.1 m	0.5 m	1.0 m	2.0 m
*Rhizophora*²	S	0	-	-	-	-	-	0	-	-	-	-	-	5	-	15·40	7·50	4·53	2·48	12	-	7·23	4·32	1·49	1·41
	M	0	-	-	-	-	-	6	-	11·22	17·18	7·18	10·8	14	-	310·27	115·23	50·30	13·47	36	-	168·23	76·24	42·24	9·36
	L	0	-	-	-	-	-	0	-	-	-	-	-	5	-	325·26	203·23	68·31	6·67	12	-	342·26	100·31	21·45	2·155
Dead stems²		0	-	-	-	-	-	9	610; 165	-	-	-	-	0	-	-	-	-	-	0	-	-	-	-	-

[1] Pneumatophore counts (N) are per plot of 1 m². Spatial coverage by the sparse (S), average (M) and dense (L) pneumatophore densities are assumed 20-60-20%, respectively.

[2] Tree counts (N) are per plot of 400 m². For the *Rhizophora* trees the total number of trees within each plot is assumed to consist of 20% smallest trees (S), 60% average trees (M) and 20% largest trees (L).

C.2 VEGETATION PARAMETERS TRANSECT PALIAN

Table C.2 – Vegetation composition and structure of the vegetation zones mapped along the Palian transect (Figure 4.2). For each tree type, the number N of individuals in a 20x20 m^2 survey plot is indicated, along with the diameter d [mm] of the tree trunk at multiple elevations z [m] above the forest floor. For the stilt root networks of *Rhizophora* trees, the number n and average diameter d [mm] of all elements are presented. For the pneumatophore cover of the forest floor, the number of pneumatophores N in three different 1x1 m^2 survey plots is presented, along with the average height h [mm] and diameter d [mm] of the pneumatophores in each plot.

Vegetation type	Category	TPI						TPII					
		N	$h; d$	$d(z)$				N	$h; d$	$d(z)$ or $n(z) \cdot d(z)$			
				0.1 m	0.5 m	1.0 m	2.0 m			0.1 m	0.5 m	1.0 m	2.0 m
Pneumatophores[1]	S	460	35;5.0	-	-	-	-	-	-	-	-	-	-
	M	516	43;5.6	-	-	-	-	-	-	-	-	-	-
	L	1728	50;4.5	-	-	-	-	-	-	-	-	-	-
Avicennia/Sonneratia[2]	XS	1	-	16	10	-	-	290	-	24	9	8	-
	S	0	-	-	-	-	-	2	-	56	44	40	28
	M	0	-	-	-	-	-	5	-	69	55	58	51
	L	0	-	-	-	-	-	0	-	-	-	-	-
	XL	3	-	870	760	660	610	2	-	750	575	490	450
Rhizophora[2]	S	0	-	-	-	-	-	21	-	19·40	5·39	1·60	1·51
	M	0	-	-	-	-	-	61	-	191·28	72·25	24·38	8·22
	L	0	-	-	-	-	-	21	-	458·29	76·36	18·50	39·18

[1] Pneumatophore counts (N) are per plot of 1 m^2. Spatial coverage by the sparse (S), average (M) and dense (L) pneumatophore densities are assumed 20-60-20%, respectively.

[2] Tree counts (N) are per plot of 400 m^2. For the *Rhizophora* trees the total number of trees within each plot is assumed to consist of 20% smallest trees (S), 60% average trees (M) and 20% largest trees (L).

PUBLICATIONS

PEER-REVIEWED JOURNAL PAPERS

Horstman, E.M., C.M. Dohmen-Janssen & S.J.M.H. Hulscher (subm.). Wave attenuation in mangroves: a quantitative approach to field observations.

Horstman, E.M., C.M. Dohmen-Janssen, T.J. Bouma & S.J.M.H. Hulscher (subm.). Tidal-scale flow routing and sedimentation in mangrove forests: combining field data and numerical modelling.

Horstman, E.M., C.M. Dohmen-Janssen & S.J.M.H. Hulscher (2013). Flow routing in mangrove forests: A field study in Trang province, Thailand. *Continental Shelf Research*, 71, 52-67. DOI: 10.1016/j.csr.2013.10.002

Balke, T., T.J. Bouma, P.M.J. Herman, **E.M. Horstman,** C. Sudtongkong & E.L. Webb (2013). Cross-shore gradients of physical disturbance in mangroves: implications for seedling establishment. *Biogeosciences*, 10(8), 5411-5419. DOI: 10.5194/bg-10-5411-2013

Friess, D.A., K.W. Krauss, **E.M. Horstman**, T. Balke, T.J. Bouma, D. Galli & E.L. Webb (2012). Are all intertidal wetlands naturally created equal? Bottlenecks, thresholds and knowledge gaps to mangrove and saltmarsh ecosystems. *Biological reviews*, 87(2), 346-366. DOI: 10.1111/j.1469-185X.2011.00198.x

Balke, T., T.J. Bouma, **E.M. Horstman**, E.L. Webb, P.L.A. Erftemeijer & P.M.J. Herman, (2011). Windows of opportunity: thresholds to mangrove seedling establishment on tidal flats. *Marine Ecology Progress Series*, 2011(440), 1-9. DOI: 10.3354/meps09364

Mulder, J.P.M., S. Hommes & **E.M. Horstman** (2011). Implementation of coastal erosion management in the Netherlands. *Ocean and Coastal Management*, 2011(54), 888-897. DOI: 10.1016/j.ocecoaman.2011.06.009

Horstman, E.M., K.M. Wijnberg, S.J.M.H. Hulscher & A.J. Smale (2009). On the consequences of a long-term perspective for coastal management. *Ocean and Coastal Management*, 52(12), 593-611. DOI: 10.1016/j.ocecoaman.2009.08.009

Horstman, E.M., K.M. Wijnberg, A.J. Smale & S.J.M.H. Hulscher (2009). Long-term coastal management strategies: useful or useless? *Journal of Coastal Research*, 2009(56), 233-237.

Horstman, E.M. (2007). Water storage to protect our polders from flooding; strategies for preventing water inconvenience resulting from intensive rainfall. *Twente Student Review*, 2007(3), 20-26. ISSN: 1873-9024

CONFERENCE PAPERS

Horstman, E.M. & C.M. Dohmen-Janssen (2013). Bio-physical interactions in mangroves. In: E. Meilianda et al. (Eds.), *Proceedings of the Aceh International Symposium on Civil Engineering* (AISCE), 19-20 September 2013, University of Syiah Kuala, Banda Aceh.

Horstman, E.M., C.M. Dohmen-Janssen & S.J.M.H. Hulscher (2013). Modeling tidal dynamics in a mangrove creek catchment in Delft3D. In: P. Bonneton & T. Garlan (Eds.), *Extended abstracts of Coastal Dynamics 2013*, 24-28 June 2013, Arcachon, France (pp. 833-844).

Horstman, E.M., C.M. Dohmen-Janssen & S.J.M.H. Hulscher (2013). Modelling mangrove dynamics; simulating flow routing and sediment deposition patterns in Delft3D. In: *Book of abstracts NCK-Days 2013*, 14-15 March 2013, Kijkduin, The Netherlands.

Horstman, E.M., C.M. Dohmen-Janssen, P. Narra, N.J.F. van den Berg, M. Siemerink, T. Balke, T.J. Bouma & S.J.M.H. Hulscher (2012). Wave attenuation in mangrove forests; field data obtained in Trang, Thailand. In: J. McKee-Smith & P. Lynett (Eds.), *Proceedings of 33rd International Conference on Coastal Engineering* (ICCE), 1-6 July 2012, Santander (pp. 1-15). DOI: 10.9753/icce.v33.waves.40

Horstman, E.M., C.M. Dohmen-Janssen, T.J. Bouma. & S.J.M.H. Hulscher (2012). Flow routing in mangrove forests: field data obtained in Trang, Thailand. In: W.M. Kranenburg, E.M. Horstman & K.M. Wijnberg (Eds.), NCK-days 2012: Crossing borders in coastal research. *Jubilee conference proceedings 20th NCK-days*, 13-16 March 2012, University of Twente, Enschede, The Netherlands (pp. 147-151). DOI: 10.3990/2.186

Bouma, T.J., P.L.A. Erftemeijer, T. Balke, **E.M. Horstman**, S.M. Yaakub, J.T.I. Tanzil, D.A. Friess, D. Galli, C.M. Dohmen-Janssen, M.C.J.L. Jeuken, P.A. Todd & E.L. Webb (2011). Sediment and Ecology: how to minimize impacts of dredging and create opportunities for restoration on tropical coasts? In: *Proceedings of the CEDA dredging days*, 10-11 November 2011, Rotterdam.

Balke, T., E. van den Elzen, **E.M. Horstman**, M.C.J.L. Jeuken, P.M.J. Herman, E.L. Webb & T.J. Bouma (2011). Tree vs. tide: thresholds to mangrove seedling establishment on tidal flats. In: S. Chalifoux (Ed.), *Conference abstracts 21st Biennial conference of the Coastal and Estuarine Research Federation*, 6-10 November 2011, Daytona Beach, Florida USA (p. 9).

Horstman, E.M., M. Siemerink, T. Balke, C.M. Dohmen-Janssen, T.J. Bouma & S.J.M.H. Hulscher (2011). Sediment dynamics in a mangrove creek catchment in Trang, Thailand. In: X. Shao, Z. Wang & G. Wang (Eds.), *Proceedings of the 7th IAHR Symposium on River, Coastal and Estuarine Morphodynamics* (RCEM), 6-8 September 2011, Tsinghua University, Beijing (pp. 675-685).

Horstman, E.M., M. Siemerink, C.M. Dohmen-Janssen, T.J. Bouma & S.J.M.H. Hulscher (2011). Sediment dynamics in a mangrove creek catchment. In: *Book of abstracts 5th International Short Conference on Applied Coastal Research*, 6 - 9 June 2011, RWTH Aachen University, Aachen, Germany (pp. 27-28).

Horstman, E.M., T. Balke, T.J. Bouma, C.M. Dohmen-Janssen & S.J.M.H. Hulscher (2011). Optimizing methods to measure hydrodynamics in coastal wetlands: evaluating the use and positioning of ADV, ADCP and HR-ADCP. In: J. McKee Smith & P. Lynett (Eds.), *Proceedings of 32nd International Conference on Coastal Engineering* (ICCE), 30 June - 5 July 2010, Shanghai (pp. 1-11). DOI: 10.9753/icce.v32.waves.51

Horstman, E.M., C.M. Dohmen-Janssen, T. Balke, T.J. Bouma, D.A. Friess, D. Galli, E.L. Webb, P.M.J. Herman & S.J.M.H. Hulscher (2010). Measuring short-term biophysical interactions in coastal mangroves in Matang, Malaysia. In: P. Hoekstra (Ed.), *Book of abstracts NCK-Days 2010*, 25-26 March 2010, Westkapelle, The Netherlands (p. 41).

Horstman, E.M., K.M. Wijnberg, A.J.P. Helder, A.J. Smale, S.J.M.H. Hulscher & C.M. Dohmen-Janssen (2009). Long-term coastal management strategies: useful or useless? In: M.J. Baptist (Ed), *Book of abstracts NCK-Days 2009*, 26-27 March 2009, Texel, The Netherlands (p. 32).

Horstman, E. M. (2008). Improved long-term coastal management as a result of a large-scale spatial perspective. In: *De Nationale Waterconferentie*, 24 september 2008, Scheveningen. Eindhoven: Studiecentrum voor Bedrijf en Overheid.

EDITORSHIP

Kranenburg, W.M., **E.M. Horstman** & K.M. Wijnberg (Eds.). (2012). NCK-days 2012 Crossing borders in coastal research. *Jubilee conference proceedings 20th NCK-days*. Enschede: University of Twente. http://proceedings.utwente.nl/165/

NON-REVIEWED PAPERS

Horstman, E.M. (2009). Lange-termijn visie kustbeheer. *ConcepTueel*, 18(1), 18-23.

Horstman, E.M., A.J.P. Helder & K.M. Wijnberg (2008). Lange-termijn visie kustbeheer vraagt grotere ruimteschalen. *Land + Water*, 48(11), 24-25.

REPORTS

Horstman, E.M. (in prep.). *Data report: Field campaign Trang, Thailand*; November 2010 - May 2011. University of Twente, Enschede, The Netherlands.

Horstman, E.M. (2012). *Ontwikkeling van de Rif-mangroven in Otrobanda; het creëren van een gezond, educatief en recreatief stadspark* (in Dutch). Stichting ABC Advies, rapport nr. 159. Willemstad, Curaçao: Stichting ABC. ISBN: 978-90-815922-5-3.

Horstman, E.M., J.P.M. Mulder & S. Hommes (2009). *Voorstel uitvoeringskader kustonderhoud* (in Dutch). Civil Engineering and Management Research Report 2009R-003/WEM-003. Enschede: Water Engineering & Management (WEM).

ABOUT THE AUTHOR

Erik Horstman was born on 6 December 1983 in Enschede, The Netherlands. He finished his pre-university education (gymnasium) in 2002 at Het Stedelijk Lyceum in Enschede. The same year, Erik started his studies in Civil Engineering and Management at the University of Twente. In 2005 he obtained his BSc degree *cum laude* after a final project on water storage strategies for excess rainwater in a Dutch polder, executed at Royal Haskoning in Rotterdam. In 2008 Erik obtained his MSc degree *cum laude* with a graduation project on long-term and large-scale coastal management strategies for the Holland coast, carried out at Witteveen+Bos in Deventer. During his studies, Erik participated in a study tour to India, organized a symposium for the study association, was seated in the study association's education committee and he has been a teaching assistant.

After his studies, Erik started as a junior researcher at the Water Engineering and Management department of the University of Twente. In his first year, he wrote two papers on his MSc thesis and he taught multiple courses of both the bachelor's and the master's programme, ranging from design projects to advanced engineering courses. In 2009, he started his PhD project on short-term bio-physical interactions in coastal mangroves. As part of this project, he worked at the National University of Singapore for nine months (2010) and he conducted field studies in southern Thailand for six months (2010-2011). Preparations and execution of this challenging field campaign were mainly managed by himself. Throughout his PhD, Erik kept on teaching a variety of courses, supervised three master's students and a bachelor's student with their final projects, and he frequently visited national and international conferences and workshops. In addition, he was seated in the faculty council and was co-organizer of a national conference.

Well aware of the beauty and value of mangrove ecosystems, Erik contributed to a mangrove fund-raising exhibition and volunteered in a consultancy project supporting the maintenance of a mangrove patch in Willemstad, Curaçao. Besides his addiction to work, Erik likes to get exhausted by cycling and running, to relax and recharge by cooking and enjoying food, and to explore the world by travelling to unfamiliar places and cultures.

Mangroves are coastal wetland ecosystems in the upper intertidal area. Salt-tolerant mangrove vegetation dwells on fine substrates in sheltered, low-energy coastal environments such as estuaries and lagoons. At the interface between land and sea, mangroves provide a plethora of regulating, habitat and provisioning services. This thesis focusses on their regulating services: sediment trapping and wave attenuation, providing coastal stabilization and safety. These processes are the result of characteristic bio-physical interactions between mangrove vegetation, hydrodynamics and sediment dynamics in the intertidal.

Understanding the mechanisms determining the contribution of mangroves to coastal safety is indispensable to pinpoint the effects of widespread mangrove losses. This understanding starts with a sound knowledge of the short-term bio-physical interactions in mangroves. In this thesis, spatially explicit observations of flow routing, sediment deposition and wave attenuation in coastal mangroves are linked to gradients in elevation and vegetation. These observational data are collected at three different field sites along the Thai Andaman coast. In addition, a numerical model of one of the study sites is set up in Delft3D. This model is used to study the sensitivity of established tidal-scale flow routing and deposition patterns in mangroves to instantaneous environmental changes.

UNIVERSITY OF TWENTE.